Synthetic and Computational Investigations of Highly Reduced Main Group Organometallics of Groups XIII and XIV

Gareth Roland Nelmes

August 2026

A thesis submitted for the degree of Doctor of Philosophy of The Australian National University.



Australian National University

© Copyright by Gareth Roland Nelmes 2026

All Rights Reserved

Declaration

This thesis contains no material which has been accepted for the award of any other degree or diploma in any university. To the best of the author's knowledge, it contains no material previously published or written by another person, except where due reference is made in the text. The author guarantees that generative AI was not used in any form in the production of this thesis.

This research was supported by the Commonwealth through an Australian Government Research Training Program Scholarship. A portion of the research within this thesis was produced at the University of Bath under the Visiting Postgraduate Scholars scheme.

Gareth R Nelmes

Acknowledgments

To have so many people to thank is a wonderful burden. Each of you has contributed to me in some intangible way, and to be loved is to be changed. Please take this small distillate of my gratitude for what fraction of emotion words can convey.

To my parents, Anne-maree and Laurence Nelmes, I owe you everything. I cannot imagine a better start to life filled with more opportunity or more unconditional love. This work, and my whole life, is only possible through you.

My triplet sisters, Felicity and Cecilia Nelmes, know me better than I know myself. Everything you have done for me, every forgiveness, every hug, meal, joke, a lifetime of memories- I love you, other portions of myself.

Jamie Hicks, we seem to have grown old. In the seven years I have known you, fire, flood, plague, and pecuniary crisis have befallen us. But there have been good times too. From you I have learnt almost all the synthesis I know, and how not to run a column. The chemical skills from you that are now mine are innumerable and worth every conflagration.

But what you have really given me is far more important, and perhaps far less deliberate. What little pragmatism I have comes from you, and my capacity for effort is from your inspiration. Your positivity is infectious and has been so necessary; I will never forget as you ran down the corridor jumping up and down yelling “We got it!” for your first DP grant. We cannot sit in adjacent chairs during a seminar because our leg bouncing is too extreme, and our mutual sudden stops have panicked many students.

You have been my mentor, exemplar, and confidant for most of my adult life. Perhaps for what I am most grateful has been your trust. Your faith in me is touching and has meant everything.

I merely hope in return for all this, I taught you a little chemistry.

My supervisor away from home, Claire McMullin made a place for me on the other side of the world. I loved my time at the University of Bath, only made possible by you, as you conveyed to me the idiosyncrasies and de rigueur standards of super computing and computational chemistry.

Similarly, Sam Neale taught me how to use a computer. I am grateful for your endless patience and gentle guidance; I could not have asked for a more supportive or hilarious officemate and I will never forget your stories about local celebrities.

What synthesis I know that did not come from Jamie has come from Fabi Kallmeier. An incredible chemist and an effective, good-hearted leader in the lab, I am lucky to have worked with you. Many thanks for putting up with my ridiculous notions for so many years, and stapling my name on so much of your good work.

No less crucial to the production of this work have been the friends and colleagues who have materially impacted my health and wellbeing, or the work itself, over the course of this composition.

For so many years you have been there for me at my best and worst, no one has proven themselves so much in my corner as Andie Delaney. Navigating chemistry, school politics, life, and nearly every aspect of this sordid existence, I can't do it without you.

My time in England was made so wonderful by John Kragskow and Edmund Little. John, sharing an office with you was the highlight of my day every day, from sharing coughing lotus pods to shaking our fists angrily at the sky. Thank you both for being so welcoming and friendly, I will never forget walking up Solsbury Hill, or the best roasts of my life, or the sloe gin.

For enduring countless hours of Spirit Island, and sometimes letting me win a little Mario Kart, John Dykstra and Ragnel Jansdotter. Thank you for reminding me what I'm worth and what is really inside.

Elsie Perry and Andy Yin, whenever we are together it feels like we were never apart. For tepid philosophy takes, DOTA2, Magic, maths, computer science, and any other nerd rubbish I can possibly contemplate, I'm grateful to always have you.

To someone who has known me for longer than I have even known myself, I thank Margaret McElhinny. For endless support, encouragement, tea, and dog walks, I cannot express my gratitude enough. You've been there for my best and worst, and many of the best parts of me come from your kindness.

Despite years of crash-outs, you're still here. Thank you for everything, Lauren Nelson-Lee. If you had your way this would have been done much sooner, so wise.

Jessica Porter, I have never met someone so authentic, so true to themselves, filled with so much creativity and love of life. Every day, you provide a little antidote for my existential mind poison, and every day, a little smile.

Until your first child, I had never held a baby. Michael Stevens, I am thankful for our shared taste in wine, and for sharing the beautiful moments of your budding family with me. Max and Eleanor, you are in good hands, and I'm proud to be your uncle.

Ryan Huo, how can I possibly thank you. Without your synthesis, the most significant work within this thesis would not exist, there would be no chapter three. I will miss the Shanghai Dumpling Cafe, and think of you every time I walk past it. Your friendship meant I was never alone throughout this work, and I could not be more proud of what you have achieved.

For enduring years of lectures, tirades, quips, and having to share an office with me writing up, my thanks to Emily Nahon. You have shown me there is more than one way to be a chemist, given me such solidarity, and not to mention again performed all the synthesis alluded to in chapter four. Here's to a fruitful career.

Li Feng Lim, thank you for teaching me everything I know about EPR. Thank you for so many historical papers, I'm grateful to have had someone who loves chemistry for its beauty and history so much as I do. You are certainly the most talented and hardworking amongst us, it is only a shame you prefer the wrong kind of spin. Do not hate the scorpion, he will never forget the clean base bath.

For teaching me how to actually run a column, Rosie Goodwin. I hope your future students give you less grief, and that your calculations always converge. Thank you most of all for your charity and guidance.

For being such friends and labmates, I am grateful to Liam Pascoe, Jacob McMullen, Becca Majchrzak, Max Les, Caitlin Lindsay, and Jingyun Wu. Each of you has made working together a wonderful thing. The Hicks and Colebatch groups have grown and changed so much over the years and I'm glad to have been there. Be good to each other.

Of your many fantastic qualities, the love you share with the world, the care you show your students, and your unwavering sense of right, overwhelm me with a sense of the goodness in the world. Dan Preston, I really ask myself "What would Dan do?", I feel it can never go wrong.

To my teachers and mentors, this work is impossible without you, but more importantly a little part of how I think was originally yours. My understanding of the world is changed by each of you, Mark Ellison, Tony Hill, Mike Hill, Nick White, Nick Cox, Edie Sevick, Peter Gill, Gottfried Otting, Mal McLeod, and Annie Colebatch.

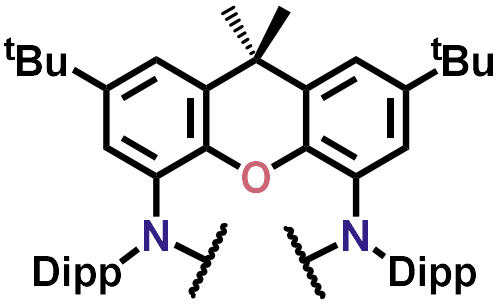
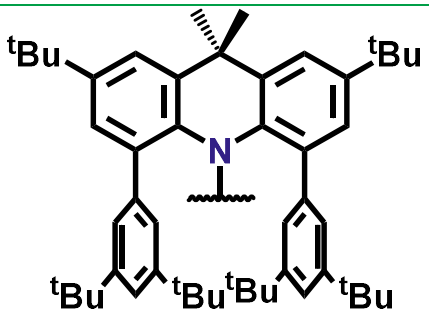
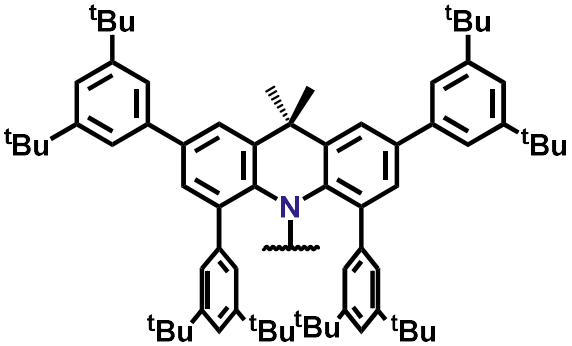
For those from whom I learn, and those to whom I teach.

Sic itur ad astra.

Abbreviations

$\oplus$	Direct Sum
∇	Del operator
∇^2	Del^2 operator
$\angle$	Angle
Δ	Change in a quantity
δ	Chemical shift relative to tetramethylsilane
ΔG	Difference in Gibbs free energy
$\Delta G^{\ddagger}$	Difference in Gibbs free energy of a transition state
π	Pi symmetry orbital
σ	Sigma symmetry orbital or isotropic shielding tensor
σ^*	Antibonding sigma symmetry orbital
$\psi(r)$	Arbitrary wavefunction
ζ_x	Exponent of an x-Type Additional Basis Function
$^nJ_{XY}$	Coupling constant through n bonds between elements X and Y
Å	Angstroms
Acr	Acridane
ADF	Amsterdam Density Functional
AMS	Amsterdam Modelling Suite
BCP	Bond Critical Point
BP86	Becke 1988 Exchange Perdew 1986 Correlation Density Functional
BSIE	Basis Set Incompleteness Error
BSSE	Basis Set Superposition Error
C_6D_6	Per-deutero benzene
C_6D_{12}	Per-deutero cyclohexane
cAAC	cyclic Alkyl Amino Carbene
CCSD(T)	Coupled Cluster singles, doubles, and perturbative triples
Cp	Cyclopentadienyl
-D3BJ	Grimme D3 dispersion correction with BJ dampening
Dep	2,6-Diethylphenyl
DFT	Density Functional Theory

Dipp	2,6-Diisopropylphenyl
e^-	Electron(s)
EDA	Energy Decomposition Analysis
ELF	Electron Localisation Function
EPR	Electron Paramagnetic Resonance
ETS-NOCV	Extended Transition State - Natural Orbitals of Common Valence
E_{xc}	Exchange-Correlation Energy
FT-IR	Fourier Transform Infrared
GGA	Generalised Gradient Approximation
$\hbar$	Reduced Planck constant
HF	Hartree-Fock
HMDS	Hexamethyldisilylazane
HOMO	Highest Occupied Molecular Orbital
IRC	Intrinsic Reaction Coordinate
k_x	Rate constant for reaction x
L	Abstract or locally defined ligand
LCAO	Linear Combination of Atomic Orbitals
LUMO	Lowest Unoccupied Molecular Orbital
M06-2X	2006 Minnesota functional with double global hybrid exchange
Me	Methyl
Mes	Mesityl
mGGA	meta Generalised Gradient Approximation
MP2	Second-order Møller-Plesset perturbation theory
NacNac	Beta-diketiminate
NBO	Natural Bonding Orbitals
NCI	Noncovalent Interactions
NHC	N-Heterocyclic Carbene
NMR	Nuclear Magnetic Resonance
NNA	Non-Nuclear Attractor

NON	
PBE	Perdew-Burke-Ernzerhof GGA density functional
PES	Potential Energy Surface
ppm	Parts per million
QTAIM	Quantum Theory of Atoms In Molecules
R	Universal gas constant
RMS	Root-Mean Square
^{t}Bu	Tertiary-butyl; 1,1-dimethylethyl
^{tBu2Ph}**AcrN**	
^{tBu2Ph}**AcrN′**	
THF	Tetrahydrofuran
TMEDA	Tetramethylethylenediamine
TMS	Tetramethylsilane
TS	Transition State
Xs.	Excess

Abstract

This thesis concerns the fundamental understanding of low-valent compounds of Groups 13 and 14 through a combination of synthetic and computational investigations. Low-valent main-group species continue to challenge conventional descriptions of chemical bonding and reactivity, frequently displaying unusual electronic structures and reaction pathways. Despite substantial advances in the field, many fundamental questions concerning the stabilisation, electronic structure, and particularly mechanisms of formation and reactivity of these compounds remain unresolved. The work presented herein seeks to address several such questions through the synthesis of novel compounds, detailed electronic structure analyses, and extensive mechanistic investigations using density functional theory.

Chapter 1 provides an introduction to low-valent main group chemistry and the computational methods employed throughout this thesis. Particular emphasis is placed upon the concepts of valency, electronic and steric stabilisation, density functional theory, and the interpretation of potential energy surfaces relevant to reaction mechanism elucidation.

Chapter 2 presents the principal synthetic component of this thesis. Two related acridanide ligands, together with their alkali-metal salts and corresponding germanium(II) and tin(II) precursor complexes, were synthesised and characterised. Reduction chemistry involving simple alkali-metal reductants and a magnesium(I) dimer produced a variety of unusual products, including the first dimagnesiogermane. Density functional theory was subsequently employed to investigate the electronic structure and mechanism of formation of this species, revealing a reductive-addition process across a magnesium-magnesium bond and providing insight into the formation of low-valent Group 14 compounds, matching analogous reactivity of isoelectronic species with zinc(I) dimer.

Chapter 3 concerns the formation of an encapsulated hexahydridosilicate dianion and its conversion into the parent silylene dianion. Benchmarking against experimental structural and spectroscopic data allowed the development of accurate density functional methodologies for low-valent chemistry. Electronic structure calculations, mechanistic investigations, and kinetic modelling were then used to examine this unprecedented transformation wherein the hexahydridosilicate loses two equivalents of dihydrogen to form the SiH_2 dianion trapped within the molecular assembly. Density functional theory revealed a reaction pathway consistent with experiment and identified an unexpected autocatalytic dehydrogenation process as the origin of the observed reactivity.

Chapter 4 investigates oxygen-extrusion reactions observed during attempts to prepare low-valent boron compounds. Extensive exploration of the relevant potential energy surfaces using density functional theory showed that closed-shell pathways were energetically inaccessible, whereas open-shell pathways involving boryl-radical intermediates were consistent with both computational predictions and experimental observations. The resulting mechanism provides an explanation for an unusual reductive skeletal-editing process involving oxygen deletion and ring contraction.

Chapter 5 briefly presents two computational studies involving aluminyl compounds. Mechanisms for the 1,4-bis activation of benzene by monomeric and dimeric aluminyl anions are examined and compared with experiment. In addition, the steric and electronic properties of a series of iron-aluminium compounds are investigated using contemporary computational descriptors and methods for quantifying ligand environment and accessibility, as is presented in the two associated publications.

Collectively, the investigations described throughout this thesis demonstrate how synthetic chemistry and modern computational methods can be used in concert to explain and predict low-valent main-group chemistry. The work expands the known chemistry of low-valent compounds of Groups 13 and 14 through the synthesis and characterisation of new molecular species, the investigation of unusual electronic structures, and the elucidation of reaction mechanisms that are otherwise experimentally inaccessible. More broadly, these studies contribute to the growing understanding of how low-valent main-group compounds activate chemical bonds, undergo redox processes, and access otherwise challenging reactivity.

Manuscripts and Publications in Support of This Work

1. Nelmes, G. R.; Brothers, P. J.; Hicks, J., Convenient one-pot synthesis and coordination chemistry of a bulky asymmetrical 9,10-dihydroacridine-based ligand, *Z. Anorg. Allg. Chem.*, **2022**, *648*, e202200127

2. Nahon, E. E.; Nelmes, G. R.; Brothers, P. J.; Hicks, J., Intramolecular C–N bond activation by a transient boryl anion, *Chem. Commun.*, **2023**, 59, 14281

3. Huo, R.; Armstrong, J. A.; Nelmes, G. R.; Lawes, D. J.; Edwards, A. J.; McMullin, C. L.; Hicks, J., Stabilisation of the $[SiH_6]^{2-}$ Anion within a Supramolecular Assembly *Chem. Eur. J.*, **2024**, *30*, e202400662

4. Kallmeier, F.; Matthews, A. J. R.; Nelmes, G. R.; Lawson, N. R.; Hicks, J., Mechanochemical synthesis of iron aluminyl complexes, *Dalton Trans.*, **2024**, *53*, 12450

5. Kallmeier, F.; Nelmes, G. R.; McMullin, C. L.; Edwards, A. J.; Hicks, J., Enhancing the nucleophilicity of aluminyl anions: targeting selective C–H activation, *Chem. Sci.*, **2025**, *16*, 10750

6. Nahon, E. E.; Nelmes, G. R.; Dallerba, E.; Lim, L. F.; Cox, N., McMullin, C. L.; Massi, M.; Kallmeier, F.; Hicks, J., Xanthene-to-fluorene skeletal editing via oxygen deletion mediated by boron and aluminium radicals, *Chem. Sci.*, **2026**, *17*, *21*, 10755

7. Nelmes, G. R. & Huo, R.; Edwards, A. J.; McMullin, C. L.; Hicks, J., Reversible Hydrogen Activation by Trapped Silicon Anions, *Manuscript in Preparation*

8. Nelmes, G. R.; McMullin, C. L.; Hicks, J., Synthesis and Characterisation of a Dimagnesiogermane, *Manuscript in preparation*

Contents

Declaration ..... **ii**

Acknowledgments ..... **iii**

Abbreviations ..... **vii**

Abstract ..... **x**

Manuscripts and Publications in Support of This Work ..... **xii**

Contents ..... **xiii**

1 Synthesis and Computation in Highly Reduced Chemistry of Groups 13 and 14 ..... **1**

1.1 Introduction to Low-Valent Chemistry 2

1.1.1 Valency 2

1.1.2 Stabilisation 4

1.2 Introduction to Computational Chemistry 18

1.2.1 Hartree-Fock Theory 21

1.2.2 Density Functional Theory 22

1.2.3 Computation of Chemical Mechanisms 28

1.3 References 35

2. Synthesis and Computation of a Dimagnesiogermane **39**

2.1 Introduction to Low-Valent Synthesis 40

2.2 Results and Discussion 45

2.2.1 Ligand Synthesis 45

2.3 Metathesis with Group 14 Precursors 56

2.4 Reduction 60

2.4.1 Introduction 60

2.4.2 Synthesis 62

2.5 Computed Mechanism 71

Reaction Pathways 72

2.5.1 Starting Points 76

2.5.2 Pathway a 76
2.5.3 Pathway b 77
2.5.4 Germylene Reduction 77
2.6 Closing Remarks 81
2.6.1 Conclusions 81
2.6.2 Future Work 81
2.7 Experimental Details 82
Synthesis and Characterisation of Ligand and Precursors 83
2.8 References 96
3. Silandiuide and Silylene Dianion 100
3.1 Introduction 101
3.2 Experimental Comparison and Benchmarking 109
3.2.1 Geometry 109
3.2.2 Stretching Frequencies 113
3.2.3 Nuclear Magnetic Resonance of the Silicon Hydrides 114
3.3 Electronic Structure 117
3.3.1 Natural Bonding Orbitals 118
3.3.2 Quantum Theory of Atoms in Molecules 121
3.3.3 EDA ETS-NOCV 124
3.4 Mechanism of Formation 135
3.4.1 Gas Phase Anion Exploration 135
3.4.2 Mechanism Within the Assembly 139
3.4.3 Density Functional Theory Explanations in Autocatalytic Dehydrogenation 141
3.4.4 Calculated Autocatalysis 144
3.5 Kinetics 147
3.5.1 Methodology 147
3.5.2 A note on experimental and computational errors. 153

3.5.3 Kinetics Plots 155
3.5.4 Autocatalysis 159
3.6 Conclusions 170
3.7 References 171
4 Boryl Radicals, Anions, and Oxygen Extrusion Reactions 173
4.1 Introduction 174
4.1.1 Experimental context for the work 174
4.1.2 A Brief History of Boron Chemistry 175
4.1.3 Boryl Radicals 177
4.1.4 Boryl Anions 177
4.2 Methodology 178
4.3 Auto-Deoxygenative Ring Contraction Mechanisms 180
4.4.2 Closed Shell Mechanisms 180
4.4.1 Radical Mechanism 194
4.4 Electronic Structure of the Reactive Species 198
4.5 Conclusion 199
4.6 References 200
5 Aluminyl Anions 201
5.1 Introduction 202
5.2 Aluminyl Anions 202
5.3 Project 1: Steric and Electronic Properties of Iron-Aluminyl Complexes 205
5.3.1 Computational Details 206
5.3.2 Percent Buried Volume 206
5.3.3 Atom Access 210
5.3.4 Vibrational Frequencies and Electronic Inferences 213
5.4 Project 2: Two-Fold Nucleophilic Attack of Benzene 215
5.4.1 Methodology 215

5.4.2 Reaction Pathways 216
5.4.3 Comparison with Experiment..... 222
5.4.4 Summary 223
5.5 References 224

1 Synthesis and Computation in Highly Reduced Chemistry of Groups XIII and XIV

"*The underlying physical laws necessary for the mathematical theory of a large part of physics and the whole of chemistry are thus completely known, and the difficulty is only that the exact application of these laws leads to equations much too complicated to be soluble."*

-Dirac, P. A. M., *Proc. A*, **1929**, *123*, *792*, 714

1.1 Introduction to Low-Valent Chemistry

This work explores electronic structure and reactivity in low-valent species of groups 13 and 14. Main-group organometallics seek to place electrons where they, if excessively anthropomorphised, would rather not be. In direct defiance of our highly oxidising and humid earthly environment, these potent reductants are the ultimate hubris of the synthetic chemist and a fanciful playground for the theoretician. I cannot wax lyrical over the potential economic or humanitarian benefits of this work, an ever-present spectre in my mind, but I can be proud of the beauty and understanding as a distillate from my efforts.

1.1.1 Valency

Chemistry is often described as the study of matter, which encapsulates all features of ordinary physical systems from such rarefied studies as bulk properties and thermodynamics in the study of engineering, to the influence of nuclear structure on hyperfine coupling in electron paramagnetic resonance.

Herein we will take the prevailingly chemical opinion that chemistry is the study of electrons; electronic structure and the atom, forming molecules, forming materials, …, *ad infinitum*. Consequently, we start our context with the structure of the atom and its influence on valency, necessary to discuss what we mean by low-valent species.

Valency grows out of the initial works of Gay-Lussac[1] and Dalton,[2] with contemporary work of Berzelius, Liebig, Frankland, and the heroic efforts of other early chemists, in an attempt to understand why elements combine in specific, integer proportions (although Frankland appears amusingly responsible for asserting the molecular weight of carbon to be relatively half its actual value, despite Berzelius' earlier accurate ratios).[3,4]

In this traditional sense, valency simply refers to the combining power of an element. For molecules such as methane (CH_4), ethylene (C_2H_4), or calcium carbide (CaC_2) it is obvious to the modern chemist that in each case carbon possesses 8 pairs of electrons in some combination of 4 bonds or lone pairs, classically (or perhaps more accurately Napoleonicly[5]) yield what would be described as "tetravalence".

Remaining with carbon, the unisolable species[6] Cl_2C: would however be described as "divalent", and as two is less than four, one feels quite comfortable describing carbenes as "low-valent". However, for the matter of the carbone (a carbon atom ligated by two L-type

ligands, neutral with two lone pairs), explicitly ascribing a valency becomes difficult; intuitively this species is quite different to the carbene, yet in the literal sense it has combined with two other moieties, and almost appears tetravalent in its possession of two bonds and two lone pairs.

The distinction remains difficult for elements with multiple oxidations states. What is the valency of tin(II) chloride? Usually, this is referred to as divalent tin, but also forms (in appropriately humid environments) hydrates with additionally bound aqua ligands. Clearly valency has difficulty with dative interactions. Tin(IV) chloride however possesses a stoichiometry of $SnCl_4$, and consequently a combining power of four. What we now consider to be multiple stable oxidation states (due to the inert pair effect[7]) was previously seen as the element possessing multiple possible valencies, so tin could be referred to as "divalent" or "tetravalent". This distinction allows for the comparison of high valent and low valent species, with a lower combining power associated with a lower valency; a low valent species could be seen as one which displays a lesser combining power than observed in other species of the same element.

It appears that the oxidation state of a species is intimately linked with its combining power and consequently its valency. For simple salts between a metal and a non-metal this essentially self-evident and one of the very first principles of chemistry a student can learn, simply balancing the charges. [8] Difficulty arises, however, in unusual bonding situations in combinations of elements of low, comparable electronegativities such as the potassium aluminyl (Figure 1).[9,10]

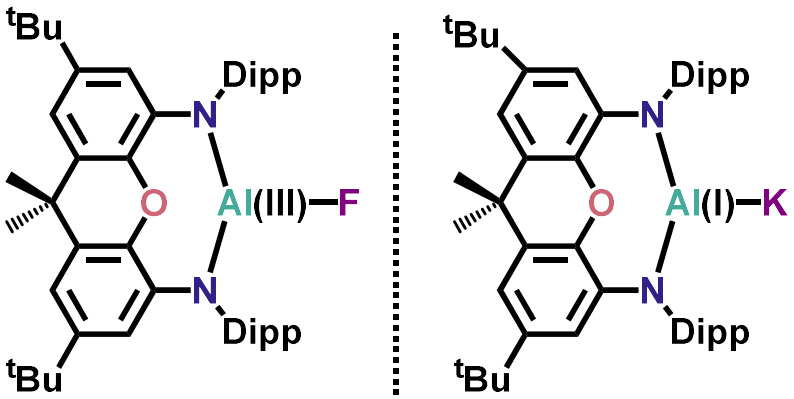


Figure 1 Ambiguity arises as to the valency of an aluminium complex when transmuting a halide for an alkali metal. Both alkali metals and halides can be considered monovalent, but when combining each with aluminium it becomes evident that oxidation state and valency are not equivalent. Aluminyl anions are universally described as low valent, but by dogmatic approaches they are merely trivalent, low oxidation state species.

In such a molecular complex (taking the amido ligands as X-type monoanionic ligands akin to halides for the purpose of combining power), the aluminium centre demonstrates a trivalent combining power. Assignment of a formal oxidation state, however, yields Al(I) rather than the expected Al(III), giving rise to a disagreement between oxidation state and valency. Certainly, no modern chemist purports a potassium aluminyl to be high valent aluminium simply because it possesses three-fold combining power, even in the face of the less combining, metastable Al(I)Cl reported by Schnöckel and coworkers[11].

Conceptually, oxidation states are the difference between the number of valence electrons "owned" an atom, and the number of valence electrons possessed by a neutral atom of the same element.[12] As is perhaps etymologically indicated, valence electrons are those which are chemically utilised in combining with other moieties to form molecular species.*ibid*

Distinctions between oxidation state and valency remain difficult for similar, relatively high electronegativities. Taking lead as the reference, with an electronegativity[13] of 2.33, an sp^3 carbon has an electronegativity of 2.30 and an sp^2 carbon of 2.60, making $PbPh_4$ formally Pb(-IV) and $PbMe_4$ formally Pb(IV), while clearly having very similar structure and reactivity and definitely the same valency in the historical sense. Transmuting carbon-based ligands for hydrides demonstrates the same inconsistency without a deliberate bad faith construction, with the original Pauling electronegativities of hydrogen as 2.20 and lead as 2.33, changing the oxidation state of lead by -8 by swapping between remarkably similar ligands.[14,15]

Despite the imprecision and ambiguity, and its inability to reconcile with coordination number, oxidation state, or nebulous combining power, the term remains popular through organometallic literature.[16] Seemingly, there is some underlying, qualitative theme that unites users of the term low-valent in their chemical ambitions. Herein we will take a fuliginous approach to linguistics and maintain a deliberate ambiguity in the term, guided by the principles of low-oxidation state, low-coordinate, or otherwise less-than-fully-combined motifs (or most usually several of the preceding) resulting in unusual electronic structure.

1.1.2 Stabilisation

Low valency leads to instability in both a thermodynamic and kinetic sense. Thermodynamically, low-valent species are notable for their difference from "ordinary" chemical species, and what leads to the normality of ordinary species is that they are frequently encountered as a consequence of their comparative immutability, which is in turn consequent

of their thermodynamic stability. Features of typical chemistry such as fulfilling the octet rule, having electronegative species bare partial negative charges, and forming coordinatively saturated complexes, each have firm theoretical bases for increasing the thermodynamic stability of their adherents. Kinetic instability can be justified from a Brønsted-Evans-Polanyi perspective: that for similar reactions, higher energy starting materials will have lower activation barriers.[17] This is of course highly related to the Hammond postulate, that in an exothermic reaction, the transition state more closely resembles the reactants than the products, requiring minimal reorganisation (and putatively minimal increase in energy), lowering their reaction barrier heights by their already presumed thermodynamic instability.[18]

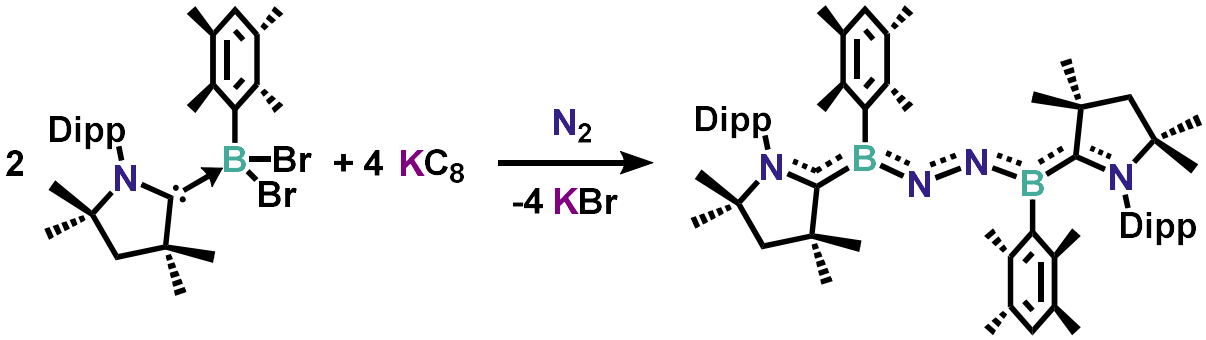


Figure 2 A landmark work in low valent main group chemistry: the first example of a p-block element reaction with dinitrogen, reactivity previously displayed only by transition metals and elemental lithium.[20]

From a reactivity perspective, these are ideal traits- it allows them to react with relatively inert substrates in mild conditions to access otherwise difficult products. A principal draw of low-valent main group species is their reaction with inert, abundant small molecules like carbon monoxide or dinitrogen (Figure 2),[19,20] without requiring expensive or toxic transition metal species. But without appropriate stabilisation, this reactivity is a curse, allowing for elemental precipitation, disproportionation, ligand activation, cluster formation, or any of a great deal of off-target reactivity which prevents the molecular species from engaging in the desired structure or reactivity.[21]

A successful mantra provided to undergraduate students is “there are only two explanations, sterics and electronics”. The idea being that all things can be described as consequent of either the electron structure of the species involved, or often if electronic structure yields predictions against experimental results then sterics is nebulously blamed. Here however, we describe how each feature can be used deliberately to stabilise otherwise unisolable species.

1.1.2.1 Electronics

Transition metals occupy a similar space in the chemical milieu, able to perform catalysis through moving between multiple energetically similar oxidation states and a large number of small, well-defined steps.[22] Often relying again on low oxidation states and vacant coordination sites, to prevent decomposition into element forms or other thermodynamic sinks, transition metal catalysts have traditionally employed electronic stabilisation.[23]

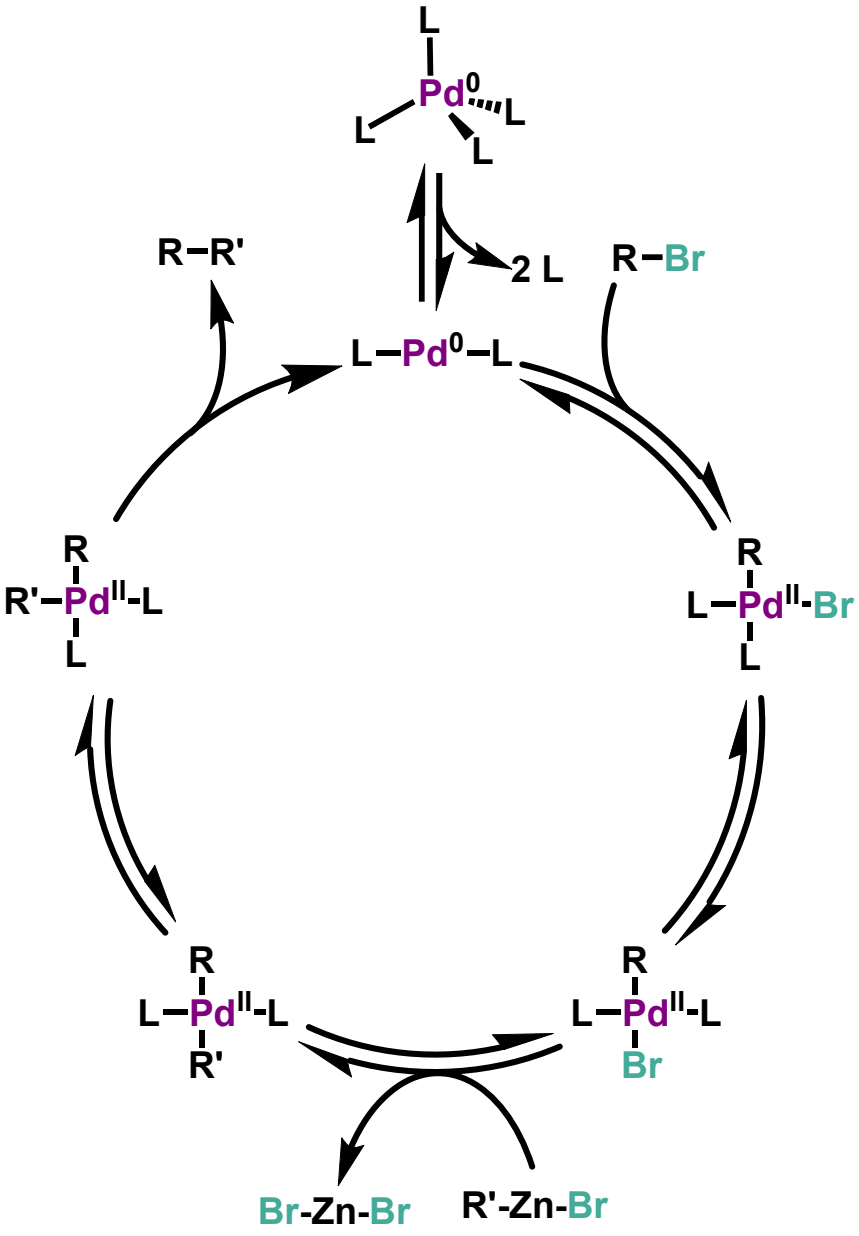


Figure 3 The palladium catalysed cross-coupling reaction is the crown jewel of organometallic chemistry, winning the 2010 Nobel Prize in chemistry.[24] Examples typically vary by choice of nucleophile, as each possesses different functional group tolerances, safety concerns, availability, and transmetallation properties. Depicted here specifically is the Negishi cross-coupling, which uses organo-zinc nucleophiles, and is so named for Ei-ichi Negishi who discovered the reaction for which he won a one third share in the 2010 Nobel Prize in Chemistry.

Typically, transition metals are relatively electropositive and have a thermodynamic tendency to form oxidised molecular species, even as simple as Fe_2O_3 in the form of rust pervading every aspect of post-industrial life.[25] While these species are sometimes intrinsically useful materials like Nd:YAG lasers[26] or for Lewis-acid catalysis[27], within organometallics the crown jewel of reactivity is the palladium cross-coupling (Figure 3).[28] Oxidative addition, followed by a series of transmetallations and isomerisations, and finally reductive elimination, forms the basis of many otherwise arduous carbon-carbon bond forming reactions. Necessary to the process is often the difficult oxidative addition step, wherein a Pd(0) complex is oxidised to form a halo-alkyl- Pd(II) species, which is only possible from the electron-rich Pd(0) centre, which without appropriate stabilisation is unstable towards elemental decomposition. Instead, through coordination of phosphine ligands to the metal centre, electron density is delocalised through a molecular species rather than on a reactive metal centre, allowing for stabilisation through a Dewar-Chatt-Duncanson mechanism.[29]

Archetypal is the carbonyl complex. Carbon monoxide binds through both the σ-donor from the carbon-based lone pair to the vacant e_g set, and through π-retrodonation from the filled metal t_{2g} set into the vacant CO π* orbitals (Figure 4).

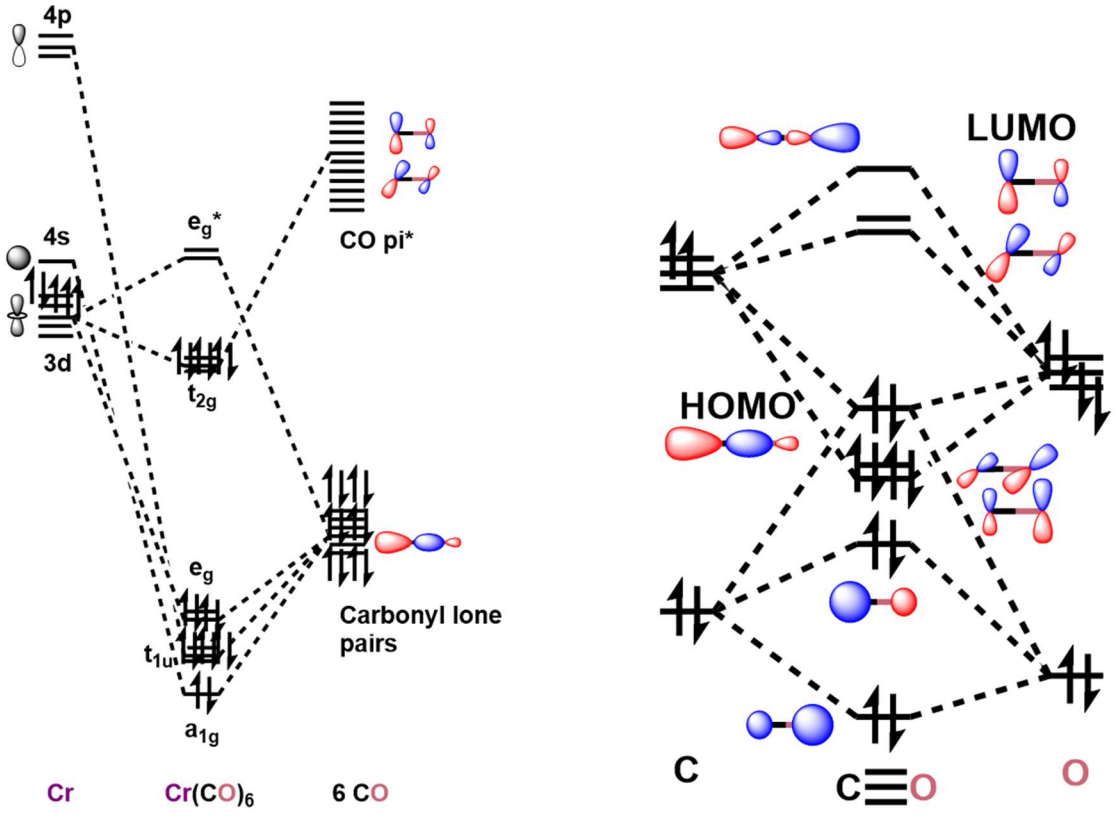


Figure 4 The molecular orbitals of carbon monoxide (right) and how they interact with transition metals to form complexes. On the left is the archetypal example of the Dewar-Chatt-Duncanson model of transition metal complexation.

Salient is the delocalisation of high-energy electrons in the HOMO of a molecular species into vacant orbitals to lower their energy overall. This is an excellent strategy for stabilising otherwise inaccessible oxidation states, but with lowered energy comes lowered reactivity. Electronic stabilisation exists within main group chemistry as well as transition metal chemistry, but the difference between electronic stabilisation and simply reducing the ligands bound to what would otherwise be the reduced metal centre can be indistinguishable. The stronger a π-acid is, the larger contribution to delocalisation it receives, until the electron is better described as localised on the ligand; such a situation is most prevalent when using cyclic alkyl amino carbenes (cAACs) due to their high π-acidity.[30]

Compared with their older, ubiquitous cousin the N-heterocyclic carbene (NHC), cAACs have significantly less occupation of the carbene p-orbital, increasing their π-acidity significantly, often to the point of reduction rather than delocalisation.

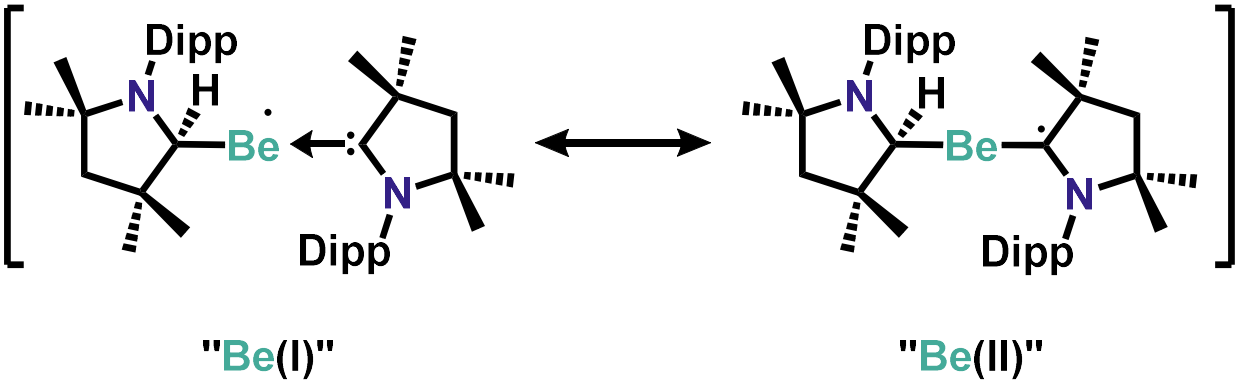


Figure 5 Resonance structures of the landmark Be(I) radical, showing the reduced cAAC and Be(I) forms, with perhaps the reduced cAAC as the more accurate Lewis representation of the species. Molecular orbital calculations (BP86-D3BJ/def2-SVP) within the original publication indicate *ca.* twice the spin density of the π-SOMO between the cAAC and the Be centre to have nearly twice the density at carbon than beryllium.

Figure 5 shows the resonance structures of what *prima facie* is a low-valent beryllium species,[31] which due to strong retrodonation from the beryllium centre to the cAAC ligand forms the comparatively innocent Be(II) species and a cAAC radical instead of the intended Be(I) radical.

Due to the much more reducing nature of most main group metals compared with transition metals, electronic stabilisation is inclined towards this behaviour, which produces ordinary electronic structures and highly reduced reactivity.

To maintain the reactive, novel electronic structure of low-valent main group species, a second approach is used for their stabilisation.

1.1.2.2 Sterics

Sterics, secretly, are electronics cleverly disguised to appeal to the intuitive idea that atoms have well defined sizes and locations, as though they are billiard balls which can hit each other. The idea that bigger moieties are more obstructive is a classically familiar one; it is easier to displace a pebble than a megalith. Similarly, from a semiclassical perspective sterics is often described as originating from the coulombic repulsion between nearby clouds of electron density, but this does not endure much scrutiny. Interpenetrating wavefunctions have necessarily less wave-wave coulombic interaction than wave-point interaction; there is actually always a coulombic *benefit* for atoms getting closer to each other (up to nucleus-nucleus repulsion dominating at very short distances).

Sterics, more surprisingly, are due to the spin statistics theorem as electrons are indistinguishable, fermionic particles. This will be explained in more detail in part 1.2, summarised here briefly. As the wavefunctions of same spin particles would overlap increasingly, the antisymmetry requirement (Pauli exclusion principle) of the overall wavefunction effectively localises the same spin particles to prevent overlap, which increases their energy through increased kinetic energy (a sharper, more localised wavefunction has a higher value of $\nabla^2\psi(r)$).

It is worth noting that explanations for the stability of eclipsed geometries, such as in alkanes, is not due to steric repulsion between adjacent groups either. Sterics is a very short-ranged effect, proportional to the overlap integral of the wavefunctions, with no universal scaling but something similar to r^{-4}, with minimal interaction beyond adjacent atoms. Instead, there is an energetic *benefit* to delocalising a CR bonding orbital into the CR* orbital of the opposite CR interaction, which has the best overlap in the antiperiplanar configuration.[32]

The nature of sterics, however, is immaterial to their function. Why large flanking groups result in more stable complexes and slower reaction rates is largely less important than the observation of those empirical properties.

In organometallic chemistry, this is clearly demonstrated in associative ligand substitution mechanisms of platinum (Figure 6) when the complex bears a sterically demanding moiety near the vacant coordination site (the authors even go as far as to call such complexes “pseudo-octahedral”.[33] When comparing phenyl, *o*-tolyl, and mesityl ligands of the same complex for the substitution of a chloride for a cyanide in methanol at 30 °C, the rate constants for the

substitution are 3.61×10^{0}, 2.34×10^{-1}, and 8.49×10^{-3} $Lmol^{-1}s^{-1}$ respectively,* changing by a factor of over 400. This can also be seen in the respective barrier heights of *ca*., 17.0, 18.6, and 20.6 $kcalmol^{-1}$ respectively, increasing the relative energy of the barrier height by over 20%.

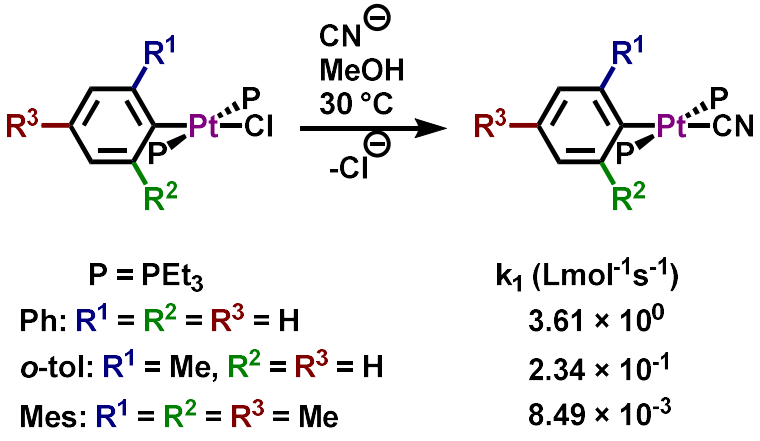


Figure 6 The differing rates of a substitution reaction of platinum with electronically similar species demonstrate how steric bulk directly influences the kinetic stability and reaction rates of related species.

In the main group, ligands are instrumental to the stabilisation of low-valent species by increasing the barrier to decomposition reactions so that they do not occur at appreciable rates under experimental conditions.

For most of modern main group chemistry, it was believed that isolation of compounds in violation of the double bond rule was errant folly. The very weak bonds and low valency of such species was thought to preclude their isolation, instead implying them as reactive intermediates or impossible curiosities.[34] However, in 1981 the first stable disilene[35] was isolated by West and co-workers *via* the irradiation of 2,2-dimesityl-1,1,3,3-hexamethyltrisilane (Figure 7*)*, presumably through a reductive elimination-like process followed by dimerisation of the resultant Mes_2Si: silylene.

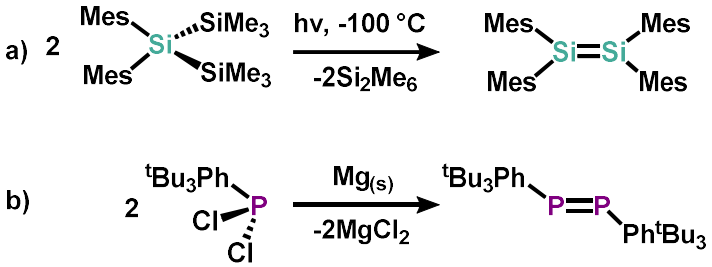


Figure 7 a) The synthesis of the first disilene, tetramesityldisilene and b) the synthesis of the first diphosphene, bis(tri-tert-butyl)phenyldiphosphene, both reported in 1981.[36]

* Units for a second order rate constant (as reported), 3 significant figures in the original work.

This compound demonstrated that the isolation of kinetically unstable main group compounds was not an insurmountable challenge. Shortly after, a cascade of similar multiply bonded main-group compounds was reported, including the first diphosphene from Yoshifuji and co-workers in the following weeks.[36]

While West's disilene and Yoshifuji diphosphenes relied upon covalently bonded substituents for their stability, another major breakthrough occurred in 2007 when Jones and coworkers applied the same principle to group II coordination chemistry, allowing for the synthesis of a series of magnesium(I) dimers[37] (Figure 8). The use of sterically demanding *Dipp* (*Dipp* = 2,6-diisopropylphenyl) groups substituting the guanidinate or β-diketiminate ligands around the Mg-Mg bond blocks disproportionation, trapping the low-valent and highly reducing magnesium(I) dimers.

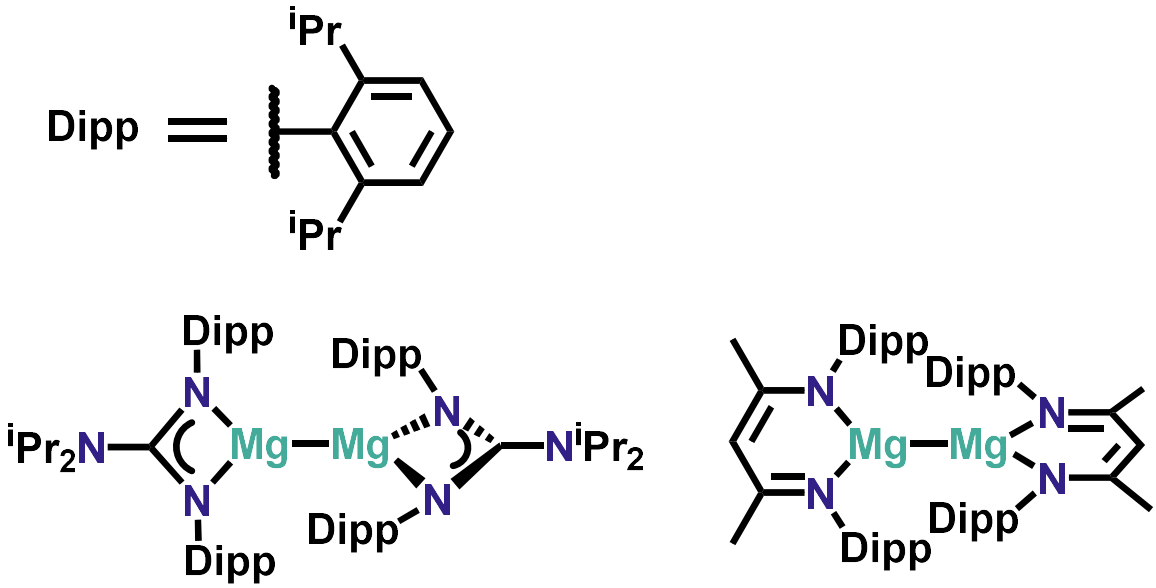
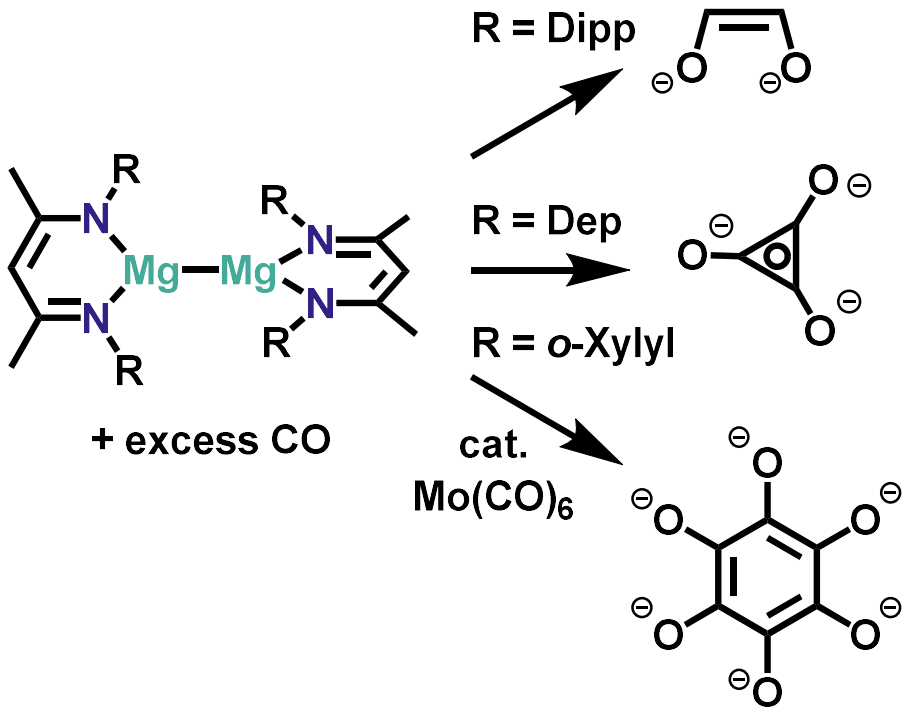


Figure 8 The first two magnesium(I) dimers reported in 2007 by Jones and co-workers, bulky guanidinate ((N^{i}Pr$_2$)C(NDipp)$_2$Mg)$_2$ (left) and bulky β-diketiminate ((HC((C(Me)NDipp)$_2$)Mg)$_2$

Sterics can also control not only the stability of the otherwise arcane species, but also the extent of their reactivity. The difference between an ethyl group and an isopropyl group can lead to differently sized oligomers seen in *Scheme 1* . In the magnesium(I) dimer induced CO coupling: the [^{Dep}NacNacMg]$_2$ complex[38] allows for the coupling of three CO units, but the slightly bulkier [^{Dipp}NacNacMg]$_2$ complex[38] allows for only two, and [^{Mes}NacNacMg]$_2$ results in the larger hexamer.[39]



Scheme 1 Small changes in sterics can result in large changes in reactivity. The difference between an ethyl group (^{Dep}Nacnac) and an isopropyl group (^{Dipp}Nacnac) at the same position leads to dimeric and trimeric products respectively. The size of the product inversely proportional to the steric bulk of the ligand used. [^{R}NacNacMg]$^{+}$ cations omitted for clarity post reaction.

In the context of this work, the (**NON**$^{2-}$) ligand (Figure 9) is tridentate, possesses two amide donors (each making use of a Dipp group) linked together using a xanthene backbone incorporating an additional ether moiety, allowing for facile coordination as required.

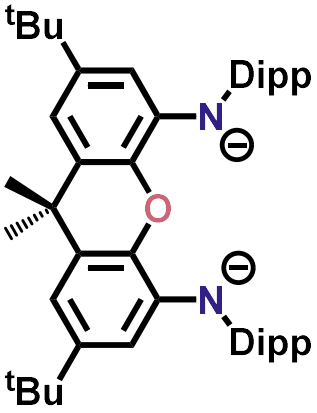


Figure 9 The NON ligand, so named for its nitrogen-oxygen-nitrogen binding motif.

This ligand forms the basis of much of the synthetic work in the group, stabilising highly reactive hydrides, aluminyl anions, and other low valent species. In chapter 3, the ligand forms the basis of a supramolecular assembly to stabilise novel low valent silicon species, and in chapter 5 the question of what it can and cannot stabilise is crucial to the work.

Theoretical or computational methods for investigating sterics are, however, often *ad hoc*, lacking in rigour, or based entirely on intuition. Widely used as a proxy for the sterics of phosphines (or other appropriate ligands[40]) is the Tolman cone angle.[41] In the original work, consistent with refinements and expansions provided in a subsequent review,[42] Tolman builds molecular models with (relative) atomic radii of the van der Waals radius of several nickel phosphine geometries, and then quickly rotates around the Ni-P bond and measures the angle from the nickel centre to the widest angle just touching the ligand "cone". This method, designed to explain differences in reactivity and stability of different nickel phosphine catalysts beyond the comparison of their Tolman electronic parameters (the relative magnitude of the A_1 carbonyl stretch in different [$LNi(CO)_3$] complexes), is an effective proxy for the reactivity of similar phosphines, but fails to give accurate reactivity predictions for even mildly obtuse substitutions such as three different R groups or R groups with a greater than perpendicular angle,[43] let alone non-phosphine, or even non-L-type ligands entirely.[44]

Theoreticians, when faced with arbitrary metrics, are often tempted to search for quantifiable, wave-function based techniques in an attempt to remove the *ad hoc*, empirical, or arbitrary nature of the existing metrics. This is evident in fields like density functional theory where there was a controversy about what drives a good density functional approximation (as the true functional is not known, *vide infra*). In the popular paper "Density functional theory is straying from the path toward the exact functional",[45] Medvedev, Bushmarinov and coworkers argue the titular position, specifically using (somewhat arbitrarily) the root-mean-square difference in electron density for the radial distribution functions of 14 atoms/atomic cations of the first row with closed shell nondegenerate ground states (including examples such as Ne^{8+}).

Contemporary articles however argue that by choosing different metrics for deviation from the true electron density, any ordering for the performance of any number of density functionals is possible (although of course, some will be more contrived than others).[46] Instead, they suggest that using the variational principle, the energy, which is an eigenfunction of the Hamiltonian and consequently an observable of the system, can be used as a "natural" metric of the error, breaking down the problem into so-called "functional driven" errors and "density driven" errors as in their seminal 2013 work.[47]

There have been similar attempts to produce similarly fundamental metrics for sterics; however sterics are a somewhat nebulous idea, and do not correspond to an observable of the wave equation. Density functional theory is uniquely unsuitable for such a task, for as discussed

earlier sterics are consequent of the reduced chance of finding a same spin particle near an identical particle (the Pauli exclusion principle), manifesting as the so-called exchange energy. This is not the only component of a density functional, also requiring at least the coulombic correlation energy, and in the true density functional these components are not separable and rely on favourable cancellation to provide the true exchange-correlation energy.[48]

Energy decomposition analysis[49] of various flavours (such as Zeigler-Rauk[50] or Morokuma[51]) attempts to break the energy of two interacting fragments into various components (typically electrostatic, exchange-correlation, and some metric of delocalisation) and ascribe chemical meaning to them. Often one of these components (usually a proxy for Pauli exchange) is deemed responsible for steric interactions yielding an energetic metric. This is an excellent approach for specific interacting fragments, or comparing interactions of different moieties with a specific substrate, so long as the metric is trustworthy and accurate. Unfortunately, it has the significant weakness that it necessarily requires the calculation of two interacting species; no universal comparison is possible to give a ranking of the size or steric protection of all possible ligands, as it will be different for each substrate. Perhaps this is the inescapable nature of sterics.

Other quantum mechanical methods including density-based methods like quantum theory of atoms in molecules (QTAIM) or electron localisation functions (ELF) attempt to describe sterics by the size of the electronic basin[52] or the distance between overlapping localised regions.[53] Noncovalent interactions (NCI) suggests that steric interactions are characterised by a low electron density and a small, positive value of the second eigenvalue of the electron density Hessian matrix, which has a strong empirical basis but limited theoretical justification, in the vein of *ad hoc* metrics, often even using a pro-molecular density with the correct tail behaviour instead of the true calculated density.[54] These methods are good indicators and often are more useful in a qualitative praxis, giving explanatory power after the fact but limited predictive power, and also suffer from the same substrate dependence of EDA.

More commonly used are modern radius-based measures in the same vein as the historical Tolman cone angle but generalised to all ligand species. The two methods used within this thesis are "Samb*V*ca" [55] (abbreviation for "Salerno at the MoLNaC Buried Volume Calculation", often referred to by its function, "Percent Buried Volume") and "AtomAccess".[56] Each uses only the geometric coordinates and van der Waals radii of the ligand of interest to

calculate a quantity which correlates the accessibility of the central atom to give quantitative insight into the protective capacity of the ligand.

AtomAccess is a tool developed by Chilton, Mills, and coworkers. Taking the geometric coordinates of a molecule from either DFT calculations or single-crystal X-ray diffraction and pruning the immaterial paraphernalia from the metal centre, ray tracing is used to determine what portion of the surface area of a sphere of a certain area is "inaccessible" due to the ligand in question. This view of sterics as access denial is an effective one for many applications. In the original work,[56] the size of the largest accessible cluster of unblocked rays was used as a proxy for the stability of the complex, with a smaller largest cluster implying a more stable complex. Applied to a series of differently coordinated dysprosocenium cations (the size of variously substituted cyclopentadienyl ligands, (Cp^R where R indicates the substitution) was varied), the program was used to determine the availability of equatorial binding sites as this was posited to adversely affect the molecules' performance as a single molecular magnet (SMM). An example output (along with compared methods, *vide infra*) is provided in Figure 10.

This was used to make theoretical predictions about the minimally substituted dysprosocenium Cp^R, suggesting $[Dy(Cp^{ttt})(Cp^*)]^+$ (Cp^{ttt} = 1,2,4-tri-tert-butylcyclopentadienyl, Cp* = pentamethylclopentadienyl) to be at the borderline of viable SMMs, which was experimentally confirmed by measuring the temperature-dependent relaxation rates of the predicted species.

The method has been widely adopted within the main group,[57] organometallic,[58] and f-block[59] communities as a facile, quantitative comparison between ligands, particularly where comparison within a series of similar ligands results in different reactivity. This is pertinent to chapter 5, wherein comparison of different steric and electronic features of related iron aluminyls is explored.

Often presented as a black box, AtomAccess actually has several tuneable parameters. Different conclusions can be reached based on the radius of the sphere ("r_{max}") and the density of the rays ("ρ"). A larger sphere includes, obviously, more distal features of the coordinated ligands which may or may not genuinely influence the chemical or physical properties of the species, and which only necessarily converges after the van der Waals radius of the most distant atom from the centre in question. The density of rays, if too sparse, does not give sufficient resolution to meaningfully distinguish between different species. Conversely, if too dense, no delineation into separate clusters is possible, however this is only meaningful if investigating

the properties of a specific, fully coordinated complex rather than when trying to make comparisons of only one specific ligand around the centre.

Little investigation of r_{max} is provided within the original manuscript, supporting information, or user manual, implicitly asserting the default distance of 5 Å to be most appropriate. Intuitively, this balances the need to include chemically relevant components of large ligands which may obstruct access to the metal centre from quite disparate approaches with the need to exclude moieties which are distant enough to have no material effect on the physical or chemical properties. Particular discussion of r_{max} dependence with respect to the iron aluminyl complexes is presented in chapter 5.

Sam*V*ca takes a similar approach. Similarly, it uses scaled van der Waals radii[60] and geometric coordinates to explicitly calculate a steric parameter. This parameter, however, is generated not by ray tracing, but instead by summing over a sphere of voxels from the central atom to the cutoff radius (R in the original work, equivalent to r_{max} in AtomAccess). If a voxel is within the van der Waals radius of an atom, it is counted as "buried", then the fraction of all the voxels which are buried gives rise to the measure percent buried volume (%BV), and its additive compliment percent unburied volume (%uBV). Similarly, there are two parameters of concern: the spherical radius, and the size of the voxels. Defining a semiempirical energy metric, the spherical radius was chosen by maximising the R^2 correlation between a DFT-calculated binding energy of an NHC to a ruthenium complex (Equation 1) and a linear combination of weakly physically motivated physical parameters a, b, and c shown in Equation 2.

$$4\mathrm{NHC} + (\mathrm{Cp^*RuCl})_4 \rightarrow 4\ \mathrm{Cp^*Ru(NHC)Cl} + E_{DFT}$$

Equation 1 The binding energy definition used by Sam*V*ca to establish an energetic motivation to which to fit Equation 2.

$$E_{Fit} = a + b \cdot \%BV + c \cdot E_{ST}$$

Equation 2 The Sam*V*ca empirical energy fit equation using free parameters a, b, and c along with the singlet-triplet gap energy E_{ST} and the steric parameter %BV.

Cavallo and coworkers demonstrate the best statistical match between E_{fit} and E_{DFT} using a spherical radius of 3.5 Å (R^2 = 0.87, a = -74.87, b = 1.53, c = 0.28), yielding the lower R^2 values of 0.79 and 0.80 for the radii 3.0 and 4.0 respectively.

The choice of density functional and methodology (BP86/Def2-TZVP) to generate the model data E_{DFT} is not justified. Even the form of Equation 2 is arbitrary, motivated by a desire to fit the same form as used by Tolman,[42] although the use of the singlet-triplet gap is an energetic

and established metric for comparison of NHC binding.[61] It cannot be said in good faith that there is much nonempirical design in the choice of the cutoff radius, although it is similar to the 5 Å of AtomAccess and similarly matches intuition. Consequently, we investigate the use of different cutoff radii with comparison to AtomAccess in chapter 5. The use of voxels as a discrete approximation to true integral volumes of course introduces additional parameters, but there is no similar use of a "cluster" and the only ambiguity is in if the grid is adequately fine, and at 3.5 Å the grid used (0.05 Å) generates *ca*. 1.4 million voxels and agrees with the true volume within 99.97%, and shows convergence within 0.06% for a demonstrative %BV after grid sizes of 0.1 Å.

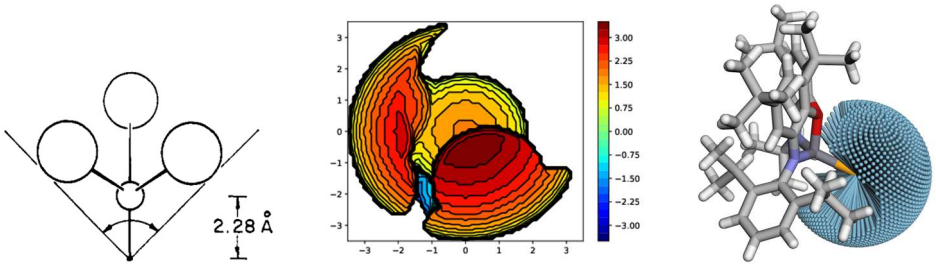


Figure 10 Examples graphical representations of three ubiquitous measures of sterics: the Tolman cone angle (left), SambVca (centre), and AtomAccess (right). The Tolman cone angle is only defined for phosphines, presented in the original manuscript, whereas SambVca and AtomAccess are generalisable to different species, concerned with either the volume or surface area of defined spheres around a centre.

Applications of sterics and more specific context to specific low valent group 13 and 14 species is presented at the beginning of the relevant chapters.

1.2 Introduction to Computational Chemistry

"*It is shown that the only obstacle to the evaluation of wave functions of any required degree of accuracy is the labour of computation."*

-S. F. Boys, *Proc. R. Soc. Lond. A*, **1949**, *200, No. 1063*, 542

Computational chemistry revolves around using theoretical models to answer questions. In inorganic chemistry this usually amounts to providing support for- and explanation of- experimental results. It is in theory fully predictive, allowing for portent guidance of synthetic chemistry, however the computational cost is currently at best prohibitive and at worst completely untenable.[62] Thus, whenever computation is involved, several things are necessary: a clear goal, a computational tractable model, and an understanding of the limitations and constraints inherent to the calculation.

According to the nonrelativistic wavefunction formulation of quantum mechanics,[63] the wavefunction of a system (herein unless otherwise specified, we will take system to mean a collection of electrons and nuclei) contains all observable about that system:

$$\Psi(1, 2, \dots, n, \mathbf{1}, \mathbf{2}, \dots, \boldsymbol{N})$$

Equation 3 A general wavefunction Ψ, a function of n electrons and N nuclei.

Where Ψ defines a wavefunction of (1, 2, …) which are electrons (ordinary numerals) and nuclei (bold numerals). The (square of the) wavefunction is, at its core, simply a description of the chance of finding a particular particle at a particular position in space.[64] Before going further it is helpful at this point to invoke the Born-Oppenheimer approximation:[65] nuclei are much more massive than electrons and consequently have much more localised wavefunctions and move much more slowly, to the point that they can be considered (for our purposes) classical point charges- whenever the nuclei move, the electrons will change their wavefunctions seemingly instantaneously. The nuclei are considered part of the external potential, and we will unceremoniously drop the nuclear portion of the wavefunction (and afterwards also the "electron" subscript) for the remainder:

$$\Psi_{electron}(1, 2, \dots, n)$$

Equation 4 A wavefunction for simply n electrons, assuming a static point-like potential of the omitted N nuclei.

Extracting information from a wavefunction is very simple. One of the core postulates of quantum mechanics[66] is that for every observable of a system there exists an operator $\hat{A}$ with set of eigenvalues $\{A\}$ which are the possible values of the measurement:

$$\hat{A}\Psi(1,2,\dots,n) = A\Psi(1,2,\dots,n)$$

Equation 5 Applying an arbitrary operator to a wavefunction yields the wavefunction multiplied by a constant, the eigenvalue associated with the magnitude of that property.

In bra-ket notation:

$$\hat{A}|\Psi\rangle = A|\Psi\rangle\,;\ \langle\Psi|\hat{A}|\Psi\rangle = A$$

Equation 6 The bra-ket form of Equation 5, where the "ket", $|\Psi\rangle$, is a wavefunction and the "bra" $\langle\Psi|$ is a linear map $f\colon |\Psi\rangle \longrightarrow \mathbb{R}$.

However, these are only necessarily true if the wavefunction is an allowed wavefunction, *i.e.* a solution to the (for simplicity, the time-independent) Schrödinger equation:[67]

$$\hat{H}|\Psi\rangle = E|\Psi\rangle$$

Equation 7 The time-independent Schrödinger equation.

Where $\hat{H}$ is the Hamiltonian operator and E is the energy of the system. The Hamiltonian operator is, analogously to classical physics, the sum of the kinetic energy and the potential energy operators:[68]

$$\hat{H} = \hat{T} + \hat{K}, \qquad \hat{T} = -\frac{\hbar^2}{2m}\nabla^2, \qquad \nabla^2 = \frac{\partial^2}{\partial x^2} + \frac{\partial^2}{\partial y^2} + \frac{\partial^2}{\partial z^2}$$

Equation 8 Components of the time-independent Schrödinger equation in operator forms.

K depends explicitly on what can be considered the environment, usually the Coulombic interaction between an electron and the charge due to a nucleus or a different electron, *e.g.*:

$$\hat{V} = \frac{1}{8\pi\varepsilon_0}\sum_{i}^{N}\sum_{j\neq i}\frac{q_i q_j}{|\boldsymbol{r_i} - \boldsymbol{r_j}|}$$

Equation 9 The potential operator for coulombic point charges with magnitudes q_x and locations r_x.

Where $\hat{V}$ is the Coulomb operator, a sum over the interactions between the charges q_p where the denominator is the distance between the charges.

Unfortunately, there is no analytical solution to the Schrödinger equation for a given potential for more than one particle,[69] necessitating approximations. The first will be "separation of variables",[70] where we will assume that the wavefunction can be described as the product of single electron wavefunctions. Core to this is the idea that the wavefunction of any individual electron is very similar to the wavefunction of an electron in an external potential provided by the nuclei *and the sum of all the other electrons charge distributions*.

$$\Psi(1,2,\dots,n) = \psi_a(1)\psi_b(2)\dots\psi_m(n)$$

Equation 10 The separation of variables takes a function of many variables and makes it into a product of many functions of only one variable each, a common strategy for solving (or in this case approximating) intractable equations.

Where $\{\psi_n(x)\}$ are evidently single particle wavefunctions.

It is also salient to note here that electrons are fermions, they possess intrinsic angular momentum which is spin of ½.[71,72] This has the consequence that the wavefunction must be antisymmetric with respect to particle permutation ($\hat{P}$) by the spin statistics theorem: [73]

$$\Psi(\dots,m,n,\dots) = -\hat{P}\Psi(\dots,m,n,\dots) = -\Psi(\dots,n,m,\dots)$$

Equation 11 The action of the permutation operator simply exchanges the position of two variables.

Which is not satisfied by the above separation of variables, which must be explicitly antisymmeterised (and renormalised), *e.g.*:

$$\Psi(1,2) = \frac{1}{\sqrt{2}}(\psi_a(1)\psi_b(2) - \psi_a(2)\psi_b(1))$$

Equation 12 The antisymmeterised, variable separated form of Ψ(1,2).

Which can be performed generally by constructing a Slater determinant,[74] renormalising the determinant of a matrix where the columns are the single particle wavefunctions and the rows are the particles:

$$\Psi(1,2,\dots,n) = \frac{1}{\sqrt{n!}}\begin{vmatrix} \psi_a(1) & \psi_b(1) & \dots & \psi_n(1) \\ \psi_a(2) & \psi_b(2) & \dots & \psi_n(2) \\ \vdots & \vdots & \ddots & \vdots \\ \psi_a(n) & \psi_b(n) & \dots & \psi_n(n) \end{vmatrix}$$

Equation 13 A general form of for variable separated, antisymmetric wavefunctions.

This has both energetic and geometric consequences. If any two columns are the same, the determinant (and thus the wavefunction) will be zero, showing that no two single-particle wavefunctions can be the same, which satisfies the Pauli exclusion principle,[75] that no two wavefunctions can have the same quantum numbers.[67]

The end consequence is that like-spin electrons have an energetic penalty for approaching each other beyond their coulombic repulsion. This manifests as a term in the potential energy operator, named the exchange operator, although this formulation of the energy is not unique but is ubiquitous throughout chemistry.

1.2.1 Hartree-Fock Theory

From the form of a wavefunction given above, it is now possible to devise a method of deriving a wavefunction *de novo*. The derivation is not warranted here, but the Fock operator, $\hat{F}$, and is the single-particle analogue of the Hamiltonian operator (*i.e.* $\hat{H}_{HF}\Psi(1,2,\dots,n) = \sum_{i=1}^{n}\hat{F}\,\psi_n + \hat{V}_{NN}$), is usually written as:[76]

$$\hat{F} = \hat{H}^0 + \sum_{i=1}^{n}\left(2\hat{J}_i - \hat{K}_i\right)$$

Equation 14 The Fock operator

$$\hat{H}^0 = \hat{T} + \hat{V}_{eN}$$

Equation 15 The single electron contribution to the Fock operator.

Where $\hat{H}^0$ contains the kinetic energy term and the electron-nucleus attraction for the electron in question. $\hat{J}_i$ is the Coulomb interaction between the electron in question and electron *i*, and $\hat{K}_i$ is the exchange interaction between the electron in question and electron *i*, $\hat{J}_i$ is multiplied by 2 because two electrons occupy the same spatial orbital, but not $\hat{K}_i$ as this only applies to electron of opposite spins. $\hat{V}_{eN}$ is the single-particle operator which gives the attraction between the given electron and the nuclei, and $\hat{V}_{NN}$ is the mutual repulsion amongst all the nuclei.

In theory, now all that must be done is to vary the single particle wavefunctions until they return a self-consistent and variational solution.[76] Unfortunately, this process does not give an experimentally accurate wavefunction. This is due to the assumption made during the separation of variables and is most simply put: the chance of finding an electron at a certain position is not independent of the chance a second electron is at another certain position. In other words, the position of the electrons is correlated with each other- if you have found an electron in one place, you are unlikely to find the second electron near it, even if the wavefunction would otherwise suggest it should be found nearby.[77] This effect is actually quite small, and Hartree-Fock (HF) theory and the separation of variables is quite a good approximation, just when the magnitude of energy in the problems concerning chemistry are on the order of 1-2 kcalmol^{-1}, and the HF energy of a hydrogen atom is ~314 kcalmol^{-1}, even a fraction of a percent error is an important deviation.

1.2.2 Density Functional Theory

There are many ways to attempt to include some (or all) of the previously absent correlation energy. The oldest, and most accurate of these methods are wavefunction-based, applying small corrections to the HF wavefunction (as in Møller–Plesset (MP) perturbation,[78] or more rarefied Rayleigh–Schrödinger perturbation[79]), which have some drawbacks in that they are no longer variational, or perhaps more importantly scale with a computationally intractable $O(N^6)$ (at best $O(N^5)$) compared with HF's notional $O(N^4)$. [80] Furthermore, other methods invoke combinations of determinants, such as the Full Configuration Interaction (Full-CI of FCI) method,[81] which theoretically captures all correlation variationally within the basis set limit, and gives exact energies for a system, but scales in a difficult to articulate way, but at least factorially(!). There are of course other methods which give excellent quality like coupled cluster methods,[82] or a combination thereof such as the gold-standard coupled-cluster singlets doublets and perturbative triplets (CCSD(T)) method.[83]

Despite their attractiveness for accuracy, wavefunction-based methods are simply too computationally expensive for routine use for more than 100 atoms. Fortunately, in 1927 Thomas and Fermi independently developed methods for calculating properties of wavefunctions with, in principle, no knowledge of the wavefunction beyond the electron density.[84] As the density is only 3-dimensional and grows simply as $O(N^3)$, this was a very attractive prospect indeed. Unfortunately, the methods they described only work in certain limiting cases, and application of Thomas-Fermi models to molecular or even most atomic systems produced results in further disagreement than crude HF solutions. In fact, Teller showed that TF models always give higher molecular energies than independent atoms and can thus never describe bonding,[85] and even after significant improvements by Dirac in 1930,[86] these theories have never found genuine application.

However, TF was an important stepping stone for later development of what is now known as density functional theory (DFT),[87] which has the same attractive qualities of describing the wavefunction with only knowledge of the electron density and excellent computability and scaling, while developing it into a method which rivals or supersedes many wavefunction-based methods.[88]

1.2.2.1 Exchange and Correlation

Density functional theory starts with the Hohenberg-Kohn Theorem,[89] which proves that:

"The external potential $V(\mathbf{r})_{ext}$ is (to within a constant) a unique functional of $\rho(\mathbf{r})$; since, in turn $V(\mathbf{r})_{ext}$ fixes $\widehat{H}$ we see that the full many particle ground state is a unique functional of $\rho(\mathbf{r})$"

This is a perhaps convoluted way of saying that the Hamiltonian is uniquely determined by the external potential (*i.e.*, the location of the nuclei), then the density must also be uniquely determined by the external potential, with each relation being an equivalence. This, in turn, is a perhaps convoluted way of saying that if one knows the density, one knows the energetic properties thereof, at least for the ground-state density (degenerate cases do not necessarily hold in the first formulation of the theorem, and still give rise to unique challenges, but were later proven to have solutions too).

The main problem with DFT is that the proof is nonconstructive, and as of yet, there is no analytical solution to finding the true Hamiltonian as it applies to electron density (*vide supra*).[90]

Kohn and Sham (KS) begin to solve this problem by creating a fictitious set of non-interacting single particle wavefunctions, very similarly to HF theory. From these orbitals, the kinetic energy can be extracted in the same way by summing $-\frac{\hbar^2}{2m}\nabla^2$ over all occupied orbitals (a value which TF methods approximate poorly). Then adding a so-called Hartree component, which is an integral over all pairwise electron interactions in terms of their density:

$$E_{Hartree} = \frac{1}{2}\iint \frac{\rho(\boldsymbol{r})\rho(\boldsymbol{r}')}{|\boldsymbol{r}-\boldsymbol{r}'|}\mathrm{d}r\mathrm{d}r'$$

Equation 16 The Hartree component of the overall energy.

Adding the kinetic energies and Hartree energies together in theory provides a similar result to the un-antisymmeterised HF case, as these two components do not include exchange or correlation. Thus the benefit of the KS formalism is that the exchange, correlation, and small amount of kinetic energy not included in the noninteracting case, can all be lumped together as a functional which takes the density and returns an energy, known as the exchange correlation energy E_{xc}.

This leads to a final expression for the energy of a density:

$$E_{KS}[\rho] = \widehat{T}_{KS}[\rho] + E_{Hartree}[\rho] + E_{xc}[\rho]$$

Equation 17 The total Kohn-Sham energy of an electron density.

The only unknown is thus the exchange correlation functional, E_{xc} (the functional and the corresponding value are often used interchangeably, similarly to inclusion and omission of the hat on an operator), which is the defining feature of DFT methods.

1.2.2.2 Anatomy of a Density Functional

Quite literally thousands of ways exist to develop density functionals,[91] and there are far too many to cover here, so only a salient selection will be shown here. There are two primary ways to design a density functional: empirically,[92] and nonempirically.[93] A nonempirical functional is one which has as few empirical parameters as possible and fixes those which it must have to physically important properties of representative species, such as the ionisation potential of noble gases.[94] The majority of the construction of a nonempirical functional comes from satisfying as many (important) features known to be true of the true exchange correlation functional as possible, such as correct asymptotic behaviour for the universal electron gas as external potentials approach certain values, or ensuring different parts of both the Fermi correlation (local exchange) and Coulomb correlation cancel appropriately. John Perdew has made undeniably monumental contributions to the field of nonempirical functionals such as the Perdew-Ernzerhof-Burke (PBE),[95] Tao-Perdew-Staroverov-Scuseria (TPSS),[96] Perdew-Wang 1991 (PW91),[97] Perdew 1986 (P86),[98] or the more recent strictly constrained and appropriately normed (SCAN)[99] family of functionals.

Empirical functionals however just choose a form, which may or may not be inspired by a sensible functional form, and add free parameters to it, which are then optimised (usually in a least-squares sense) to give the closest values to those of a training set. Semiempirical functionals are ones which take a sensible form, *i.e.* one expected to follow the expected behaviour of the true functional, and then leaving some free parameters and training them on an appropriate set of training data. By far the most famous semiempirical functional is the Becke 3-paramter Lee-Yang-Par functional B3LYP,[100] although many others exist, built for specific functions. Famously, the PBE functional has "0" parameters (although GGA functionals are unable to mutually satisfy the known constraints at the time of publication, and which of the mutually unsatisfiable constraints to include could be considered to be a "parameter"), and even its more commonly used and empirically corrected form PBE0-D3BJ has only 4,[101] compared with Truhlar's ultimately empirical family of Minnesota functionals such as M06-2X which possesses 42.[102] This thesis will not discuss any neural network model functionals or related machine learning derived functionals due to their necessarily over-

parameterised natures, and their ideal performance only "learning" the foibles of the electronic structure method of their training sets.[103]

As might be expected, empirical functionals can perform very well for cases similar to their training data, with M06-2X usually considered a top performer (in its rung, *vide supra*) for organic/main-group thermochemistry calculations. Nonempirical functionals are expected to perform well for all cases, demonstrated by PBE0-D3BJ outperforming M06-2X in most classes of "difficult" problems.

Of special note is the Becke 1997 (B97) class of functionals,[104] initially proposed by Becke, and expanded upon by Grimme, and Head-Gordon and coworkers. This method takes the gradient corrections (a key ingredient in modern density functionals) and expands them in an arbitrarily large polynomial basis, which is a systematic way to create the best empirical functional for any given set of ingredients. These functionals, particularly ωB97X-D, ωB97M-D, ωB97X-V, and ωB97M-V are of exceptional quality.[105] Becke writes on this particular philosophy:

> *"Before we proceed, however, we anticipate the obvious criticism: are the resulting fitted functionals empirical? Do they lack a reliable theoretical foundation? The basic philosophy of fitting the exchange-correlation functional to experimental data is sound in principle, since the Kohn–Sham formalism is complete and perfectly rigorous. E_{XC} of any electronic system is certainly a unique functional of its spin density distributions. Whether the underlying, universal functional dependence is obtained from purely theoretical arguments (very difficult), or from fits to experimental data (much more practical), is entirely irrelevant. Information on the ''shape'' of the Kohn–Sham functional, revealed by whatever means, is of fundamental value and utility. In short, the object we are trying to fit is known to exist."*
>
> *–Becke, A. D., Phys. Rev. A,* ***1988****,* 38*, 3098*

Mostly physicists develop nonempirical functionals, and chemists empirical ones. Paramount to the physicist is how correct, mathematically beautiful, and "true" their equations are. To a chemist, usually the ability to accurately predict and explain experiment is of more value. It is difficult to decide which approach is more valuable, and more difficult still to trust the validity of either. Even Perdew now agrees that the exact form of the exchange correlation functional is either unknowable or so complex that it is of little computational value.[99] At the end of the

day, it comes down to, as it always has, using the appropriate functional for the appropriate problem, at least until artificial intelligence in all its earthly perfection stumbles across the true form.[106]

Until now, the functionals were all presented as though they were pure functionals of only the density. Broadly, this is referred to as local spin density approximation (LSDA or LDA) and has little predictive power- it is very similar to Thomas-Fermi theory. Instead, modern density functionals include additional "ingredients" which allow them to fulfil more known conditions of the true functional or grant them more parametric flexibility. These are most often organised onto rungs of "Jacob's Ladder", an idea originally proposed by Perdew[107] as a way to systematically improve functionals. Imperative to note is that *there is no guarantee including more ingredients will result in an improved functional*,[108] a fact due to the nature of the HK theorem. Merely, these serve as a guide as to where to go if more ingredients seem necessary or desirable, many functionals on higher rungs actually perform worse than their lower counterparts, evidenced by the enduring success of the PBE functional although it is notionally surpassed by the TPSS and PKZB[109] functionals (the latter being unfortunately unpredictive).

Reasonably, the first additional ingredient is the gradient of the electron density, $\nabla\rho$. These are the most prominent and broadly successful functionals, including PBE and BP86, they are entitled "generalised gradient approximations" or GGAs. The most natural extension is again, the gradient of the gradient of the electron density, $\nabla^2\rho$. This adds a significant computational cost for seemingly a small amount of benefit, although this rung homes TPSS and B97 and are called meta-GGAs (mGGAs). Further gradients have been proven not to contribute, and so the fourth rung searches for new sources of exchange energy: introducing an admixture of "exact" exchange from the original HF formulation, using the KS orbitals as presented in the immortalised B3LYP paper. This admixture can be a global percentage, or scale from very little for short-range exchange to a large amount for long range exchange (predictably called range-separated), and this can apply to a parent functional which was any of LSDA, GGA, or mGGA- the rungs become quite indistinct from here. HF-exchange admixtures are usually called hybrids, although sometimes are referred to as hyper-(m)GGAs. The final rung then becomes quite abstract: adding "knowledge of unoccupied orbitals". Usually this means incorporation of a fraction of wave-function based correlation, in almost every case MP2.

1.2.2.3 Corrections to Density Functionals

Some aspects of electronic structure fundamentally escape density functional theory. Multiconfiguration species are those which are not well described by a single determinant,[110] a rule of thumb being those which have multiple major resonance contributors/low-lying excited states, and they are said to have "static" correlation. Examples include conjugated systems with low-lying LUMOs like 1,3-butadiene, or radicals like nitrogen monoxide. Correlation that is not static is dynamical and is due to the instantaneous interactions between electrons as discussed earlier. Formal definitions differentiating the two do exist, but are inconsistent across the literature and unimportant in this context.[111] Density functional theory does not typically perform well for difficult cases with large amounts of static correlation, and methods attempting to correct it typically perform poorly and use multireference methods, which defeats the computationally tractable goal of DFT. It should be noted that these are hard classes of problems for all computational methods, and HF theory also performs poorly in these cases. In fact, hybrid functional with larger proportions of HF-admixture tend to be outperformed by their pure counterparts on systems with large amounts of static correlation. The best solution is to use range-separated hybrids with small global fractions and quite sharp attenuation. This is best observed in transition metal chemistry, which tends to have highly degenerate, very localised ground states due to partially occupied d-orbitals, particularly in the 3d metals. ωB97X-D, which tends to be a well-performing functional across the board, has consequently and reasonably become the workhorse of transition metal chemistry.[112]

The dispersion interaction is principally due to long-range correlation effects, so it might be reasonable to expect that DFT can naturally capture it. When using mGGAs which have been trained on appropriate data sets, the inclusion of gradients can ensure that the electron density maintains the correct shape over medium distance, by forcing agreement between the electron density and its gradients over intermediate distances.[102] All "knowledge" of distant electron density however is lost, and so self-consistent solutions do not capture long distance tails and nonuniformity in the low-density, distant regions indicative of long-range dispersion.[113] Thus, an empirical correction must be added. Most commonly, and perhaps successfully, this is Grimme's D3 correction,[114] tailor made for each functional it adds an artificial attraction between nuclei in the fashion of a forcefield with a potential designed to emulate the r^{-6} scaling nature of dispersion while not double counting short-medium range dispersion already accounted for in the functional. Excellent agreement with experiment for geometries and other

dispersion-dependent geometries has been found with this computationally almost-free correction.

Another, less empirical, method to introduce dispersion was offered by Vydrov and van Voorhis, in its modern form the VV10 correction.[115] This involves doing an explicit 2-electron integral over the entire species and using a semi-empirical functional on the 2-electron density, which is in the same spirit as DFT and can be constructed quite nonempirically. On the surface, this appears to be computationally intractable, however the 2-electron integrals can be performed on a very coarse integration grid (unlike that for underlying parent functional) seemingly without any loss in performance.

1.2.3 Computation of Chemical Mechanisms

More material to the work at hand is the calculation of mechanisms. While electron density is an observable (which has been well characterised for some species in the solid state through electron diffraction studies,[116] allowing for experimental assessment of *ab initio* densities,[117] typically high-level wavefunction-based are touted *ex cathedra* as true densities for all other species), and energy is available for some species through spectroscopy, the "electronic structure" (particularly from DFT) is perhaps a joint hallucination of the theoretical community. In any case, the interpretation of electronic structure data as a guide for physical and chemical properties is predominantly qualitative (particularly in the organometallic community).[118]

Calculations should make predications which are verifiable from experimental data to support or disprove models and understanding of the underlying chemistry.[119] Within the context of low valent main group chemistry, where the field is young and reactivity unusual, an important goal of computational chemistry is to present mechanisms and reaction pathways which align with the experimental evidence to yield a theoretical understanding.

1.2.3.1 Potential Energy Surfaces

To this end, we introduce the potential energy surface (PES). As discussed previously, within the constraints of the Born-Oppenheimer approximation the energy of a system is a function of the nuclear coordinates ($\mathbf{Q} = \{\mathbf{q}_1, \ldots, \mathbf{q}_n\}$ where $\mathbf{q}_n$ defines an internal positional degree of freedom of the system). For every set of nuclear coordinates (of a specific set of elements) there exists a corresponding unique ground state energy (the lowest eigenvalue of the Hamiltonian), and due to the properties of Hilbert spaces (to which all reasonable

wavefunctions belong), the energies of wavefunctions within small variations **Q** form a hypersurface which is continuous and smooth. This hypersurface E = f(**Q**) is known as the potential energy surface, and is why such detailed calculations of the energy of a system are required in the first place.

Simple examples are difficult to imagine. Diatomic molecules possess only one internal degree of freedom, the distance between the nuclear coordinates "r". Consequently E = f(r) is an ordinary graph of the familiar form y = f(x), which is formally a surface but is not very informative. The most intuitive and illustrative example would be one with two internal degrees of freedom, so that we could provide a 3D plot E = f(x_1, x_2) and encourage generalisation to arbitrary dimension. However no system with only two internal degrees of freedom is possible, as for linear systems of N atoms the number of internal degrees of freedom is 3N-5, and for nonlinear systems it is 3N-6; neither expression can give an integer number of atoms for two internal degrees of freedom. Regardless, slices of the hypersurface can always be imagined for a fixed set {$\mathbf{q_1, \ldots, q_{n-2}, x_1, x_2}$} $E_{q1\text{-}qn\text{-}2}$ = f(x_1, x_2), or even reducing to the one-dimensional case.

Without loss of generality, the system can always be reduced to the one-dimensional case by defining a parametric curve. Take t ∈ [-1,1], each $\mathbf{q_x}$ varies between the reactants and the products, varying smoothly over some representation of the reaction, so $\mathbf{q_x}$ varies from its value at the reactants, and that of the products. In this sense, $\mathbf{q_x}$ could be taken to be a function of how far the reaction has progressed; arbitrarily we can take t to be the reaction progression, $\mathbf{q_x}$ can be stated as a function of t, $\mathbf{q_x}(t)$, t varying from -1 at the reactants and 1 at the products (often with 0 being the transition state). Other parameterisations are possible, this one merely being simple. In this case, there is an energy associated with the configuration at an arbitrary t, so a 1D PES is always possible to describe as E(t), the "t" axis usually described as the reaction coordinate, with differing units depending on the specific parameterisation.[120]

Importantly, intrinsically stable configurations **Q** are those for which variations of any $\mathbf{q_x}$ results in an increase in the energy of the system, *i.e.* Equation 18.

$$\forall q_x \in \boldsymbol{Q} \left(\left(\frac{\partial}{\partial q_x} \mathrm{E}(\mathbf{Q}) = 0 \right) \wedge \left(\frac{\partial^2}{\partial {q_x}^2} \mathrm{E}(\mathbf{Q}) \in \mathbb{R}^+ \right) \right)$$

Equation 18 The requirements of a local minimum on the potential energy surface.

Chemically speaking, such stable configurations are molecules. These are potentially bottleable species and include reactants, products, and possible intermediates.

A reaction is merely the path a molecule takes over a PES, linking two local minima, usually taking a molecule from a high energy starting material to a relatively low energy end product, in a standard exergonic reaction. Potential energy surfaces are often whimsically described using mountaineering terms, relating the familiar topography of a 3D surface (*i.e.* the real world) to its topological analogue in hyperspace. Local minima, those aforementioned intermediates and potentially isolable species, are the analogues of valleys. If, however, one coordinate is a local maximum while leaving the others minima, as Equation 19:

$$\forall q_x \in \boldsymbol{Q}/\boldsymbol{q_a} \left(\left(\frac{\partial}{\partial q_x}\mathrm{E}(\mathbf{Q}) = 0\right) \wedge \left(\frac{\partial^2}{\partial {q_x}^2}\mathrm{E}(\mathbf{Q}) \in \mathbb{R}^+\right)\right) \wedge \left(\left(\frac{\partial}{\partial q_a}\mathrm{E}(\mathbf{Q}) = 0\right) \wedge \left(\frac{\partial^2}{\partial {q_a}^2}\mathrm{E}(\mathbf{Q}) \in \mathbb{R}^-\right)\right)$$

Equation 19 The requirements of a first-order critical point on the potential energy surface.

then this corresponds to a "col", the lowest meeting point between two adjacent mountains, the highest point of a pass. It is a first-order saddle point, and the highest energy point between two minima- such a coordinate is a transition state.

There exists a path within the potential energy surface between a valley and a col such that at any point there exists only one partial derivative which is nonzero,[†] called a "riverbed walk". This is called the intrinsic reaction coordinate (IRC) after the seminal work of Fukui.[121] Topologically, there are not necessarily only two riverbed walks associated with one col (one towards the reactant valley and one towards the product) as one may expect. Such occasions are called bifurcations and are chemically difficult to handle, where one transition state is formally associated with multiple reactions. Bifurcations are often associated with a specific symmetry of the system at hand and are ubiquitous throughout very simple reactions; bifurcations can also occur at noncritical points, splitting one riverbed into two. Such surfaces can be arbitrarily complex, but unless specifically looking for such situations, bifurcations are rare in chemically relevant systems. Within this work, as is standard, they are presumed absent and all transition states are presumed to be associated with exactly two intermediates and riverbed walks are assumed to possess no splitting or ambiguity.

Higher-order critical points (*i.e.* coordinates analogous to Equation 19 but for multiple $\mathbf{q_a}$) are not typically chemically relevant.[122] A peak, which is a third order critical point (and the highest possible order critical point in three dimensions), have no impact on chemical kinetics as they are not physically observable, or rate determining as there is always a lower energy

[†] More accurately, there is only one eigenvalue of the Jacobian matrix, even if this does not correspond exactly to any specific $\mathbf{q_x}$ unless **Q** is the eigenbasis.

pathway available (by the intermediate value theorem).[123] In fact, a qth-order critical point is often not even possible or an object of any interest, as the energy of such a point on the PES would likely be impossibly high. To the best of my understanding, a second-order critical point does not possess a standard mountaineering namesake, merely being the inflection point along an arête (an arête being the second order equivalent of a riverbed walk, often called a ridge when the surface around it is fairly flat). Similar to a peak, critical arêtes typically have minimal impact on chemical kinetics as again, there are lower energy pathways for molecules to take, although some multireference calculations have been performed to investigate the impact of low-energy second order critical points on reaction kinetics, often seemingly relevant in excited state mechanisms (such as those involving photoexcitations).[124]

1.2.3.2 Traversing Energy Landscapes

Importantly, PESs are characterised in order to model the relative rates and pathways molecules take to convert between each other, a singularly important goal of chemistry.

Even prior to the widespread acceptance of atoms and molecules,[125] it was accepted that substances could convert between each other, and that such processes (as all things must) occurred over time.[126] Naturally of concern became the magnitudes of the rates of conversion and their evident temperature dependence, culminating in the seminal works of Arrhenius, van't Hoff, and Mellor.[127,128,129,130] Concurrently, the works of Boltzmann[131] and Gibbs[132] developed statistical mechanics (and the necessary notion of Gibbs free energy), which when applied to the problem of chemical kinetics by Eyring, Polanyi, and Evans, culminated in the Eyring equation (Equation 20) which relates the temperature, relative barrier height (with both enthalpic and entropic components), and reaction rate in modern transition state theory (TST).[133]

$$k = \kappa \frac{k_b}{h} T e^{-\frac{\Delta G^{\ddagger}}{RT}}$$

Equation 20 The Eyring equation. The rate, k, is proportional to k_b/h, the Boltzmann constant divided by the Planck constant, the temperature, and the exponential of the barrier height $\Delta G^{\ddagger}$ divided by the universal gas constant and temperature. An additional constant, κ, accounts for reflection about the barrier.

The essential premise being that once you have a potential energy surface, molecules will classically traverse it until reaching equilibrium. Temperature dictates the distribution of energy among molecules in the ensemble, which in turn dictates how many particles possess the required energy to move from one basin to another. Equilibrium is established when molecules exist in ratios satisfying the Boltzmann distribution for the current temperature.

Of course, this presumes semiclassical behaviour and ignores features such as full-molecule tunnelling, which can be relevant at low temperatures and light particles, particularly mechanisms principally involving hydrogen.[134] Some formulations include a constant, κ, to include reflection off the barrier, although in the absence of experimental data there are no *a priori* ways to determine its value and it is typically presumed to be 1, ignoring tunnelling and reflection. Fully characterising the potential energy surface and calculating tunnelling and reflection probabilities using methods such as Wentzel-Kramers-Brillouin (WKB) approximation[135] can yield such probabilities for simple cases like high, narrow, barriers, however this still produces difficult downstream calculations such as crossing attempts, and rarely matches chemically relevant situations.

Applications of relativistic, time-dependent formulations of quantum mechanics could overcome such a shortcoming by propagating the wave equation through the potential energy surface,[136] but in physically relevant settings *i.e.* temperatures between 200 and 400 Kelvin, 0.1-10 atmospheres of pressure, and any atoms heavier than hydrogen, the semiclassical form of the Eyring equation is sufficiently predictive.

This set of assumptions allows the characterisation of a reaction pathway simply by characterising all of the intermediate species and the transition states which link them, allowing for a long riverbed walk from the starting material to the products.

The rate determining step becomes that which has the largest activation energy between the largest previous minimum and the barrier; assuming heat transfer is much faster than the chemical reactions, then all species remain approximately at thermal equilibrium, which conceptually accounts for the idea that molecules cannot rest along a pathway. Any intermediate of higher energy, in thermal equilibrium, is already populated proportionally (N_1 and N_2 in Figure 11): the barrier from the higher energy species multiplied by the thermal population of that intermediate results in the same effective barrier height as though the barrier were that between the lowest energy valley and the highest energy col.

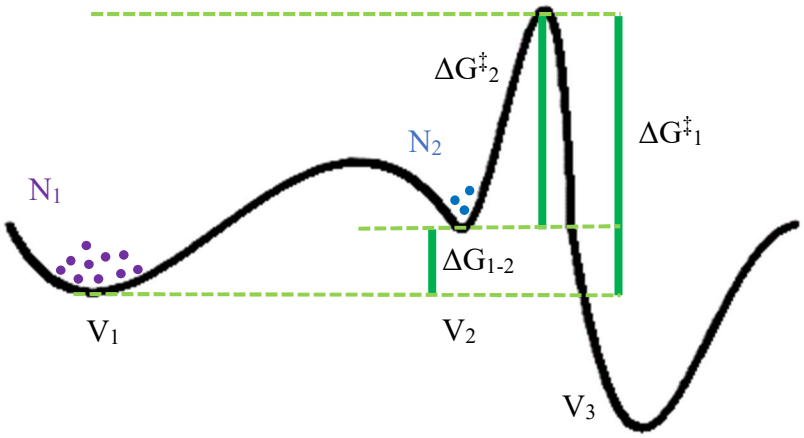


Figure 11 Molecules traversing a potential energy surface cannot "rest" at minima to overcome larger barriers, the rate for particles to traverse the barrier $\Delta G^{\ddagger}_1$ is the same regardless of the existence of the minimum V_2, see text for details.

From Figure 11, we can readily derive that the rate starting from the lower valley V_1 is equal to the rate when starting from the higher valley V_2 when accounting for the thermal population difference between the two[131] (omitting all components of the Eyring equation which are equal between the two quantities, i.e. $e^{1/RT}$, k_b/h, T):

$$k_1 \propto N_1 e^{-\Delta G^{\ddagger}_1};\ k_2 \propto N_2 e^{-\Delta G^{\ddagger}_2}$$

$$\frac{N_2}{N_1} = e^{-\Delta G_{1-2}}$$

$$\therefore N_2 = N_1 e^{-\Delta G_{1-2}}$$

$$\Delta G^{\ddagger}_1 = \Delta G_{1-2} + \Delta G^{\ddagger}_2 \ (from \text{ Figure 11})$$

$$\vdash k_2 = N_2 e^{-\Delta G^{\ddagger}_2} \equiv N_1 e^{-\Delta G_{1-2}} e^{-\Delta G^{\ddagger}_2}$$

$$= N_1 e^{-(\Delta G_{1-2} + \Delta G^{\ddagger}_2)}$$

$$= N_1 e^{-\Delta G^{\ddagger}_1}$$

$$= k_1$$

$$\therefore k_1 = k_2$$

Equation 21 Informal proof of the independence of the rate constant on the shape of the PES beyond the largest barrier height, assuming thermal equilibrium.

Consequently, for simple reactions just the knowledge of the magnitude of the barrier for the rate determining step is enough to characterise the rate of the reaction at an arbitrary temperature. The clue is in the name. This matches the intuition as energy is a state-based function, and any other result allows for the violation of the second law of thermodynamics- changing the path cannot change the energy, and cannot change the rate; one could imagine changing the potential energy surface to remove the minimum at V_2, yielding the same result.

This allows for the experimental ratification of computed reaction mechanisms based on approximate rates. *E.g.* a reaction which occurs overnight (*ca.* 16 hours) at room temperature should have a half-life in the region of 4 hours, implying a rate constant of $\ln(2)/4 \approx 0.173$ h^{-1}, implying a barrier height of *ca.* 23.4 $kcalmol^{-1}$. Depending on implied uncertainties, this might discount a calculated barrier height of 27 $kcalmol^{-1}$, or a calculated barrier height of 18 $kcalmol^{-1}$ might call into question the identity of the reactants or the validity of the methodology.

Describing an unusual PESs is crucial to all subsequent chapters of this work. Chapter 2 constitutes experimental work which offers a previously unreported theoretical process as way of explanation, the PES of a system of silicon hydrides and its experimental corroboration constitutes the majority of chapter 3,[137] and chapter 4 similarly involves the construction of many PESs related to low-valent boron chemistry.[138] Chapter 5, for completeness, discusses the published mechanism of the reaction of aluminyl anions with benzene.[139]

1.3 References

[1] Gay-Lussac, J. L., *Mémoires de la Société d'Arcueil,* **1809**, *2*, 207
[2] Dalton, J., *A New System of Chemical Philosophy*, **1808**, 1, Manchester
[3] Frankland, E., *Phil. Trans. R. Soc,* **1852**, *142,* 417
[4] Berzelius, J. J. *Lärbok i kemien*., **1808**, 1, Stockholm
[5] Tolstoy, L., *Война и мир*, **1865-1867**, The Russian Messenger
[6] Chu, G.; Moss, R. A.; Sauers, R. R., *J. Am. Chem. Soc.*, **2005**, *127*, *41*, 14206
[7] Norman, N. C.; Winter, M. J, *Chemistry*, **2025**, *7*, 170
[8] Ruddick, K. R.; Parril, A. L., *J. Chem. Ed.,* **2012**, *89*, *11*, 1436
[9] Hicks, J.; Vasko, P.; Goicoechea, J. M; Aldridge, S., *Nature,* **2018***, 557*, 92
[10] Jackson, R. A.; Matthews, A. J. R., Vasko, P.; Mahon, M. F.; Hicks, J.; Liptrot, D. J., *Chem. Commun.*, **2023**, *59*, 5277
[11]Tacke, M.; Schnöckel, H., *Inorg. Chem.*, **1989**, *28*, *14*, 2895
[12] Any introductory chemistry text, see for example: Burrows, A.; Holman, J.; Lancaster, C.; Overton, T.; Parsons, A.; Pilling, G.; Price, G., *Chemistry³: Introducing Inorganic, Organic and Physical Chemistry*, **2017**, 4th ed.; Oxford University Press
[13] Jensen, B. J., *J. Chem. Educ.*, **1996**, *73*, *1*, 11
[14] Pauling, L., *The Nature of the Chemical Bond*, **1960**, Cornell Univ., USA, 3rd ed.
[15] Hoffmann, R., *Angew. Chem. Int. Ed.,* **1982**, *21*, 711
[16] Karen, P.; Armelao, L.; Butler, I. S.; Tomišić, V.; Yamashita, M., *Pure Appl. Chem.,* **2025**, *97*, *2*, 149
[17] Evans M. G.; Polanyi, M., *Trans. Faraday Soc.*, **1938**, *34*, 11
[18] Hammond, G. S., *J. Am. Chem. Soc.*, **1955**, *77*, *2*, 334
[19] Koch, D; Chen, Y.; Golub, P.; Manzhos, S., *Phys. Chem. Chem. Phys*., **2019**, *21*, 20
[20] Légaré, M.-A.; Bélanger-Chabot, G.; Dewhurst, R. D.; Welz, E.; Krummenacher, I.; Engels, B.; Braunschweig, H., *Science*, **2018**, *359*, 89
[21] a) Feng, Z.; Tang, S.; Su, Y.; Wang, X., *Chem. Soc. Rev.*, **2022**, *51*, 6071; b) Fischer, R. C.; Power, P. P., *Chem. Rev.*, **2010**, *110*, 3877
[22] Marciniec, Bogdan; Pietraszuk, Cezary; Pawluć, Piotr; Maciejewski, Hieronim, *Chem. Rev.*, **2022**, *122*, 3996
[23] Buchhorn, M.; Deeth, R. J.; Krewald, V., *Chem. Eur. J.*, **2022**, *28*, e202103775
[24]NobelPrize.org., www.nobelprize.org/prizes/chemistry/2010/summary/
[25] Rabaté, J.-M., *Forum for Modern Language Studies*, **2018**, *54*, 510
[26] Bowers, M. S.; Canalias, C.; Mirov, S.; Nilsson, J.; Saraceno, C. J.; Schunemann, P. G., *Opt. Express*, **2022**, 30, 20762
[27] Yamamoto, H.; Futatsugi, K., *Angew. Chem. Int. Ed.*, **2005**, *44*, 1924
[28] Colacot, T. J., *Metall. Rev.*, **2011**, *55*, 84
[29] a) Dewar, M. J. S., *Bull. Soc. Chim. Fr.,* **1951**, *18*, C79; b) Chatt, J.; Duncanson, L. A., *J. Chem. Soc.*, **1953**, 2939
[30] Melaimi, M.; Jazzar, R.; Soleilhavoup, M.; Bertrand, G., *Angew. Chem. Int. Ed.*, **2017**, *56*, 10046
[31] Czernetzki, C.; Arrowsmith, M.; Fantuzzi, F.; Gärtner, A.; Trçster, T.; Krummenacher, I.; Schorr, F.; Braunschweig, H., *Angew. Chem. Int. Ed.*, **2021**, 60, 20776
[32] Pophristic, V.; Goodman, L., *Nature*, **2001**, *411*, 565
[33] Faraone, G.; Ricevuto, V.; Romeo, R.; Trozzi, M., *Inorg. Chem.*, **1970**, *9*, *6*, 1525
[34] Pitzer, K. S., *J. Am. Chem. Soc.,* **1948**, *70*, *6*, 2140
[35] West, R.; Fink, M. J.; Michl, J., *Science*, **1981**, *214*, 4527
[36] Yoshifuji, M.; Shima, I.; Inamoto, N.; Hirotsu, K.; Higuchi, T., *J. Am. Chem. Soc.*, **1981**, *103*, *15*, 4587
[37] A. Stach, C. Jones, *Science*, **2007**, *318,* 1754-1757
[38] Lalrempuia, R.; Kefalidis, C. E.; Bonyhady, S. J.; Stasch, A.; Jones, C., *J. Am. Chem. Soc.*, **2015**, *137*, *28*, 8944
[39] Paparo, A.; Yuvaraj, K.; Matthews, A. J. R.; Douair, I., Maron, L.; Jones, C., *Angew. Chem. Int. Ed.*, **2021**, *60*, 630
[40] Bilbrey, J. A.; Kazez, A. H.; Locklin, J.; Allen, W. D., *J. Comput. Chem.*, **2013**, *34*, 1189
[41] Tolman, C. A., *J. Am. Chem. Soc.*, **1970**, *92*, *10*, 2956
[42] Tolman, C. A., *Chem. Rev.*, **1977**, *77*, *3*, 313
[43] Miiller, T. E.; Mingos, D. M. P., *Transition Met. Chem.*, **1995**, *20*, 533
[44] Escayola, S.; Bahri-Laleh, N.; Poater, A., *Chem. Soc. Rev.*, **2024**, *53*, 853

[45] Medvedev, M. G.; Bushmarinov, I. S.; Sun, J.; Perdew, J. P.; Lyssenko, K. A., *Science*, **2017**, *355*, 49
[46] Sim, E.; Song, S.; Burke, K., J. *Phys. Chem. Lett.*, **2018**, *9*, *22*, 6385
[47] Kim, M.-C.; Sim, E.; Burke, K., *Phys. Rev. Lett.*, **111**, 073003
[48] These views are relatively accepted. See for example: a) Perdew, J. P.; Chevary, J. A.; Vosko, S. H.; Jackson, K. A.; Pederson, M. R.; Singh, D. J.; Fiolhais, C. *Phys. Rev. B*, **1992**, *46*, 6671 b) Erratum: Perdew, J. P.; Chevary, J. A.; Vosko, S. H.; Jackson, K. A.; Pederson, M. R.; Singh, D. J.; Fiolhais, C., *Phys. Rev. B*, **1993**, *48*, 4978
[49] Phipps, M. J. S.; Fox, T.; Tautermann, C. S.; Skylaris, C.-K., *Chem. Soc. Rev.*, **2015**, *44*, 3177
[50] Zeigler, T.; Rauk, A., *Theoret. Chim. Acta (Berl.)*, **1977**, 46, 1
[51] Morokuma, K., *J. Chem. Phys.*, **1971**, *55*, 1236
[52] Eskandari, K.; Vila, A.; Mosquera, R. A., *J. Phys. Chem. A*, **2007**, *111*, 8491
[53] Becke, A. D.; Edgecombe, K. E., *J. Chem. Phys.*, **1990**, *92*, 5397
[54] Johnson, E. R.; Keinan, S.; Mori-Sánchez, P.; Contreras-García, J.; Cohen, A. J.; Yang, W., *J. Am. Chem. Soc.*, **2010**, *132*, 6498
[55] Falivene, L.; Cao, Z.; Petta, A.; Serra, L.; Poater, A.; Oliva, R.; Scarano, V.; Cavallo, L., *Nat. Chem.*, 2019, **11**, 872
[56] Gransbury, G. K.; Corner, S. C.; Kragskow, J. G. C.; Evans, P.; Yeung, H. M.; Blackmore, W. J. A.; Whitehead, G. F. S.; Vitorica-Yrezabal, I. J.; Oakley, M. S.; Chilton, N. F.; Mills, D. P., *J. Am. Chem. Soc.*, **2023**, 145, *41*, 22814
[57] a) Hemsworth, J.; Tomeček, J.; Hasija, A.; Whitehead, G. F. S.; Kaltsoyannis, N.; Mills, D. P.; Willcox, D., *Chem. Eur. J.*, **2026**, *32*, *11*, e03282; b) McMillan, A. J.; Sienkowska, M.; Di Lorenzo, P.; Gransbury, G. K.; Chilton, N. F.; Salamone, M.; Ruffoni, A.; Bietti, M.; Leonori, D., *Angew. Chem. Int. Ed.*, **2021**, *60*, 7132 amongst others
[58] Jones, R. S.; Krämer, T.; Nichol, G. S.; Mahon, M. F.; Kragskow, J. G. C.; Uzelac, M., *Chem. Commun.*, **2025**, *61*, 15834
[59] Emerson-King, J.; Baldwin, J.; Corner, S. C.; Blackmore, W. J. A.; Chilton, N. F.; Mills, D. P., *J. Am. Chem. Soc.,* **2025**, *147*, 35555
[60] Specifically those of Bondi, A., *J. Phys. Chem.*, **1964**, *68, 3*, 441
[61] a) Nemcsok, D.; Wichmann, K.; Frenking, G., *Organometallics*, **2004**, *23*, 3640; b) Jacobsen, H.; Correa, A.; Costabile, C.; Cavallo, L, *J. Organomet. Chem.*, **2006**, *691*, 4350; c) Zois, K. P.; Danopoulos, A. A.; Tzeli, D., *ChemPhysChem*, **2025**, *26*, e202500012
[62] Becke, A. D., *J. Chem. Phys.*, **2014**, *140*, 18301
[63] McEvoy, J. P.; Zarate, O., **2004,** *Introducing Quantum Theory*, Totem Books
[64] Baggott, J., 'Born's Interpretation of the Wavefunction: Quantum Probability', The Quantum Cookbook: Mathematical Recipes for the Foundations for Quantum Mechanicsm, **2020**, Oxford Academic Press
[65] Born, M.; Oppenheimer, R., *annalen der physik*, **1927**, *389*, *20*, 457-484
[66] M^{c}Mahon, D., *Quantum Mechanics Demystified*, **2006**, McGraw-Hill
[67] Schrodinger, E., *Phys. Rev.*, **1926**, *28*, *6*, 1049-1070
[68] Hamilton, W. R., "On a general method of expressing the paths of light, & of the planets, by the coefficients of a characteristic function", **1833**, P. D. Hardy, Dublin
[69] Pines, D., *Frontiers in Physics*, The Many-Body Problem, **1961**
[70] Miller, W., *Symmetry and Separation of Variables*, **1984**, Cambridge University Press
[71] Uhlenbeck, G. E.; Goudsmit, S. A., *Die Naturwissenschaften*, **1925**, *13*, 953
[72] Gerlach, W.; Stern, O., *Z. Physik*, **1922**, *9*, 349
[73] Pauli, W., *Phys. Rev.*, **1940**, *58*, 716
[74] Slater, J. C., *Phys. Rev.*, **1929**, 34, 1293
[75] Pauli, W., *Z. Physik*, **1925**, 31, 765
[76] Hartree, D. R., *Mathematical Proceedings of the Cambridge Philosophical Society*, **1928**, *24*, *1*, 111
[77] Löwdin, P.-O., *Phys. Rev.*, **1955**, 97, 1509
[78] Møller, C.; Plesset, M. S., *Phys. Rev.*, **1934**, *46*, 618
[79] Rayleigh, J. W. S., *The Theory of Sound*, **1894**, *1*, 113
[80] Nagy, P. R.; Samu, G.; Kallay, M., *J. Chem. Theory Comput.*, **2016**, *12*, *10*, 4897
[81] Ross, I. G., *Trans. Faraday Soc.*, **1952**, *48*, 973
[82] Cizek, J., *J. Chem. Phys.*, **1966**, *45*, 4256
[83] Ghose, K. B.; Piecuch, P.; Adamowicz, L., *J. Chem. Phys.*, **1995**, *103*, 9331
[84] Thomas, L. H., *Mathematical Proceedings of the Cambridge Philosophical Society*, **1927**, 23, 5, 542
[85] Teller, E., *Rev. Mod. Phys.*, **1962**, *34*, 627

[86] Dirac, P. A. M., *Mathematical Proceedings of the Cambridge Philosophical Society*, **1930**, 26, 3, 376
[87] Hohenberg, P.; Kohn, W., *Phys. Rev. B.*, **1964**, *136*, 864-871
[88] Kozuch, S.; Martin, J. M. L., *Phys. Chem. Chem. Phys.*, **2011**, 13, 20104-20107
[89] Levy, M., *Proc. Natl. Acad. Sci. USA*, **1979**, *76*, *12*, 6062-6065
[90] Wrighton, J.; Albavera-Mata, A.; Rodriguez, H. F.; Tan, T. S.; Cancio, A. C.; Dufty, J. W.; Trickey, S. B., *Lett. Math. Phys.*, **2023**, 113, 41
[91] Mardirossian, N.; Head-Gordon, M., *Molecular Physics*, **2017**, *115*, *19*, 2315
[92] Adamson, R. D.; Gill, P. M. W.; Pople, J. A., *Chem. Phys. Lett.*, **1998**, *284*, 6
[93] Bremond, E.; Ciofini, I.; Sancho-Garcia, J. C.; Adamo, C., *Acc. Chem. Res.*, **2016**, *49*, *8*, 1503
[94] Klimes, J.; Bowler, D. R.; Michaelides, A., *Phys. Rev. B*, **2011**, 83, 195131; b) Ivanov, S., Levy, M., *J. Phys. Chem. A* **1998**, 102, 3151; c) Springer, M.; Svendsen, P. S.; von Barth, U., *Phys. Rev. B*, **1996**, 54, 17392; d) Mardirossian, N.; Head-Gordon, M., *J. Chem. Phys.*, **2015**, 142, 074111.
[95] Perdew, J. P.; Burke, K.; Ernzerhof, M., *Phys. Rev. Lett*., **1996**, *77*, *18*, 3865
[96] Tao, J.; Perdew, J. P.; Staroverov, V. N.; Scuseria, G. E., *Phys. Rev. Lett*., **2003**, *91*, *14*, 146401
[97] Perdew, J. P.; Wang, Y., *Phys. Rev. B*, **1992**, *45*, *23*, 13244
[98] Perdew, J. P.; Wang, Y., *Phys. Rev. B*, **1986**, *33*, 8800
[99] Furness, J. W.; Kaplan, A. D.; Ning, J.; Perdew, J. P.; Sun, J., *J. Phys. Chem. Lett.*, **2020**, *11*, 8208
[100] Becke, A. D., *J. Chem. Phys.*, **1993**, *98*, *2*, 1372
[101] Perdew, J. P.; Ernzerhof, M.; Burke, K., *J. Chem. Phys.*, **1996**, *105*, *22*, 9982
[102] Zhao, Y.; Truhlar, D. G., *Theor. Chem. Account*, **2007**, *120*, 215
[103] a) Akashi, R.; Sogal, M.; Burke, K., arXiv:2503.01709, **2025**, currently unreviewed; b) Zhao, H.; Gould, T.; Vuckovic, S., *Phys. Chem. Chem. Phys.*, **2024**, *26*, 12289; c) Kirkpatrick, J.; McMorrow, B.; Turban, D. H. P.; Gaunt, A. L.; Spencer, J. S.; Matthews, A. G. D. G.; Obika, A.; Thiry, L.; Fortunato, M.; Pfau, D.; Castellanos, L. R.; Petersen, S.; Nelson, A. W. R.; Pushmeet, K.; Mori-Sanchez, P.; Hassabis, D.; Cohen, A. J., *Science*, **2021**, *373*, 1385
[104] Becke, A. D., *Phys. Rev. A*, **1988**, *38*, 3098
[105] a) Chai, J.-D.; Head-Gordon, M., *Phys. Chem. Chem. Phys.*, **2008**, *10*, 6615; b) Mardirossian, N.; Head-Gordon, M., *Phys. Chem. Chem. Phys.*, **2014**, *16*, 9904
[106] Huang, B.; von Rudorff, G. F.; von Lilienfeld, O. A., *Science*, **2023**, *381*, *6654*, 170
[107] S. F. Sousa, P. A. Fernandes, M. J. Ramos, *J. Phys. Chem. A,* **2007**, *111*, *42*, 10439
[108] Pribram-Jones, A.; Gross, D. A.; Burke, K., *Annu. Rev. Phys. Chem.*, **2015,** *66,* 283
[109] Perdew, J. P.; Kurth, S.; Zupan, A.; Blaha, P., *Phys. Rev. Lett.*, **1999**, *82*, 2544
[110] Gill, P. M. W., *Annual Reports on the Progress of Chemistry C*, **2011**, 107, 229
[111] Lehtola, S.; Tubman, N. M.; Whaley, K. B.; Head-Gordon, M., *J. Chem. Phys.*, **2017**, *147*, *15*, 154105
[112] Goerigk, L.; Hansen, A.; Bauer, C.; Ehrlich, S.; Najibi, A.; Grimme, S., *Phys. Chem. Chem. Phys.,* **2017**, *19*, 32184
[113] Lifshitz, E. M., *Perspect. Theor. Phys.*, **1992**, 329
[114] Grimme, S.; Hansen, A.; Brandenburg, J. G.; Bannwarth, C., *Chem. Rev.*, **2016**, *116*, *9*, 5105
[115] Vydrov, O. A.; van Voorhis, T., *J. Chem. Phys.*, **2010**, *133*, 244103
[116] Hickstein, D. D.; Cole, J. M.; Turner, M. J.; Jayatilaka, D., *J. Chem. Phys.*, **2013**, 139, 064108
[117] Kleemiss, F.; Dolomanov, O. V.; Bodensteiner, M.; Peyerimhoff, N.; Midgley, L.; Bourhis, L. J.; Genoni, A.; Malaspina, L. A.; Jayatilaka, D.; Spencer, J. L.; White, F.; Grundkötter-Stock, B.; Steinhauer, S.; Lentz, D.; Puschmann, H.; Grabowsky, S., *Chem. Sci.,* **2021**, *12*, 1675
[118] Bursch, M.; Mewes, J.-M.; Hansen, A.; Grimme, S., *Angew. Chem. Int. Ed.*, **2022**, *61*, e202205735
[119] Popper, K., *Logik der Forschung*, **1934**, *Springer*; English translation *The Logic of Scientific Discovery*, **1959**, *Routledge*
[120] Stachó, L. L.; Bán, M. I., *Theor. Chim. Acta.*, **1992**, *83,* 433
[121] a) Fukui, K., *J. Phys. Chem.*, **1970**, 74, 4161; b) Fukui, K.; Kato, S.; Fujimoto, H., *J. Am. Chem. Soc.*, **1975**, 97, 1; c) Fukui, K., *Acc. Chem. Res.*, **1981**, 14, 363
[122] Yadav, K.; Pradhan, R.; Lourderaj, U., *Faraday Discuss.*, **2022**, *238*, 183
[123] Bolzano, B., *Beyträge zu einer begründeteren Darstellung der Mathematik*, **1810**, Prague
[124] Mirzanejad, A.; Muechler, L., *ChemPhysChem*, **2025**, *26*, e202400786
[125] a) Škvarla, J., *Arch. Hist. Exact Sci.*, *78*, *6*, 833; b) Perrin, J., *Les Atomes*, **1913**, Félix Alcan, Paris
[126] Zeno's paradoxes of motion (specifically of The Arrow), reported through second hand account: Aristotle, *Physics*, *ca.* 400 B.C., Athens; English translation Hardie, R. P.; Gaye, R. K., *Physica*, **1930**, 2
[127] Laidler, J. K., *J. Chem. Educ.*, **1984**, *61*, *6*, 494

[128] Arrhenius, S., *Zeitschrift für Physikalische Chemie*, **1889**, 4, 226
[129] Van't Hoff, J. H., *Etudes de dynamique chimique*, **1884**, F. Muller and Co., Amsterdam
[130] Mellor, J. W., *Chemical Statics and Dynamics*, **1904**, Longmans, Green & Co., London
[131] Boltzmann, L., *Sitzungsberichte der Kaiserlichen Akademie der Wissenschaften*, **1872**, *66*, 275
[132] Gibbs, J. W., *Elementary Principles in Statistical Mechanics Volume II*, **1902**, Longmans Green and Company, New York
[133] Eyring, H., *J. Chem. Phys.*, **1935**, *3*, 107
[134] Qiu, Y.; Wu, C.-H.; Schaefer, H. F., III; Allen, W. D.; Agarwal, J., *Phys. Chem. Chem. Phys.*, **2016**,*18*, 4063
[135] Wentzel, G. *Zeitschrift für Physik,* **1926**, *38*, *6,* 518; b) Kramers, H. A., *Zeitschrift für Physik,* **1926**, *39*, *10*, 828; c) Brillouin, L., *C. R. Acad. Sci. Paris*, **1926**, *183,* 24
[136] Miller, W. H.; Zhao, Y.; Ceotto, M.; Yang, S., *J. Chem. Phys.*, **2003**, *119*, 1329
[137] a) Huo, R.; Armstrong, J. A.; Nelmes, G. R.; Lawes, D. J.; Edwards, A. J.; McMullin, C. L.; Hicks, J., *Chem. Eur. J.*, **2024**, *30*, e202400662; b) Huo, R. & Nelmes, G. R.; Edwards, A. J.; McMullin, C. L.; Hicks, J., *Manuscript in Preparation*, **2026**
[138] Nahon, E.; Nelmes, G. R.; Dallerba, E.; Lim, L.-F.; Cox, N.; McMullin, C. L.; Massi, M.; Kallmeier, F.; Hicks, J., *Chem. Sci.*, **2026**, Advance Article
[139] Kallmeier, F.; Matthews, A. J. R.; Nelmes, G. R.; Lawson, N. R.; Hicks, J., *Dalton Trans.*, **2024**, *53*, 12450

2. Synthesis and Computation of a Dimagnesiogermane

"*Lentement dans la souffrance, J'ai reconquis… le sentiment de ma dignité d'être humain…*"

-S. Weil, *Factory Notebooks*, **1934**

2.1 Introduction to Low-Valent Synthesis

Perhaps the most general class of chemical transformation possible is the reduction-oxidation (redox) process of formally transferring electrons from one place to another.[1]

Nucleophile-electrophile chemistry encompasses vast swathes of molecular chemistry, and while formal oxidation states do not always change in such processes, certainly most intermediates and products possess significantly different electronic structures from the reactants and from each other, indicative of at least a redistribution of electron density if not a formal electron transfer process. In many ways a chemical process has only occurred if electrons are moved, and thus all chemical processes are in some way redox.[2]

Within inorganic chemistry, redox chemistry is monarch.[3] The galvanic cell was first described in 1780 by Galvani in frog's legs,[4] and shortly after generalised to the inorganic by Volta in 1790,[5] and now represents a fundamental technology crucial to every aspect of modern life. The electrochemical cell forms the basis of battery technology to this day,[6] driving lithium as an economically essential mineral. In Australia, lithium exports were valued at *ca*. $4.8 billion AUD in 2025, nearly 4% of total gross domestic product.[7]

Beyond the economic implications, redox chemistry is responsible for the formation of simple salts, and reactions between elemental oxygen and a metal, semimetal, or metalloid form most of the rocky features of our planet from silicates to feldspars.[8] Reduction of the naturally occurring metal oxides has been a driving force for human development for millennia, founding the bronze and then iron ages,[9,10] giving access to new tools and technologies. In many ways the production of elemental phosphorus (*via* reduction of biologically relevant molecules) by Brand in 1669 marks the beginning of modern chemistry.[11] Particularly the subsequent filling out of the nascent periodic table by Davy,[12] Berzelius,[13] and many other early chemists in the late 1700s and early 1800s, of course to be assembled by Mendeleev in the seminal work "Соотношение свойств с атомным весом элементов",[14] relationship of properties with atomic weight of elements in 1869. Evidently, to reduce is human nature.

The triboelectric effect is somewhat of a macroscopic counterpart to redox processes, and was known by Thales of Miletus *ca*. 585 BCE by the rubbing of amber on wool (with the prefix tribo derived from τρίβος (tribos), Greek for rub, and even electron derived from ἤλεκτρον (electron) as Greek for amber).[15] Although the theoretical origins (and even empirical predictions) of the triboelectric effect are still hotly debated to this day,[16] even macroscopic

redox processes are crucial to our understanding of electronic structure and are describable as the earliest evidence of quantum theory, as classical charges fail to account for the build-up of charge solely through contact (*e.g.* Figure 1).[17]



Figure 1 The triboelectric effect can induce charges on other materials, and in this case, the reduced feline electrostatically attracts the Styrofoam peanuts. Photo: Sean McGrath, Saint John, NB, Canada, Creative Commons CC BY 2.0.

More pertinent to the work at hand, redox processes are extremely useful in molecular chemistry. Transition metal catalysis is described as occurring through simple, well understood steps including ligand association and dissociation, insertion, and isomerisation/pseudorotations among others, including the essential oxidative addition and reductive elimination.

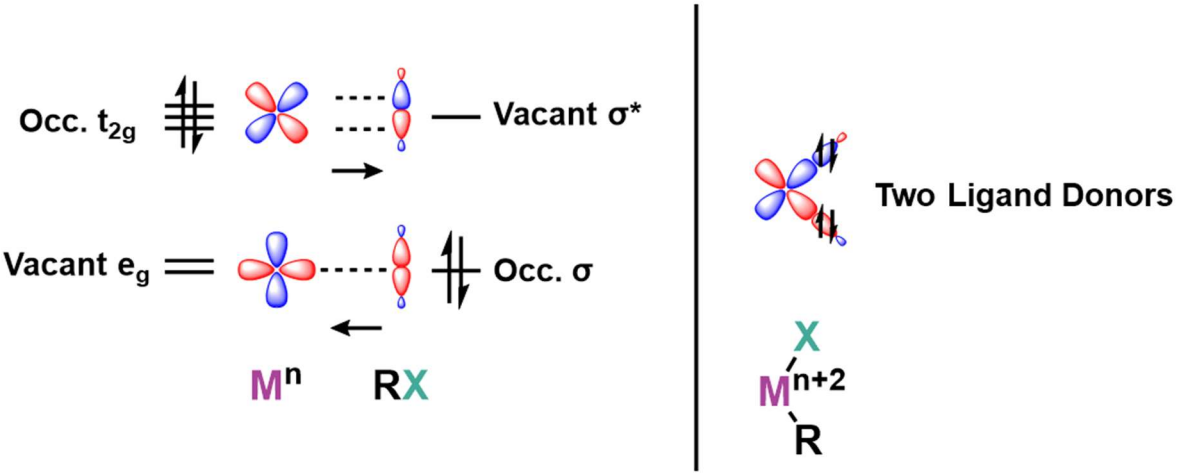


Figure 2 Oxidative addition in transition metals is typically considered to be a concerted process with two necessary components, displayed on the left as donation from the filled substrate bond into a vacant orbital of appropriate energy (typically the e_g LUMO), forming one ligand-metal bond, and the donation from the filled metal based orbitals into the antibonding orbital of the substrate, forming the second metal-ligand bond and formally oxidising the metal centre. The net process generates two metal-ligand bonds and an oxidised metal centre, loosely shown on the right. Spectator ligands on the metal centre are omitted, and the oxidation state is represented by n/n+2.

Oxidative addition occurs through addition of a pair of electrons at a metal centre into the antibonding orbital of another element-element bond, usually a transition metal and a C-X bond, so as to formally break the C-X bond and produce two new metal-element bonds. This net process oxidises the metal by two electrons and provides two new X-type ligands (bearing formal negative charges) for the metal centre, consequently the name "oxidative addition".

Reductive elimination is the reverse process: two X-type ligands on a transition metal form a bond and forfeit the two excess electrons to the transition metal centre, formally reducing it. Many catalytic cycles make use of oxidative addition of one substrate, formally metathesizing one of the new ligands for a different one, then reductively eliminating the desired bond.

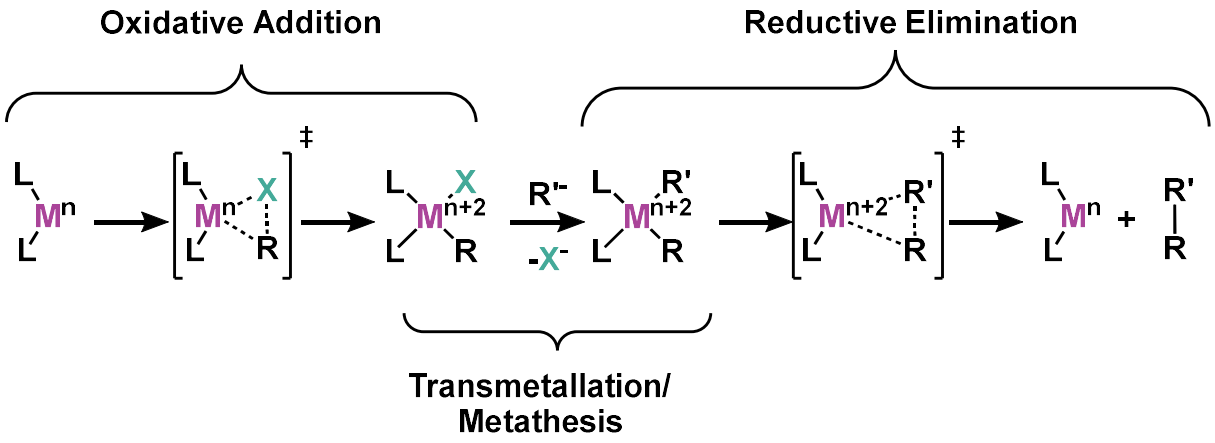


Figure 3 Oxidative addition and reductive elimination are two sides of the same coin, the same process going in two different directions, and are fundamental steps crucial in much of organometallic chemistry.

This process first oxidises and then reduces the metal centre by 2, and also changes the coordination number by first +2 and then -2, resulting in no net change of the active species as is required for a catalyst. Two core features of transition metals are necessary for these types of reactions: both a donor and acceptor orbital of the appropriate occupancy and energy on the same atomic centre, and at least two nearby oxidation states of comparable energy.

Some authors suggest oxidative addition to be exclusive to transition metals, however similar insertion oxidation processes have been reported for metalloids and even nonmetals, such as phosphorus in specific, T-shaped constrained geometries such as those reported by Radosevich and coworkers.[18] Although often in the main group, such processes occur through stepwise mechanisms like nucleophilic attack followed by migration, rather than a truly concerted process.[19]

Relevant to this work is oxidative addition at a germanium(II) centre, the germylene lone pair acts as a nucleophile, and the vacant p-orbital acts as the electrophile, which is able to add many different substrates, including traditionally difficult examples such as H_2 and C-H bonds.[20,21]

However, the notion of oxidative addition relies on the assignment of formal oxidation states of the ligands and of the metal centre. When the ligands are more electronegative than the centre, as is almost universally the case, then formally each ligand "owns" the electrons in the metal-ligand bond, so the electrons which were previously in an occupied metal orbital are transferred to an occupied ligand orbital, nominally oxidising the centre.

During the course of this work, however, Crimmin and coworkers[22] published a remarkable work describing essentially the same "oxidative addition" process, but instead of using a species which would produce two electronegative ligands after addition, demonstrated the addition of a zinc-zinc bond across a silicon centre (along with the corresponding aluminium, gallium, and indium carbene analogues), shown in Figure 4.

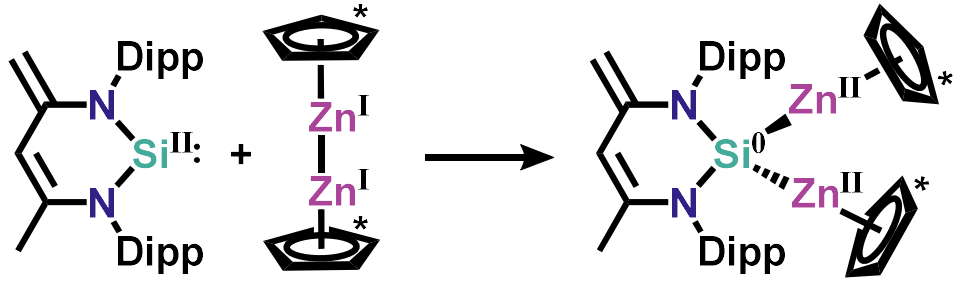


Figure 4 The seminal reductive addition of a zinc-zinc bond across a silylene centre, subverting the typical redox process observed in addition. * indicates the pentamethyl substitution on the Cp ligands.

Crucially, zinc possesses a Pauling electronegativity of 1.65 and silicon possesses the higher value of 1.90. This implies that the two ligand-based orbitals of Figure 2 (right) are, while maintaining a similar spatial form to a traditional addition product, formally "owned" by the silicon centre. Consequently, after the insertion into the zinc-zinc bond, the silicon centre has formally gained two electrons, reducing from Si(II) to Si(0). This net process involves the addition of "ligands" across a single centre with two vacant coordination sites in the same fashion as oxidative addition, but instead of raising the oxidation state of the centre by two (oxidation), it has lowered the oxidation state by two (reduction). The authors subsequently label this novel type of reaction to be "reductive addition", adding detailed nuance about a continuum between oxidative, redox neutral, and reductive addition processes based on the

electronic structures of reactants and products, particularly their differences in the nebulous and differing scales of electronegativity.

Some of the complexity in the original work arises from the modest electronegativity difference between silicon and zinc, as well as the electronic structure of transition metals, giving rise to stronger, less localised bonding through retrodonative mechanisms and the intricacy of highly degenerate d-orbitals and their significant radial extension. Additionally, the demonstrated centres are all relatively electropositive (Si, Al, Ga, In, and Be possess Pauling electronegativities of 1.90, 1.61, 1.81, 1.78, and 1.57 respectively), further muddying the waters about their electron accepting capabilities.

Part of the ability to form such complexes is due to the highly reducing nature of the Zn(I) dimer, its polarisable Zn-Zn bond, and the sterically demanding nature of the zincyl ligands protecting the otherwise kinetically unstable daughter. Zinc, however, is not alone: being in group 12, is often considered as a pseudo-group two element, having a filled, perhaps core-like d-shell the vast majority of zinc chemistry reflects that of the alkali earth metals.[23] Particularly, it has somewhat similar physical and chemical properties with magnesium, including (Zn *cf.* Mg:) covalent radius (1.22 *cf.* 1.41 Å), electronegativity (1.65 *cf.* 1.31), melting point (420 *cf.* 650 °C) and ns^2 atomic ground state configuration.

The Zn(I) dimer was originally reported in 2004 by Carmona and coworkers in an unusual metathesis between [Cp^*_2Zn] (Cp^* = pentamethylcyclopentadienide) and [$ZnEt_2$] forming [Cp*ZnZnCp*] through an unclear and accidental mechanism.[24] Evidently the kinetic stabilisation of the low-valent zinc is required as the identical reaction using unsubstituted cyclopentadienide simply results in the expected metathesis product ([CpZnEt]). In fact, axial coordination in linear species of the form L-M-M-L is calculated to be destabilising[25] compared with nonaxial coordination using a ligand such as ^{Dipp}NacNac (^{R}NacNac = {[(R)NC(Me)]$_2$CH}], Dipp = diisopropylphenyl) which has been able to stabilise not only a corresponding Zn(I) dimer[26,27] but also the magnesium analogue in a landmark paper by Jones and coworkers in 2007, the first Mg(I) dimer, later coined a "quasi-universal" reducing agent.[28]

Such magnesium(I) dimers share an electronic structure with zinc(I) dimers by the previously discussed similarities between zinc and magnesium. However, due to its lower electronegativity and lack of a filled d-shell, the magnesium-magnesium bond is significantly weaker, more reducing, and more polarisable than in the zinc case, even forming a nonnuclear attractor (NNA) at the centre of the sigma bond (the first experimentally characterised example

of such an esoteric electronic feature),[29] somewhat more akin to Mg(II)-$(\uparrow\downarrow)^{2-}$-Mg(II) than Mg(I)-Mg(I), with the NNA not present in the zinc analogue. Seemingly magnesium(I) dimers are attractive candidates for reductive addition reactions.

Considering instead the oxidising metal centre, Germanium, when compared with silicon, is similarly well disposed. Due to the inert pair effect and its greater electronegativity (Pauling 2.01 *vs*. 1.90), heavy analogues of silylenes, known as germylenes, appear predisposed towards reductive addition. *Prima facie*, germanium is more inclined to stabilise a lower oxidation state

This chapter presents the notable synthetic efforts performed over the course of this work in its progress to produce a ligand for novel low-valent main group chemistry, and its culmination in the serendipitous chancing upon of the first example of reductive addition across a magnesium-magnesium bond to from an isolable dimagnesio-species, specifically by a germylene. This species and its mechanism of formation is investigated computationally.

2.2 Results and Discussion

2.2.1 Ligand Synthesis

2.2.1.1 Background & Ligand Design

Experimental work for the project began by attempting to synthesise a novel ligand for low-valent main group chemistry. Inspiration began with the prolific [(**NON)**H_2] proligand (Figure 5) initially synthesised by Emslie and coworkers.[30] The [(**NON**)H_2] proligand has proven very successful in its ability to stabilise low-valent main group species across the periodic table, notably in group 14 chemistry it demonstrated the ability to produce tetryl radical anions of germanium, tin, and lead in work by Lim *et al*. within the group.[31] Evidently, the framework is an effective one, however the dianionic nature is not appropriate for all species. In preceding work,[32] a monoanionic form of the ligand was targeted, replacing the neutral O donor with a deprotonatable NH moiety, and the previously deprotonatable NH "arm" moieties with neutral donors. Over the course of the project, however, it became evident that cross-coupling more than one secondary amine onto the 4,5 sites of the precursor complex 4,5-dibromo-2,7-di-tert-butyl-9,9-dimethylacridane proved synthetically challenging, and a readily accessible unsymmetrical form (replacing an amine donor with an ethereal donor) was instead isolated. However, to complex anything beyond an alkali metal leads to scission of the second protecting group.[32] Consequently, this project (which was undertaken in my honours year) matured in a different direction.

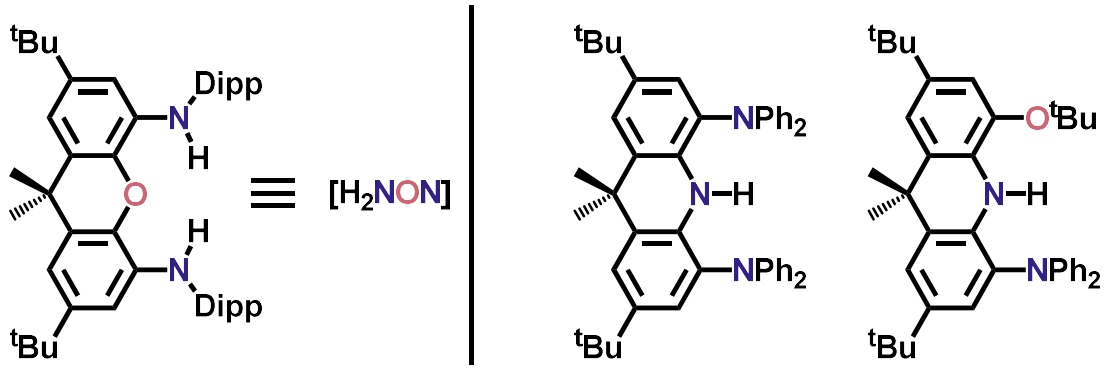


Figure 5 The original inspirational [NONH$_2$] proligand and its two monoanionic analogues which were the subject of prior exploratory work in reference 32.

Alternatively, Hinz has reported many highly successful works with a somewhat similar ligand backbone to the acridane, including isolable 1-coordinate tetrylenium cations,[33,34] instead using a carbazole skeleton (which differs by simply removing the dimethylmethylene linker in the acridane and joining the arenes). Interestingly, Hinz was able to use no supporting donors at all, instead utilising flanking arenes bonded directly to the 4,5 positions.

The goal of this work was thus to combine the [**NON**H$_2$] proligand with Hinz's successful carbazole, to make a smaller pocket for great steric protection, and perhaps coordination of the flanking arenes.

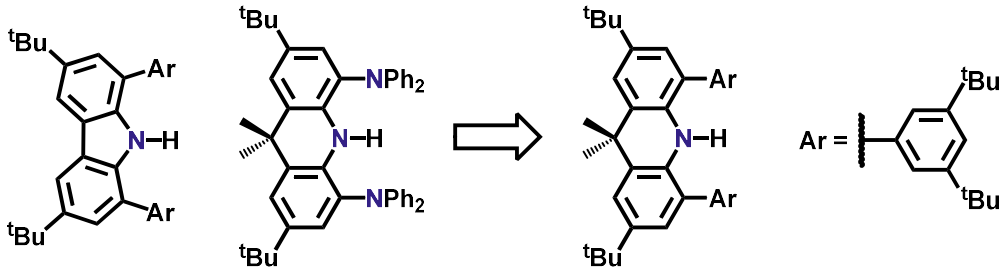


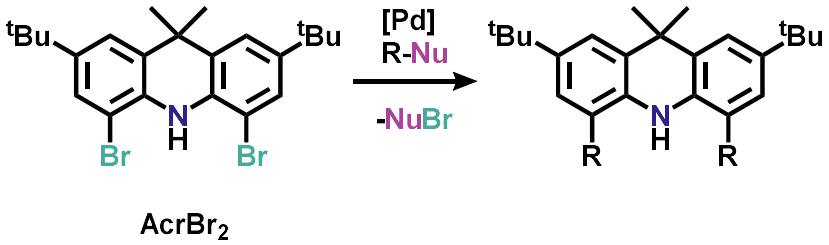
Figure 6 The synthetic aim of this work was to produce a novel ligand (right) for the stabilisation of low-valent main group species, particularly of group 14, by combining the successful motifs of Hinz's carbazole and Hicks' acridane.

"Acridane" is used throughout as the reduced form of acridine (*i.e.* acridane = 9,10-dihydroacridine) for simplicity, which has some literature precedent.[35,36,37]

2.2.1.2 Cross-Couplings

As the dibromide, AcrBr$_2$ (Scheme 1), was previously reported and provides a scalable, obvious synthetic equivalent for the electrophile synthon in the CC-coupling disconnect for installing the R groups of the final ligand, synthesis of the target was performed *via* palladium catalysed cross-coupling from AcrBr$_2$ (Scheme 1).[32] Many aryl nucleophilic partners exist as

synthetic equivalents of the nucleophile synthon, including Grignards for a Kumada reaction,[38] organozinc for Negishi,[39] and organotin for Stille couplings,[40] but for this project we chose boronic acids for a Suzuki coupling.[41] This was due to their bench stability, synthetic ease and low toxicity, especially in light of the large scales that would be required, and following the preparation for the carbazole ligand using the same procedure by Hinz.[33]



$AcrBr_2$

Scheme 1 General procedure for palladium catalysed cross-coupling for the formation of the target ligand, reacting the previously reported dibromoacridane with a nucleophilic arene partner, R-Nu.

Our first choices for arenes were diisopropylphenyl (Dipp) or mesityl (Mes) for their previously discussed favourable steric properties, and also for the absence of *ortho*-protons, which had already proven to be a facile decomposition route for Hinz's silylene cation.[34] Such arenes would also conformationally lock the flanking groups perpendicular to the acridane plane, in a position that would allow coordination of a metal centre (as opposed to possible rotation and less rigid conformation in *ortho*-hydrogen arenes).[42]

Attempts to cross-couple $DippB(OH)_2$ or $MesB(OH)_2$ with $AcrBr_2$ resulted in no reaction, or debromination of the starting material regardless of solvent, temperature, palladium source, base, phosphine, or additive. It appears that the steric bulk intended to protect the metal centre also prevented the cross-coupling. It is also salient to note that while some coupling procedures are accessible to the related xanthenes (the same heterocycle with an oxygen instead of NH moiety), historically we have had difficulties repurposing such procedures to acridanes.[32] Some cross-coupling protocols exist which can combine an *ortho*-N-substituted bromide with a di-*ortho*-substituted nucleophile,[43] however they are low-yielding and require esoteric or extremely toxic reagents. Due to no success coupling with *ortho*-substituted arenes, the less ambitious but successful coupling partner 3,5-di-tert-butylphenyl boronic acid was used, allowing for the isolation of the target ligand, 2,7-di-tert-butyl-4,5-bis(3,5-di-tert-butylphenyl)-9,9-dimethylacridane [^{tBu2Ph}**AcrNH**]) (see section 2.6 for synthetic details).

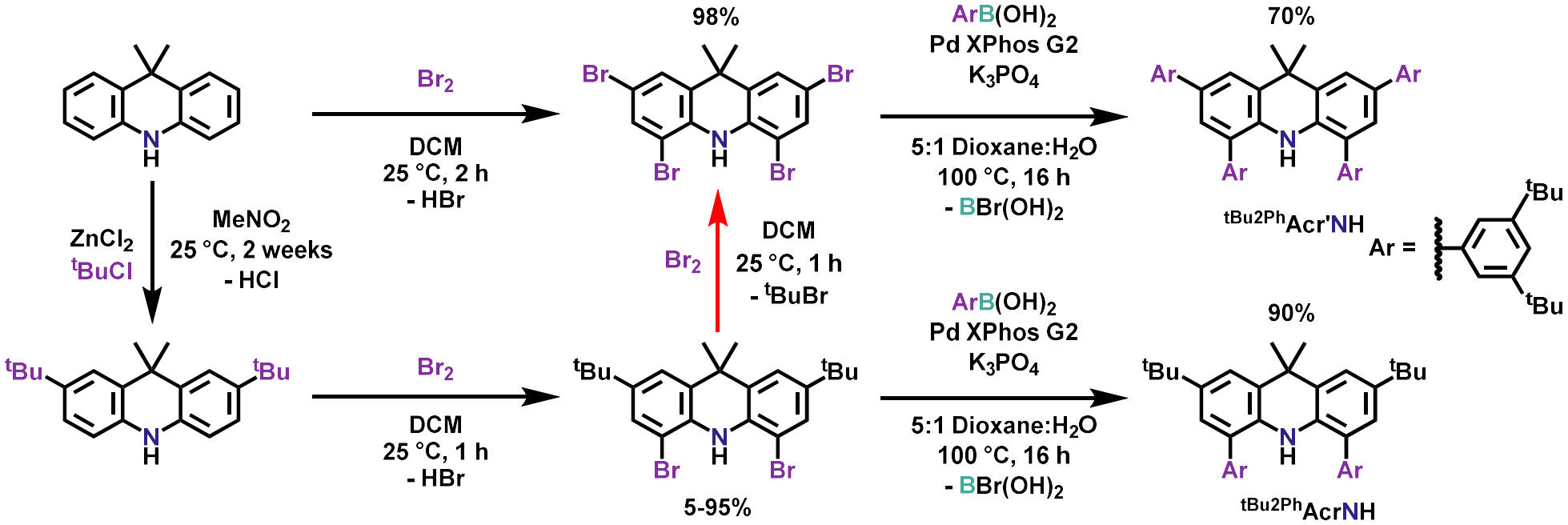
The 2,7-tert-butyl moieties are on the ligand for the primary purpose of protecting the 2,7 sites from bromination, to produce only the 4,5-dibromide. This was for the previous, tridentate form of the proligand,[32] with heteroatoms bonded to the acridane framework at the 4,5

positions, additional substitution would result in undesirable potential coordination sites to metals. With only arenes, however, there is little difference between a tert-butyl group and an arene for our purposes. This is useful as it prevents the need for the installation of the tert-butyl groups in an additional synthetic step, it also makes the bromination step much easier, as bromination of 2,7-di-tert-butyl-9,9-dimethylacridane results unpredictably in cleavage of the tert-butyl groups and isolation of 2,4,5,7-tetrabromo-9,9-dimethylacridane (or other partial bromination and even oxidation products). If all four sites are appropriate for cross-coupling, then bromination of 9,9-dimethylacridane to the tetrabromide is trivial and can be performed on at least 50 g scale. Furthermore, four-fold cross-coupling proceeded cleanly and in high yields under similar conditions to the 2-fold coupling (Scheme 2).

Attempts to use either N-bromosuccinimide or elemental bromine as the brominating agents both resulted in similar mixtures of products, both with varying loss of the tert-butyl groups as indicated in the original publication. This is posited to be possibly due to formation of radical intermediates from varying degrees of oxygen, residual catalyst from the alkylation, light, rates of addition, or variations in temperature, particularly evidenced by the formation of the oxygenated product 4,5,7-tribromo-9,9-dimethylacridin-2-one in *ca*. 40% yield from one attempt. It remains unclear why the 2,7-dimethyl analogue does not appear to suffer the same off-target reactivity, perhaps the dealkylation proceeds through a β-elimination of isobutene unavailable to the methyl derivative.

Consequently, some early work was performed using the bis-di-tert-butylphenyl proligand [^{tBu2Ph}**AcrN**H], but the majority of the body was performed using the tetrakis-di-tert-butylphenyl arene proligand, [^{tBu2Ph}**AcrN′**H]. As no differences between the two ligands or complexes (beyond crystallisation conditions) were ever salient, for all intents and purposes the ligands can be viewed as being the same.

Both proligands were crystallographically characterised, with their solid-state structures shown in Figures 7 and 8. As is typical for the acridane structural motif, each acridane core is essentially coplanar with no “hinging” through the central ring (observed for metallated species, *vide infra*). The substituent arenes sit in the expected local “biphenyl-esque” geometry with dihedrals between 52° and 56° (*cf*. biphenyl 44.4°). Differences between the two are likely due to crystal packing effects as the distance between the 2 & 4 and 5 & 7 positions is too large and the electronic difference between an aryl and tert-butyl moiety to explain and other differences, although the two proligands exhibit no salient differences.



Scheme 2 Synthetic pathways resulting in the formation of [^{tBu2Ph}AcrNH] and [^{tBu2Ph}AcrN′H] from the previously reported 9,9-dimethylacridane.[32] The red arrow indicates the synthetic challenge in ^{tBu2Ph}AcrNH over ^{tBu2Ph}AcrN′H due to the facile removal of the protecting tert-butyl groups.

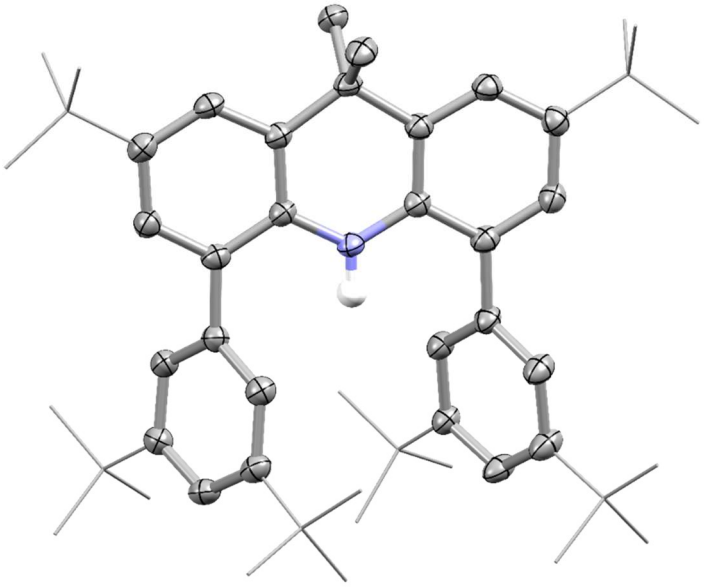


Figure 7 Solid state structure of the [^{tBu2Ph}AcrNH] proligand. In the protonated form, the acridane backbone adopts an essentially planar geometry, and the aryl substituents display very minor distortion from the expected local "biphenyl-esque" geometry. Key geometric parameters: ∠Aryl centroid-aryl C1-acridane4/5: 176.03(6)°/176.27(6)° (a measure of the buckling of the flanking groups, with the ideal angle at 180°), ∠AcridaneC4-C5-Aryl-C1-C2 dihedral 52.98(4)°/52.71(4)°, compared with the experimental biphenyl angle 44.4(2)°.[44] Hydrogens (except the N-H), solvent benzenes and minor components of tert-butyl disorder, are omitted, tert-butyl groups shown in wireframe and ellipsoids shown at the 50% level. Nitrogen blue, carbon grey, and hydrogen white.

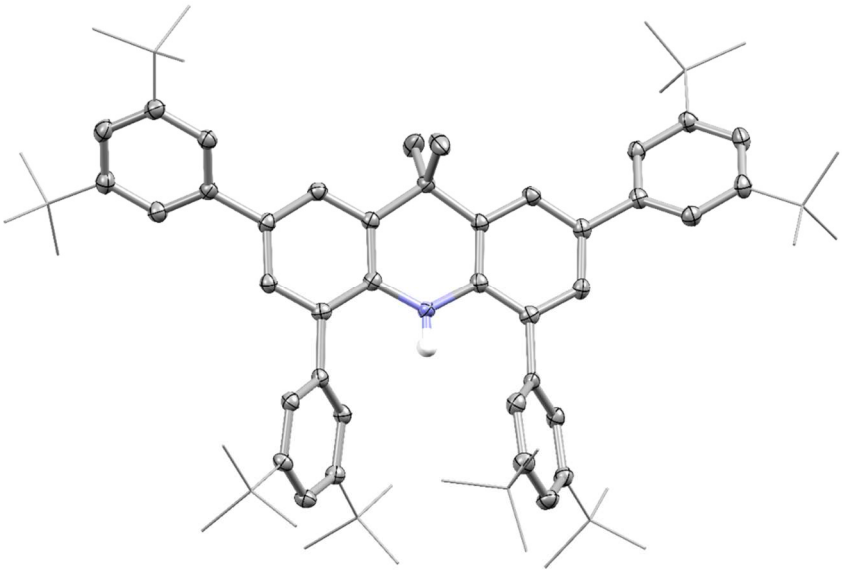


Figure 8 Solid state structure of the [^{tBu2Ph}AcrN′H] proligand. The geometry is nearly identical to [^{tBu2Ph}AcrNH], merely with the 2,9-tert-butyl groups replaced with 3,5-di-tert-butylphenyl substituents, which sit in the expected biphenyl-esque conformation with respect to the acridane backbone. Key geometric parameters: ∠Aryl centroid-aryl C1-acridane4/5: 174.10(7)°/174.33(7)°, ∠AcridaneC4-C5-Aryl-C1-C2 dihedral 54.03(5)°/55.66(5)°. Hydrogens (except the N-H), solvent benzenes and minor components of tert-butyl disorder, are omitted, tert-butyl groups shown in wireframe and ellipsoids shown at the 50% level. Nitrogen blue, carbon grey, and hydrogen white.

2.2.1.3 Group 1, 2, and 13 Complexes

Many low-valent main-group species are generated by installation of the main-group metal in the ligand *via* transmetalation with a group 1 or 2 salt before subsequent reduction,[45] and consequently the next goal was to isolate such species. The group 1 salts proved surprisingly difficult to generate. Alkyl lithium reagents are usually used at very cold temperatures, usually in a dry ice cold bath (*ca.* -80 °C), under which conditions N-H protons are readily deprotonated, or during gradual warming to room temperature. When such a reaction was attempted with both ^{n}BuLi, or its more reactive counterpart ^{t}BuLi, with [^{tBu2Ph}**AcrN′**H] or [^{tBu2Ph}**AcrN**H], no reaction was observed at or below room temperature, in hydrocarbons, ethers, or with catalytic amounts of TMEDA.[46] When the reactions were performed in ethereal solvents, the alkyl lithium reagents reacted with the solvent before the proligand, and the resulting alkoxide, expectedly, did not react with the proligand either. The lithium salts were formed by refluxing the proligand with 4 equivalents of ^{n}BuLi in benzene for 6 hours, presumably forming PhLi, which is only sparingly soluble in benzene, but eventually formed the intended species, [^{tBu2Ph}**AcrN′**Li] and [^{tBu2Ph}**AcrN**Li], characterised by single-crystal X-ray diffraction (Figures 10 and 11), FT-IR spectroscopy, ^{1}H and ^{13}C{^{1}H} NMR spectroscopy, and elemental analysis.

The potassium salt proved more readily accessible. Stirring the proligand with excess benzyl potassium [47] in benzene at room temperature overnight yields [^{tBu2Ph}**AcrN′**K] and [^{tBu2Ph}**AcrN**K], each characterised as described in the experimental. [^{tBu2Ph}**AcrN**K] was additionally characterised by single crystal X-ray diffraction and its solid state structure is shown in Figure 9. The complexes are also accessible from potassium hydride, although this takes several days in refluxing benzene. It is suggested that the ready formation of the potassium salt is due to the greater basicity of benzyl potassium than alkyl lithiums, but also because of the ligand's greater accommodation for the potassium cation than lithium. The deprotonated ligand has a much more suitable interaction with the softer potassium: the N-K distance is just outside the sum of covalent radii (2.74 Å), instead the potassium preferentially forms an η^6-interaction with each arene (Figure 9).

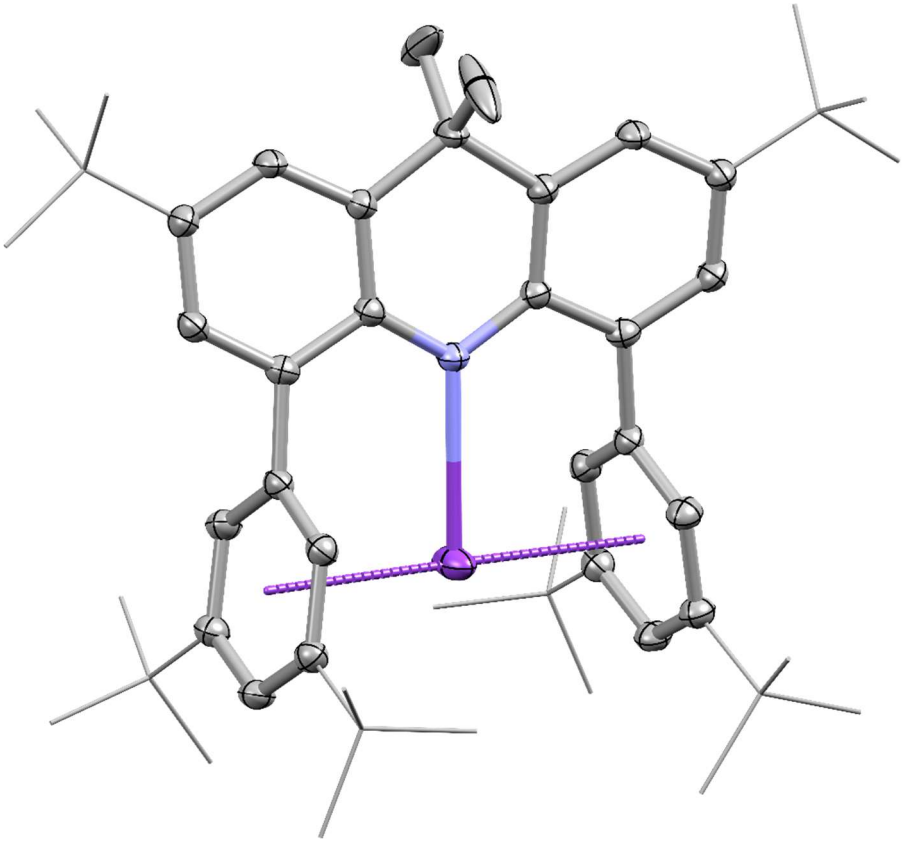


Figure 9 The solid-state structure of potassium salt [^{tBu2Ph}AcrNK]. Most saliently, the flanking arenes sit much closer to perpendicular to the acridane backbone. A slight outward buckling of the flanking aryl groups is seen due to the size of potassium. Key geometric parameters: K-N: 2.7720(13) Å; K-Aryl centroid 2.796(9) Å (only just outside the sum of covalent radii (2.76), although the length to each carbon is longer than to the centroid); ∠Aryl centroid-aryl C1-acridane C4: 172.72(9)°; and ∠AcridaneC4-C5-Aryl-C1-C2 dihedral: 75.15(11)° (two flanking aryls equal by symmetry). Hydrogens, solvent benzene molecules and minor components of tert-butyl disorder, are omitted, tert-butyl groups shown in wireframe and ellipsoids shown at the 50% level. Nitrogen in blue, potassium purple, and carbon grey.

The ligand is too sterically demanding to form stabilising aggregates of lithium like in classic alkyl lithiums,[48] but gives little enthalpic compensation to deprotonation beyond the more stable amide (*cf.* carbanion), with the lithium bonded primarily to the nitrogen of the ligand, with an η^2 interaction with each flanking arene in the solid-state structure (Figures 10 and 11).

The same structural motif is observed in [^{tBu2Ph}**AcrN′**Li] as in [^{tBu2Ph}**AcrN**Li], possessing N-Li distances of 1.884(3) and 1.890(3) respectively, identical within uncertainty, and relatively short compared with the sum of covalent radii of 1.99 Å, likely due to the electron poor lithium centre resulting from its low coordination when compared with typical tetrahedral lithium complexes.

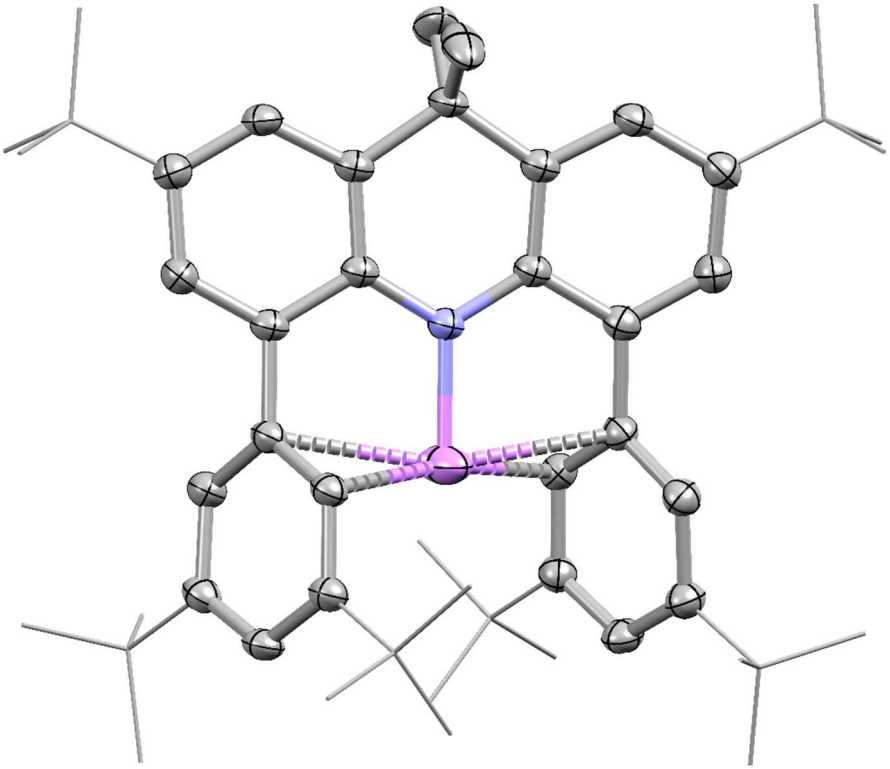


Figure 10 Solid-state structure of the lithium salt [^{tBu2}PhAcrNLi]. Due to the smaller size of lithium and its lower cation-π affinity, the lithium sits bound primarily to the nitrogen, with each flanking arene rotated so as to bring one carbon closer and support an η^2 interaction. The biphenyl-esque dihedral is very similar to that of the proligand. Key geometric parameters: N-Li 1.890(3) Å; Li-C: 2.474(3), 2.239(3), 2.474(3), and 2.254(3) Å; ∠Aryl centroid-aryl C1-acridane C4: 177.56(14)°, 178.28(14)°; ∠AcridaneC4-C5-Aryl-C1-C2 dihedral: 54.70(11)° 55.53(11)°. Hydrogens, solvent benzene molecules and minor components of tert-butyl disorder, are omitted, tert-butyl groups shown in wireframe and ellipsoids shown at the 50% level. Nitrogen blue, carbon grey, and lithium pink.

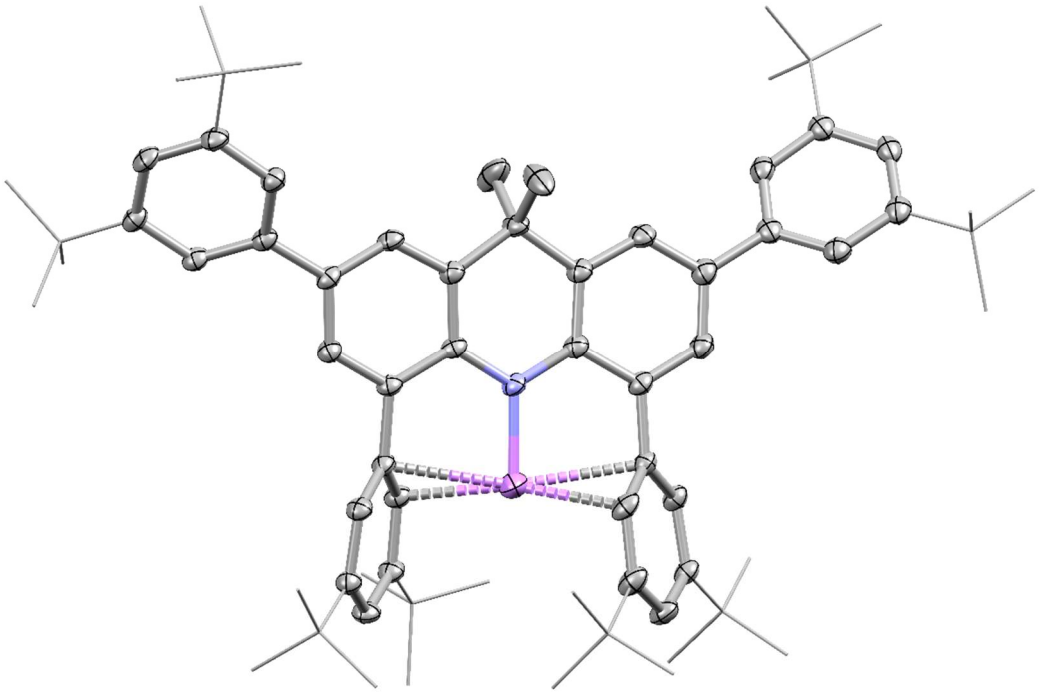


Figure 11 Solid-state structure of the lithium salt [^{tBu2}PhAcrN′Li], very similar to the above [^{tBu2}PhAcrNLi] as might be expected. Key geometric parameters: N-Li: 1.884(3) Å; Li-C 2.565(4), 2.215(4), 2.512(4), and 2.236(4) Å; ∠Aryl centroid-aryl C1-acridane C4: 175.92(21)° 177.44(21)° ∠AcridaneC4-C5-Aryl-C1-C2 dihedral: 53.04(12)°, 55.18(12)°. Hydrogens, solvent benzene molecules and minor components of tert-butyl disorder, are omitted, tert-butyl groups shown in wireframe and ellipsoids shown at the 50% level. Nitrogen in blue, carbon grey, and lithium pink.

Interestingly, attempted deprotonation of the proligand using a Grignard reagent (MeMgBr 2.1 molar in diethyl ether) proved unfruitful. Refluxing the solution in THF or benzene with TMEDA also showed no reaction by ^{1}H NMR spectroscopy, only reacting with the trace grease before subsequent decomposition over a 7-day period. Similarly, no reaction was observed with di-n-butylmagnesium. Metathesis with MgI_2 or $MgCl_2$ from [^{tBu2Ph}**AcrN′**Li] or [^{tBu2Ph}**AcrN′**K] also proved unsuccessful in aromatic or ethereal solvents. Consequently, no magnesium salt of the ligand was isolated.

Similarly, reactions with CaI_2, $CaCl_2$, or $Ca(HMDS)_2$ in hydrocarbon or ethereal solvents with either the potassium or lithium salts of the ligand ($Ca(HMDS)_2$ with the proligand) were also unsuccessful. No calcium salt of the ligand was isolated.

With no success in forming group 2 salts, the aims of the project became limited by salts which would metathesise. Turning to group 13, reaction between [^{tBu2Ph}**AcrN**K] and AlI_3 in C_6D_6 produced broad resonances in the alkyl and aryl regions by ^{1}H NMR spectroscopy from which no meaningful conclusion could be inferred. However, the deep purple colour of the solution indicates the potential formation of I_2 and we therefore suspect redox processes occurred,[49]

potentially induced by the steric pressure on the redox-predisposed iodines in the intended complex. No product was ever elucidated from the reaction.

Reaction between [^{tBu2Ph}**AcrN**K] and $AlCl_3$, however, results in one product with two unsymmetrical ligand environments by ^{1}H NMR spectroscopy. Single crystal X-ray diffraction experiments (Figure 12) elucidated the product to be the "di-ate" salt of the ligand, forming the intended [^{tBu2Ph}**AcrN**$AlCl_2$] only as an adduct of KCl and [^{tBu2Ph}**AcrN**K], again revealing the ligand's strong preference for potassium.

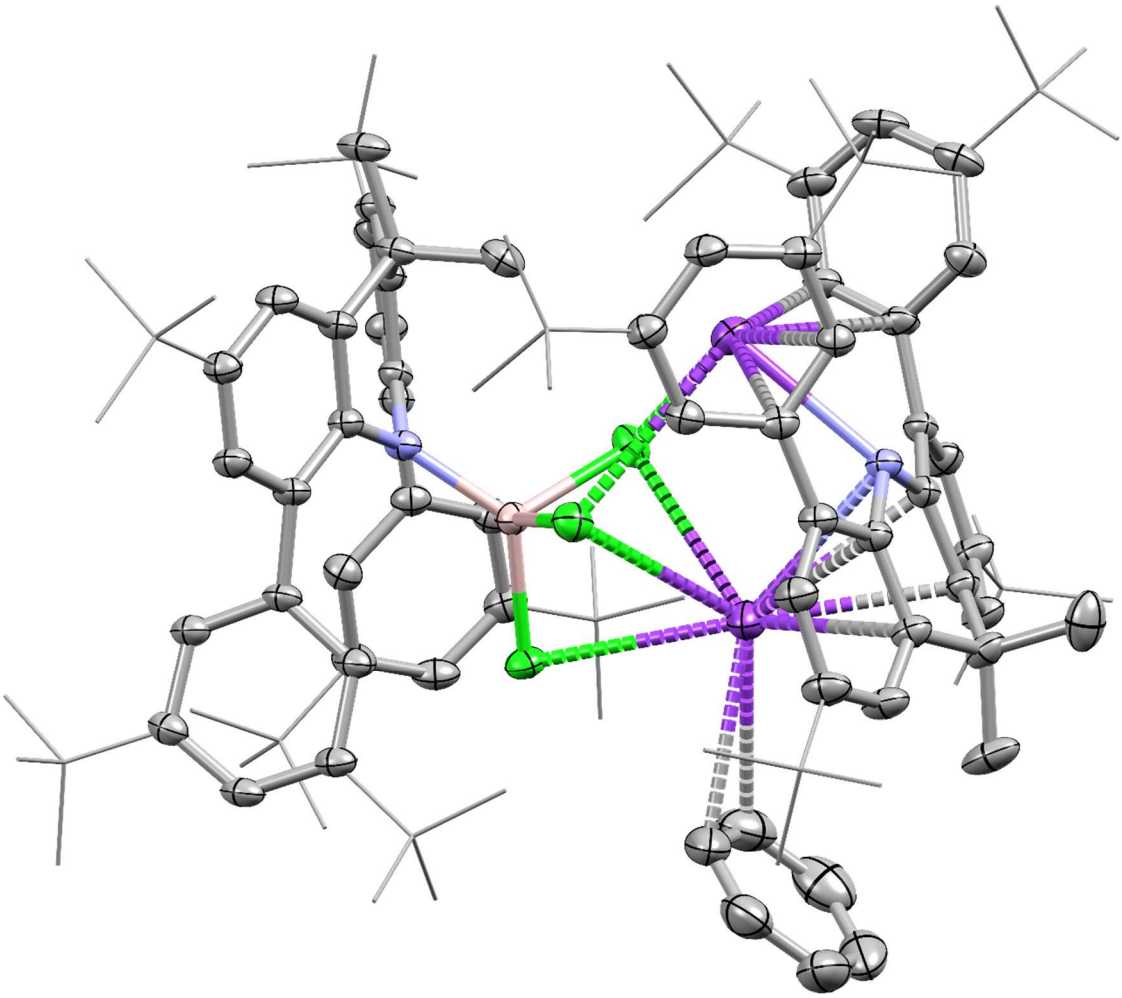


Figure 12 The solid-state structure of the "di-ate" salt [$AlCl_2$(^{tBu2Ph}AcrN).(KCl).(^{tBu2Ph}AcrNK)].C_6H_6) exclusively formed by the metathesis of [^{tBu2Ph}AcrNK] with $AlCl_3$. The tetrahedral aluminium centre is far from the intended, sheltered position and the warping of the flanking arenes demonstrates the difficulty of coordinating the ligand to complexes containing other ligands. Key geometric parameters: Al-N 1.8285(17) Å; Al-Cl: 2.1872(8), 2.1839(8), 2.1413(7) Å; K-Cl bonds outside the sum of covalent radii (3.05 Å), within 3.2128(7) to 3.4436(7) Å. Tert-butyl groups and ^{Mes}NacNac methyl groups shown in wireframe for clarity, non-coordinating solvent benzene molecules and minor components of tert-butyl disorder omitted, and ellipsoids shown at the 50% level. Aluminium in pink, chlorine in green, and potassium in purple.

The rather inert product [^{tBu2Ph}**AcrN**$AlCl_2$.(KCl).(^{tBu2Ph}**AcrN**K)] formed regardless of stoichiometry, solvent, or slow addition of one reagent to the other; the last is particularly surprising, as slow addition of [^{tBu2Ph}**AcrN**K] to a large excess of $AlCl_3$ might be expected to form [^{tBu2Ph}**AcrN**$AlCl_2$] rapidly, with each molecule forming the aluminium salt before adduction with [^{tBu2Ph}**AcrN**K] could occur, however the adduction process appears at least kinetically more facile if not also the thermodynamic product. The aluminium is also outside the intended coordination pocket, and the flanking "arm" arenes are significantly buckled away from their position in the proligand (the expected colinear biphenyl-esque geometry), suggesting that the difficulty in forming other complexes may be because they cannot form either stable species in the pocket as intended due to the large steric bulk, and also cannot form stable adducts like in the aluminium case to pay the enthalpic cost of warping the ligand enough to coordinate to the nitrogen.

2.3 Metathesis with Group 14 Precursors

Fortuitously, metathesis between the [^{tBu2Ph}**AcrN**K] and $GeCl_2$.dioxane proceeded extremely rapidly at room temperature in C_6D_6 by ^{1}H NMR spectroscopy, yielding the intended [^{tBu2Ph}**AcrN**GeCl] complex (86% isolated crystalline yield). The complex was characterised by single-crystal X-ray diffraction (Figure 13) (see section 2.7 for further characterisation). The metathesis proceeds equally well from the lithium salt. The dioxane, is easily removed *in vacuo*, yielding a rare two-coordinate chlorogermylene.

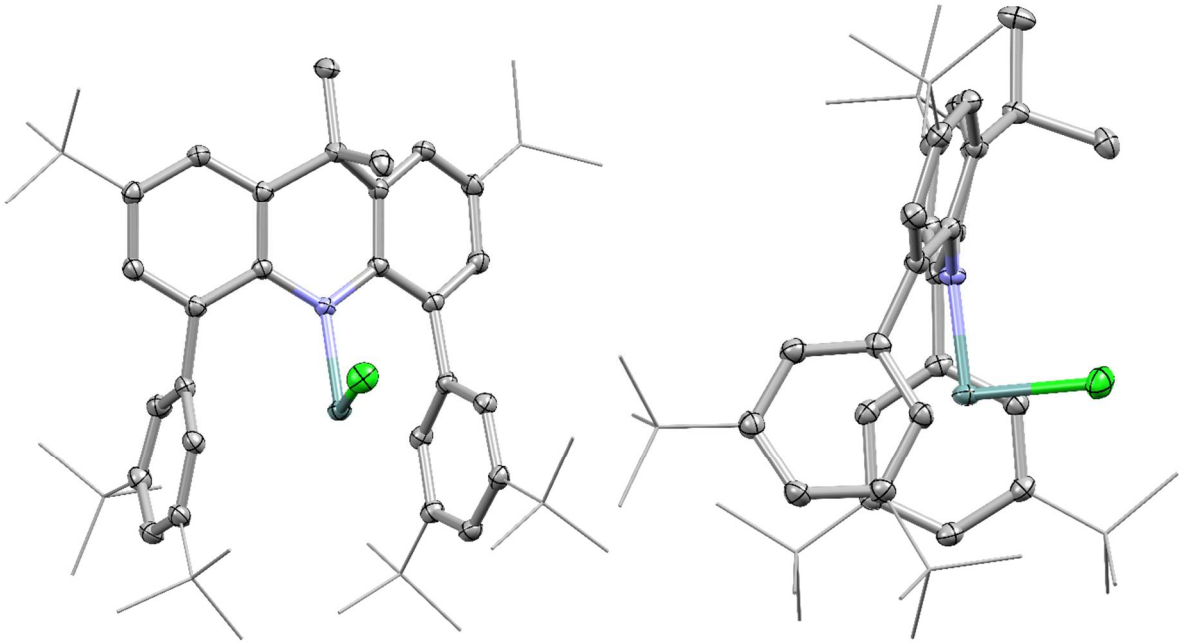


Figure 13 Two perspectives of the solid-state structure of the chlorogermylene isolated by metathesis of [^{tBu2Ph}AcrNK] with $GeCl_2$.dioxane. The flanking arenes are highly distorted from the idealised geometry seen in the proligand, with particularly salient aryl centroid-aryl C1-acridane C4 angle of 172.88(6)° for the more distorted flanking group. Other key geometric parameters: N-Ge 1.9505(9) Å; Ge-Cl 2.3195(3) Å; ∠NGeCl 92.55(3)°. Tert-butyl groups shown in wireframe for clarity, solvent benzene molecules and minor components of tert-butyl disorder omitted, and ellipsoids shown at the 50% level.

The resultant germylene possesses a 92.55(3)° N-Ge-Cl angle, which is very nearly 90°, indicating a strong influence from the inert pair effect[50] and primarily p-character in its bonding orbitals. By ^{1}H NMR spectroscopy, the flanking arenes possess asymmetry between the tert-butyl groups and ortho hydrogens on the chlorine side and chlorine-absent side, and the dimethylmethylene methyl groups are also inequivalent on the ^{1}H NMR spectroscopy timescale, indicating a high degree of conformational rigidity after coordination of the germanium (which may or may not be present in the lithium salts and proligand, but the molecular symmetry prevents facile determination of the aryl rotation speed by NMR spectroscopy).

In the [^{tBu2Ph}**AcrN′**GeCl] analogue, also readily produced by metathesis from a group 1 salt with $GeCl_2$.dioxane, the 2,7-aryl moieties do not show asymmetry by ^{1}H NMR spectroscopy, indicating facile rotation. The compound was also characterised by X-ray crystallography and the solid-state structure shown in Figure 14. The important features are essentially identical to the solid-state structure of [^{tBu2Ph}**AcrN**GeCl], with the N-Ge-Cl angle within 0.5° and Ge-N bond length within 0.01 Å.

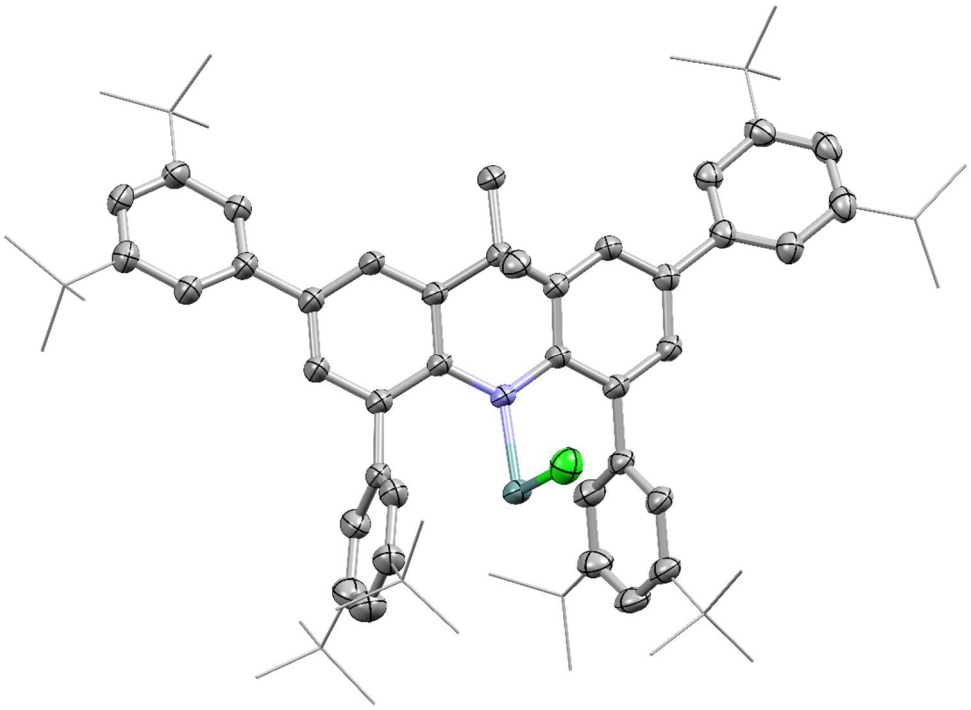


Figure 14 Solid-state structure of the chlorogermylene isolated by metathesis of [^{tBu2Ph}AcrN′K] with $GeCl_2$.dioxane. N-Ge 1.964(2) Å; Ge-Cl 2.2994(9) Å; ∠NGeCl 93.170(8)°; ∠aryl centroid-aryl C1-acridane C4: 178.77°, 172.44°; ∠AcridaneC4-C5-Aryl-C1-C2 dihedral: 69.68° 81.38. Tert-butyl groups shown in wireframe for clarity, solvent benzene molecules and minor components of tert-butyl disorder omitted, and ellipsoids shown at the 50% level. Carbon in grey, nitrogen blue, germanium teal, and chlorine in green.

Similarly, the metathesis from the lithium salt works with $SnCl_2$, albeit much more slowly, requiring sonication at 40 °C overnight, likely due to the low solubility of the $SnCl_2$ in benzene. The product was again characterised by single crystal X-ray diffraction (Figure 15) (see section 2.7 for further characterisation).

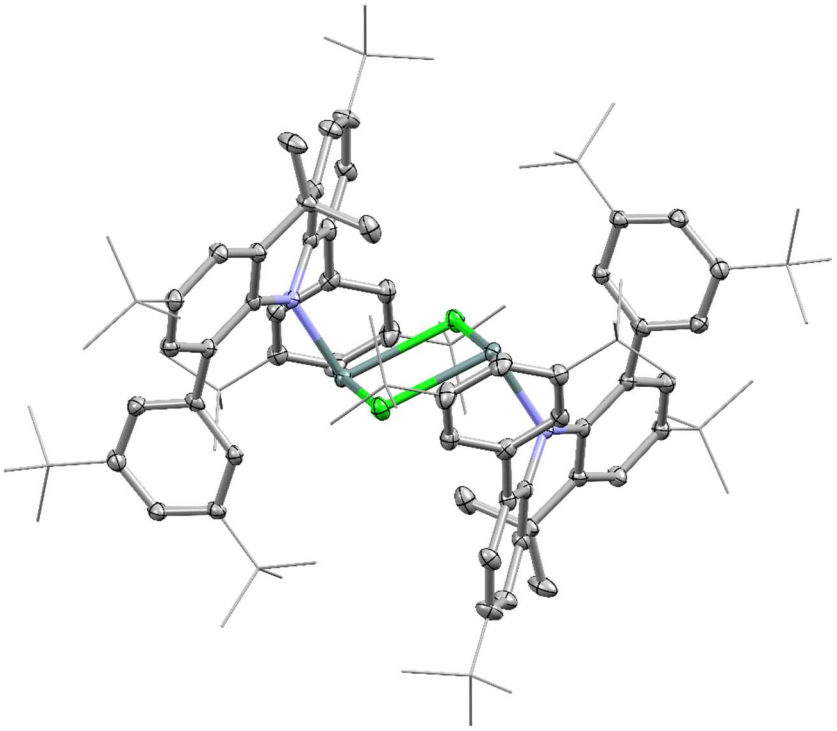


Figure 15 Solid state structure of the dimeric [^{tBu2Ph}AcrNSnCl]$_2$ resultant from the metathesis of [^{tBu2Ph}AcrNK] with $SnCl_2$, the larger coordination sphere and lesser electronegativity of tin compared with germanium allows for the larger congener to form the chloride-bridged dimer. Key geometric parameters: Sn-Sn 4.202(1) Å; Sn-Cl 2.6936(7) Å; Sn-N 2.141(2) Å; ∠Cl-Sn-Cl′ 77.504(12)°; ∠N-Sn-Cl 91.855(7)° ∠aryl centroid-aryl C1-acridane C4: 172.14(11)°, 166.01(11)°, ∠dimethylmethylene C-N-Sn 137.25(10)°, ∠AcridaneC4-C5-Aryl-C1-C2 dihedral: 64.00(9)°, 56.33(9)°. Tert-butyl groups shown in wireframe for clarity, solvent benzene molecules and minor components of tert-butyl disorder omitted, and ellipsoids shown at the 50% level. Carbon in grey, nitrogen blue, tin teal, and chlorine in green.

Due to the large covalent radius and greater ionic character of tin, the resultant chlorostannylene is dimeric, but maintains the near 90° N-Sn-Cl bonding motif between each ligand (∠N-Sn-Cl = 91.855(7)°, ∠N-Sn-Cl = 94.950(7)°) as expected for Sn(II). The acridane backbone is mildly hinged, with the two distal rings forming a 149.8(6)° angle between them, possibly to allow for the nitrogen to form the optimal σ-interaction with the Sn centre, and to allow for the best π-stacking between the two ligands. One "arm" runs nearly parallel to the Sn-Cl bond, but to avoid steric clashes the other adopts a conformation to minimise the interaction with the other arm and opposite ligand. The structure is tightly congested.

The corresponding [^{tBu2Ph}**AcrN′**SnCl] was never synthesized due to time constraints and the following difficulties associated with the reductions of [^{tBu2Ph}**AcrN**SnCl]$_2$, reactivity of the tin complex was not pursued further.

2.4 Reduction

2.4.1 Introduction

Stannylenes and germylenes are already notionally low-valent main group species,[51] as they possess an oxidation state below that in which they are commonly found. However, these lone pairs are quite stabilised by the inert pair effect,[50] simple Sn(II) species like $SnCl_2$ even being bench-stable in the solid state for extended periods of time before oxidation to various Sn(IV) oxides and hydroxides.[52] To induce characteristic low-valent main group reactivity, they must be reduced further, below the +2 oxidation state.

Monovalent dimeric congeners are known as the heavy analogues of alkynes: digermynes[53] and distannynes.[54] Such species have interesting electronic structures, principally due to the mixing of a low vacant σ* orbital from the out of phase combination of the two s orbitals with a high-energy π bonding orbital to make a "slipped" π-bond. Going down group 14, the s-p gap decreases due to reduced density at the nucleus of the s-orbitals resulting in comparatively less difference in stabilisation between the s and p orbitals due to shielding; the s-p gap (by transition energy $ns^2np^2 \rightarrow ns^1np^3$ transition wavelength, E_h) for C, Si, Ge, and Sn respectively: 0.48, 0.21, 0.19, and 0.18, (the Pb $6s^26p^2 \rightarrow 6s^16p^3$ transition has, to the best of my knowledge, never been observed experimentally, favouring $6s^26p^17s^1$ instead).[55] This is partly counteracted by the inert pair effect relativistically stabilising the ns orbital, although evidently not more than due to the change in shielding. Additionally, the larger size of the atoms prevents them from forming shorter bonds, leading to significantly weaker π-bonds.[56]

The net result is a weak, s-s σ-bond and its low-lying σ*-antibond, and two weak π-bonds due to poor facial overlap between the large atoms. Perturbation from linearity of the X-E-E angle in X-E-E-X (while maintaining coplanarity of the donor atoms and metals) results in nonzero overlap between a π-bond and the σ* orbital, the resulting slipped π-bond has more lone-pair character on each metal than a true π-bond, but a lower energy from the orbital mixing. Slipped π-bonds have significantly reduced bonding character, but the resultant orbital is lower in energy, perhaps akin to a lone pair which is spread across two centres. This distortion from linear to lower the energy of the slipped π-bond can be considered consequent of second-order Jahn-Teller distortion.[57]

The effect increases quite smoothly going down the group, with alkynes being of course linear with a triple bond, and diplumbynes possessing 90° L-Pb-Pb angles and what is usually considered to be only a single bond, with silicon, germanium, and tin each intermediary.[58]

A 0-valent terylene analogue is also conceivable by replacing one of the ligands with an electropositive element such as a group 1 or 2 metal. One such species was isolated by Frenking, Jones, and coworkers[59] which was prepared by reducing a bulky germylene chloride with an esoteric zinc-magnesium bond to produce a "zincagermylene" (Figure 16). This species is isoelectronic with the intended product of Scheme 3 (*vide infra*), only in our case with magnesium instead of zinc.

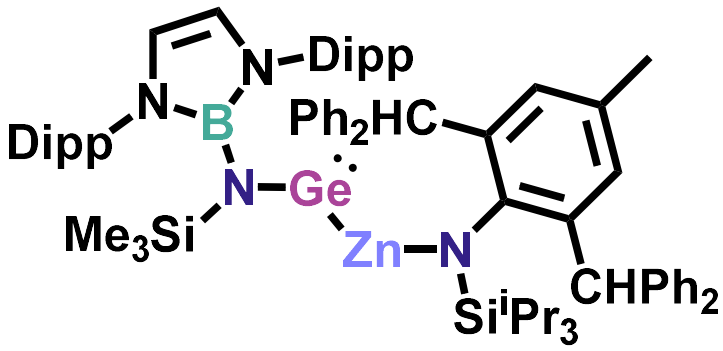


Figure 16 Frenking, Jones and coworkers' zincagermylene, isoelectronic to the intended product of Scheme 3.

Other 0-valent examples of germanium and tin are known which are not isoelectronic to the terylenes.[60] These examples possess two lone pairs and two L-type donors and are isoelectronic to carbones, and are thus aptly called germylones and stanylones,[61] and have been isolated principally by the efforts of Driess and coworkers. They usually require electronic stabilisation using chelating NHCs or other relatively π-acidic ligands to stabilise the high-energy p-like lone pair on the group 14 atom, and can possess quite large double bond character between the metal and the ligands.[62]

Substituted heavy analogues of cyclopentadieneide including one heavy atom in the ring are known for germanium in the reduced forms: taking butadiendiide to be a chelating ligand to a Ge(II) centre, one can imagine a neutral germylene with an sp^2-like lone pair on the germanium centre stabilised by the inert pair effect.[63] However, this neutral heterocycle possesses only 4 electrons within its π-system, making it formally antiaromatic by Huckel's rules. Instead, the doubly reduced form is more stable, formally reducing the Ge(II) centre to Ge(0) by populating its empty p orbital, formally satisfying Huckel's rules and becoming aromatic. These doubly reduced species typically form inverse sandwich complexes with a potassium cation coordinating each face of the reduced germylene ring.[64]

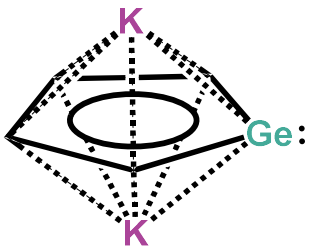
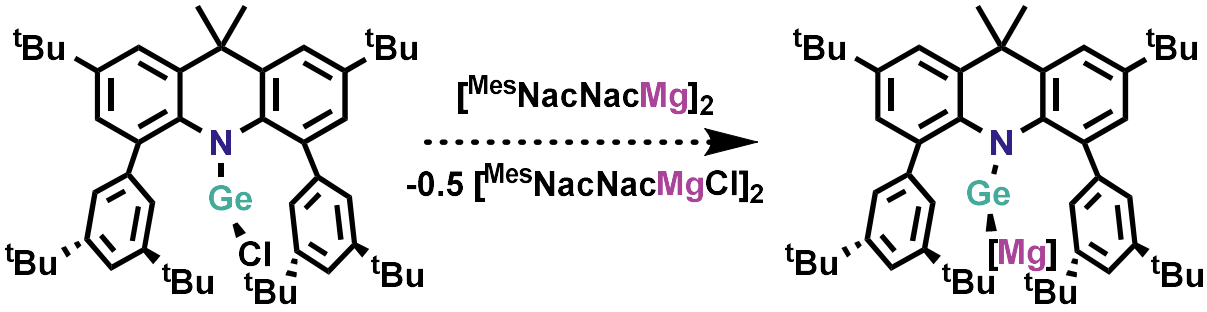


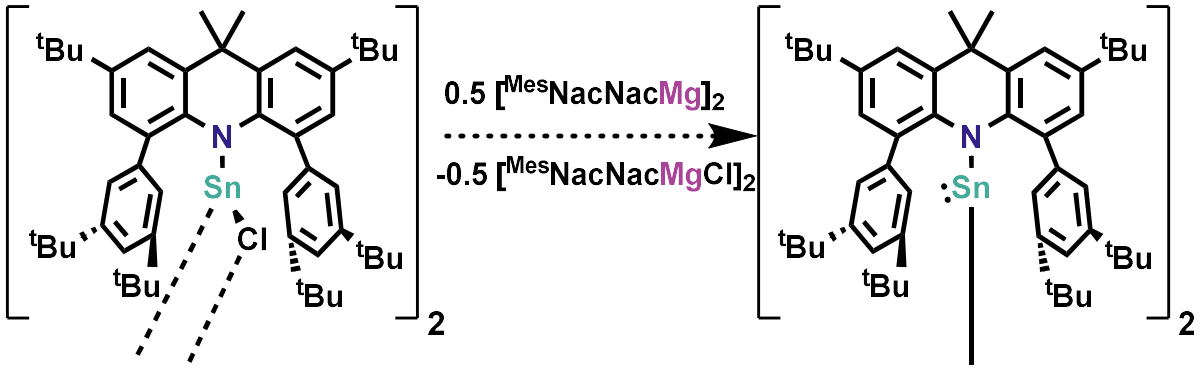
Figure 17 Heavy cyclopentadiene analogue as an inverse sandwich complex. The germanium does not possess a hydrogen as would be expected in germata cyclopentadienide, instead deprotonating and rearranging the potassium cation from the in-plane position to the η^5 coordination mode, likely due to the inert pair effect of the sp^2-like lone pair on germanium.

2.4.2 Synthesis

With the chlorogermylene and stannylene in-hand, we attempted reductions. Using potassium reductants KC_8, potassium mirror, or K/KI all resulted in over reduction to the potassium salts of the ligand and presumably germanium/tin metal. The germylene does not react with lithium ribbon in C_6D_6 with small amounts of diethyl ether, either by sonication or heating. Instead, magnesium(I) dimer in the form of $[^{Mes}NacNacMg]_2$ ($^{Mes}NacNac$ = (Mesityl-NCMe)$_2$C)$^-$),[28] which is soluble in hydrocarbons solvents and also possesses significant steric protection around the electropositive magnesium centre, was utilised in the hopes of forming a digermyne or potentially the first example of a "germylene Grignard", the aforementioned 0-valent germanium isoelectronic with a germylene (Scheme 3). The same reaction was attempted with the stannylene precursor as well, which we shall address first. Due to the already dimeric nature of the stannylene, we expected the magnesium dimer to abstract the chlorides and result in the corresponding distannyne (Scheme 4).

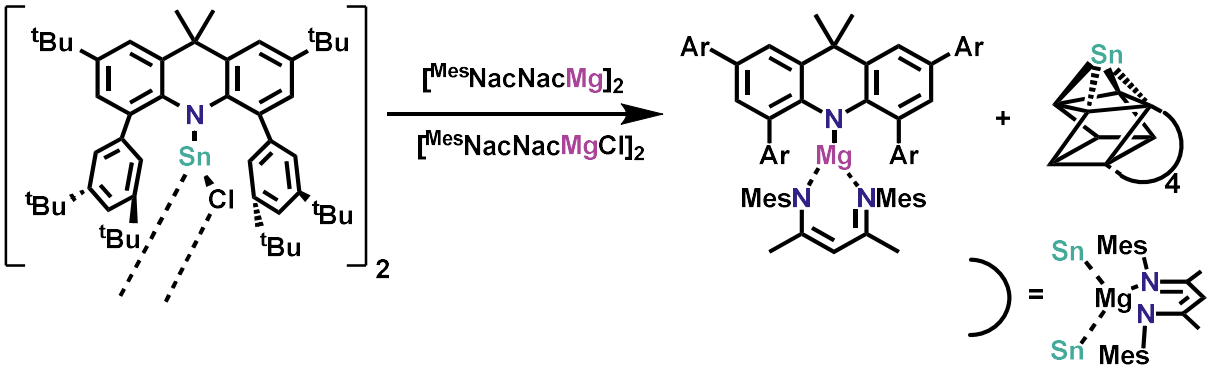


Scheme 3 Proposed reduction of the chlorogermylene with magnesium(I) dimer to form the magnesio-germylene, or "germylene Grignard".



Scheme 4 Proposed reduction of the dimeric stannylene chloride with magnesium(I) dimer to a proposed distannyne.

Dissolving a mixture of [^{Mes}NacNacMg]$_2$ and [^{tBu2Ph}**AcrN′**SnCl] in C_6D_6 instantly creates a blood red, almost black solution. By ^{1}H NMR spectroscopy the reaction proceeded to completion almost instantly; observed was a complex mixture of products including one set of ligand (**^{tBu2Ph}AcrN′**) resonances, unsymmetrical in the flanking arenes as observed previously, and one set of ^{Mes}NacNac resonances. The ^{Mes}NacNac resonances are expected, as [^{Mes}NacNacMgCl]$_2$ is expected as a side product from the reaction, although they did not match the literature values.[65] Concentrating the solution was expected to crystallise the colourless, poorly soluble [^{Mes}NacNacMgCl]$_2$, so that the ligand-containing species could be fractionally crystallised from the mother liquor. The first crystallisation instead yielded a large amount of excellent blood-red blocks suitable for single-crystal X-ray diffraction, which yielded an unexpected result: a mono-capped square antiprism Zintl cluster[66] of nine tin atoms, with four [^{Mes}NacNacMg]$^+$ cations ligating 4 edges (Scheme 5).



Scheme 5 The actual reduction of the dimeric chlorostannylene with magnesium(I) dimer forms a mono-capped square antiprism tin cluster ligated by supporting [^{Mes}NacNacMg]$^+$ cations, and a proposed magnesium complex presumed from the tin disproportionation.

The identity and stoichiometry of any of the species in the ^{1}H NMR spectrum is unknown, but the formation of the tin cluster (with a formal oxidation state of -4/9 per tin) is presumed to be due to disproportionation of an intermediate stannylmagnesium species, and we consequently

posit the corresponding formation of [^{tBu2Ph}**AcrN′**Mg^{Mes}NacNac] as the major ligand-containing species. Such group 14 mono-capped square antiprisms with 4 axial ligands are known with TMEDA for both tin and germanium through well-known Zintl chemistry.[67] The Sn Zintl cluster [(^{Mes}NacNacMg)$_4$Sn$_9$] was characterised by X-ray crystallography and the solid state structure is shown in Figure 18.

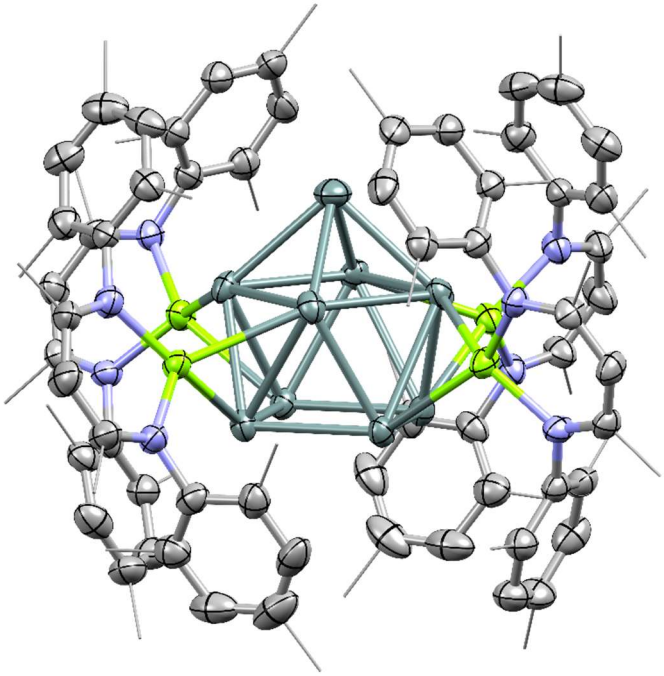


Figure 18 The tin Zintl cluster stabilised by [^{Mes}NacNacMg]$^{+}$ cations produced by the reduction of [^{tBu2Ph}AcrNSnCl]$_2$ stannylene chloride dimer by [^{Mes}NacNacMg]$_2$. Taking the capping Sn to be apical (A), the immediately bonded tins to be middle (M) and the remaining tins to be basal (B), key geometric parameters are: B-M 2.9607(7) Å; 3.1447(6) Å; B-B: 2.8943(6) Å; M-M 3.1107(7) Å ; M-A 2.9467(7) Å; 2.9580(7) Å; Mg-B 2.894(2) Å, 2.885(2) Å; Mg-M 2.960(2) Å, 3.002(2) Å. All inter-Sn distances in good agreement with literature values. Space group Pccn. ^{Mes}NacNac methyl groups shown in wireframe for clarity, solvent benzene molecules omitted, and ellipsoids shown at the 50% level. Carbon in grey, nitrogen in blue, magnesium in green, and tin in teal.

Reduction of the chlorogermylene [^{tBu2Ph}**AcrN′**GeCl**]** under the same conditions results in a very similar deep red solution, except the ^{1}H NMR spectrum of the reaction mixture was much more complex. Reproducibly, concentration of the reaction mixture led to first crystallisation of the [NacNacMgCl]$_2$ by-product, then concentration of the mother liquor yields crystals of excess magnesium(I) dimer, then concentration of the mother liquor a third time yields crystals of proligand, and final concentration leads to the formation of yellow needles. These crystals only formed upon removal of almost all solvent, and proved difficult to isolate for crystallography as they were highly air and moisture sensitive, and dissolved in all attempted crystallography oils within a few minutes. The final crystallisation seems to yield only a single

product, with all the crystals the same yellow needles. Isolated crystalline yield was very variable and purity proved difficult to verify by NMR, usually *ca*. 20% (4-26% observed).

The single-crystal X-ray diffraction revealed an unexpected product with tetrahedral germanium centre bonded to the ligand amide donor, the ortho-position of one of the flanking aryl groups (which was previously a hydrogen), and two magnesium centres (Figure 19):

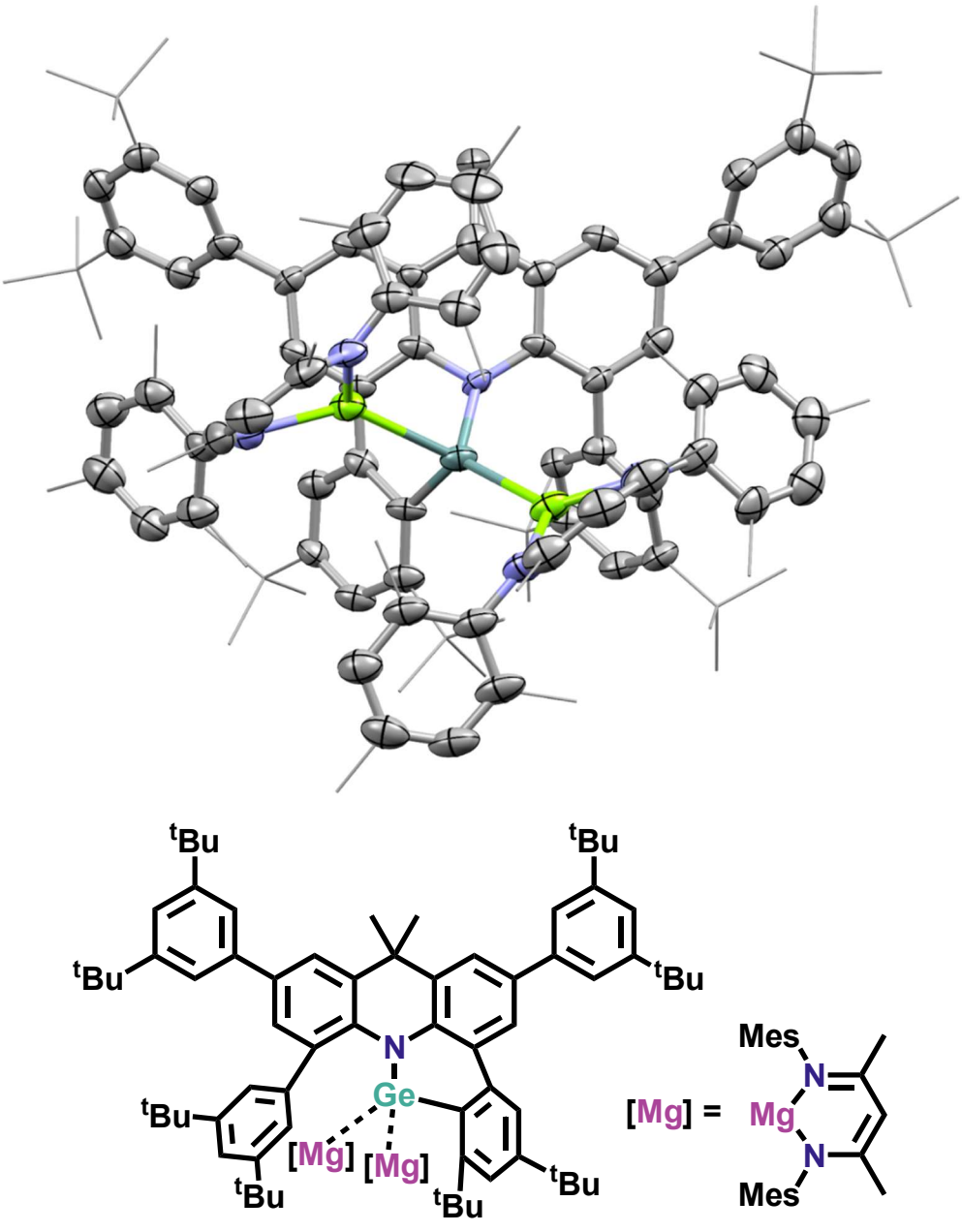


Figure 19 (top) Solid-state structure of the dimagnesiogermane, showing the tetrahedral germanium bonded to the ligand N-donor and the ortho-carbon of a flanking arene as well as two [^{Mes}NacNacMg]$^{+}$ cations, selected groups shown in wireframe for clarity. (bottom) Skeleton structure provided as a visual aid in interpreting the solid-state structure. Ge-Mg1 2.737(3) Ge-Mg2 2.634(3) Ge-N 1.967(6) Ge-C 2.021(7) N-Ge-C 90.8(3) Mg-Ge-Mg 111.02(2) Mg1-Ge-N 99.93(18) Mg2-Ge-N 123.44(19) Mg1-Ge-C 97.4(2) Mg2-Ge-C 128.4(2) τ_4 = 0.767 (implies reasonably tetrahedral). Mg1 is the top left. Tert-butyl groups and ^{Mes}NacNac methyl groups shown in wireframe for clarity, solvent benzenes and minor components of tert-butyl disorder omitted, and ellipsoids shown at the 50% level

It is our understanding that this complex is the first example of a dimagnesiogermane, and the first example of a four-coordinate zero-valent germanium centre, with germylones[68] (the majority of zero-valent germanium species) possessing a two-coordinate geometry and all previously reported dilithiogermanes lithium-bridged dimers, 5-coordinate at germanium.[69] To investigate the electronic structure, the canonical orbitals and Quantum Theory of Atoms in Molecules (QTAIM)[70] (Figure 21) were investigated.

In the extreme interpretation, covalent, pseudo-tetrahedral geometry at the germanium centre would imply isolobality with methane in a molecular orbital regime, with the eight valence electrons exhibiting $t_{1u} \oplus a_{1g}$ irreducible representations, with the triply degenerate t_{1u} set higher in energy. At the other end of the spectrum, a totally ionic representation (now ignoring the magnesium centres) moves the germanium to a C_{2v}-like geometry, with the valence electrons in a $2a_1 \oplus b_1 \oplus b_2$ fashion. With $a_1 \oplus b_1$ for the bonds between the germanium and the ligands, this leaves $a_1 \oplus b_2$ for the lone pairs: a higher energy p orbital and an sp^n hybrid orbital. If the orbitals are sufficiently diffuse, like on a poorly electronegative atom with a low formal charge, ionic interactions may be more favourable interacting with merely one close-by cloud rather than perturbing the geometry of the germanium centre, giving unsymmetrical Mg centres. The two likely possibilities are either three similar orbitals, two of which are interacting with the magnesium centres, or a p-orbital and an sp^n orbital.

Due to the broken symmetry and large electronegativity difference between carbon, nitrogen, and magnesium, the germanium orbitals more closely represent the latter case, with the HOMO a p-orbital orthogonal to the C-Ge-N plane, and an sp^n HOMO-1 approximately coplanar. Figure 20 shows the HOMO and the HOMO-1 canonical orbitals essentially localised on the germanium centre in an approximate sp^2/p hybridisation with each orbital polarised towards the two magnesium centres. The difference in Ge-Mg bond lengths and angles with the C-Ge-N plane support an ionic interpretation, demonstrating a flat PES with limited preference for specific geometries. The magnesium approximately coplanar with C-Ge-N has a reduced Mg–Ge bond length (2.634(3) Å compared with 2.737(3) Å), possibly owing to the reduced radial extension of the sp^n-like orbital compared with the p-like orbital.

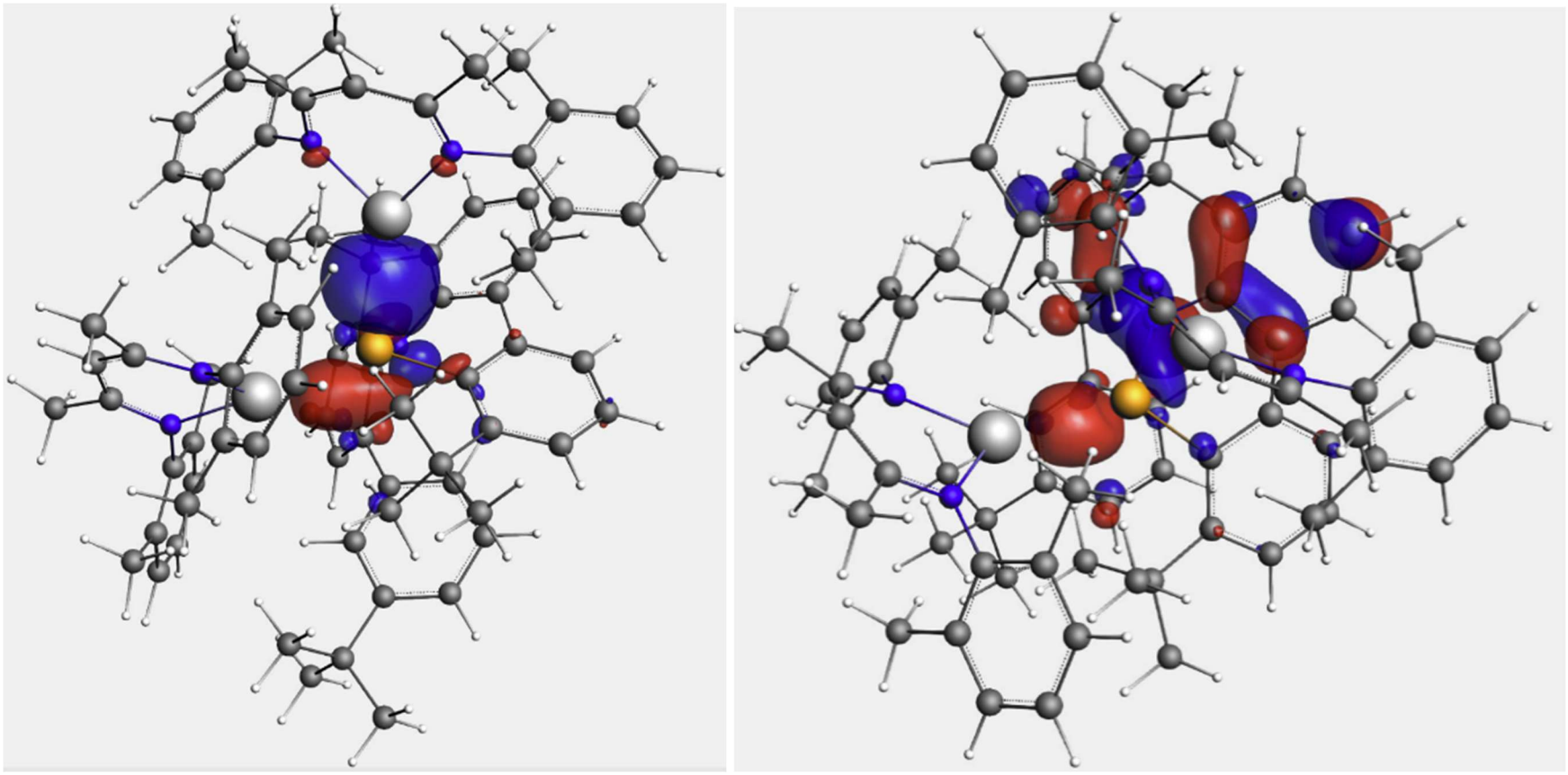


Figure 20 The canonical molecular orbitals of the dimagnesiogermane. (left) The HOMO, an essentially polarised germanium p-orbital. (right) The HOMO-1, an sp^2-like Ge orbital polarised towards a magnesium. Germanium in yellow, magnesium in silver, carbon in grey, and nitrogen in blue. Calculated at the PBE0-D3BJ/TZVP//PBE0-D3BJ/SVP level of theory using Amsterdam Density Functional (ADF) in Amsterdam Modelling Suite (AMS).[71]

Geometrically, the C-Ge-N atoms define a plane. The two Ge-Mg interactions each form an angle with the plane. In the idealised sp^2-Mg donation and p-Mg donation, it is expected to have a 0° angle and a 90° angle; in the idealised tetrahedral case the expected angle is $[\cos^{-1}(1/3)]/2 \approx 54.7°$. Equivalently this is also reflected in the shortest distance from the magnesium centres to the plane, 0 Å and equal to the Ge-Mg bond length (*ca*. 2.686 Å) in the donor case and both the bond length × sin(54.7°) ≈ 2.192 Å. No formal quantitative metric for the difference between the two circumstances exists, so we shall simply use the root-mean square (RMS) difference between the two values for comparison (although RMS may be inappropriate for nonlinear scaling differences like angles, the qualitative point remains about greater and smaller differences regardless of the statistical validity). At least qualitatively, Table 1 shows the better description of the ionic Ge-Mg orbital-wise donor interactions.

	θ(°)	φ(°)	RMS Difference
Ideal Tetrahedral	54.7	54.7	25.8
Ideal Ge-Mg Orbital Donor Angles	0	90	18.6
Experimental	25.8	77.5	-

Table 1 A comparison of the two likely geometric arrangements of the magnesium centres around the germanium centre, showing the superior agreement with orbital-wise interactions.

Clearly the electronic structure lies between the extreme cases, but is slightly closer to the orbital donor angles. However, the geometry is also perturbed by the repulsion between the sterically demanding ligands bound to each of the metals.

Beyond the canonical orbitals, the electron density grants insights into the electronic structure. QTAIM analysis, alluded to in chapter 1 and explained in detail in chapter 3, examines electronic structure through a density-based lens. The electron density is characterised at every point by the density (ρ(r)), its gradient (∇ρ(r)), and the gradient of the gradient of the density ($\nabla^2\rho(r)$, or more often the corresponding matrix $H_{ij}(\rho(r)) = \frac{\partial^2}{\partial x_i \partial x_j}\rho(r)$). In principle, this could be measured experimentally (most easily through X-ray diffraction), however the required accuracy to make even qualitative evaluations is beyond most experimental limits, and computational models are almost exclusively employed.[72] NoSpherA2 (No Spherical Atoms in Olex2)[73] uses a mixed method, using a self-consistently generated wavefunction to generate an electron density for comparison with the Fourier inverse of the X-ray diffraction pattern. However, this proved untenable for our large systems with disorder components, and the experimental diffraction limitations of the acicular crystals.

Points of the electron density where ∇ρ(r) is zero and two of three eigenvalues of the Hessian matrix are negative (a (3, -1) critical point) are referred to as bond critical points (BCPs).[70] The magnitude of the density at the critical point joining two atoms correlates with the strength of the interaction, and its position along the bond critical path and relative magnitude of the Hessian matrix eigenvalues give indications about the nature of the interaction.[57]

As expected for two relatively large electropositive elements, the bond appears weak. The magnitude of the bond critical points is 3.52×10^{-2} and 3.58×10^{-2} $e^{-}Bohr^{-3}$ for the Ge-Mg1 and Ge-Mg2 respectively. The shorter Ge-Mg2 interaction has a slightly higher density, indicating a slightly stronger interaction, as expected, although the two are very similar. These values are exceptionally small, for comparison the value of the Ge-C and Ge-N BCPs are 1.13×10^{-1} and 1.02×10^{-1} $e^{-}Bohr^{-3}$ respectively, almost three times the magnitude and typically considered to be relatively weak, labile bonds to begin with. The ellipticity at the BCP, which is conventionally the ratio of the negative Hessian eigenvalues less unity (with the ratio necessarily greater than or equal to unity) (although a greater relation to true elliptical eccentricity would be given by $\sqrt{1-(\frac{\lambda_1}{\lambda_2})^2}$ rather than $\frac{\lambda_1}{\lambda_2}-1$ while still preserving the intended metric), indicates the degree of rotational anisotropy at the BCP, with a larger ellipticity indicating a higher degree of asymmetry. Perfectly symmetrical bonds such as that of H_2 possess an ellipticity of 0, while strong double bonds with a greater amount of electron density on one axis than the other can possess values typically of 10 or higher. Predictably, the ellipticity of the Ge-Mg1 and Ge-Mg2 BCPs is very close to 0, at 7.78×10^{-2} and 2.84×10^{-2} $e^{-}Bohr^{-5}$ respectively, indicating essentially only local sigma character in the interaction. As well as the ratios being close to unity, the absolute magnitudes of the Hessian eigenvalues are very small as well, with none of the 4 negative eigenvalues having a greater magnitude than 3×10^{-2} $e^{-}Bohr^{-5}$, again indicating a very flat PES for both magnesium centres. The distance of the BCP along the bond critical path also indicates the very ionic nature of the interaction, with the large, diffuse electron density of the germanium protruding a great distance along the interaction, >68% in each case.

From both canonical orbital and QTAIM perspectives, the nature of the Ge-Mg interactions in the dimagnesiogermane are diffuse, weak, and ionic. However, what remains unanswered is not *what* the dimagnesiogermane is, but *how* it came to be. The next subchapter undertakes mechanistic investigation in the formation of this unanticipated species.

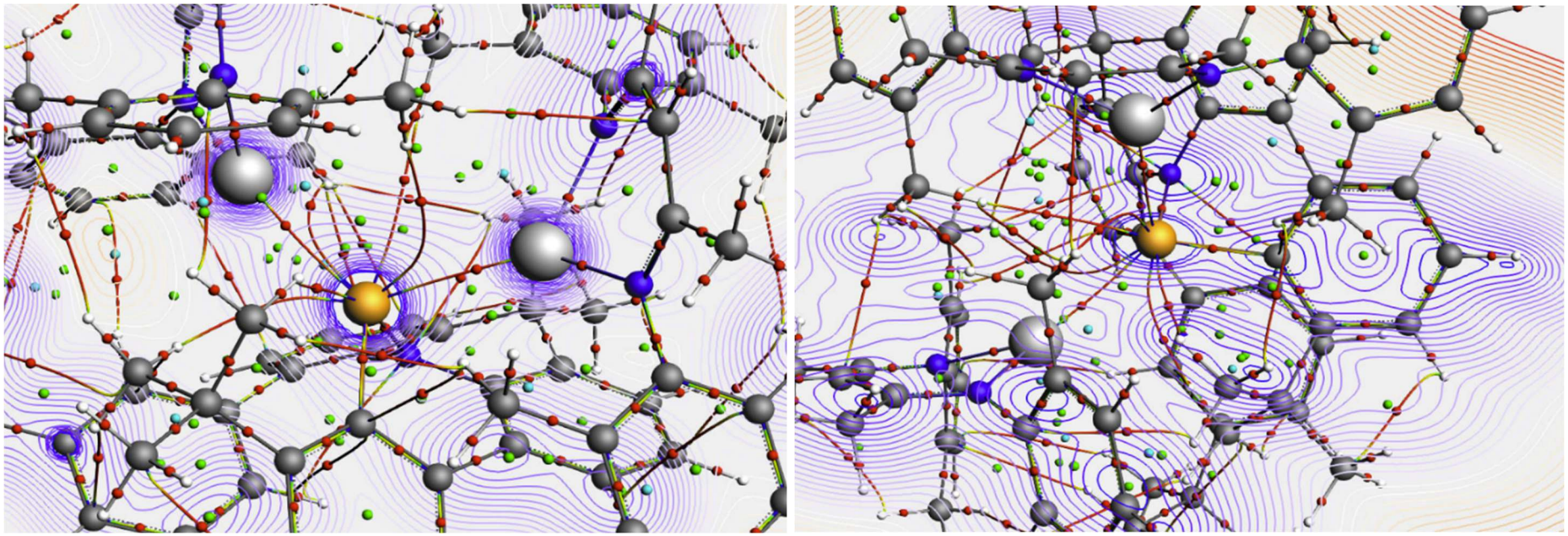


Figure 21 QTAIM plots of the dimagnesiogermane, viewed through the Mg Ge Mg plane (left), and the C Ge N plane (right) showing their electrostatic vs. covalent natures. Germanium in yellow, magnesium in silver, carbon in grey, and nitrogen in blue.

2.5 Computed Mechanism

We start assuming that the simplest initial reduction product, the germylene Grignard, was able to form and the cascade to the observed dimagnesiogermane occurs from there. This is highly precedented in the earlier discussed zincagermylene,[59] but also broadly observed in the "inorganic Grignard" class of complexes pioneered by Hicks *et al*.[74,75]

Density functional theory (DFT) calculations for geometry optimisation were performed using the Gaussian 16 program[76] using the BP86 density functional approximation,[77] Stuttgart ECPs and associated basis sets[78] for Ge (ζ_d = 0.230) and Mg with the listed additional polarisation function, using the 6-31G** basis set[79] for all other atoms (BS1), and the fine integration grid. The structures were confirmed as minima on the potential energy surface *via* analytical frequency calculations, yielding no negative eigenvalues, except for transition states, which were verified as saddle points on the potential energy surface, each with a single negative eigenvalue. The corresponding imaginary modes were verified as connecting the appropriate intermediates *via* the intrinsic reaction coordinate method. Thermochemical properties were calculated at a pressure of 1.0 atmosphere, unscaled frequencies, and at a temperature of 298.15 K.

The system studied was highly truncated (Figure 22) due to the excessive computational time required to compute the experimental system, and due to convergence issues in computing the experimental system from the very large number of degrees of freedom. The original solid-state structure (with the same spatial arrangements of atoms as the one presented herein but at greatly reduced resolution) was a little too far from a local minimum and was very difficult to converge. In the ligand, the 2,7-bis-(3,5-di-tert-butyl)-phenyl moieties were truncated to hydrogens, and the 2,7-bis-(3,5-di-tert-butyl)phenyl moieties were truncated to phenyl substituents. Similarly, the mesityl groups in the ^{Mes}NacNac-containing species were truncated to phenyl substituents, although the methyl groups of the β-diketiminate part were preserved as they proved necessary to preserve planarity of the ligand. We felt that the core features of the processes would be captured by this truncation if not necessarily realistic barrier heights.

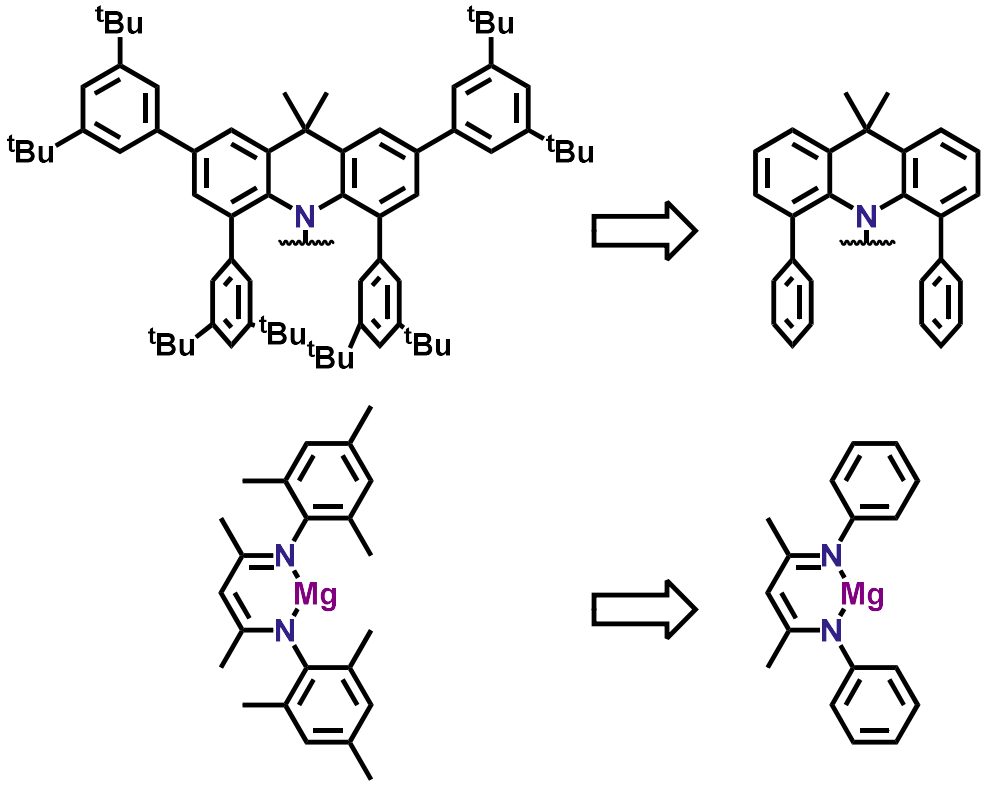


Figure 22 The truncations used in the theoretical model for the calculation of the formation of the dimagnesiogermane.

Relaxed potentials energy surface (PES) scans (referred to just as "scans" henceforth) were performed at the BP86/BS1 level of theory with the GDIIS algorithm, SCF=conver=6, maxcyc=10, and the "fine" integration grid in Gaussian09 A.02 [80] in attempt to find a computationally tractable, but qualitatively accurate characterisation of the PES in question along the suspect major contributor to the reaction coordinate. Once a PES of appropriate shape was found, the highest energy point, ideally with the lowest gradient, was then subjected to a formal transition state search in Gaussian16 using the opt(ts, noeigen, calcfc) options at the BP86/BS1 level of theory, ultrafine integration grid and default convergence criteria.

The lowest energy point with the smallest gradient on the novel side of the peak of the PES was also subject to geometry minimisation as described above.

Reaction Pathways

We propose two similar pathways for the decomposition of the intended [LGe{Mg}] (L = 9,9-dimethyl-4,5-diphenylacridanide, {Mg} = diphenylNacNac magnesium) complex into the (pruned, computational analogue of the) dimagnesiogermane. In both pathways, the intended [LGe{Mg}] complex is assumed to form as intended, then reacts intramolecularly into the observed products. The difference between the **a** pathway and the **b** pathway is whether the initial oxidative addition by the germanium centre across the indicated CH bond occurs with

the hydrogen “above” or “below” the C-N-Ge plane, with the **a** pathway above and the **b** pathway below. The oxidative addition then leads to two diastereomers, which then undergo a series of hydride transfers and conformational changes until what will become a terminal hydride is in an appropriate arrangement to leave. The pathways then link in **8**, a C,N-chelated germylene, for the final reduction with a second equivalent of [{Mg}$_2$] down to the observed dimagnesiogermane **14**, summarised in Figure 23, details presented below.

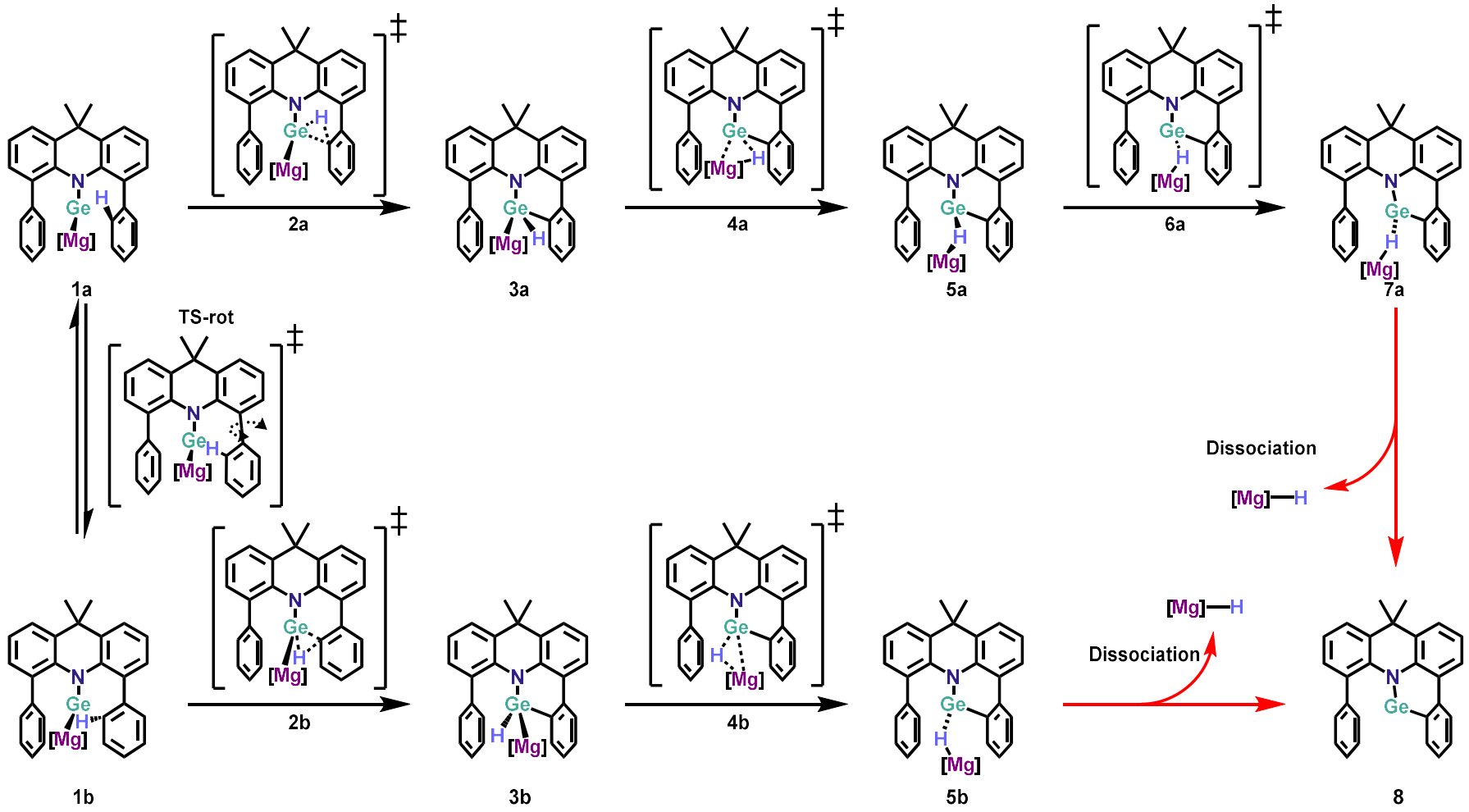


Figure 23 The two computed pathways theorised for the formation of the C,N-chelated germylene 8. Oxidative addition by the electron-rich low-valent germanium is proposed across the CH bond of a flanking phenyl group. This results in diastereomeric germane species, which go through a series of rearrangements and hydride transfers until ½[NacNacMgH]$_2$ is expelled from the system, resulting in the C,N-chelated germylene 8. The germylene then reacts with an additional equivalent of magnesium dimer, as shown below. Red arrows indicate reactions without elucidated transition states.

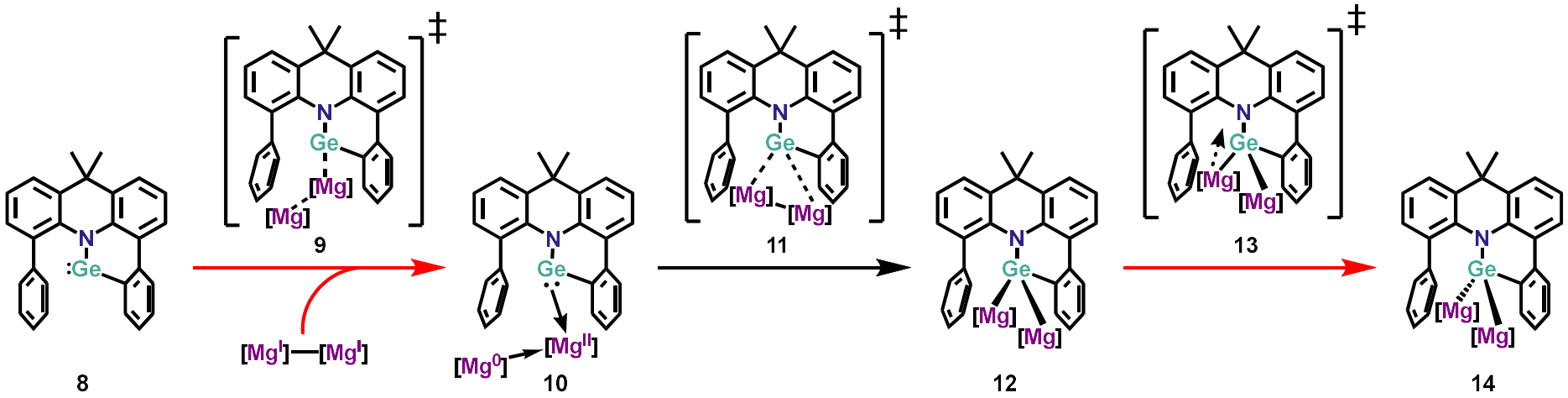


Figure 24 Computed pathway for the reaction between the C,N-chelated germylene and an additional equivalent of magnesium dimer in a net "reductive addition" to form the experimentally observed product 14. Red arrows indicate reactions without elucidated transition states.

2.5.1 Starting Points

1a and **1b** were found from a geometric minimisation from the intrinsic reaction coordinate method from **2a** and **2b** respectively (*vide supra*). The computed structures of **2a** and **2b** are given in Figure 25 to clarify the "above" and "below" the germylene positions of the activated C-H bond. Due to the existence of the two possible starting rotamers, a scan along the C-C-C-C dihedral angle was performed to try and interconvert between the two, which resulted in both $\mathbf{TS_{rot}}$ and consequently **1b** *via* IRC. As stated above, the essential difference between the two pathways is whether the initial oxidative addition of the **1x** (x = **a**,**b**) into the CH bond comes from "above" or "below" the N-Ge-C plane, leading to diastereomeric intermediates **3a** and **3b**. Their precursors, **1a** and **1b,** are very similar in energy, with **1b** higher by only 1.2 kcalmol^{-1}, and the barrier to interconversion is very low at only 9.2 kcalmol^{-1}. The energetic difference and barrier to interconversion are likely both significantly larger in a more physically realistic system with distinct steric interactions from the unpruned moieties, but the purpose of this introductory investigation is only to show mechanistic feasibility of the transformation of **1** into **14**, and so for the rest of this work we will refrain from comment on the energetic differences between **a** and **b**, particularly due to the inadequate level of theory for post-geometry properties.

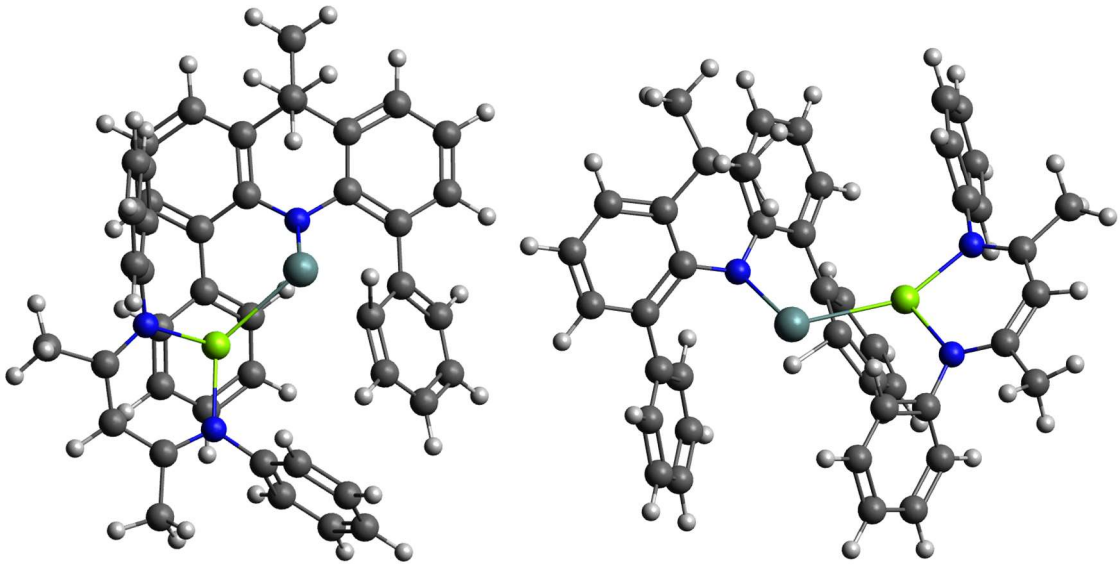


Figure 25 The computed structures of 2a (left) and 2b (right) for 3-dimensional clarification.

2.5.2 Pathway a

Pathway **a** begins with oxidative addition of the formally Ge(0) species across the ortho-CH bond of a flanking aryl group to form the germyl-magnesium species **3a**, which then undergoes a series of conformational changes resulting in the hydride-bridged complex **7a**, which is then

able to dissociate a ½[NacNacMgH]$_2$ fragment and the germylene **8**. At this point, a similar process in **b** also leads to **8** and the two pathways link for the final reduction of the germylene with Mg(I) dimer to result in the pruned analogue **14** of the experimentally observed product.

3a was found by taking the solid-state structure of [GeCNMg$_2$] and replacing the "top" [Mg] with a hydride and performing geometry optimisation. Scanning along the corresponding decreasing C-H coordinate leads to the O.A. transition state **2a**, which links to **1a** *via* the IRC method. Scanning along a decreasing Mg-H distance from **3a** however leads to **4a**, which is essentially a hydride migration TS from Ge to Mg. The frequency is -75.02 cm^{-1}, which has a small magnitude for a hydride migration, which appears to be due to significant movement from both the Ge and Mg in the mode in addition to the H migration. IRC from **4a** results in **5a**, best described as a dative interaction from the terminal hydride on the [NacNacMg-H] into the empty p-orbital on the germylene fragment.

It would normally be expected to next find a barrier-less dissociation of the [NacNacMg-H] fragment from the complex, however scanning along an increasing Ge-H distance elucidates another transition state and associated intermediate, **6a** and **7a**, which appear to partially linearize the Ge-H-Mg interaction. Continuing the Ge-H lengthening scan from **7a** indeed resulted in the expected **8** and ½[NacNacMgH]$_2$.

2.5.3 Pathway b

The process for the alternative pathway was found in essentially an identical fashion to the one described above for the **a** pathway. **3b** was found by replacing the "bottom" [Mg] in [GeCNMg$_2$] with a hydride and optimising. Again, **2b** (and consequently **1b**) was found by scanning along the corresponding shortening CH bond distance, and **4b** and **5b** were found by scanning along the increasing Ge-H distance. Unlike in **a**, **5b** dissociates into **8** without further intermediates upon increasing the Ge-H distance again.

2.5.4 Germylene Reduction

From **8**, the reunited reaction pathway was probed in the forward direction. [NacNacMg]$_2$ was placed *ca.* 3 Å away from the germanium and then scanned along a shortening Ge-Mg coordinate. This results in the smooth association of the magnesium dimer to the germylene in **10**, **9** proved inelucidatable. **10** appears to be the germylene adduct of the magnesium dimer, giving a tetrahedral Mg(II) centre ligated by the germylene, the NacNac, and a Mg(0) donor. Scanning along a decreasing Ge Mg(0) coordinate gives rise to **11** and **12**, transfer of the Mg(0) donor from the Mg(II) to the Ge centre. In **12**, the two [Mg] fragments are parallel and closely

associated, requiring the geometric relaxation step **13** (for which we were unable to find a true transition state, but it is difficult to imagine a high barrier for rearrangement of fragments on the same centre) to reorganise to the experimental product **14**.

Overall, the mechanism post-production of the germylene is very similar to that reported by Crimmin and coworkers for the reductive addition of the zinc dimer: first coordinating the germylene to one magnesium centre, followed by transfer of the second magnesium to the germanium in a stepwise process. It is difficult to compare the energies of the two mechanisms as they are performed at significantly different levels of theory (Crimmin reports a more reliable M06L/def2-TZVPP/PCM(benzene)//M06L/mixed DZ compared with this BP86/ mixed DZ level of theory), but a qualitatively similar barrier (*ca*. 14.23 kcalmol^{-1} comparably taking the germylene as 0) as the authors report for gallium (15.7 kcalmol^{-1}) is intuitively sensible, as the coordination to the germanium is more difficult with the sterics of the flanking arene (reflected in the more uphill intermediate energy), but the labile magnesium-magnesium bond results in a lower barrier height, ending up in a similar energetic positon.

Figure 26 and Figure 27 show the elucidated reaction profile for both the monomeric and dimeric pathways. In pathway **a**, the rate determining step is the oxidative addition ($\Delta G^{\ddagger}$ = 18.7 kcalmol^{-1}), whereas in pathway **b** the rate determining step is the [NacNacMgH] dissociation from the germylene ($\Delta G^{\ddagger}$ 15.0 = kcalmol^{-1}), however the oxidative addition for **b** ($\Delta G^{\ddagger}$ 13.4 = kcalmol^{-1}) is the same within error, and we suggest growing the truncated system to a physically realistic system will increase the barrier to O.A. more than the dissociation barrier.

Overall, the mechanism supports the observed side products, and results in barrier heights sensible for the observe temperatures (although these barriers are crude approximations). The experimental and computational evidence together supports the first example of reductive addition to form a stable product using magnesium(I) dimer or at a germanium centre, also resulting in the first dimagnesiogermane and seemingly the first 4-coordinate Ge(0) species.

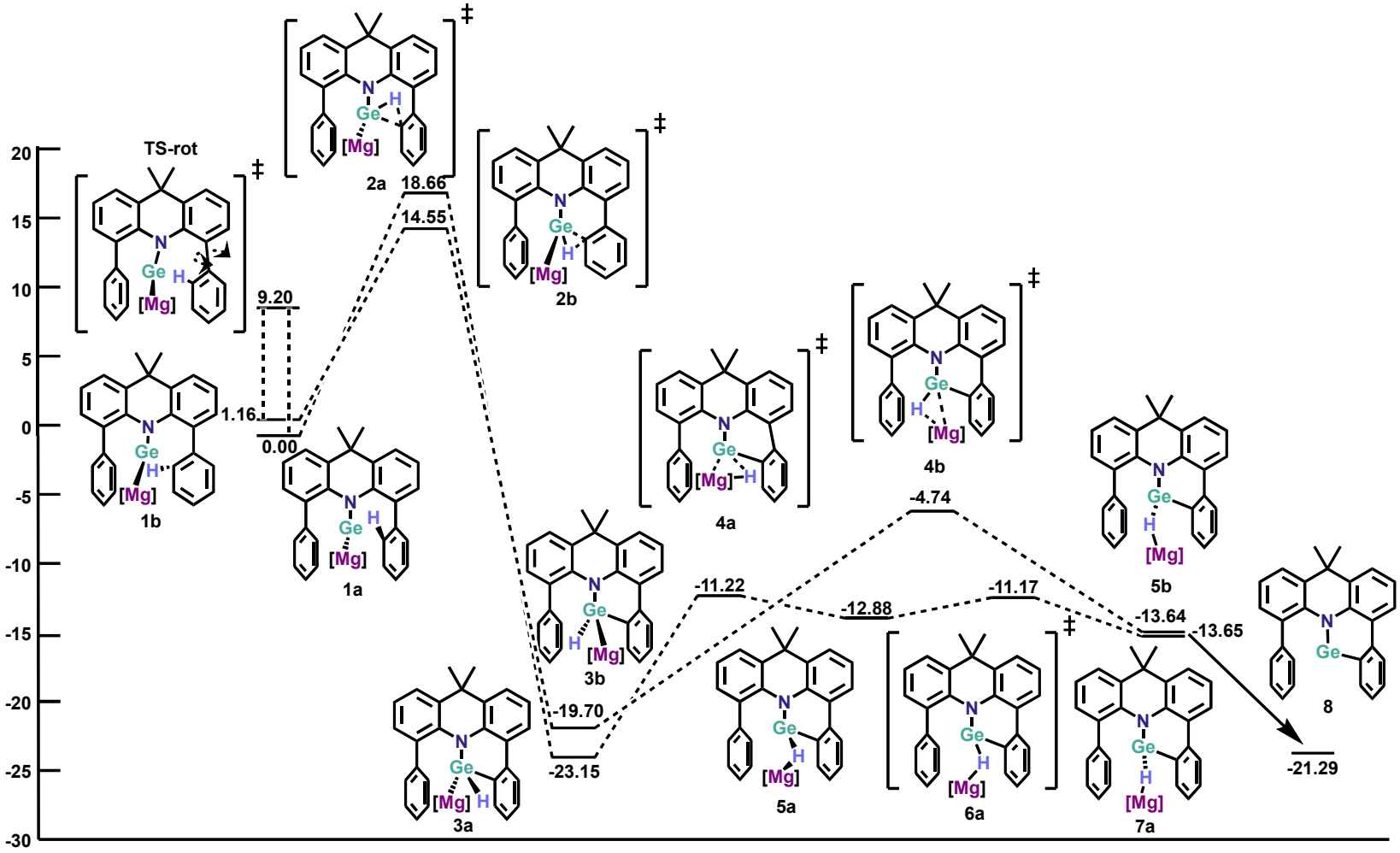


Figure 26 The elucidated reaction profile for both the a and b pathways at the BP86/BS1 level of theory, intended only to demonstrate a possible pathway *sans* significant energetic interpretation. Both begin with the implied intermediate complex [LGe{Mg}] in two rotamers, 1a and 1b, interconvertible *via* TS_{rot}. Each then undergoes oxidative addition to form the diastereomers 3a and 3b, which then undergo a series of rearrangements to extrude ½[NacNacMgH]$_2$ and produce the two-coordinate germylene 8. Relative Gibbs free energy in kcalmol^{-1}.

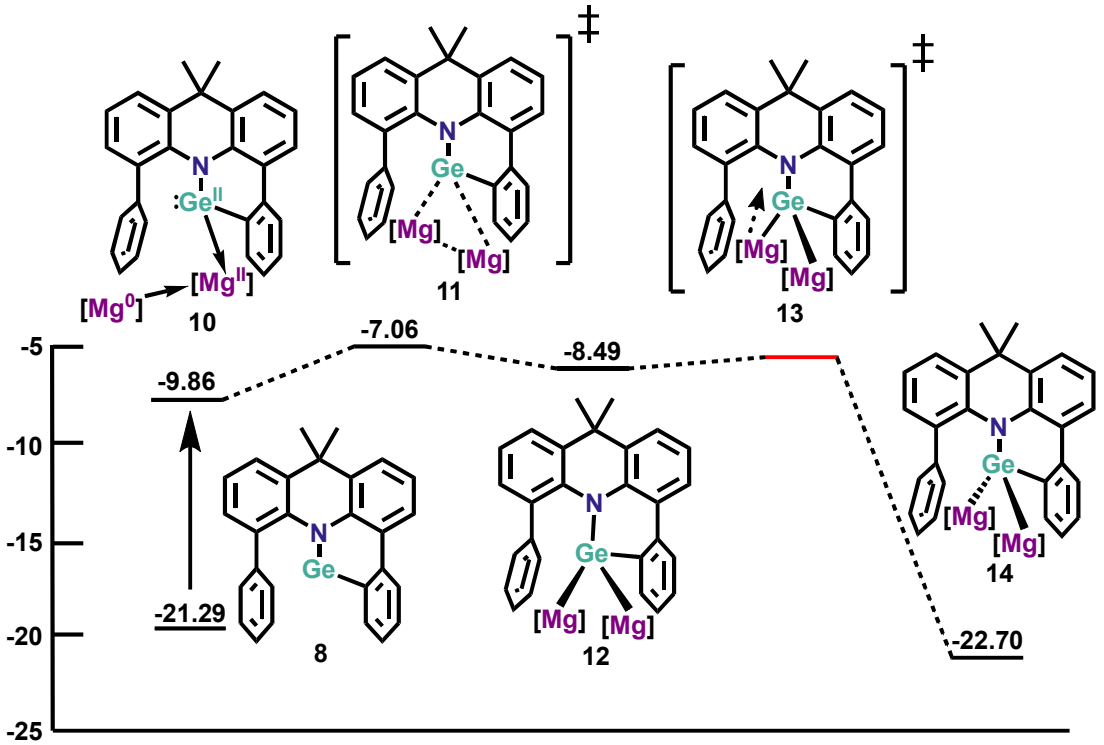


Figure 27 Coordination of [Mg$_2$] to the germylene 8 before undergoing a formal "reductive addition" across the Mg-Mg bond to produce the pruned analogue of the experimentally observed species. Low-barrier conformational changes result in the pruned analogue of the experimentally observed dimagnesiogermane, 14. Transition state 13 was never elucidated.

2.6 Closing Remarks

2.6.1 Conclusions

This chapter presented the synthesis and characterisation of two novel, one-coordinate acridanide ligands substituted with sterically demanding substituents intended for the stabilisation of low-valent main group compounds, inspired by a hybrid of Emslie's diamido xanthene framework[30] and Hinz's one-coordinate bulky carbazoles.[33]

With these, the lithiation and potassiation was explored for the purpose of metathesis to main group elements, of which group 14 proved the most amenable. The isolation of two-coordinate chlorogermylenes, and a chloride-bridged chlorostannylene demonstrates the steric demands and coordination features of the ligands.

Reduction of the chlorostannylene, while extruding the intended ligand to presumed disproportionation products, showed a facile and high yielding molecular route to a soluble and readily accessible mono-capped square antiprism Zintl cluster.

The same reactivity with the corresponding germylene chloride, however, when combined with computational endeavours revealing the electronic structure and mechanism of formation, matching that reported by Crimmin and coworkers,[22] indicated the remarkable result of the first isolated magnesium(I) dimer reductive addition product, and the first example of reductive addition at a germanium centre.

2.6.2 Future Work

Unfortunately, some species remain incompletely characterised, particularly the dimagnesiogermane. The difficulty lies in the 7-step linear sequence with the lowest-yielding steps at the end, so scaling of this low-yielding and necessarily high by-product reaction is not facile, and purification of the thin yellow needles proved a multi-year challenge. While the reproducibility of the reaction and the visual uniformity of the product is promising, it has led to incomplete characterisation by typical organometallic standards: the ^{1}H NMR spectrum remains contaminated by NacNac resonances and proligand ligand, which make the greater than 40 unique resonances in the product difficult to distinguish, and the $^{13}C\{^{1}H\}$ NMR spectrum indecipherable. Future work for publication would require a more complete spectroscopic characterisation.

Additionally, the mechanistic work is only for a qualitatively similar model system. In order to draw more quantitative inferences from the work, investigation of at least the rate-determining

steps with a more complete molecular model and a higher level of theory (particularly with respect to the basis set) would be required.

The work does, however, indicate future directions for research into reductive addition. Work within the group already yields promising results into reductive addition with magnesium(I) dimer across a more intended, and appropriately designed germylene.

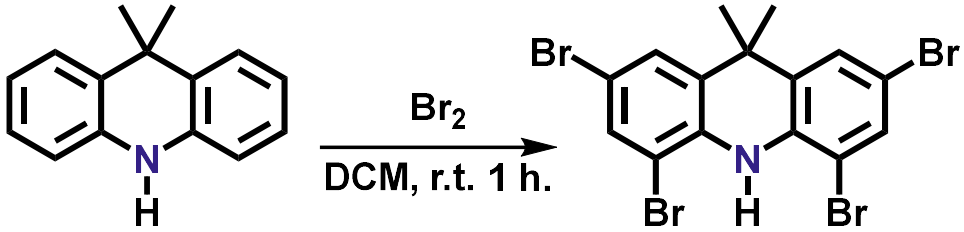
2.7 Experimental Details

All manipulations were carried out using standard Schlenk line or dry-box techniques under an atmosphere of argon. Solvents were degassed by sparging with argon and dried by passing through a column of the appropriate drying agent. NMR spectra were measured in benzene-d_6 or cyclohexane-d_{12}, which were dried over potassium metal, distilled under reduced pressure and stored under argon in a Teflon valve ampoule. NMR spectroscopy samples were prepared under argon in 5 mm Norell Select Series NMR Spectroscopy Tube fitted with J. Young Teflon valves. ^{1}H and $^{13}C\{^{1}H\}$ NMR spectra were recorded on a Bruker Avance 400 MHz spectrometer at 298 K and referenced internally to residual protio-solvent (^{1}H) or solvent ($^{13}C\{^{1}H\}$) resonances and are reported relative to tetramethylsilane ($\delta = 0$ ppm). Assignments were confirmed using two-dimensional experiments detailed in the individual methods. Chemical shifts are quoted in δ (ppm) and coupling constants in Hz. Elemental analyses were carried out by Elemental Microanalysis Ltd., Devon, UK. All reagents were used as received from commercial suppliers. Single-crystal X-ray diffraction data were collected using an Oxford Diffraction Supernova dual-source diffractometer equipped with a 135 mm Atlas CCD area detector. Crystals were selected under Paratone-N oil, mounted on Micromount loops and quench-cooled using an Oxford Cryosystems open flow N_2 cooling device. Data were collected at 150 K (unless otherwise stated) using either mirror monochromated Cu Kα radiation (λ = 1.5418 Å, Rigaku Oxford Diffraction Supernova) or Mo Kα radiation (λ = 0.71073 Å, Rigaku Oxford Diffraction Supernova). Data collected were processed using the CrysAlisPro package, including unit cell parameter refinement and inter-frame scaling (which was carried out using SCALE3 ABSPACK within CrysAlisPro). Equivalent reflections were merged and diffraction patterns processed with the CrysAlisPro suite. Structures were subsequently solved using SHELXT-2018 and refined on F2 using the SHELXL 2018 package and the graphical interface Olex2.[81,82,83,84] The .cif files are available on request and are being submitted to the Cambridge Crystallographic Data Centre, having passed CheckCIF validation.[83, 85] IR spectra were collected as either powder or crystalline samples in Nujol on a Perkin-Elmer device, depending

on whether the powder was stable enough to avoid autoignition in air. This research was undertaken with the assistance of resources and services from the National Computational Infrastructure (NCI), which is supported by the Australian Government. Computations were performed using the programs specified in each section on the NCI's Gadi supercomputer or on the Anatra computing cluster at The University of Bath.[86]

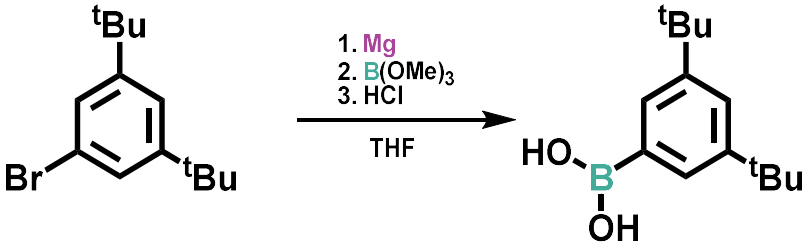
Synthesis and Characterisation of Ligand and Precursors

Preparation of $AcrBr_4$ (2,4,5,7-tetrabromo-9,9-dimethylacridane)



This is a modified procedure to that presented by Nelmes *et al.* for a 2,7-di-tert-butyl analogue.[32] 9,9-dimethylacridane (20.79 g, 99.34 mmol) was dissolved in argon-sparged chloroform (1 L) under an atmosphere of argon, forming a pale green solution. To this, bromine (21.7 mL, 67.7 g, 423 mmol, 4.26 eq.) was added dropwise over 15 minutes, with local boiling of the chloroform with each drop and rapid evolution of HBr gas, which was passed through a sodium carbonate bubbler. After addition of bromine was complete, the solution was stirred at r.t. for an additional 1 h before extraction with water (800 mL), saturated sodium thiosulfate solution (250 mL × 2) with violent shaking in the separation funnel until the brown-yellow bromine colour had fully dissipated, and water (500 mL × 2). The organic layer was then dried with magnesium sulphate and solvent removed *in vacuo* at 40 °C, yielding a pale-bone-green powder (2,4,5,7-tetrabromo-9,9-dimethylacridane, 51.08 g, 98.09 mmol, 99%) which was used without further purification. All characterisation matched that previously reported.[32]

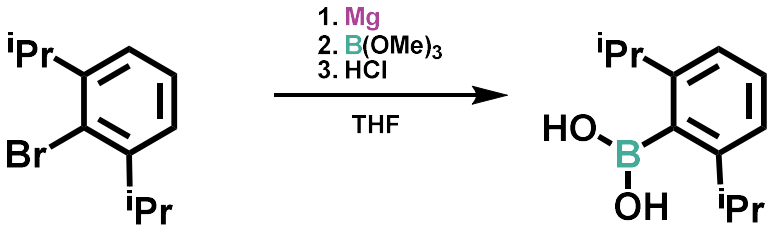
Preparation of $^{tBu2}PhB(OH)_2$ (3,5-di-tert-butylphenyl boronic acid)



3,5-di-tert-butyl-bromobenzene (28.049 g, 49.276 mmol) was dissolved in dry degassed THF (150 mL) in an anerobic dropping funnel under argon above a 1L 3-neck round bottom flask

equipped with a reflux condenser and filled with activated magnesium turnings (6.018 g, 247.55 mmol, 1 crystal I_2) in dry degassed THF (250 mL). The 3,5-di-tert-butyl-bromobenzene solution was added to the magnesium turnings at 0 °C first at *ca.* 80 mL to begin reflux and then dropwise to maintain reflux, moving to room temperature for the dropwise addition. Once all the bromide had been added, the solution was refluxed for an additional 1 h to ensure reaction completion. This freshly prepared, pale grey-brown Grignard was then filtered under anerobic conditions into a solution of trimethyl borate (17.6 mL, 16.4 g, 158 mmol, 3.2 eq.) in dry, degassed THF (50 mL) under argon, instantly precipitating a snowy white powder. Once the filtration was complete, the solution was stirred for an additional 15 min. To this, diethyl ether (300 mL) was added, and washed with HCl (1 $molL^{-1}$, 500 mL) and water (500 mL) before isolating the organic layer and removing solvent. The resultant white residue was dissolved in aqueous sodium hydroxide (5 $molL^{-1}$, 2.5 L) and filtered to remove a small amount of yellow oil, then the mother liquor was acidified to pH 1 dropwise using saturated HCl, precipitating the snowy white powder (29.068 g, approx. quantitative) which was isolated and air dried using vacuum filtration. This method produces two products in variable ratios by ^1H NMR, the expected boronic acid and its corresponding trimer, however the ratio of the two products seems unimportant to the outcome of further reactions and subsequently used as quantitative. All characterisation matched that previously reported.[33]

Preparation of $DippB(OH)_2$ (2,6-diisopropylphenyl boronic acid)

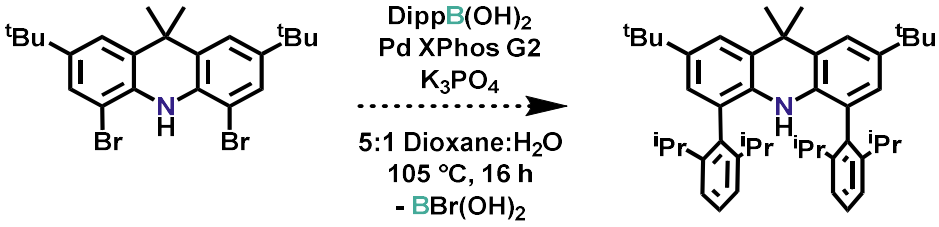


This synthesis is very similar to that of $^{tBu2}PhB(OH)_2$, however yields only the uncyclized monomer due to the increased steric bulk around the boron centre.

2,6-diisopropylbromobenzene (25.0 g, 104 mmol) was dissolved in dry degassed THF (150 mL) in an anerobic dropping funnel under argon above a 1L 3-neck round bottom flask equipped with a reflux condenser and filled with activated magnesium turnings (6.108 g, 247.55 mmol, 1 crystal I_2, 1 crystal 1,2-diiodoethane) in dry degassed THF (250 mL). The 2,6-diisopropylbromobenzene solution was then added to the magnesium turnings in an ice-bath, *ca.* 80 mL to begin reflux and then dropwise to maintain reflux, moving to room temperature for the dropwise addition. Once all the bromide had been added, the solution was refluxed for

an additional 1 h to ensure reaction completion. This freshly prepared, pale grey-brown Grignard solution was then filtered under anerobic conditions into a solution of trimethyl borate (15.0 mL, 135 mmol, 1.3 eq.) in dry, degassed THF (50 mL) under argon, instantly precipitating a snowy white powder. Once the filtration was complete, the solution was stirred for an additional 15 min.. To this, diethyl ether (300 mL) was added, and washed with HCl (1 $molL^{-1}$, 500 mL) and water (500 mL) before isolating the organic layer and removing solvent. The resultant white residue was dissolved in aqueous sodium hydroxide (5 $molL^{-1}$, 2.5 L) and filtered to remove a small amount of yellow oil, then the mother liquor was acidified to pH 1 dropwise using saturated HCl, precipitating the snowy white powder (16.7 g, 79%) which was isolated and air dried using vacuum filtration. All characterisation matched that previously reported.[87]

Attempted Preparation of [^{dipp}AcrNH] (2,7-di-tert-butyl-4,5-bis(2,6-diisopropylphenyl)-9,9-dimethylacridane)

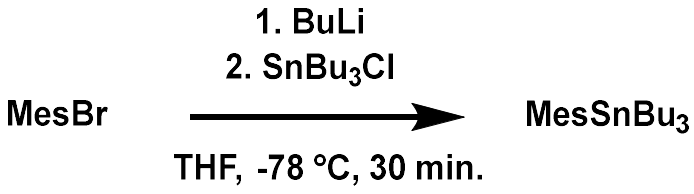


This procedure is based on a modified version of a synthesis reported by Hinz.[33]

Acr^{t}Bu$_2$Br$_2$ (109.5 mg, 0.2285 mmol), DippB(OH)$_2$ (173.6 mg, 0.8424 mmol, 3.686 eq.), potassium phosphate tribasic trihydrate (250.7 mg, 0.9412 mmol, 4.119 eq.), and palladium XPhos G2 (40.2 mg, 0.0511 mmol, 0.112 eq. w.r.t. bromines) were dissolved/suspended under anerobic conditions with argon in degassed 5:1 dioxane:water (15 mL) in a 25 mL J. Young's flask, which was then brought near reflux at 105 °C at atmospheric pressure before sealing the vessel refluxing overnight. By TLC and ^{1}H NMR spectroscopy, no reaction occurred.

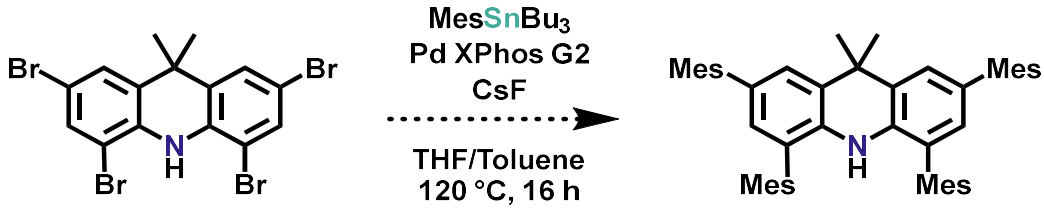
Similar attempts with other phosphines, solvents, bases, and palladium sources all gave the same result.

Preparation of MesSnBu$_3$ (mesityltri-n-butylstannane)



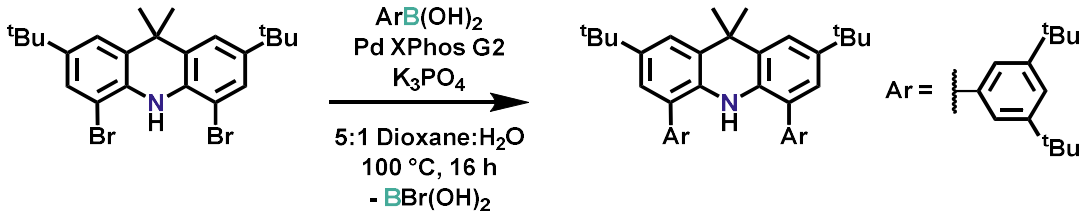
This is a modified literature procedure.[88] Mesityl bromide (0.8 mL, 1.0 g, 5.2 mmol) was added to dry THF (25 mL) under anhydrous, anaerobic conditions in a dry ice bath/acetone bath. To this, n-BuLi in hexanes (3.9 mL, 1.6 molL^{-1}, 6.2 mmol, 1.2 eq.) was added dropwise and stirred for 25 min.. To this, tri-n-butyltin chloride (1.8 mL, 6.6 mmol, 1.3 eq.) was added, stirred for 2 min. and then allowed to warm to room temperature, stirred overnight. This yielded the intended mesityl-tri-n-butyltin (1.9 g, 5.1 mmol, 98%). All characterisation matched that previously reported.[88]

Attempted Preparation of [^{Mes}AcrN'H] (2,4,5,7-tetramesityl-9,9-dimethylacridane)



$AcrBr_4$ (500.8 mg, 0.9541 mmol), caesium fluoride (1.29 g, 8.49 mmol, 8.9 eq.), $MesSnBu_3$ (1.6955 g, 4.1429 mmol, 4.34 eq.), and palladium Xphos G2 (79.4 mg, 0.101 mmol, 0.106 eq.) were dissolved in anaerobic but not anhydrous 1:1 THF:toluene (*ca*. 25 mL) and sealed in a 50 mL J. Young's flask. This was heated to 120 °C overnight, turning a familiar pale brown colour from the activated catalyst, still with white powder suspended (presumed to be CsF). An aliquot of this solution was taken, dried, and subjected to ^{1}H and ^{29}Sn NMR spectroscopy. The spectroscopy showed a large amount of unreacted $MesSnBu_3$, and no discernible acridane containing signals. Column chromatography also failed to isolate any novel components of the reaction mixture.

Preparation of [^{tBu2Ph}AcrNH] (2,7-di-tert-butyl-4,5-bis(3,5-di-tert-butylphenyl)-9,9-dimethylacridane)

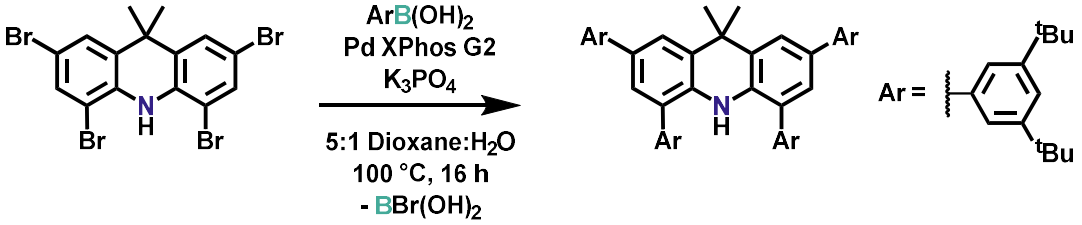


This is based on a modified version of a synthesis reported by Hinz.[33]

$Acr^{t}Bu_2Br_2$ (1.3996 g, 2.9201 mmol), 3,5-$^{t}Bu_2$-$PhB(OH)_2$ (2.1439 g, 9.1565 mmol, 3.1357 eq.), potassium phosphate tribasic trihydrate (4.4478g, 16.7041 mmol, 5.7204 eq.), and palladium XPhos G2 (456.8 mg, 0.5806 mmol, 0.09941eq. w.r.t. bromines) were dissolved/suspended

under anerobic conditions with argon in degassed 5:1 dioxane:water (*ca*. 10 mL) in a 25 mL J. Young's flask, which was then brought near reflux at 105 °C at atmospheric pressure before sealing the vessel and refluxing for 3 days. This was then extracted with toluene (50 mL) and the organic layer washed with water (50 mL), sat. NaOH solution (50 mL) and sat. brine (50 mL). The organic layer was isolated and solvent removed, yielding a pale brown powder. This powder was then washed with 3:1 acetone:water, followed by drying the resultant white powder under high vacuum to 5 × 10^{-2} mbar, yielding the target proligand (1.6686 g, 2.3944 mmol, 82%). The identity of the ligand was confirmed by ^{1}H and ^{13}C{^{1}H} NMR spectroscopy and supporting 2D experiments (COSY, HSQC, HMBC), single-crystal X-ray crystallography, and IR spectroscopy. ^{1}H NMR: (400 MHz, C_6D_6, 298 K): δ= 7.79 (s, 1H, N-H), 7.65 (d, $^{4}J_{HH}$ = 2.3 Hz, 2H,), 7.34 (accidental s, 6H, Acr(3,5-(C(CH_3)$_3$)$_2$)-C_6H_3)$_2$), 7.32 (d, $^{4}J_{HH}$ = 2.3 Hz, 2H,), 1.89 (s, 6H, C(CH_3)$_2$), 1.37 (s, 18H, Acr(2,7-C(CH_3)$_3$)$_2$), 1.17 (s, 36H, Acr(3,5-(C(CH_3)$_3$)$_2$)-C_6H_3)$_2$); ^{13}C{^{1}H} NMR: (101 MHz, C_6D_6) δ = 30.5 (Acr(3,5-(C(CH_3)$_3$)$_2$)-C_6H_3)$_2$), 30.6 (Acr(2,7-C(CH_3)$_3$)$_2$), 32.2 (C(CH_3)$_2$), 33.2 (Acr(2,7-*C*(CH_3)$_3$)$_2$), 33.7 (Acr(3,5-(*C*(CH_3)$_3$)$_2$)-C_6H_3)$_2$), 36.3 (*C*(CH_3)$_2$), 120.6 (3,5-^{t}Bu-Ar *para*), 121.4 (Acr*C*1/8), 122.5 (3,5-^{t}Bu-Ar *ortho*), 125.8 (Acr*C*3/6), 127.9 ((C(CH_3)$_2$)*C*), 131.9 (HN*C*), 138.4 (Acr*C*2/7), 139.6 (3,5-^{t}Bu-Ar *meta*), 142.6 (Acr*C*4/5), 151.3 (3,5-^{t}Bu-Ar*C*1).

Preparation of [^{tBu2Ph}AcrN′H] (2,4,5,7-tetrakis(3,5-di-tert-butylphenyl)-9,9-dimethylacridane)

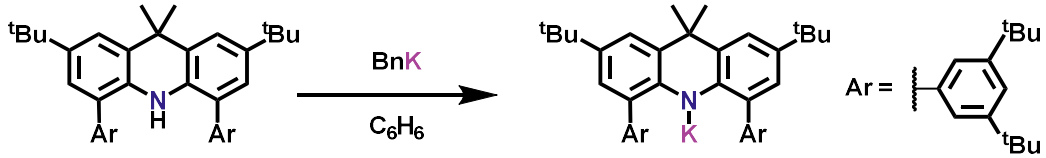


This is based on a modified version of a synthesis reported by Hinz and is very similar to the synthesis of the bis-aryl form above ([^{tBu2Ph}AcrNH]) with a different purification method.[33]

AcrBr$_4$ (9.4226 g, 17.952 mmol), 3,5-^{t}Bu$_2$-PhB(OH)$_2$/(3,5-^{t}Bu$_2$-PhBO)$_3$ boronic acid/trimer mixture (equiv. 24.4 g boronic acid, 104 mmol, 5.80 eq.), potassium phosphate tribasic trihydrate (8.3434 g, 31.334 mmol, 1.7454 eq.), and palladium XPhos G2 (1.0232 g, 1.300 mmol, 0.072 eq.) were dissolved/suspended under anerobic conditions with argon in degassed 5:1 dioxane:water (180 mL) in a 350 mL J. Young's flask, which was then brought near reflux at 105 °C at atmospheric pressure before sealing the vessel and refluxing for 3 days. As the solution was heated it turned the expected brown colour of the active catalyst with white

suspension, and over time the reaction precipitated more precipitate which was very fine and a pale grey colour as well as a significant amount of yellow oil. Once complete, the reaction was cooled to room temperature and extracted with diethyl ether (800 mL) and water (1 L) until all the solids were dissolved except the black palladium residue, which was separated with the denser aqueous layer. The organic layer was then extract with saturated brine (500 mL) and dried with a mixture of magnesium sulfate and silica (to remove any remain palladium) before removing solvent *in vacuo* at 40 °C revealing a pale-yellow powder. This powder was subsequently suspended in boiling methanol (*ca.* 500 mL) and sonicated for 6 h before filtering, isolating the solid, and repeating the process 3 times until the methanol ran clear and the powder was completely white, followed by drying the powder under high vacuum to 5×10^{-2} mbar, yielding the target ligand (15.561 g, 16.166 mmol, 90%). The identity of the ligand was confirmed by ^{1}H and ^{13}C{^{1}H} NMR spectroscopy and supporting 2D experiments (NOESY, HSQC, HMBC), single-crystal x-ray crystallography, IR spectroscopy, and high-resolution mass spectrometry. ^{1}H NMR: (400 MHz, C_6D_6, 298 K) δ = 8.05 (s, 1H, N*H*), 7.94 (d, $^{4}J_{HH}$ = 2.0 Hz, 2H, 1,8-Acr*H*), 7.71 (d, $^{4}J_{HH}$ = 1.8 Hz, 4H, 2,7-(*o*-Ar*H*)-Acr), 7.67 (d, $^{4}J_{HH}$ = 2.0 Hz, 2H, 3,6-Acr*H*), 7.56 (t, $^{4}J_{HH}$ = 1.8 Hz, 2H, 2,7-(*p*-Ar*H*)-Acr), 7.44 (d, $^{4}J_{HH}$ = 1.8 Hz, 4H, 4,5-(*o*-Ar*H*)-Acr), 7.38 (t, $^{4}J_{HH}$ = 1.8 Hz, 2H, 4,5-(*p*-Ar*H*)-Acr), 1.90 (s, 6H, $Ar_2C(CH_3)_3$), 1.34 (s, 36H, 2,7-(*m*-Ar(C(CH_3)$_3$)$_2$-Acr), 1.15 (s, 36H, 4,5-(*m*-Ar(C(CH_3)$_3$)$_2$-Acr); ^{13}C{^{1}H} NMR (101 MHz, C_6D_6) δ = 151.58 (Ar*C*), 151.44 (Ar*C*), 142.37 (Ar*C*), 138.94 (Ar*C*), 136.08 (Ar*C*), 134.49 (Ar*C*), 130.02 (Ar*C*), 128.76 (Ar*C*), 128.59 (Ar*C*), 123.71 (Ar*C*), 122.10 (Ar*C*), 117.10 (Ar*C*), 37.43 ($Ar_2(CH_3)_2C$), 35.05 ($(CH_3)_3C$), 34.92 ($(CH_3)_3C'$), 33.27 ($Ar_2(CH_3)_2C$), 31.71 ($(CH_3)_3C$), 31.66 ($(CH_3)_3C'$). IR: 3415 (s, w, NH), 3070 (m, w, CH aryl), 3090 (m, w, CH aryl), 3035 (m, m, CH aryl), 2903 (s, m, CH alkyl), 2865 (s, m, CH alkyl), 1593, 1480, 1477, 1245, 1091, 878, 714, 468.

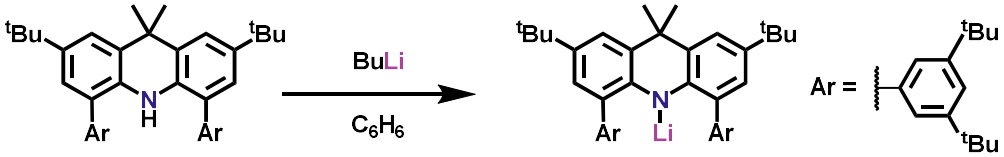
Preparation of [^{tBu2Ph}AcrNK] (potassium 2,7-di-tert-butyl-4,5-bis(3,5-di-tert-butylphenyl)-9,9-dimethyl-9H-acridin-10-ide)



[^{tBu2Ph}AcrNH] (504.3 mg, 0.7223 mmol) was dissolved in anhydrous, anaerobic benzene (*ca.* 60 mL) and benzyl potassium (232.0 mg, 1.781 mmol, 2.466 eq.) was suspended in the same solution at r.t.. This formed a brilliant yellow solution which was stirred for 2 h. before

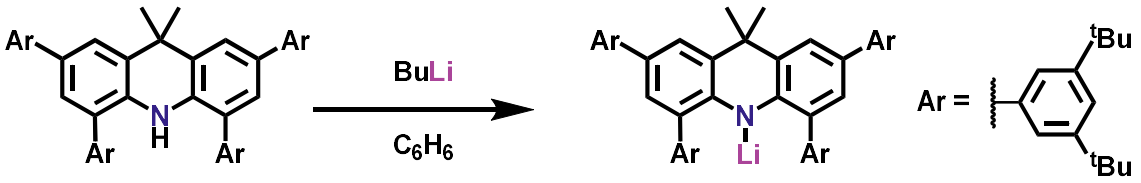
filtration. The vibrant orange mother liquor was concentrated to incipient crystallisation, heated to 50 °C, and allowed to cool slowly overnight, yielding bright orange crystals of the intended product (453.3 mg, 0.6163 mmol, 85%). The product was characterised *via* ^{1}H spectroscopy and single crystal X-ray diffraction. ^{1}H NMR: (400 MHz, C_6D_6, 298 K) ^{1}H NMR: (400 MHz, C_6D_6, 298 K) δ = 7.72 (s, 2H, Acr*H*1/8), 7.43 (s, 4H, 4,5-(*o*-Ar*H*)-Acr), 7.12 (s, 2H, 4,5-(*p*-Ar*H*)-Acr), 7.11 (s, 2H, Acr*H*3/6), 2.10 (s, 6H, C(C*H*$_3$)$_2$), 1.50 (s, 18H, 2,7-C(C*H*$_3$)$_3$-Acr), 1.07 (s, 46H, 4,5-(3,5-(C(C*H*$_3$)$_3$)$_2$-Ar)-Acr). Resolution insufficient to resolve $^{4}J_{HH}$ couplings.

Preparation of [^{tBu2Ph}AcrNLi] (lithium 2,7-di-tert-butyl-4,5-biskis(3,5-di-tert-butylphenyl)-9,9-dimethyl-9H-acridin-10-ide)



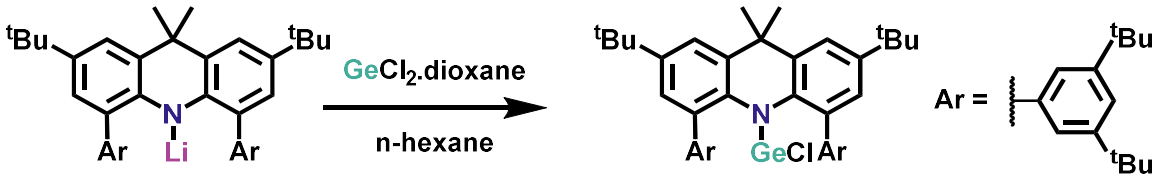
[^{tBu2Ph}AcrNH] (506.3 mg, 0.7252 mmol) was dissolved in anhydrous anaerobic benzene (4.5 mL), then n-butyllithium (1.81 mL, 1.6 molL^{-1}/hexanes, 2.9 mmol, 4.00 eq.) was added and heated to 80 °C with an atmospheric vent for 1 h. and then sealed for a further 2 h. to ensure completion. This caused a red powder to precipitate from solution, presumed to be phenyl lithium from reaction of the excess n-BuLi with the solvent. A hot filtration was performed, and the mother liquor was slowly cooled to room temperature in a large oil bath overnight, resulting in large bright orange crystals, which were confirmed to be the intended product [^{tBu2Ph}AcrNLi].3C_6H_6 as the benzene adduct (258.6 mg 0.3673 mmol, 51%) by ^{1}H, ^{13}C{^{1}H} NMR spectroscopy, and single-crystal X-ray diffraction. ^{1}H NMR: (400 MHz, C_6D_6, 298 K) δ = 7.73 (d, 2H, $^{4}J_{HH}$ = 2.5 Hz, Acr*H*1/8), 7.38 (d, 4H, $^{4}J_{HH}$ = 1.9 Hz, 4,5-(*o*-Ar*H*)-Acr), 7.20 (t, 2H, $^{4}J_{HH}$ = 1.9 Hz, 4,5-(*p*-Ar*H*)-Acr), 7.09 (d, 2H, $^{4}J_{HH}$ = 2.5 Hz, Acr*H*3/6), 2.13 (s, 6H, C(C*H*$_3$)$_2$), 1.46 (s, 18H, Acr-C(C*H*$_3$)$_3$), 1.00 (s, 36H, 4,5-Ar(C(C*H*$_3$)$_2$)-Acr); ^{13}C{^{1}H} NMR (101 MHz, C_6D_6) δ = 154.2 (4,5-(*m*-Ar*C*)-Acr), 147.5 (4,5-Acr*C*), 146.9 (LiN*C*), 136.8 (2,7-Acr*C*), 129.8 ((C(CH$_3$)$_2$)*C*), 128.6 (4,5-(1-Ar*C*)-Acr), 125.5 (3,6-Acr*C*), 124.1 (1,8-Acr*C*), 123.5 (4,5-(*o*-Ar*C*)-Acr), 121.1 (4,5-(*p*-Ar*C*)-Acr), 37.9 (*C*(CH$_3$)$_2$), 35.8 (C(*C*H$_3$)$_2$), 35.0 (4,5-(3,5-(*C*(CH$_3$)$_3$)$_2$-Acr), 34.2 (2,7-(*C*(CH$_3$))$_2$-Acr), 32.1 (2,7-(C(*C*H$_3$))$_2$-Acr), 31.4 (4,5-(3,5-(C(*C*H$_3$)$_3$)$_2$-Acr).

Preparation of [^{tBu2Ph}AcrN′Li] (lithium 2,4,5,7-tetrakis(3,5-di-tert-butylphenyl)-9,9-dimethyl-9H-acridin-10-ide)



[^{tBu2Ph}AcrN′H] (478.2 mg, 0.4968 mmol) was dissolved in minimal hexane (~5 mL), forming an almost colourless cream solution. To this, TMEDA (0.7765 gmL^{-1}, 6 µL, 5 mg, 0.04 mmol, 0.1 eq.) and then n-BuLi in hexane (1.6 $molL^{-1}$, 0.42 mL, 0.67 mmol, 1.4 eq.) was added at 0 °C, which rapidly turned the solution a bright orange colour and precipitated a canary yellow powder. *It is salient to note that only catalytic TMEDA is necessary and only at r.t., it is difficult to remove from the product and interferes with subsequent transmetalation to germanium. The potassium salt is for this reason preferred.* The resulting solution was allowed to stir at room temperature overnight, then cooled again to 0 °C and filtered, collecting the filtrate. The yellow powder [^{tBu2Ph}AcrN′Li] was dried to 5×10^{-2} mbar (365.7 mg, 0.3776 mmol, 76%). The identity of the product was confirmed by ^{1}H and $^{13}C\{^{1}H\}$ NMR spectroscopy and supporting 2D experiments (HSQC, HMBC, COSY), single-crystal X-ray crystallography, IR spectroscopy, and elemental analysis. ^{1}H NMR: (400 MHz, C_6D_6, 298 K) δ = 8.08 (d, $^{4}J_{HH}$ = 2.3 Hz, 2H, 1,8-Acr*H*), 7.79 (d, $^{4}J_{HH}$ = 1.8 Hz, 4H, 2,7-(*o*-Ar*H*)-Acr), 7.51 (d, $^{4}J_{HH}$ = 2.3 Hz, 2H, 3,6-Acr*H*), 7.50 (t, $^{4}J_{HH}$ = 1.8 Hz, 2H, 2,7-(*p*-Ar*H*)-Acr), 7.44 (d, $^{4}J_{HH}$ = 1.9 Hz, 4H, 4,5-(*o*-Ar*H*)-Acr), 7.22 (t, $^{4}J_{HH}$ = 1.9 Hz, 2H, 4,5-(*p*-Ar*H*)-Acr), 2.16 (s, 6H, $Ar_2C(CH_3)_3$), 1.36 (s, 36H, 2,7-(*m*-$Ar(C(CH_3)_3)_2$-Acr), 0.99 (s, 36H, 4,5-(*m*-$Ar(C(CH_3)_3)_2$-Acr); $^{13}C\{^{1}H\}$ NMR (101 MHz, C_6D_6) δ = 154.50 (Ar*C*), 151.06 (Ar*C*), 148.24 (Ar*C*), 146.63 (Ar*C*), 143.18 (Ar*C*), 131.08 (Ar*C*), 130.57 (Ar*C*), 130.02 (Ar*C*), 128.59 (Ar*C*), 128.32 (Ar*C*), 128.31 (Ar*C*), 128.30 (Ar*C*), 128.08 (Ar*C*), 128.07 (Ar*C*), 128.06 (Ar*C*), 128.05 (Ar*C*), 127.84 (Ar*C*), 127.82 (Ar*C*), 126.60 (Ar*C*), 123.41 (Ar*C*), 121.67 (Ar*C*), 121.46 (Ar*C*), 119.70 (Ar*C*), 37.63 ($Ar_2(CH_3)_2C$), 35.44 ($(CH_3)_3C$), 35.05 ($(CH_3)_3C'$), 35.02 ($Ar_2(CH_3)_2C$), 31.80 ($(CH_3)_3C$), 31.39 ($(CH_3)_3C'$); IR: 3070, 2960, 2865, 1592, 1451, 1478, 1460, 1362, 1246, 870, 673, 501. anal. calc. for $C_{71}H_{94}LiN.C_6H_6$: C: 88.37%, H: 9.63%, N: 1.34% found: C: 87.21%, H: 10.34%, N: 1.03%.

Preparation of [^{tBu2Ph}AcrNGeCl] (10-(chloro-λ^2-germyl)-2,7-di-tert-butyl-4,5-bis(3,5-di-tert-butylphenyl)-9,9-dimethyl-9,10-dihydroacridinide)

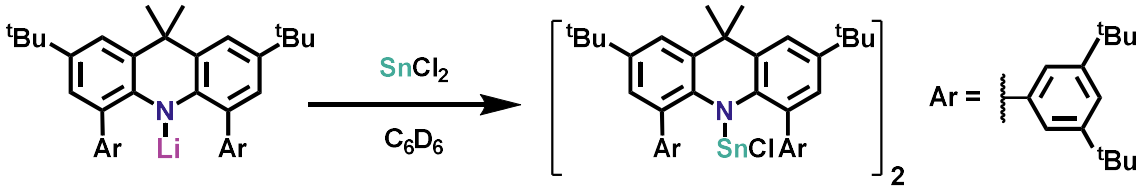


[^{tBu2Ph}AcrNLi.3C_6H_6] (103.2 mg, 0.1100 mmol) and germanium(II) chloride dioxane adduct (31.1 mg, 0.134 mmol, 1.22 eq.) were dissolved in toluene (*ca*. 2.5 mL) in a 10 mL Schlenk flask, instantly fading from bright orange of the lithium salt to a pale yellow and forming a precipitate, which was then filtered after 30 minutes of stirring, and the mother liquor isolated and solvent removed. The resulting yellow powder was then recrystallised from hexane (*ca.* 5 mL), resulting in yellow needles of the intended product (88.6 mg, 0.110 mmol, 99%), which was characterised by ^{1}H, ^{13}C{^{1}H} NMR spectroscopy, and single-crystal X-ray diffraction; notably the broadness of the *tert*-butyl groups on the flanking arenes were inequivalent (although broad) from the now bent germanium-chloride centre in the ligand, reflected in the solid-state structure. ^{1}H NMR: (400 MHz, C_6D_6, 298 K) δ = 7.81 (s (broad), 2H, 4,5-(*o*-ArH_b)-Acr), 7.70 (d, 2H, $^{4}J_{HH}$ = 2.4 Hz, 1,8-Acr*C*), 7.48 (t, 2H, $^{4}J_{HH}$ = 1.9 Hz, 4,5-(*p*-Ar*H*)-Acr), 7.37 (s (broad), 2H, 4,5-(*o*-ArH_a)-Acr), 7.15 (d, 2H, $^{4}J_{HH}$ = 2.4 Hz, 3,6-Acr*C*), 2.04 (s (broad), 3H, C(CH_{3a})(CH_{3b})), 1.87 (C(CH_{3a})(CH_{3b})), 1.32 (s, 18H, 2,7-(C(CH_3)$_3$)$_2$-Acr), 1.23 (s, 18H, 4,5-(3-(C(CH_3)$_{3a}$)-5-(C(CH_3)$_{3b}$)-Ar)-Acr), 1.17 (s, 18H, 4-(3-(C(CH_3)$_{3a}$)-5-(C(CH_3)$_{3b}$)-Ar)-Acr); ^{13}C{^{1}H} NMR (101 MHz, C_6D_6) δ = 151.3 (Ar*C*), 143.4 (Ar*C*), 142.5 (Ar*C*), 132.8 (Ar*C*), 128.8 (Ar*C*), 128.4 (Ar*C*), 127.1 (Ar*C*), 126.4 (Ar*C*), 126.1 (Ar*C*), 125.3 (Ar*C*), 121.5 (Ar*C*), 37.5 (2,7-(C(*C*H$_3$)$_3$)$_2$-Acr), 35.6 (C(*C*H$_3$)$_b$(CH$_3$)$_a$), 35.4 (C(CH$_3$)$_b$(*C*H$_3$)$_a$), 31.8 (2,7-(*C*(CH$_3$)$_3$)$_2$-Acr), 31.7 (*C*(CH$_3$)$_b$(CH$_3$)$_a$), 31.5 (4-(3-(C(*C*H$_3$)$_{3a}$)-5-(C(CH$_3$)$_{3b}$)-Ar)-Acr), 31.1 (4-(3-(C(CH$_3$)$_{3a}$)-5-(C(*C*H$_3$)$_{3b}$)-Ar)-Acr).

There is a suspicion that side "a" is the chloride side as side b the resonances have more similar shifts to the protonated ligand (which has the notable absence of chloride), but in the absence of heteronuclear NOE experiments, notably ^{1}H-^{35}Cl HOESY, we are unable to confirm this (although it is my understanding such an experiment has only ever been performed in the solid state).[89] This was quite convenient in that the less shifted resonances also formed the same spin systems by 2D experiments, demonstrating no inconsistencies in the assignment. Two fewer quaternary aromatic carbons are observed than expected, likely due to the broadness combined with their low intensity, tentatively suspected as being the 2,7-(*m*-Ar*C*)-Acr carbons (one on

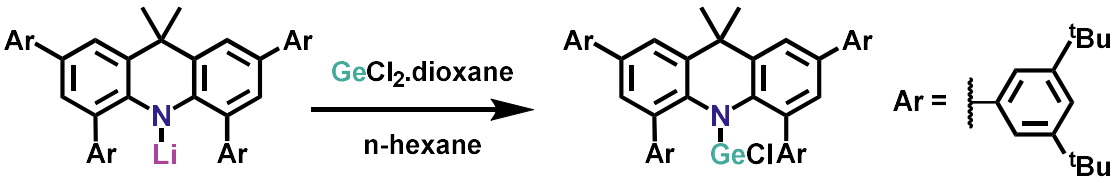
the chloride side, one on the vacant side). Similarly, the quaternary tert-butyl carbons on the 3,5-di-tert-butyl groups were also not observed.

Preparation of [^{tBu2Ph}AcrNSnCl]$_2$ (10-(chloro-stannyl)-2,7-di-tert-butyl-4,5-bis(3,5-di-tert-butylphenyl)-9,9-dimethyl-9,10-dihydroacridinide) dimer



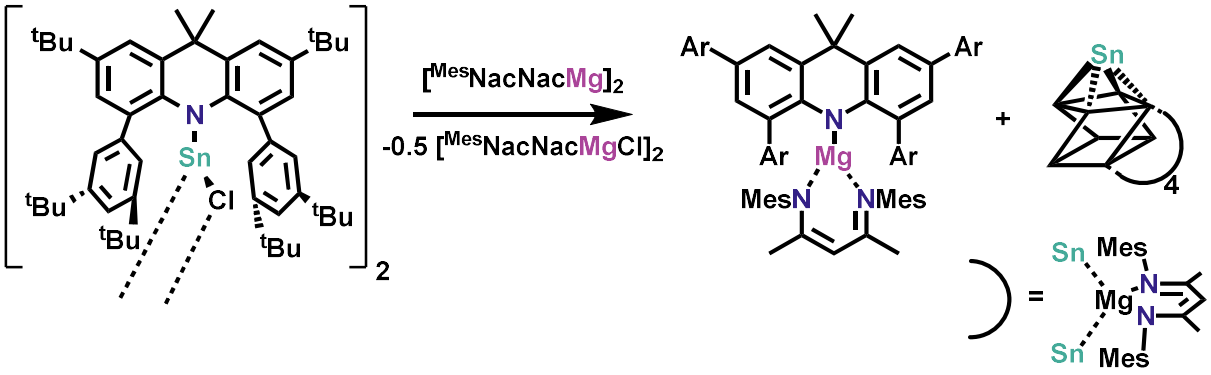
[^{tBu2Ph}AcrNLi.3C$_6$H$_6$] (52.1 mg, 0.0555 mmol) and anhydrous SnCl$_2$ (16.8 mg, 0.0886 mmol, 1.60 eq.) were added to a J. Young's NMR tube under anhydrous, anaerobic conditions and dissolved in C$_6$D$_6$ (*ca.* 0.4 mL). This caused no reaction evident by ^{1}H NMR or any visual change from the bright orange starting material. Heating produced no reaction, however prolonged sonication (overnight) caused the solution to fade to a pale-yellow colour, which proved to have quantitatively produced the intended product after characterisation by ^{1}H NMR spectroscopy. The solution was then filtered through a Teflon frit and the mother liquor concentrated, allowing for single-crystal X-ray diffraction of the resultant yellow needles, showing the species to be dimeric in the solid state. ^{1}H NMR: (400 MHz, C$_6$D$_6$, 298 K) δ = 7.76 (d, 2H, $^4J_{HH}$ = 1.7, 1.7 Hz, 4,5-(3,5-(C(CH$_3$)$_3$)$_2$-*o*-Ph*H*HH) 7.72 (d, 2H, $^4J_{HH}$ = 2.4 Hz, 1,8-Acr*H*), 7.48 (dd, 2H, $^4J_{HH}$ = 1.7, 1.7 Hz, 4,5-(3,5-(C(CH$_3$)$_3$)$_2$-*p*-PhH*H*H), 7.39 (dd, 2H, $^4J_{HH}$ = 1.7, 1.7 Hz, 4,5-(3,5-(C(CH$_3$)$_3$)$_2$-*o*-PhHH*H*), 7.10 (d, 2H, $^4J_{HH}$ = 2.4 Hz, 3,6-Acr*H*), 2.08 (s, 3H, C(C*H*$_3$)(CH$_3$)), 1.83 (s, 3H, C(CH$_3$)(C*H*$_3$)), 1.35 (s, 18H, 2,7-C(C*H*$_3$)$_2$-Acr), 1.23 (s, 18H, 4,5-(3-C(C*H*$_3$)$_3$-5- C(CH$_3$)$_3$-PhH$_3$), 1.13 (s, 18H, 3-C(CH$_3$)$_3$-5- C(C*H*$_3$)$_3$-PhH$_3$).

Preparation of [^{tBu2Ph}AcrN′GeCl] (10-(chloro-λ^2-germyl)-2,4,5,7-tetrakis(3,5-di-tert-butylphenyl)-9,9-dimethyl-9,10-dihydroacridinide)



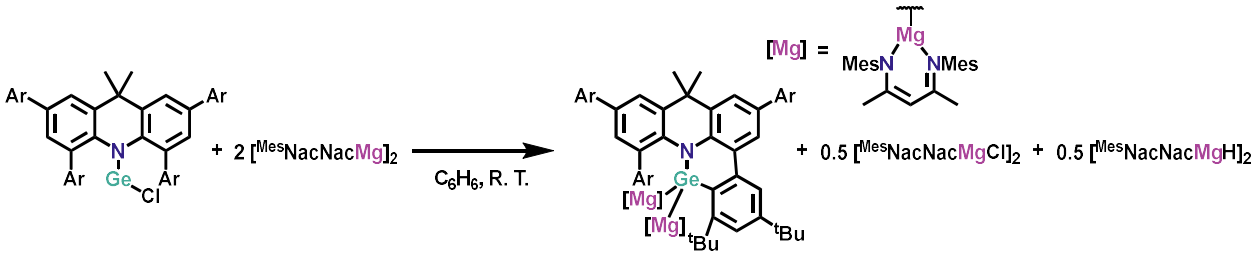
[^{tBu2Ph}AcrN′Li] crystals (470.0 mg, 0.4853 mmol) and germanium chloride dioxane adduct (201.3 mg, 0.8690 mmol, 1.791 eq.) were dissolved in anhydrous benzene (*ca*. 10 mL) under an inert atmosphere, turning rapidly from the bright orange solution of the lithium salt to a pale yellow. After stirring at room temperature for 2 h., the solvent was removed and the mixture dried to 5×10^{-2} mBar. The mixture was then dissolved/suspended in hexane (*ca*. 20 mL), and the excess germanium chloride filtered off. The resultant yellow solution was then concentrated and crystallised to form pale yellow crystals (233.7 mg, 0.2184 mmol, 45%) of [^{tBu2Ph}AcrN′GeCl]. A persistent contamination of *ca*. 10% protonated ligand always occurred, and cannot easily be separated from the product. This is presumably resultant from a minor HCl contaminant in the $GeCl_2$.dioxane. The identity of the product was confirmed by ^{1}H and $^{13}C\{^1H\}$ NMR spectroscopy and supporting 2D experiments (HSQC, HMBC, COSY), single-crystal X-ray crystallography, IR spectroscopy, and elemental analysis. ^{1}H NMR: (400 MHz, C_6D_6, 298 K) δ = 8.01 (d, $^4J_{HH}$ = 2.2 Hz, 2H, 1,8-Acr*H*), 7.90 (s (broad), 2H, 4,5-(2-Ar*H*)-Acr), 7.71 (d, $^4J_{HH}$ = 1.8 Hz, 4H, 2,7-(*o*-Ar*H*)-Acr), 7.58 (d, $^4J_{HH}$ = 2.2 Hz, 2H, 3,6-Acr*H*), 7.54 (t, $^4J_{HH}$ = 1.8 Hz, 2H ,2,7-(*p*-Ar*H*)-Acr), 7.47 (t, $^4J_{HH}$ = 1.9 Hz, 2H, 4,5-(*p*-Ar*H*)-Acr), 7.43 (s (broad), 2H, 4,5-(6-Ar*H*)-Acr), 2.03 (s (broad), 3H, $Ar_2C(CH_3)(CH_3')$), 1.87 (s (broad), 3H, $Ar_2C(CH_3)(CH_3')$), 1.31 (s, 36H, 2,7-(*m*-Ar(C(CH_3)$_3$)$_2$-Acr), 1.24 (s (broad), 18H, 4,5-(3-ArC(CH_3)$_3$-Acr), 1.14 (s (broad), 18H, 4,5-(5-ArC(CH_3)$_3$-Acr); $^{13}C\{^1H\}$ NMR (101 MHz, C_6D_6) δ = 151.0 (Ar*C*), 144.7 (Ar*C*), 141.4(Ar*C*), 135.1 (Ar*C*), 133.5 (Ar*C*), 129.3 (Ar*C*), 126.1 (Ar*C*), 123.7 (Ar*C*), 123.3 (Ar*C*), 121.7 (Ar*C*), 120.4 (Ar*C*), 34.9 (C(CH$_3$)$_b$(CH$_3$)$_a$), 34.7 (C(CH$_3$)$_b$(CH$_3$)$_a$), 34.5 (2,7-(3,5-Ar-(C(CH$_3$)$_3$)$_2$)$_2$-Acr), 31.6 (C(CH$_3$)$_b$(CH$_3$)$_a$), 31.3 (2,7-(3,5-Ar-(C(CH$_3$)$_3$)$_2$)$_2$-Acr), 31.3 (4-(3-(C(CH$_3$)$_{3a}$)-5-(C(CH$_3$)$_{3b}$)-Ar)-Acr), 31.2 (4-(3-(C(CH$_3$)$_{3a}$)-5-(C(CH$_3$)$_{3b}$)-Ar)-Acr), 30.6 (2,7-3-(C(CH$_3$)$_{3a}$)-5-(C(CH$_3$)$_{3b}$)-Ar-Acr). anal. calc. for $C_{71}H_{94}ClGeN$: C: 79.73%, H: 8.86%, N: 1.31%; found: C: 78.12%, H: 8.89%, N: 0.53%.

Reduction of [^{tBu2Ph}AcrN′SnCl] (10-(chloro-stannyl)-2,4,5,7-tetrakis(3,5-di-tert-butylphenyl)-9,9-dimethyl-9,10-dihydroacridinide) with ^{Mes}NacNac Magnesium(I) Dimer



[^{Mes}NacNacMg]$_2$ was prepared using a method by Jones *et al.*.[90] [^{tBu2Ph}AcrNLi] (77.2 mg, 0.0797 mmol), finely ground anhydrous $SnCl_2$, and C_6D_6 were added to a J. Young's NMR tube and sonicated for 3 hours, replicating the results from the synthesis of [^{tBu2Ph}AcrNSnCl]$_2$, then filtered into another J. Young's NMR tube through a Teflon frit. To the mother liquor, [^{Mes}NacNacMg]$_2$ (62.4 mg, 0.0872 mmol, 1.09 eq.) was added, instantly forming a black-blood-red solution. This solution was subjected to ^{1}H NMR spectroscopy, showing the spectrum presented below. In particular, the aromatic region ~>7 ppm shows only two things: protonated ligand signals and δ = 7.90 (s (broad), *ca*. 4H), 7.82 (d, $^4J_{HH}$ = 1.8 Hz, 4H), 7.59 (t, $^4J_{HH}$ = 1.8 Hz, 2H), 7.23 (t, $^4J_{HH}$ = 1.8 Hz, 2H), which matches a novel ^{tBu2Ph}AcrN′- containing product. Additionally, δ = 4.78 (s, 1H) matches the 4-position proton on a NacNac-containing species, and expected corresponding singlets in the (rather intractable) alkyl region. No other meaningful NMR data could be inferred from the spectrum. The solution was filtered into another J. Young's NMR tube through a Teflon frit and concentrated to crystallise blood red blocks. Single-crystal X-ray diffraction of these crystals showed mono-capped square antiprisms of tin ligated by four [^{Mes}NacNacMg]$^+$ units, one on every second equatorial edge. Unfortunately, there is no recorded yield for this product, however, ^{1}H NMR indicates *ca*. >70%.

Reduction of ^{t}AcrN′GeCl with ^{Mes}NacNac Magnesium(I) Dimer



[^{Mes}NacNacMg]$_2$ was prepared using a method by Bonyhady *et al.*[90] The magnesium dimer (195.3 mg, 0.2729 mmol, 4.79 eq.) was dissolved in benzene (*ca.* 25 mL), and [^{tBu2Ph}AcrN′GeCl] (60.9 mg, 0.0569 mmol, 1.00 eq.) was dissolved in a separate portion of benzene. The germanium complex solution was added dropwise to the [^{Mes}NacNacMg]$_2$, turning a bright, pigeon blood red, stirred for 6 hours. The solvent was then removed *in vacuo* and the precipitate suspended in hot hexane (*ca.* 20 mL, *ca.* 50 °C), and solvent collected *via* cannula filtration. The red solution was concentrated to incipient crystallisation, then left overnight to remove the [NacNacMgCl]$_2$ byproduct not fully removed by the filtration (as it is quite insoluble in hexane), then concentration of the mother liquor yields crystals of excess magnesium(I) dimer (again not entirely removed by the hexane filtration, but more soluble than the chloride and seemingly unable to crystallise under the same conditions), then concentration of the mother liquor a third time yields crystals of proligand (very soluble in hexane, but forms excellent, colourless hexagonal crystals from benzene), and final concentration leads to the formation of yellow needles. These needles are very soluble in tiny fractions of any hydrocarbon solvent and only form almost at dryness, despite the three molecules of lattice benzene in the sold state structure. Repeated heated and cooling of the red-yellow semi-solid is necessary to grow crystals appropriate for single-crystal X-ray diffraction. ($C_{117}H_{151}GeMg_2N_5.3C_6H_6$; Orthorhombic Pbca; Cell: 28.3023(9) Å, 23.0169(6) Å, 37.9836(14) Å, 90°, 90°, 90°; volume: 24743.7(14) Å^3; reflections (Unique/I>2σI): 21587/12913; Parameters: 1440; residual max/min: 0.781/-0.817; Goodness of Fit: 1.087; R1 (all/I>2σI) 0.1306/0.1886; wR2 (all/I>2σI): 0.2872/0.3132, Temperature 150.01(10) K; Radiation: Cu Kα, 1.54184 Å). The product was characterised by ^{1}H NMR spectroscopy however the ^{13}C{^{1}H} was indiscernible from noise. ^{1}H NMR: (400 MHz, C_6D_{12}, 298 K) δ = 7.39 (t, $^{4}J_{HH}$ = 1.7 Hz, 1H, Ar*H*), 7.37 (br., 2H, Ar*H*), 7.35 (t, $^{4}J_{HH}$ = 1.7 Hz, 1H, Ar*H*), 7.29 (br., 2H, Ar*H*), 7.28 (d, $^{4}J_{HH}$ = 1.7 Hz, 2H, Ar*H*), 7.23 (d, $^{4}J_{HH}$ = 1.7 Hz, 1H, Ar*H*), 7.14 (d, $^{4}J_{HH}$ = 1.7 Hz, 1H, Ar*H*), 7.00 (d, $^{4}J_{HH}$ = 1.7 Hz, 1H, Ar*H*), 6.88 (br., 1H, Ar*H*), 6.84 (t, $^{4}J_{HH}$ = 1.7 Hz, 1H, Ar*H*), 6.76 (br. 2H, Ar*H*), 6.55 (br. 1H) , Ar*H*, 6.41 (br. 1H, Ar*H*), 6.34 (d, $^{4}J_{HH}$ =

1.7 Hz, 1H, Ar*H*), 6.29 (s, 2H, Ar*H*), 6.19 (d $^4J_{HH}$ = 1.7 Hz, 1H, Ar*H*), 6.07 (br., 1H, Ar*H*), 5.87 (t, $^4J_{HH}$ = 1.6 Hz, 1H, Ar*H*), 4.68 (s, 1H, NCC*H*), 4.59 (s, 1H, NCC*H*), 2.61 (s, 3H, CH_3), 2.30 (s, 3H, CH_3), 2.17 (s, 3H, CH_3), 2.12 (s, 3H, CH_3), 2.07 (s, 3H, CH_3), 2.01 (s, 3H, CH_3), 2.00 (s, 3H, CH_3), 1.79 (s, 3H, CH_3), 1.69 (s, 3H, CH_3), 1.60 (s, 3H, CH_3), 1.51 (s, 3H, CH_3), 1.45 (s, 18H, C(CH_3)$_3$), 1.36 (s, 18H, C(CH_3)$_3$), 1.33 (s, 18H, C(CH_3)$_3$), 1.16 (s, 3H, CH_3), 1.13 (s, 3H, CH_3), 1.11 (s, 3H, CH_3), 1.08 (s, 3H, CH_3), 0.69 (s, 9H, C(CH_3)$_3$), 0.65 s, 6H, CH_3), 0.52 (s, 3H, CH_3), 0.49 (s, 9H, C(CH_3)$_3$).

2.8 References

[1] Haustein, C. H., *The Gale Encyclopedia of Science*, **2014**, "Oxidation-reduction reaction", link.gale.com/apps/doc/CV2644031629/SCIC?
[2] Parr, R. G.; Pearson, R. G., *J. Am. Chem. Soc.*, **1983**, *105*, 7512
[3] Taube, H., *Science*, **1984**, *226*, 1028
[4] Galvani, L., *De Viribus Electricitatis In Motu Musculari*, **1791**, *Ex Typographia Instituti Scientiarium, Bononiae*, Bologna.
[5] Volta, A., *Proc. R. Soc. Lond.*, **1800**, *90*, 403
[6] Ngoy, K. R.; Lukong, V. T.; Yoro, K. O.; Makambo, J. B.; Chukwuati, N. C.; Ibegbulam, C.; Eterigho-Ikelegbe, O.; Ukoba, K.; Jen, T.-C., *Renewable and Sustainable Energy Reviews*, **2025**, *223*, 115971
[7] Expert Market Research Claight Report, **2026,** expertmarketresearch.com.au/reports/australia-lithium-market
[8] Lodders, K.; Hazen, R. M., *American Mineralogist*, **2026**, *111*, *5*, 701
[9] Sheridan, A., *Bronze Age Review*, **2008**, *1*, 57
[10] Collins, J., *The European Iron Age*, **1984**, B. T. Batsford, London
[11] No primary publication by Brand exists, but Robert Boyle discusses the discover in detail with allusion to Brand in 1680: Boyle, R., *The Aerial Noctiluca: Or Some New Phœnomena, and a Process of A Factitious Self-Shining Substance.*, **1680**, Thomas Snowden, London
[12] a) Davy, H., *Philos. Trans. R. Soc. Lond.*, **1808**, *98*, 333; b) James, F. A. J. L., *Ambix*, **2025**, *72*, *2*, 143
[13] Berzelius, J. J., *Afhandlingar i Fysik, Kemi och Mineralogi*, **1818**, 6, 42; amongst other less clear examples
[14] Mendeleev, D. I., *Zhurnal russkogo khimicheskogo obshchestva*, **1869**, *1*, 60. *N. b.* This is often erroneously cited as volume 18 c, page 22, seemingly due to mistaking the pre-reform Russian filing numbers of a widely available digital copy for the journal sequencing numbers.
[15] Iversen, P.; Lacks, D. J., *Journal of Electrostatics*, **2012**, 70, 309
[16] Lacks, D. J.; Shinbrot, T., *Nat. Rev. Chem.*, **2019**, *3*, 465
[17] Alicki, R.; Jenkins, A., *Phys. Rev. Lett.*, **2020**, *125*, 186101
[18] Zhao, W.; McCarthy, S. M.; Lai, T. Y.; Yennawar, H. P.; Radosevich, A. T., *J. Am. Chem. Soc.*, **2014**, *136*, 17634
[19] For example, O'Reilly, A.; Booth, A. M. S.; McMullin, C. L.; Fulton, J. R.; Coles, M. P., *Polyhedron*, **2024**, *264*, 117226
[20] For example, Miller, K. A.; Bartolin, J. M.; O'Neill, R. M.; Sweeder, R. D.; Owens, T. M.; Kampf, J. W.; Banaszak Holl, M. M.; Wells, N. J., *J. Am. Chem. Soc.*, **2003**, *125*, *30*, 8986
[21] Caise, A.; Hicks, J.; Heilmann, A.; Aldridge, S., *Chem. Commun.*, **2023**, *59*, 7251
[22] Yang, W.; White, A. J. P.; Crimmin, M., *Nat. Synth.,* **2025**, *4*, 995
[23] Barak, P.; Helmke, P. A., *The Chemistry of Zinc.* In: *Robson, A.D. Zinc in Soils and Plants. Developments in Plant and Soil Sciences*, **1993**, *55*, Springer, Dordrecht
[24] Resa, I.; Carmona, E.; Gutierrez-Pubela, E.; Monge, A., *Science*, **2004**, *305*, 1136
[25] Xie, Y.; Schaefer III, H. F.; Jemmis, E. D., *Chem. Phys. Lett.*, **2005**, *402*, 414
[26] Griffin, L. P.; Aldridge, S., *Chem. Sci.*, **2024**, *15*, 19577
[27] Bowles, A. W. J.; Liu, Y.; Stevens, M. P.; Viorica-Yrezabal, I. J.; McMullin, C. L.; Ortu, F., *Chem. Eur. J.*, **2023**, *29*, e202301850
[28] Green, S. P.; Jones, C.; Stasch, A., *Science*, **2007**, *318*, 1754
[29] Platts, J. A.; Overgaard, J.; Jones, C.; Iversen, B. B.; Stasch, A., *J. Phys. Chem. A*, **2011**, *115*, 194
[30] Cruz, C. A.; Emslie, D. J. H.; Harrington, L. E.; Britten, J. F.; Robertson, C. M., *Organometallics*, **2007**, *26*, *3*, 692
[31] Lim, L. F.; Judd, M.; Vasko, P.; Gardiner, M. G.; Pantazis, D. A.; Cox, N.; Hicks, J., *Angew. Chem. Int. Ed.*, **2022**, *61*, e202201248
[32] Nelmes, G. R.; Brothers, P. J.; Hicks, J., *Z. Anorg. Allg. Chem.*, **2022**, 648, e202200127
[33] Hinz, A., *Chem. Eur. J.*, **2019**, *25*, 3267
[34] Hinz, A., *Angew. Chem. Int. Ed.*, **2020**, *59*, 19065
[35] Drigo, N. A.; Kudriashova, L. G.; Weissenseel, S.; Sperlich, A.; Huckaba, A. J.; Nazeeruddin, M. K.; Dyakonov, V., *J. Phys. Chem. C*, **2018**, *122*, *39*, 22796
[36] Pfeuffer-Rooschüz, J.; Heim, S.; Prescimone, A.; Tiefenbacher, K., *Angew. Chem. Int. Ed.*, **2022**, *61*, e202209885
[37] Wang, Y.; Ma, Y.; Ogumi, K.; Wang, B.; Nakagawa, T.; Fu, Y.; Matsuo, Y., *Commun. Chem.*, **2020**, *3*, 93

[38] a) Tamao, K.; Sumitani, K., Kumada, M., *J. Am. Chem. Soc.*, **1972**, *94*, *12*, 4374; b) Corriu, R. J. P.; Masse, J. P., *J. Chem. Soc., Chem. Commun.,* **1972**, 144
[39] King, A. O.; Okukado, N.; Negishi, E.-I., *J. Chem. Soc., Chem. Commun.*, **1977**, 683
[40] J. K. Stille, *Angew. Chem. Int. Ed.*, **1986**, 25, 6, 508
[41] Miyaura, N.; Yamada, K.; Suzuki, A., *Tet. Lett.*, **1979**, *20*, *36*, 3437
[42] Johansson, M. P.; Olsen, J., *J. Chem. Theory Comput.*, **2008,** *4*, *9*, 1460
[43] Su, W.; Urgaonkar, W.; McLaughlin, P. A.; Verkade, J. G., *J. Am. Chem. Soc.*, **2004**, *126*, 16433
[44] Almenningen, A.; Bastiansen, O.; Fernholt, L.; Cyvin, B. N.; Samdal, S., *J. Mol. Struct.*, **1985**, *128*, *3*, 59
[45] Uzelac, M.; Mulvey, R. E.; *Chem. Euro. J.*, **2018**, 24, 31, 7786
[46] Stanetty, P.; Mihovilovic, M. D., *J. Org. Chem.*, **1997**, *62*, *5*, 1514
[47] Johnson, S. A.; Kiernicki, J. J.; Fanwick, P. E.; Bart, S. C., *Organometallics*, **2015**, *34*, *12*, 2889
[48] Gessner, V. H.; Däschlein, C.; Strohmann, C., *Chem. Eur. J.*, **2009**, *15*, 3320
[49] Luján-Montelongo, J. A.; Mateus-Ruiz, J. B.; Valdez-García, R. M., *Eur. J. Org. Chem.*, **2023**, *26*, e202201156
[50] Schwerdtfeger, P.; Heath, G. A.; Dolg, M.; Bennett, M. A., *J. Am. Chem. Soc.*, **1992**, *114*, *19*, 7518
[51] a) Ghosh, M.; Sen, N.; Khan, S., *ACS Omega*, **2022**, *7*, *8*, 6449; b) Dasgupta, R.; Khan, S., *Advances in Organometallic Chemistry*, **2020**, *74*, 105
[52] Leger, J. M.; Haines, J.; Atouf, A., *J. Phys. Chem. Solids*, **1996**, *57*., *1*, 7
[53] Stender, M.; Phillips, A. D.; Wright, R. J.; Power, P. P., *Angew. Chem. Int. Ed.*, **2002**, *41,* 1785
[54] Hadlington, T. J.; Jones, C., *Chem. Commun.*, **2014**, 50, 2321
[55] Kramida, A., Ralchenko, Yu., Reader, J., and NIST ASD Team, *NIST Atomic Spectra Database (ver. 5.12)*, **2024**, physics.nist.gov/asd
[56] Power, P. P., *Organometallics*, **2020**, *39*, 4127
[57] a) Bader, R. F. W., *Can J. Chem.*, **1962**, *40*, *6*, 1164; b) Wedler, W. B.; Wendelboe, P.; Power, P. P., *Organometallics*, **2018**, *37*, *18*, 2929
[58] Hanusch, F.; Groll, L.; Inoue, S., *Chem. Sci.*, **2021**, *12*, 2001
[59] Juckel, M. M.; Hicks, J.; Jiang, D.; Zhao, L.; Frenking, G.; Jones, C., *Chem. Commun.*, **2017**, *53*, 12692
[60] Yao, S.; Kostenko, A.; Xiong, Y.; Lorent, C.; Ruzicka, A.; Driess, M., *Angew. Chem. Int. Ed.*, **2021**, *60*, 14864
[61] Yao, S.; Xiong, Y.; Saddlington, A.; Driess, M., *Chem. Commun.*, **2021**, *57*, 10139
[62] a) Tonner, R.; Öxler, F.; Neumüller, B.; Petz, W.; Frenking, G., *Angew. Chem. Int. Ed.*, **2006**, *45*, 8038; b) Tonner, R.; Öxler, F.; Neumüller, B.; Petz, W.; Frenking, G., Angew. Chem. Int. Ed., **2006**, *45*, 5263
[63] Norman, N. C.; Winter, M. J., *Chemistry*, **2025**, *7*, *5*, 170
[64] Dong, Z.; Albers, L.; Müller, T., *Acc. Chem. Res.*, **2020**, *53*, *2*, 532
[65] Jones, C., *Nat. Rev. Chem*., **2017**, *1*, 59
[66] Diehl, L.; Khodadadeh, K.; Kummer, D.; Strähle, J., *Chem. Ber.*, **1976**, *109*, 3404
[67] Ponou, S.; Fassler, T. F., *Z. Anorg. Allg. Chem.*, **2007**, *633*, 393; b) Queneau, V.; Sevov, S. C., *Angew. Chem., Int. Ed. Engl.*, **1997**, *36*, 1754
[68] Su, B.; Ganguly, R.; Li, Y.; Kinjo, R., *Chem. Commun.*, **2016**, *52*, 613
[69] Sekiguchi, A.; Izumi, R.; Ihara, S.; Ichinohe, M.; Ya. Lee V., *Angew. Chem. Int. Ed.*, **2002**, *41*, 1598
[70] a) Popelier, P.L.A., Atoms in Molecules: An Introduction, Pearson Education, Harlow, 2000; b) Fradera, X.; Austen, M. A.; Bader, R. F. W., *J. Phys. Chem. A*, **1999**, *103*, *2*, 304
[71] Baerends, E. J.; Aguirre, N. F.; Autschbach, J.; Bickelhaupt, F. M.; Bulo, R.; Capelli, C.; van Duin, A. C. T.; Egidi, F.; Fonseca Guerra, C.; Förster, A.; Franchini, M.; Goumans, T. P. M.; Heine, T.; Hellström, M.; Jacob, C. R.; Jensen, L.; Krykunov, M. V.; van Lenthe, E.; Michalak, A.; Mitroaj, M.; Neugebauer, J.; Nicu, V. P.; Philipsen, P. H. T.; Ramanantoanina, H.; Rüger, R.; Schreckenbach, G.; Stener, M.; Swartm M.; Thijssen, J. M.; Trnka, T.; Visscher, L.; Yakovlev, A. L.; van Gisbergen, S. J. A., *J. Chem. Phys.*, **2025**, 162, 162501
[72] Platts, J. A.; Overgaard, J.; Jones, C.; Iverson, B. B.; Stasch, A., *J. Phys. Chem. A*, **2011**, *115*, 194
[73] Kleemis, F.; Dolomanov, O. V.; Bodensteiner, M.; Peyerimhoff, N.; Midgley, L.; Bourhis, L. J.; Genoni, A.; Malaspina, L. A.; Jayatilaka, D.; Spencer, J. L.; White, F.; Grundkötter-Stock, B.; Steinhauer, S.; Lentz, D.; Horst, P.; Grabowsky, S., *Chem. Sci.*, **2021**, *12*, *5*, 1675
[74] Hicks, J.; Hoyer, C. E.; Moubaraki, B.; Manni, G. L.; Carter E.; Murphey, D. M.; Murray, K. S.; Gagliardi, L.; Jones, C., *J. Am. Chem. Soc.*, **2014**, *136*, 5283
[75] Hicks, J.; Underhill, E. J.; Kefalidis, C. E.; Maron, L.; Jones, C., *Angew. Chem. Int. Ed.*, **2015**, *54*, 10000
[76] Gaussian 16, Revision C.01, Frisch, M. J.; Trucks, G. W.; Schlegel, H. B.; Scuseria, G. E.; Robb, M. A.; Cheeseman, J. R.; Scalmani, G.; Barone, V.; Petersson, G. A.; Nakatsuji, H.; Li, X.; Caricato, M.; Marenich, A. V.; Bloino, J.; Janesko, B. G.; Gomperts, R.; Mennucci, B.; Hratchian, H. P.; Ortiz, J. V.; Izmaylov, A. F.; Sonnenberg, J. L.; Williams-Young, D.; Ding, F.; Lipparini, F.; Egidi, F.; Goings, J.; Peng, B.; Petrone, A.;

Henderson, T.; Ranasinghe, D.; Zakrzewski, V. G.; Gao, J.; Rega, N.; Zheng, G.; Liang, W.; Hada, M.; Ehara, M.; Toyota, K.; Fukuda, R.; Hasegawa, J.; Ishida, M.; Nakajima, T.; Honda, Y.; Kitao, O.; Nakai, H.; Vreven, T.; Throssell, K.; Montgomery, J. A., Jr.; Peralta, J. E.; Ogliaro, F.; Bearpark, M. J.; Heyd, J. J.; Brothers, E. N.; Kudin, K. N.; Staroverov, V. N.; Keith, T. A.; Kobayashi, R.; Normand, J.; Raghavachari, K.; Rendell, A. P.; Burant, J. C.; Iyengar, S. S.; Tomasi, J.; Cossi, M.; Millam, J. M.; Klene, M.; Adamo, C.; Cammi, R.; Ochterski, J. W.; Martin, R. L.; Morokuma, K.; Farkas, O.; Foresman, J. B.; Fox, D. J., *Gaussian Inc.*, Wallingford CT, **2016**

[77] Becke, A. D., *Phys. Rev. A*, **1988**, *38*, *6*, 37

[78] a) Bergner, A., Dolg, M., Küchle, W., Stoll, H., Preuß, H., *Mol. Phys.*, **1993**, *80*, 1431-1441, b) Fuentealba, P., Preuß, H., Stoll, H., Szentpály, L. V., *Chem. Phys. Lett.*, **1982**, 89, 418

[79] (a) Hariharan, P. C., Pople, J. A., *Theor. Chim. Acta.*, **1973**, *28*, 213; (b) Hehre, W. J., Ditchfield, R., Pople, J. A., *J. Chem. Phys.*, **1972**, *56*, 2257

[80] Gaussian 09, Revision A.02, M. J. Frisch, G. W. Trucks, H. B. Schlegel, G. E. Scuseria, M. A. Robb, J. R. Cheeseman, G. Scalmani, V. Barone, G. A. Petersson, H. Nakatsuji, X. Li, M. Caricato, A. Marenich, J. Bloino, B. G. Janesko, R. Gomperts, B. Mennucci, H. P. Hratchian, J. V. Ortiz, A. F. Izmaylov, J. L. Sonnenberg, D. Williams-Young, F. Ding, F. Lipparini, F. Egidi, J. Goings, B. Peng, A. Petrone, T. Henderson, D. Ranasinghe, V. G. Zakrzewski, J. Gao, N. Rega, G. Zheng, W. Liang, M. Hada, M. Ehara, K. Toyota, R. Fukuda, J. Hasegawa, M. Ishida, T. Nakajima, Y. Honda, O. Kitao, H. Nakai, T. Vreven, K. Throssell, J. A. Montgomery, Jr., J. E. Peralta, F. Ogliaro, M. Bearpark, J. J. Heyd, E. Brothers, K. N. Kudin, V. N. Staroverov, T. Keith, R. Kobayashi, J. Normand, K. Raghavachari, A. Rendell, J. C. Burant, S. S. Iyengar, J. Tomasi, M. Cossi, J. M. Millam, M. Klene, C. Adamo, R. Cammi, J. W. Ochterski, R. L. Martin, K. Morokuma, O. Farkas, J. B. Foresman, and D. J. Fox, Gaussian, Inc., Wallingford CT, **2016**.

[81] Cosier, J.; Glazer, A.M., *J. Appl. Cryst*, **1986**, *19*, 105

[82] CrysAlisPro v.1.171.35.8 (Agilent Technologies, 2011)

[83] Sheldrick, G. M., *Acta Cryst.*, **2015**, *C71*, 3

[84] Barbour, L. J., *J. Supramol. Chem.*, **2001**, *1*, 189

[85] Dolomanov O. V.; Bourhis L. J.; Gildea R. J.; Howard J. A. K.; Puschmann, H., *J. Appl. Cryst.,* **2009,** *42*, 339

[86] te Velde, G.; Bickelhaupt, F. M.; Baerends, E. J.; Fonseca Guerra, C.; van Gisbergen, S. J. A.; Snijders, J. G.; Ziegler, T., *J. Comp. Chem.*, **2001**, *22*, *9*, 931

[87] Trost, B. M.; Schultz, J. E.; Chang, T.; Maduabum, M. R., *J. Am. Chem. Soc.*, **2019**, *141*, 9521

[88] Maudrich, J.-J.; Sindlinger, C. P.; Aicher, F. S. W.; Eichele, K.; Schubert, H.; Wesemann, L., *Chem. Eur. J.*, **2017**, *23*, 2192

[89] Iuga, D.; Corlett, E. K.; Bronw, S. P., *Magn. Reson. Chem.*, **2021**, *59*, *9*, 1089

[90] Bonyhady, S. J.; Jones, C.; Nembenna, S.; Stasch, A.; Edwards, A. J.; McIntrye, G. J., *Chem. Eur. J.*, **2010**, *16*, 938

3. Silandiuide and Silylene Dianion

"And if I only could

I'd make a deal with God

And I'd get him to swap our places […]

Let me steal this moment from you now […]

Let's exchange the experience"

-Bush, K., *Running Up That Hill*, *Hounds of Love*, **1985**

3.1 Introduction

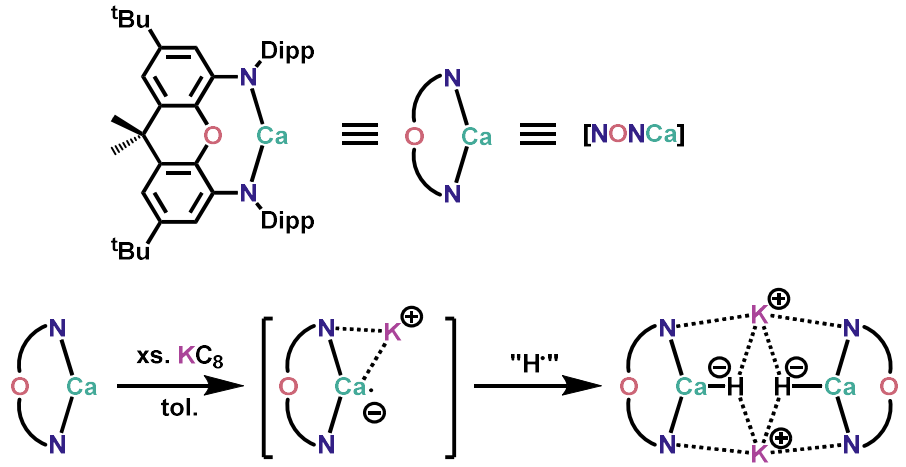
Life within the eukaryote domain[1] is dependent on our oxidising atmosphere, converting adenosine diphosphate to adenosine triphosphate under aerobic conditions with the help of the mitochondrion in a series of reactions so well understood that most physicians fondly tell you of a time they once had to memorise the citric acid cycle.[2]

Life, even more broadly across all domains Archaea, Bacteria, and Eukarya, is dependent on carbon's remarkable commitment to the octet rule[3], the narrow range of temperatures on Earth matching the kinetic and thermodynamic properties of the molecules we associate with life, and the fact that our local thalassogen is denser as a liquid than as a solid.[4]

Herein we discuss the theoretical and computational aspects of the reversible, autocatalytic release of hydrogen from a recently reported hexahydridosilicate dianion encapsulated within a supramolecular assembly,[5] and its unprecedented "silylene dianion" daughter compound.[6] The system is exceptionally sensitive to air and moisture: it implicates pyrophoric silane gas, utilises only the most inert hydrocarbon solvents, and requires a narrow, elevated temperature range to undergo these processes.

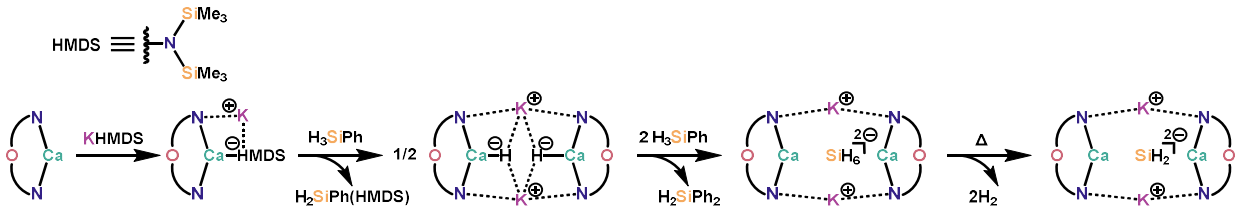
Perhaps it is disingenuous to compare the system to potential Martian molecular machinery. On a planet with a surface temperature above 60 °C, a reducing atmosphere, and unreactive, nonpolar oceans of methane or even silane,[7] however, such weaknesses may seem strengths. One might even imagine mechanisms of cellular hydrogen fixation to be very reasonable sources of crucial, life-sustaining energy, and the autocatalysis is of course one of the only crucial features of biology. To me, xenobiology is just as reasonable motivation for this work as hydrogen storage, potent reductants, or even esoteric electronic structure. This work was undertaken because the results were mysterious, unprecedented, curious, and beautiful- the authors have not forgotten they are alive and feel the insatiable urge to build pyramids.

During his PhD studies within the group, Ryan Huo worked on improving the synthesis of a molecular anionic calcium hydride complex, essentially the dimeric potassium hydride adduct of [**NON**Ca].[8] The method reported by McMullen *et al.* in the original work relies on the unreliable reaction of potassium graphite with the [**NON**Ca], under the presumption that a short-lived Ca(I) radical intermediate forms and rapidly abstracts a proton from the environment to form the desired product (Scheme 1).



Scheme 1 Antiquated synthesis of the dimeric molecular calcium hydride complex [K{NONCa}H]$_2$, using the strong reductant KC$_8$ to presumably form the proposed short-lived calcium radical, which rapidly abstracts an "H·" radical from the solvent to form the product.

Amongst many variations to the synthetic procedure best described by Huo,[9] a metathesis reaction between the anionic calcium amide K[(NON)Ca(NSiMe$_3$)] and phenylsilane gave the best yield of the molecular anionic calcium hydride complex (Scheme 2). However, the addition of excess phenylsilane resulted in the unusual hexahydridosilicate dianion [K$_2${NONCa}$_2$(SiH$_6$)]. This compound's subsequent reactivity, specifically the elimination of two equivalents of dihydrogen to give [K$_2${NONCa}$_2$(SiH$_2$)], is that with which this chapter concerns itself.



Scheme 2 Improved synthesis of the molecular hydride complex and its unexpected downstream products, the hexahydridosilicate [K$_2${NONCa}$_2$(SiH$_6$)] and the unprecedented silylene dianion [K$_2${NONCa}$_2$(SiH$_2$)].

It is at this point warranted to briefly contextualise silane, silicate, and silanuide chemistry.

Silicon is, of course, the 2nd congener of group 14 and draws much of its chemistry through analogy with carbon. Silicon compounds are similarly dominated by sigma bonds and species which obey the octet rule, silanes are most often tetrahedral 4-coordinate species. However, the element differs fundamentally from carbon in some crucial ways. Being significantly larger (covalent radius of 1.11 Å versus carbon's 0.76 Å)[10] and significantly less electronegative (Pauling electronegativity of 1.90 versus carbon's 2.55)[11], as well as a slightly smaller energy difference in the valence atomic orbital energies (E_h, 2 d.p.: C 2s: −0.71, 2p: −0.43, Δ = 0.27;

Si 3s −0.54 3p −0.30, Δ = 0.24)[12] leads silicon to be able to form hypervalent complexes, intrinsically weak multiple bonds, and makes many of the complexes unstable towards air and moisture (*c.f.* indefinitely shelf-stable hydrocarbons).

The larger size, and consequently less steric repulsion between geminal moieties, enable delocalized three-centre-four-electron (3c-4e$^-$) bonding and access to coordination numbers beyond four, a phenomenon classically described as hypervalency.[13] Figure 1 broadly shows (to a qualitative linear combination of atomic orbitals (LCAO) approximation) that even for elements with energetically inaccessible p- or d- orbitals, 3c-4e$^-$ bonding provides electronic stabilisation simply through the out-of-phase linear combination of atomic orbitals being nonbonding (under the presumption any orbitals of the main group element of the appropriate irreducible representation are too high in energy to appreciably mix) and the in-phase LCAO of ligand orbitals forming a strong σ-bond with the central atom. Many theoreticians actually suggest that 3c-4e$^-$ bonding is actually the principal interaction for the majority of the periodic table, eliminating the need to spuriously invoke high-energy p-orbitals for transition metal complexes or high-energy d-orbitals for main-group species.[14] The second row remains unique in the sense that it is the only place where by default, the steric interaction between geminal moieties is larger than the benefit of 3c-4e$^-$ bonding.

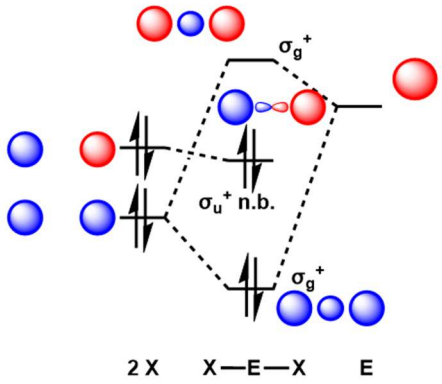
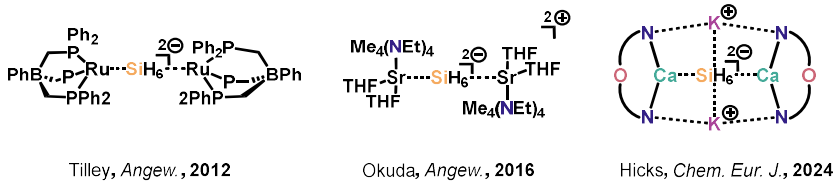


Figure 1 Qualitative molecular-orbital diagram for 3-centre-4-electron bonding, demonstrating that the overall energy of the two occupied molecular orbitals σ_{u^+} and σ_{g^+} is lower than the energy of two free donors, where X is an electronegative X-type ligand and E is a 3rd+ row main group element such as silicon. The "nonbonding" orbital may also drop in energy due to small interactions with the E p orbital or through purely coulombic interactions.

From Figure 1 it is also immediately obvious why such hypervalent species prefer highly electronegative ligands. The energy of the formally nonbonding combination 2σ is dependent almost entirely on the energy of the donor orbitals which produced it, which are to a first order approximation dependent on the effective nuclear charge of the donor nucleus, of which a high Z_{eff} results in a high electronegativity.

Combined with the large bond enthalpy of Si-F and Si-O bonds (565 and 452 kjmol^{-1} respectively),[15] much naturally occurring silicon is octahedral with highly electronegative moieties, as malladrite ($Na_2(SiF_6)$) or thaumasite (containing $(Si(OH)_6)^{2-}$ anions).[16]

Comparatively, hydrogen has insufficient electronegativity to stabilise the nonbonding contribution. Even beyond this, the weaker Si-H bonds (393 kjmol^{-1}) and facile reaction with the formal hydride lead to high moisture sensitivity in hydride-rich silanes and silicates. To date, there are only 3 reported solution-stable hexahydridosilicates: in 2012, Lipke and Tilley reported a bridging, ruthenium stabilised example, Okuda and coworkers reported a hexahydridosilicate in 2022 bridging two strontium centres, and our example from 2024 (Figure 2).[17,18] These species require stringently anaerobic and anhydrous environments, as well as sterically demanding or electronically-stabilising coordination environments to prevent disproportionation, loss of dihydrogen, or formation of silanides (SiR_3^-). Okuda's example decomposes with loss of dihydrogen to the silanide at room temperature.



Tilley, *Angew.*, **2012** Okuda, *Angew.*, **2016** Hicks, *Chem. Eur. J.*, **2024**

Figure 2 The three reported examples of molecular hexahydridosilicates. Tilley and co-worker's example is stabilised by delocalisation of the silicate electron density into vacant, low-energy ruthenium orbitals; Okuda and co-worker's example uses entirely neutral ligands (beyond the silicate) yielding a dicationic complex, stabilised by the consequent coulombic attraction and stronger Sr-SiH$_6$ interactions but remains stable only to approximately 0 °C; the most recent example by Hicks and co-workers remains indefinitely stable at room temperature in solution, stabilised by encapsulation within a supramolecular assembly.

Potassium hexahydridosilicate ($K_2(SiH_6)$) is intrinsically unstable in solution but may be isolated as a crystalline solid in appropriate anhydrous, anaerobic, high-pressure conditions.[19] This comprehensive work by Häussermann and co-workers discusses the vibrational spectroscopy, electronic structure, phononic structure, and thermodynamics of the anion in great detail, although no mechanistic accounts are provided. Particularly salient is their Gibbs free energy analysis of the formation of $K_2(SiH_6)$ from solid silicon, potassium hydride, and hydrogen gas, suggesting a positive Gibbs free energy of formation at atmospheric pressure of the salt beyond *ca*. 200 Kelvin. They also suggest that the compound becomes more stable by replacing the potassiums with rubidiums, positing that the larger elements make the SiH_6^{2-} moieties further apart in the lattice, which may indicate that decomposition pathways occur through interactions between the anions. They do not, however, suggest the decomposition to silane gas and KH, presumably because it is unrelated to the mechanism of formation in their

experiments. Calculations performed in this work use the PBE density functional on the projected augmented wave method, as implemented in VASP.

The final reaction within Scheme 2 is a most unprecedented and unusual reaction, involving the spontaneous evolution of dihydrogen gas from the hexahydridosilicate to produce an unusual anion within the supramolecular assembly, "SiH_2^{2-}". The broad electronic structure of which is shown in Figure 3 *via* comparison with the parent carbene and oxidane and will be discussed in detail within the chapter.

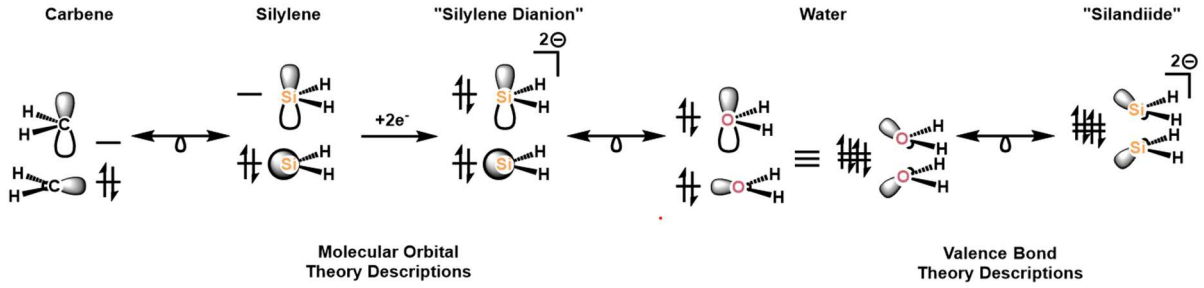


Figure 3 Comparison of qualitative valence electronic structure *via* isolobal analogy from a molecular orbital and valence bond description. The silylene dianion is compared as a formal 2e⁻ reduction of the parent silylene, which is evidently isolobal with the parent carbene. Equally by an alchemical transmutation, the silylene dianion is isolobal with water, which can be considered from a non-degenerate molecular orbital approach, or by a "bunny ears" valence bond description with two equivalent lone pairs. Reversing the transmutation from the bunny ears description results in a two lone-pair understanding as a doubly deprotonated silane, or a silandiide.

Prima facie, SiH_2^{2-} could be considered to be the two-fold deprotonated form of silane, SiH_4. By IUPAC, the process of subsequent deprotonation $SiH_4 \rightarrow SiH_3^- \rightarrow SiH_2^{2-}$ IR-6.4.4 in the Red Book[20] follows silane, silanide, silandiide respectively. However, despite the goals of the Red Book, the naming is not unambiguous, as one can take the substitutive approach (*vide supra*), or an additive approach, which could lead to the idea of adding two hydrides to atomic silicon: dihydridiosilicate(2-), or something as esoteric as dihydro-λ^0-silandiuide⁉ *Obiter dicta,* SiH_6^{2-} takes the more intuitive forms hexahydridosilicate(2-) or silandiuide, barring the egregious hexahydro-λ^4-silandiuide. Official nomenclative quibbling aside, we choose the more descriptive "silylene dianion", borrowing from the commonplace, but unofficial, convention of taking the neutral form of a species and indicating the charge (*e.g.* aluminyl → aluminyl anion for $X_2Al\cdot \rightarrow X_2Al:^-$).[21] This approach indicates that the species is most similar to the parent silylene, SiH_2, reduced by two electrons to form the silylene dianion, SiH_2^{2-} as we will later argue as most appropriate.

As discussed earlier, there is no privileged perspective of the wavefunction and any unitary transformation of the density matrix preserves the observables of the system. Consequently,

there are several equally valid phenomenological perspectives of the wavefunction, particularly here there are two qualitative interpretations. From valence bond theory a wave function is generated from intuition, typically following sensible Lewis structures and a linear combination of single-determinantal wavefunctions matching Lewis descriptions is taken to generate an electronic structure, or a molecular orbital approach builds from the ground up a single determinant from linear combinations of atomic orbitals solved self-consistently. From a valence bond description, two lone pairs on the same atom are equivalent, reminiscent of the "bunny ear" description of water (H_2O, the parent oxidane)[22] (Figure 3, right), which is actually isolobal to SiH_2^{2-} (moving from group 16 to group 14 merely adds two electrons, and moving from period 2 to 3 changes only the approximate energies). This two equivalent lone pair perspective is natural only from a Lewis/valence bond theory perspective, but is exactly what is implied by the silandiide or dihydriosilicate naming convention. Molecular orbital perspectives however are pervasive in the modern zeitgeist, and many textbooks discuss the inequivalence of oxygen lone pairs by default,[23] more naturally explaining their spectroscopy, directional preference in bonding, and position in the spectrochemical series. To this end, we take the molecular orbital description as more appropriate of single determinantal molecules to be more appropriate, and consequently take the corresponding nomenclature to be more natural, reinforcing our usage of "silylene dianion".

Silylenes are isoelectronic with carbenes, which are neutral two-electron σ-donors and π-acceptors, which can be either singlet or triplet in the ground state depending on the electronic properties of the bound X-type ligands.[24] Due to the inert pair effect, the s-p separation in the silylenes is greater and all are considered to be singlet in the ground state from the greater s-contribution to the "sp^2" orbital. Silylenes are considered stronger σ-donors than carbenes due to the higher energy of the donor orbital however, as silicon's decreased electronegativity raises the energy of all its parent atomic orbitals; similarly they are worse π-acceptors due partly to their higher energy vacant p-orbital but also due to worse possible orbital overlap with the vacant orbital consequent of silicon's increased atomic radius. This makes them highly reactive, short-lived Si(II) species.[25] Many isolable examples have been synthesised, making use of the ubiquitous sterically demanding ligands, or even as Lewis-base stabilised 3-coordinate corresponding species.[26]

We also draw the parallel between reduced silylenes and "silylones", as silylones share the same electronic structure, a formally Si(0) centre with two lone pairs, however such species utilise two L-type ligands for both steric and electronic stabilisation.[27] In fact, depending on

the magnitude of π-acceptor character on the L-type ligands one might even consider the ligands to be reduced and the silylone p-orbital to perhaps be formally vacant (*e.g.* cyclic alkyl amino carbenes).[28] The continuum of reduced silylene to silylone (and perhaps even bent silaallene) is perhaps intrinsically unclear and dependent on an artificially imposed view of electronic structure.

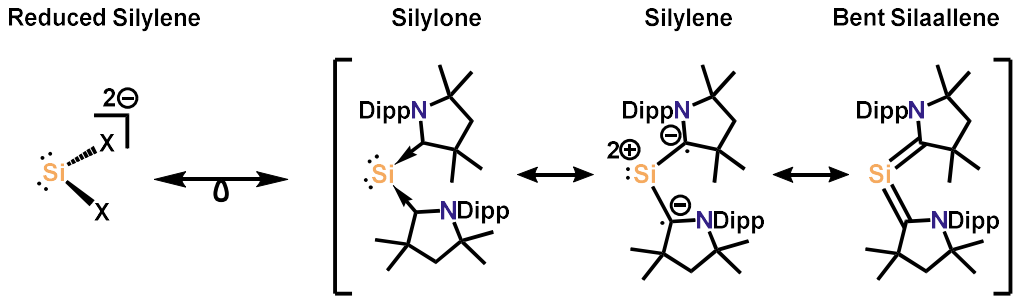


Figure 4 A reduced silylene could be seen as isoelectronic to a silylone, merely with X-type ligands for the silylene dianion and L-type ligands for the silylone. This is particularly clear when the nature of the L-type ligands is called into question as in the Si(cAAC)$_2$ system.

Computationally, few investigations into silicon hydride chemistry of the main group have been reported. A wide range within transition metal chemistry which focus on Si-H bond coordination and subsequent scission for hydrosilylation mechanisms or for selectivity of specific catalysts, but are beyond the scope of this work.[29a-f]

Hejda, Hupf, Beckmann and co-workers report redox cycling with tellurium,[30] promoting the hydrosilylation of benzoquinone to silylhydroquinone, but understandably they mechanistically focuses on the interaction between the telleriums and Si-H bonds, modelling similarly to ordinary oxidative addition processes in transition metals. Hu and co-workers model gas phase reactions of silane and diborane using second-order perturbation theory (MP2/6-311++G**//MP2/6-31+G*) in attempts to model the decomposition of silane gas to elemental silicon in the hopes of understanding deposition processes.[31] They offer several mechanisms for H_2 generation from the system, based on using B_2H_6 as a Lewis acid and SiH_4 as a weak Lewis base, although the H_2 forming events actually occur at the boron centres, with the exception of one extremely high energy (80.69 kcal·mol^{-1}) transition state wherein one of the borane hydride directly deprotonates the silane, leaving a bridging SiH_3^- moiety in its place.

Harder and co-workers report imine hydrosilylation with group 2 molecular metal hydride catalysts, reporting a wide range of Si-H scission barriers across calcium, strontium, and barium between 11 and 15 kcal·mol^{-1} using a model system of gas phase CaH_2 using DFT at the B3PW91/6-311++G(2df,p) level of theory.[32] Again, silicon is principally a substrate in

these mechanisms and does not undergo any reaction independent of the group 2 metals or any produces H-H coupling.

Evidently, hydride coupling mechanisms exclusively at silicon are relatively unexplored, and we find ourselves uniquely situated with a model system to do so.

In summary, this chapter seeks to investigate two principal aims: firstly, to describe the electronic features of the novel complexes [K_2{**NON**Ca}$_2$(SiH_6)] and [K_2{**NON**Ca}$_2$(SiH_2)] shown in Scheme 2, and secondly devise a computational method supported by kinetic modelling for the process of their interconversion.

3.2 Experimental Comparison and Benchmarking

3.2.1 Geometry

The discussion above establishes the conceptual stakes of the system but does not, *ipso facto*, establish its structural legitimacy. Any mechanistic or electronic argument that rests upon a hypervalent silicon hydride must first be grounded in a defensible description of the geometry and bonding of the parent silicate itself, because small deviations in Si-H distances, coordination asymmetry, or metal-hydride contacts propagate directly into orbital ordering, vibrational assignments, and energetic landscapes. Moreover, the encapsulation of the [SiH_6^{2-}] unit within a supramolecular assembly introduces additional degrees of freedom relative to both gas-phase anions and solid-state lattices, and it cannot be assumed *a priori* that the geometry observed crystallographically represents either an artefact of packing or a faithful proxy for the solution structure. It is therefore necessary, before proceeding to electronic structure analysis or mechanistic speculation, to benchmark the geometry of the silicate rigorously against experiment and across multiple computational descriptions, and to establish which features of the structure are robust with respect to functional choice and which are not. Section 3.2 addresses this requirement by comparing optimised geometries to diffraction and spectroscopic observables, thereby fixing the structural framework on which the remainder of the chapter relies.

Throughout the work, the tert-butyl groups substituting the NON ligand at the 2,9 positions were deemed to have limited effect on the mechanism or electronic structure of the relevant species, and were consequently truncated to methyl groups to avoid computational cost. *Caveat emptor*, such a truncation ultimately saved limited computational resources, if any, due to the facile rotation of a methyl group around the methyl-aryl bond. In difficult transition state searches, this was often the elucidated transition state over the intended productive pathway.

Results are presented in Figure 6. All functionals used the same basis set (6-31G**)[33] with relativistic Stuttgart effective core potentials on Ca, K, and Si and associated additional polarisation d-functions (BS1).[34] Data were calculated by subtracting the experimental value (from neutron diffraction studies, necessitated by the low sensitivity of X-ray diffraction to low electron density species such as hydrides, but the comparatively large and accurate interaction of neutrons with the protons gives accurate geometric data) from the calculated value, dividing the result by the experimental value, and multiplying by 100.

Due to the very large number of degrees of freedom, principally on the ligand framework, just comparing all the atomic coordinates between calculation and experiment would not be enlightening as it would just reproduce known features of each density functional about organic fragments. Instead, 10 key parameters were used to ensure the accuracy around the chemically interesting portion of the system, *i.e.* the size and shape of the cavity and the accuracy of the silicate dianion. Unfortunately, the hexahydridosilicate crystalises in the $P\bar{1}$ space group with the centre of inversion symmetry element at the silicon, which reduces the degrees of freedom available to the silicate as the geometric parameters must also satisfy this inversion symmetry at silicon, resulting in the 10 following parameters (shown in Figure 5 as red lines):

1. The three symmetrically independent Si-H bond lengths (3)
2. The three symmetrically independent Ca-H bond lengths (3)
3. The Si-Ca length (1)
4. The Si-K length (1)
5. The K-H distance for the short symmetrically independent K-H lengths (2)

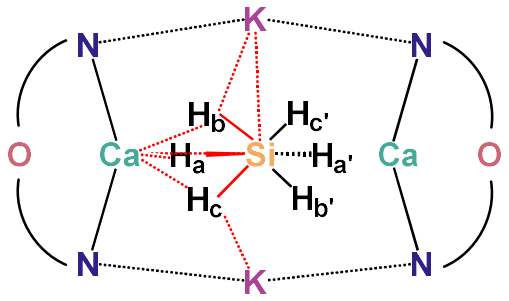


Figure 5 Parameters used for geometry benchmarking shown in red.

After standard geometry optimisation (confirming each structure to be a minimum on the potential energy surface *via* frequency analysis) starting from the neutron diffraction data, the optimised parameters were compared with the experimental ones as percentage differences, then the root mean square and mean (and standard deviation) for these percentage differences calculated thereof. This is tabulated in Table 1 and summarised in Figure 6.

Parameter	Experimental value (std. dev.)(Å)	Percentage difference from Neutron diffraction data (%) (std. dev.)					
		PBE0-D3BJ[35]	BP86[36]	B3LYP[37]	PBE0[38]	B3PW91[39]	ωB97X-D[40]
Si-H_a	1.609(18)	-0.50	0.37	-0.56	-0.25	-0.31	-0.37
Si-H_b	1.598(17)	1.69	2.69	1.69	2.07	2.07	0.88
Si-H_c	1.628(18)	-0.68	0.37	-0.55	-0.18	-0.18	-0.31
Ca-H_a	2.34(2)	0.64	2.96	3.04	2.31	3.17	1.24
Ca-H_b	2.39(2)	0.04	3.57	4.28	2.39	3.52	0.04
Ca-H_c	2.42(2)	-1.70	1.74	2.99	0.87	2.20	-0.91
Ca-Si	2.96(3)	-0.64	2.70	3.24	1.59	2.77	-0.30
Si-K	3.37(4)	-0.86	1.63	1.16	0.89	1.45	-1.51
K-H_b	2.57(3)	-1.25	1.48	0.82	0.51	1.05	-2.69
K-H_c	2.55(3)	-1.49	1.18	0.67	0.43	1.14	-1.22
RMS (10)		3.4	6.8	7.3	**4.5**	6.6	**3.8**
Mean (10)		-0.5 (1.0)	1.9 (1.0)	1.7 (1.6)	**1.1 (0.9)**	1.7 (1.2)	**-0.5 (1.1)**
RMS (Si-H only)		1.9	2.7	1.9	2.1	2.1	1.0
Mean (Si-H only)		0.2 (1.1)	1.1 (1.1)	0.2 (1.1)	0.5 (1.1)	0.5 (1.1)	0.1 (0.6)

Table 1 Geometry benchmarking data for different density functionals (using the same modified 6-31G basis BS1), showing the percentage difference from the experimental neutron diffraction data.**

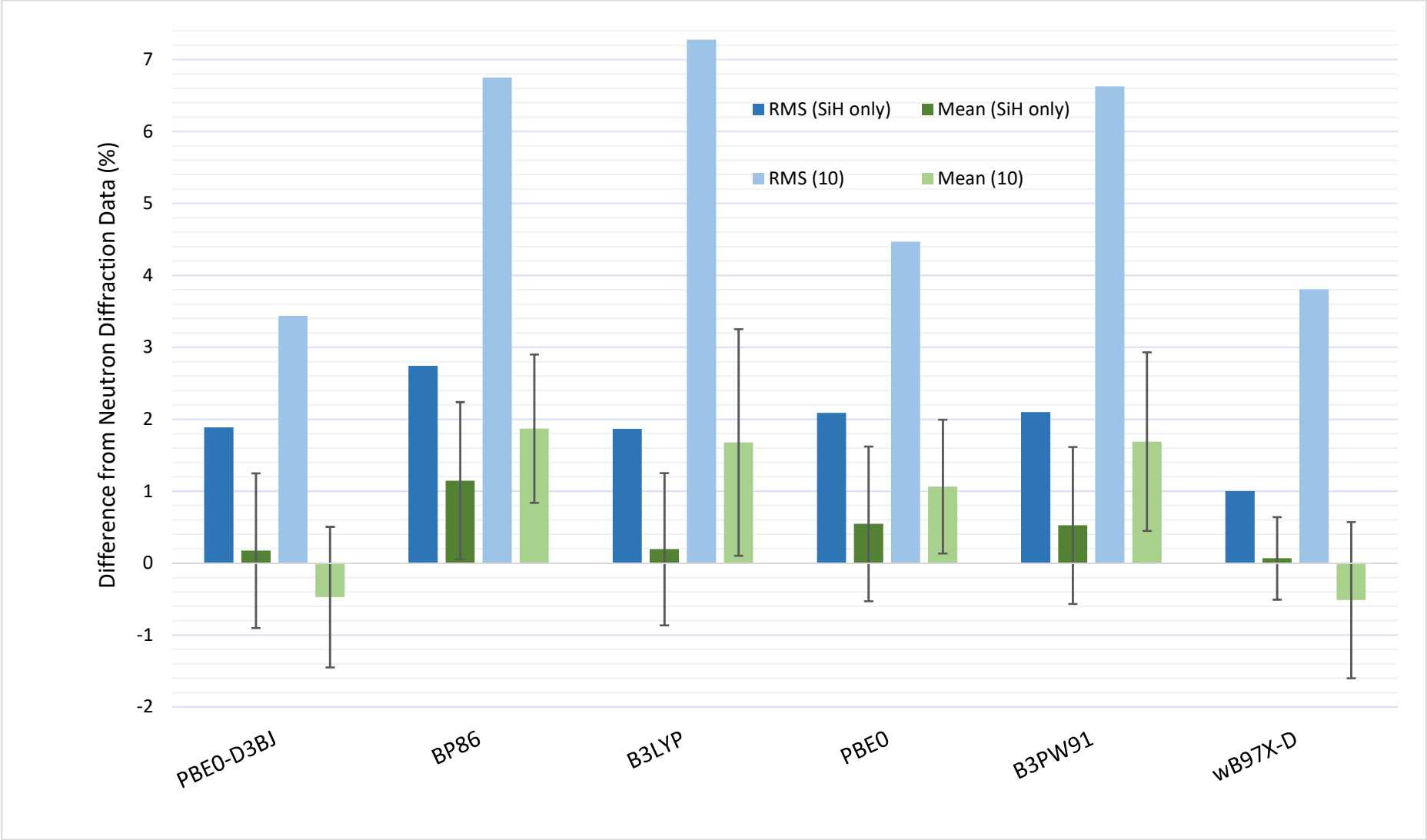


Figure 6 Comparison of structural parameters for various optimisations of the hexahydridosilicate $[K_2\{NONCa\}_2(SiH_6)]$using DFT functionals (DF/BS1) against neutron diffraction data. Error bars on the means represent the respective standard deviations.

The data show best performance for PBE0-D3BJ and ωB97X-D, by lowest deviation from the experimental neutron diffraction data, specifically with respect to the established geometric parameters. This shows most clearly the necessity of an empirical dispersion correction to accurately reproduce the geometries by comparison of global hybrid GGA PBE0 compared with its dispersion-corrected form PBE0-D3BJ. Both PBE0-D3BJ and ωB97X-D are empirically dispersion corrected hybrid GGAs, with the difference being that ωB97X-D is a range-separated hybrid instead of the global hybrid, giving greater parametric flexibility, and that PBE0 is derived fully from first principles and has no empirical parameters fit to data, whereas ωB97X-D is fully empirical (although systematically derived, *vide infra*). Our final functional choice was PBE0-D3BJ, for its good performance, lowest RMS percentage differences, and as a non-empirical functional should best describe this non-standard system which is not necessarily well described in the training data for ωB97X-D.

Geometric benchmarking was not performed against the silylene dianion, instead for sake of comparison and consistency with the existing published work the described method was utilised again.

3.2.2 Stretching Frequencies

By way of additional comparison of experiment, the stretching frequencies of the hexahydridosilicate anion were investigated. This was particularly useful early in investigation when single crystal X-ray diffraction data were unreliable to demonstrate the existence of hydride moieties surrounding the central silicon.

Having 7 atoms, assuming the anion tumbles relatively freely within the cavity (and in agreement with Puhakainen et al.[19]) the silicate anion should possess 3N-6 vibrational degrees of freedom, or 15 vibrational modes. While the silicate dianion cannot possess true octahedral symmetry in the cavity as it will interact differently with the non-octahedral ligand, we shall consider such coordination environment differences to be small perturbations on an idealised octahedral environment, indicated by replacing true spectroscopic notation such as "t_{1u}" with the corresponding "t_{1u}-like" suffix.

The full set of 15 principally hexahydridosilicate harmonic vibrational modes were calculated (scaled by 0.938, cm^{-1}) to be: a_{1g}-like at 1746; e_g-like at 1462 and 1442; t_{1u}-like stretching at 1603, 1539, and 1497; t_{2g}-like at 1153, 1065, and 1037; t_{1u}-like bending at 1052, 1036, and 967; and t_{2u}-like at 646, 501, and 259 cm^{-1}, of which the a_{1g}-, e_g-, and t_{2g}-like modes are

expected to be Raman-active (although due to experimental limitations we did not collect Raman spectra), with only the t_{1u}-like sets IR active (and t_{2u} entirely inactive). This is in good agreement with the experimental IR spectroscopic data, with stretches appearing at *ca*. 1620, 1558, and 1503 cm^{-1}; and also weak bending modes at 1053, 1013, and 976 cm^{-1}. These resonances are not observed in the parent anionic calcium hydride or the silylene dianion (*vide infra*).

3.2.3 Nuclear Magnetic Resonance of the Silicon Hydrides

^{29}Si nuclear magnetic resonance is notoriously difficult due to its wide chemical shift range, low natural abundance, and long T_1 relaxation period. This is exacerbated by the limited reported examples of low-valent silicon hydrides and large, high multiplicity proton coupling, which made it difficult for authors Huo and Lawes to elucidate the hexahydridosilicate resonance. Consequently, we sought to calculate the shifts from first principles as a guide to finding the resonances and in part to support their identity by comparison with theoretical predictions, which proved fruitful. This was performed as described below, modified from the original publication:[5]

Several DFT functionals (DF) were tested by first performing a geometry optimisation for tetramethylsilane (TMS) using PBE0-D3BJ/BS1, and then calculating the isotropic shielding constants for the atoms in TMS using the gauge-including atomic orbitals (GIAO) method (DF/Def2-TZVPP[41]), averaging all constants for the same types of atoms, and comparing them with the experimental isotropic shielding constants. The results are presented in Table 2. Density functionals used do not include empirical dispersion corrections (except for ωB97X-D as this is inseparable, but inconsequential) as they are all performed on the same geometry, and empirical dispersion does not influence electronic structure (for a specific set of nuclear coordinates).

Chemical shifts (δ) can be calculated from isotropic shielding constants according to the equation:[42]

$$\delta = \sigma_{standard} - \sigma_{species}$$

Equation 1 Isotropic shift calculation.

Where δ is the chemical shift (in ppm), and σ_x is the calculated isotropic shielding constant (in ppm) for the compound. In our case, the standard isotropic shielding constants ($\sigma_{Standard} = \sigma_{TMS}$ for both $\delta_{1H}/\delta_{29Si}$) used were those of the silicon and the average of the hydrogens in

tetramethylsilane at the PBE0/6-311G(2df,2pd)//PBE0-D3BJ/BS1 level of theory using the GIAO method, full uncontracted basis.[43]

Density Functional (DF)	Isotropic Shielding Constant, σ (ppm)			Difference from Experiment (%)		
	^{29}Si	^{13}C	^{1}H	^{29}Si	^{13}C	^{1}H
Experimental[42]	376.40	188.04	30.78	-	-	-
PBE	326.56	183.55	31.39	13.24	2.39	-1.97
PBE0	**343.88**	**187.59**	**31.45**	**8.64**	**0.24**	**-2.17**
B3LYP	328.26	182.82	31.61	12.79	2.78	-2.68
BP86	325.36	183.16	31.45	13.56	2.60	-2.17
B97	337.79	182.78	31.61	10.26	2.80	-2.67
ωB97X-D	343.00	187.86	31.57	8.87	0.10	-2.56

Table 2 NMR spectroscopy benchmarking for $SiMe_4$ using DF/6-311G(2df,2pd)//PBE0-D3BJ/BS1

For TMS, evidently the PBE0 and ωB97X-D functionals were found to be the best performers as in the geometry for the silicate dianion, with PBE0 having the lowest percentage difference of all functionals for both ^{29}Si and ^{1}H. ωB97X-D shows greater accuracy only for the ^{13}C nuclei, which is immaterial to our investigation of silicon hydrides. Due to its excellent performance and matching the methodologies already used in the study, PBE0 was chosen to compute the NMR spectroscopic data. It is salient to note that perhaps PBE0 outperforms the other functionals *because* it was also used to generate the geometry (*viz*. PBE0-D3BJ) for TMS, and so its electronic structure should also be the most accurate for this set of nuclear coordinates in a sort of self-consistent fashion. Unfortunately, we are committed to the geometries for the low-valent silicon hydrides which were optimised at the same PBE0-D3BJ/BS1 level of theory as shown the in the geometry benchmarking and are unable to perform costly geometry optimisations for every potential methodology. Thus, we settle on the seemingly reliable PBE0/6-311G(2df,2pd)//PBE0-D3BJ/BS1 methodology for nuclear magnetic resonance calculations.

The final chemical shift data calculated for the hexahydridosilicate were ^{29}Si = –263.98 ppm and ^{1}H = 5.97 ppm for the associated hydrides, with an average $^{1}J_{SiH}$ = –96.76 Hz. This allowed experimental elucidation of the experimental ^{29}Si shift (–261.2 ppm), which was in very good agreement, and close to the experimental ^{1}H shift (5.38 ppm), and similar agreement with the corresponding experimental absolute value coupling constant (114 Hz).

The same methodology was applied to the silylene dianion $[K_2\{(NON)Ca\}_2(SiH_2)]$. The ^{29}Si and ^{1}H shifts were calculated for the silylene dianion. While showing similarly excellent agreement with the ^{29}Si resonance (-159.38 ppm calculated *cf.* -168.5 ppm experimental), the average ^{1}H resonances (0.85 ppm) were experimentally significantly downfield from the experimental values (-1.55 ppm). We suggest that this is due to the much greater geometric freedom of the silylene dianion compared with the hexahydridosilicate, as many conformations are possible for the bent SiH_2 moiety within the cavity, each of comparable energy and consequently large populations in solution but possibly of different magnetic properties. Regardless, the small difference is not enough to suggest a different identity for the calculated and experimental species, nor to justify the large computational resources required to repeat the calculations on the other conformers of the silylene dianion, as they would not lead to any different interpretation.

3.3 Electronic Structure

The electronic structure of hypervalent species is well understood from a molecular orbital perspective. Taking the 6 hydride moieties as equivalent 1s orbitals in the O_h point group, then taking the character and decomposing it using the great orthogonality theorem provides 6 LCAOs, which then have appropriate irreducible representations to mix with the valence atomic orbitals on the silicon. The relative energies of these combinations depend on the overlap and energies of the parent atomic orbitals but result in a qualitative molecular orbital diagram (Figure 7, centre):

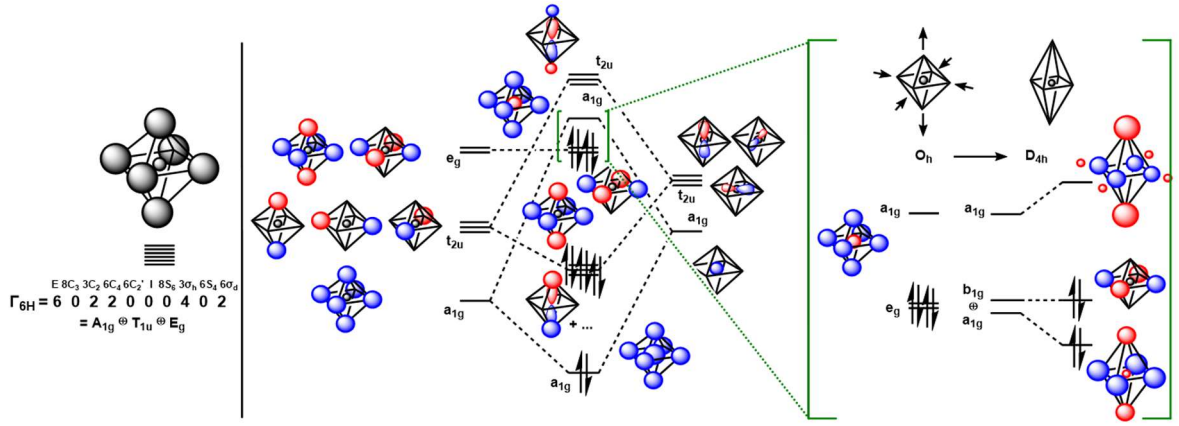
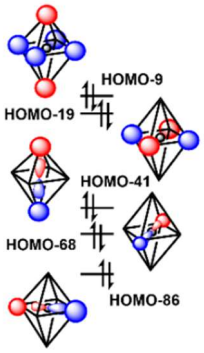


Figure 7 LCAO description of the hexahydridosilciate dianion and justification for second-order JT splitting by demonstration of the LUMO being the same symmetry as the HOMO after declining in symmetry.

This is evidently reminiscent of the well-known dianion SiF_6^{2-}, a stable and noncoordinating anion widely used throughout chemistry. This adopts an essentially perfect octahedral geometry owing to the very electronegative nature of the fluorides and the ionic nature of the bonding. In the hexahydridosilicate however, the hydrides are significantly less electronegative and the bonding more covalent. From a molecular orbital perspective, this manifests as the vacant a_{1g} orbital in the octahedral environment being very high in energy in SiF_6^{2-}, but in SiH_6^{2-} the vacant a_{1g} orbital is very close in energy. A low-lying vacant orbital in this case results in second-order Jahn-Teller distortion from O_h to D_{4h} by elongating one axis and compressing the orthogonal two, breaking the degeneracy of the HOMO from e_g to $a_{1g} \oplus b_{1g}$, one component of which matches the vacant LUMO, allowing mixing and consequently electronic benefit (Figure 7, right). Of course, multiconfigurational calculations of the different states would have to be calculated and their avoided crossing investigated to confirm second-order JT distortion over simply a difference in coordination environment, particularly as the reported IR spectrum[19] of the solid $K_2(SiH_6)$ shows no distortion away from octahedral.

Within our own calculated geometry, this declension is evident from the Si-H bond lengths: 1.617, 1.609 and 1.598 Å. In practice, the local change in environment is likely more influential, evident from the larger energy change in the p-like t_{1u} set than in in what would be the e_g like set expected to drive the JT distortion, shown in Figure 7 on the right, so the new b_{1g} orbital ends up lower in energy than the a_{1g} after considering relaxation with the moved t_{1u} orbitals. The canonical orbitals which correlate with the SiH_6^{2-} orbitals end up being the HOMO-9, -13, -41, -68, -86, and -185 with respective energies of -6.462, -6.834, -9.172, -9.989, -10.546, and -15.389 eV.



Of course, as discussed previously, the canonical orbitals do not necessarily occupy a privileged position when investigating electronic structure, perhaps particularly in this case due to long orthogonalisation tails from the central dianion with respect to the supramolecular framework, and the symmetry-breaking coordination environment. Consequently, we use several electronic structure methods to investigate the hexahydridosilicate.

3.3.1 Natural Bonding Orbitals

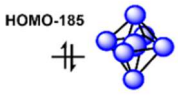


Figure 8 Relative energies of the canonical molecular orbitals for the $[SiH_6]^{2-}$ dianion within the assembly.

Natural Bonding Orbital[44] (NBO) analysis is a localisation procedure that recasts an electron density generated by another electronic structure program (herein the Gaussian suite), into a set of chemically legible one- and two-centre functions that approximate features of Lewis structures. In practice, the method proceeds by constructing natural atomic orbitals (NAOs) from the density matrix, combining them into natural hybrid orbitals (NHOs), and then forming natural bond orbitals (NBOs) and, where required, natural localised molecular orbitals (NLMOs), such that occupancies, hybridisations, and natural charges emerge in a manner that can be compared directly with chemical intuition. It is "natural" in the sense that the resultant orbitals are maximally occupied orthogonalised orbitals associated with a certain partition of the density matrix, i.e. to produce 2-centre 2-electron interactions (or potentially more sophisticated, non-Lewis features) in situations intrinsically unable to be described adequately.

NBO analysis of the hexahydridosilicate structure $[K_2\{(NON)Ca\}_2(SiH_6)]$ was not wholly insightful. The automatic partitioning does not place the $[SiH_6]^{2-}$ moiety in the same molecular unit, instead opting for an SiH_4 and two H_1 units, to be expected by searches for normal 8-electron species. The program was also unable to partition according to user specifications (3

partitions: [SiH_6][K_2][else]; or 10 partitions: [Si][H]$_6$[K_2][else]), instead always reverting to partitions that bifurcate the dianion, even when including options for 3c-2e$^-$ or more sophisticated bonding patterns. This is reflected in the NBO determination, wherein we see the expected (less Rydberg contributions) number of electrons from the NAOs to produce the appropriate charge on the dianion, but they are not appropriately symmetrical (Figure 9 and Table 3).

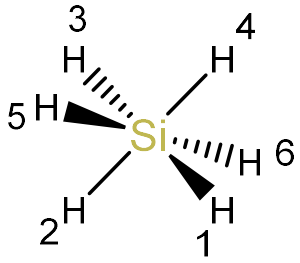


Figure 9 Hydride numberings for the orientation of the hexahydridosilicate as shown in Figure 10. Ther numbering here differs from the original publication for ease of understanding and that the original atom numbers are not discussed in this work.

NBO	Type	Atoms	Occupancy
154	Lone Pair	H1	1.33833
155		H2	1.33405
422	Antibonding	Si-H3	0.31885
423		Si-H4	0.31515
424		Si-H5	0.34011
425		Si-H6	0.34052
Total			**3.98701**
166	Bonding	Si-H3	1.94532
167		Si-H4	1.94496
168		Si-H5	1.92439
169		Si-H6	1.92450
Total			**7.73917**
Total			**11.72618**

Table 3 NBO Occupancy Data for the [SiH_6]$^{2-}$ anion in [K_2{(NON)Ca}$_2$(SiH_6)] (PBE0-D3BJ/BS2//PBE0-D3BJ/BS1)

MP2 interaction energies between the first set of NBOs (154-155, 422-425) shows strong interactions between the "Lone Pair"-s that are 154 and 155 and the only partially occupied "Antibonding" orbitals 422-425, which would originally have better been described as another set of 2 bonding orbitals in the fashion of NBOs 166-169 Table 4 and Figure 10).

Donor NBO	Acceptor NBO	MP2 Interaction Energy (kcal·mol^{-1})
154	422	106.88
	423	43.11
	424	51.06
155	423	106.32
	424	52.47
	425	44.38

Table 4 NBO MP2 Interaction Energies in kcal·mol^{-1} for the $[SiH_6]^{2-}$ anion in $[K_2\{(NON)Ca\}_2(SiH_6)]$ (PBE0-D3BJ/BS2//PBE0-D3BJ/BS1).

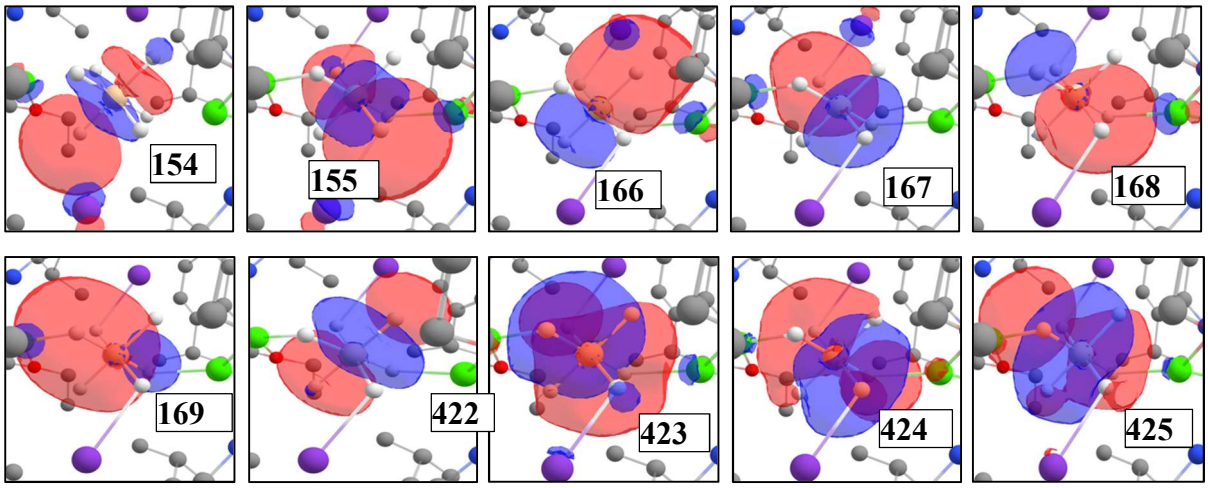


Figure 10 Visualised NBOs of $[K_2\{(NON)Ca\}_2(SiH_6)]$ associated with the $\{SiH_6\}^{2-}$ unit (PBE0-D3BJ/Def2-TZVPP//PBE0-D3BJ/BS1).

Unlike the parent silicate, NBO and NLMO analysis for the parent silylene dianion should be very effective, as it is essentially an isolated, electron-precise species. NBO suggests four valence orbitals localised to the silylene dianion with the following occupancies and proportions:

Orbital	Type	Occupancy	Composition
140	Lone Pair	1.89369	Si: $sp^{2.47}$ (28.83% s, 71.12% p)
141	Lone Pair	1.88060	Si: $sp^{1.57}$(38.84% s, 61.07% p)
160	Bonding	1.96989	38.88% Si: 0.6236$sp^{5.16}$ (16.14% s, 83.30% p) 61.12% H: 0.7818s (99.55% s)
161	Bonding	1.96983	39.42% Si: 0.6279$sp^{5.11}$ (16.26% s, 83.18% p) 60.58% H: 0.7783s (99.53% s)

Table 5 Relevant NBO compositions and occupancy for the $[SiH_2]^{2-}$ anion in $[K_2\{(NON)Ca\}_2(SiH_2)]$, showing the Lewis description of the species as the silylene dianion, isoelectronic to water.

This reflects somewhat of a "bunny ears" description, with each lone pair on the silicon having an average hybridisation of $sp^{2.02}$. Even though the p-character of the two orbitals is significantly different, clearly no separation into an unhybridised p orbital as required from a symmetry-preserving decomposition (which NBO is not). From an envelope hybridisation point of view, this leaves $p^{0.98}$ to form bonds with the hydrogen atoms, which is evident in the ~40% contribution from the silicon in each Si-H bond, each with p ~83% p character.

The associated natural charges and natural population analysis support a similar conclusion, yielding natural populations of Si: $3s^{1.55}3p^{3.75}$ and H: $1s^{1.19}/s^{1.20}$ and consequently natural charges of -1.33, -0.19 and -0.20 respectively. NLMO, however, reproduces the expected p and sp^2 lone pairs expected of the silylene dianion.

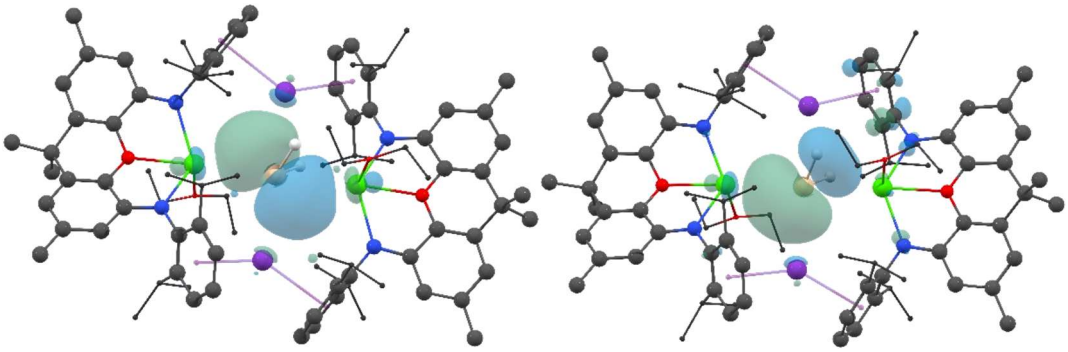


Figure 11 The NLMO lone pairs of the silylene dianion in $[K_2\{(NON)Ca\}_2(SiH_2)]$, left the p-like lone pair and right the sp^2-like lone pair.

3.3.2 Quantum Theory of Atoms in Molecules

Quantum theory of atoms in molecules (QTAIM), or often simply Bader analysis, draws information on structure and bonding directly from the topography of the electron density of a molecule. Pertinent to our analysis is the bond critical point (BCP), a point of zero gradient ($\nabla\rho(r) = 0$, where ∇ is the del operator) along a bond critical pathway between two atom critical points (ACP) with rank 3 signature -1 ((3,-1) critical points). In general, a larger value of the density ($\rho(r)$) at a critical point indicates a stronger interaction. Further information can be gained from the Hessian at the critical point, from both the magnitude of the Laplacian, $\nabla\rho^2(r)$, and the relative magnitudes of the eigenvectors of the Hessian at the BCP (representative of the ellipticity of the BCP, which can indicate different types of bonding such as covalent, noncovalent, σ, or π.

Figure 12 shows the QTAIM topological map of the silylene dianion $[K_2\{(NON)Ca\}_2(SiH_2)]$. Important are the BCPs between the silicon and each of the 4 metals, and the BCPs between

the silicon and each of its hydrides. These are of course further from the hydride than from the silicon, and further from the silicon than each of the metals, qualitatively showing the donor nature of the hydrides to the silicon, and the silylene dianion to the assembly.

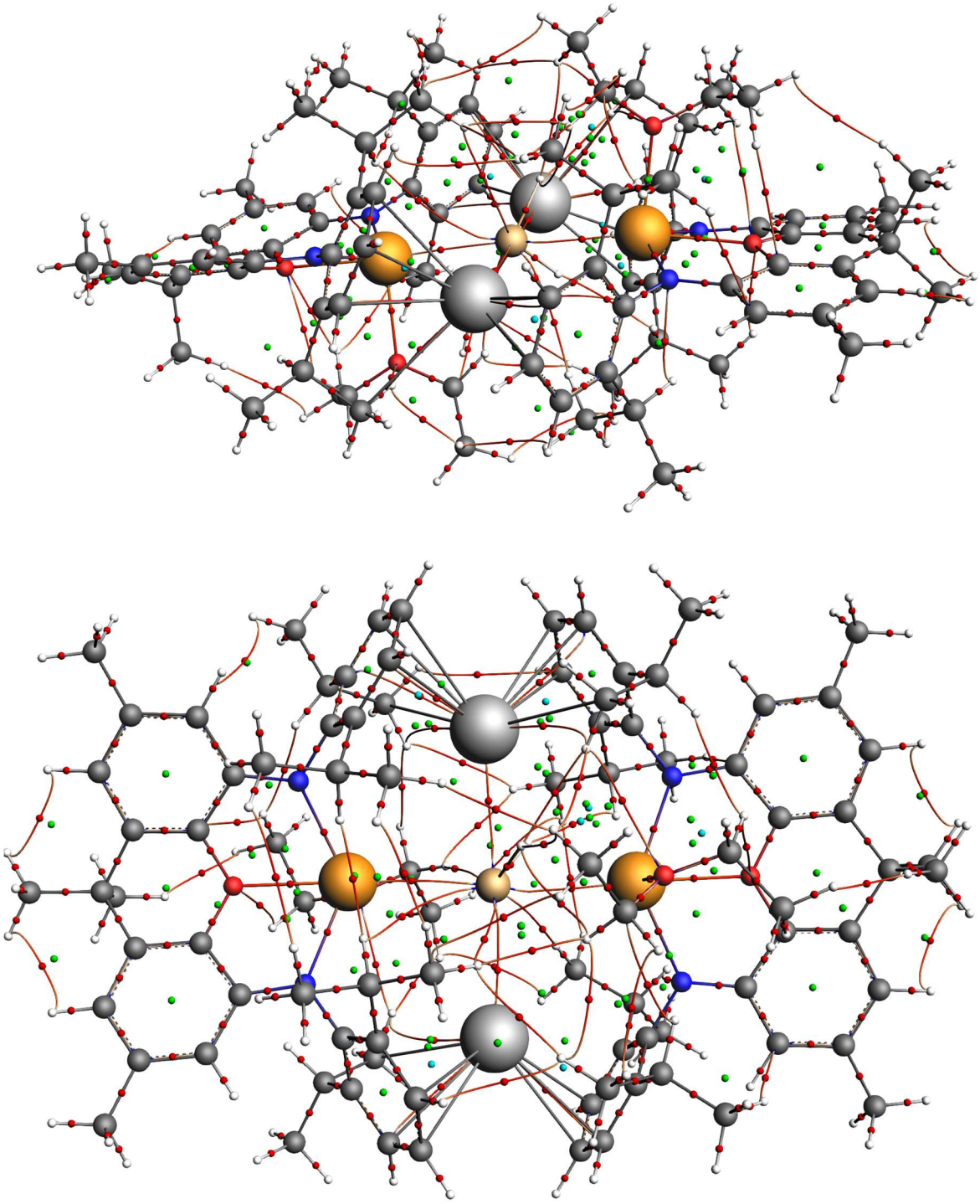


Figure 12 QTAIM topology maps of the [K_2{(NON)Ca}$_2$(SiH_2)] complex as seen from two different angles. BCPs are in red and link ACPs via displayed bond critical paths, green spheres are ring critical points and light blue spheres are cage critical points. Calcium in orange, potassium in silver, silicon in beige, and hydrogen in white.

Pertinent to our investigation are the interactions between the silylene dianion and the assembly, and the interactions within the silylene dianion. These are presented in Table 6. Other BCPs are present between both the silicon and various protons in the assembly and the hydrides and various protons in the assembly, however none of these have a density greater than 0.006 e^- $Bohr^{-3}$ and are essentially artefacts of long-range exponential density decay.

Bond Critical Point	ρ (e^- $Bohr^{-3}$)	$\nabla^2\rho$ (e^- $Bohr^{-5}$)	Hessian eigenvalues
Si-Ca1	0.024	0.042	λ_1 0.075 λ_2 -0.018 λ_3 -0.016
Si-Ca2	0.022	0.046	λ_1 0.069 λ_2 -0.013 λ_3 -0.010
Si-K1	0.016	0.038	λ_1 0.057 λ_2 -0.011 λ_3 -0.0090
Si-K2	0.013	0.039	λ_1 0.047 λ_2 -0.0055 λ_3 -0.0048
Si-H1	0.095	0.145	λ_1 0.36 λ_2 -0.12 λ_3 -0.10
Si-H2	0.093	0.149	λ_1 0.37 λ_2 -0.12 λ_3 -0.10

Table 6 QTAIM data for the silylene dianion within the assembly.

These values align well with the expected results. The magnitude of ρ(r) at the Si-H BCPs is slightly smaller than in typical silane complexes (0.12-0.14 e^- $Bohr^{-3}$) but in good agreement with the density as a function of Si-H distance (for 1.56 in the silylene dianion compared with 1.46-1.49 in the previously calculated silanes).[45] This is to be expected from formal hydrides bonding to a 0-valent silicon centre; this follows also from the trend of Si-H bond elongation with less electronegative ligands (*ad absurdum* absence of a ligand).

Similarly, the BCPs between the Si and the metals are very small, *ca.* ¼ of the density between the silicon and the associated hydrides. The interactions with the more positively charged calciums are marginally larger than the potassiums, and each seems to have limited dependence on the direction – the calcium and the potassium on the opposite side of the silicon from the hydrides have BCPs only a few milli-$e^{-}Bohr^{-1}$. None of the 6 BCPs have any appreciable ellipticity, *i.e.* $\lambda_2 \approx \lambda_3$, expectedly indicative of only sigma electron density; additionally, the comparatively large value for the Si-H bonds indicates covalency, compared with the small value of $\nabla^2\rho$ for the Si-M interactions indicating noncovalent interactions.

3.3.3 EDA ETS-NOCV

The ETS-NOCV energy decomposition method[46] is a way of taking the energetic interactions between separated, geometrically unrelaxed fragments of a larger complex and decomposing those interactions into what would be the responsible parent orbitals.

The interaction energy is described as:

$$\Delta E_{int} = \Delta E_{elstat} + \Delta E_{Pauli} + \Delta E_{orb} + \Delta E_{disp}$$

Equation 2 Interaction energy in the EDA ETS-NOCV regime.

Where the total interaction energy (ΔE_{int}) is the sum of the components of semiclassical electrostatic interaction between the overlapping, electronically unrelaxed fragments (ΔE_{elstat}), the energy of the subsequently antisymmeterised orbitals (ΔE_{Pauli}), and then the electronically relaxed orbitals. ΔE_{disp} is the dispersion energy between the fragments, but is not uniquely defined and uses only the empirical, atom pair-wise energy, so is the same regardless partition and grants very limited insight into the actual interactions unless it is the dominant contribution.

Most pertinent to the investigation at hand is the consequent ability to distinguish between different possible charge descriptions of the fragments. If the noninteracting fragments have a similar density to the interaction fragments, then the relaxation associated with ΔE_{orb} will be small, but if the fragments have significantly different densities ΔE_{orb} will be comparatively larger. As such, it is possible to distinguish between the most appropriate way to describe the fragments based upon which has the most similar density to the interacting case.

The two obvious possible charge combinations for the presented system are either a neutral silylene (SiH_2) within a neutral assembly, or a charged silylene dianion (SiH_2^{2-}) within a charged assembly (Figure 13). We chose to only investigate singlet fragments as we have no

reason to believe either a) the parent silylene to be triplet, or b) pairing of spins between the host and the guest.

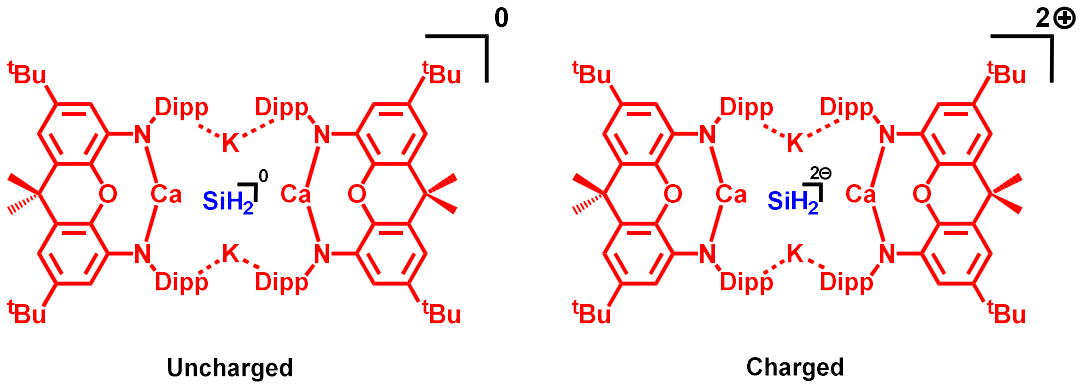


Figure 13 Possible fragment charge choices for [K$_2${(NONCa)$_2$(SiH$_2$)] in the EDA-NOCV analysis, with the fragments coloured red and blue to distinguish demarcations. Left: neutral, singlet fragments; Right: inner fragment silylene dianion, outer fragment dicationic assembly.

The qualitative analysis of the ETS-NOCV method principally relates to the deformation density, $\Delta\rho(r)$:

$$\Delta\rho(r) = \rho_{A+B}(r) - (\rho_A(r) + \rho_B(r))$$

Equation 3 Deformation density in the ETS-NOCV regime.

Where $\rho_x(r)$ represents the electron density as a function of space for fragment x.

Each NOCV is defined as an eigenvector of the deformation density matrix, using the fragment molecular orbitals as a basis, allowing for a qualitative assessment from and to whence electron density flows. The magnitude of the eigenvalue gives the magnitude of the electron density migration, and so the analysis is most useful when only a few orbitals have significant eigenvalues, and come in pairs, the sum of which gives $\Delta\rho_n(r)$, where $\Delta\rho_n(r)$ is the nth eigenvector.

	$[SiH_2]^{2-}$ + $[\mathbf{NON}CaK]_2^{2+}$	$[SiH_2]$ + $[\mathbf{NON}CaK]_2$
ΔE_{elstat} (kcal·mol^{-1})	-602.95	-213.86
ΔE_{Pauli} (kcal·mol^{-1})	273.06	375.91
ΔE_{orb} (kcal·mol^{-1})	**-122.28**	**-269.01**
ΔE_{disp} (kcal·mol^{-1})	-10.83	-10.83
ΔE_{int} (kcal·mol^{-1})	-462.99	-117.79

Table 7 Energy decomposition analysis of the two candidates, silylene and silylene dianion forms of the pairs. The comparatively small ΔE_{orb} for the silylene dianion case indicates this to be a better description of the system, supported by the specific deformation densities (vide supra).

Ultimately, the analysis supports the interpretation of a silylene dianion encapsulated in the pocket. $\Delta E_{orb\text{-}charged}$ is -122.25 kcal·mol^{-1} vs $\Delta E_{orb\text{-}neutral}$ is -269.01 kcal·mol^{-1}, which is over twice the benefit of relaxation, and similar to other reported relaxations such as N_2^{2-} $[(BDI)Ca(THF)]_2^{2+}$ (ΔE_{orb} = −225.2 kcal·mol^{-1}) reported by Harder, Frenking and co-workers.[47]

3.3.3.1 Uncharged Case $[SiH_2]$ + [**NON**CaK]$_2$

In the uncharged case, there are only three deformations with significant eigenvalues, with one clearly dominant deformation. $\Delta\rho_1(r)$ is excess assembly-based density flowing into the vacant p-orbital on the silylene fragment for a full 2 electrons, "forming" the silylene dianion, while the others are essentially just accompanying relaxations. $\Delta\rho_1(r)$ accounts for 93% of the total ΔE_{orb} and a similar proportion of the charge migration. Interrogating the relaxation charge per atom using the atomic basis functions gives Si = -1.47, K1 = 0.23, K2 = 0.35, Ca1 = 0.71, and Ca2= 0.60 (no other atom has a greater than 0.06 absolute relaxation. Sum metals = +1.89) showing that the silicon essentially receives ¾ of an electron pair basically entirely from the metals. Evidently, in the neutral case the metals take on a lower oxidation state amongst themselves and then transfer these excess electrons to the guest, seemingly from one diffuse sigma orbital shared between all the metals (Figure 18).

The remaining Δρ (-6.0 kcal·mol^{-1}, 2.2%) is evidently much less significant.

3.3.3.2 Charged Case $[SiH_2]^{2-}$ + [**NON**CaK]$_2^{2+}$

In the charged case, however, there are four "significant" ΔE_{orb}s, each smaller than -26 kcal·mol^{-1} and totalling to only 48.4% of the total ΔE_{orb}. $\Delta\rho_1(r)$ appears to be a "tightening" of the HOMO p-orbital on the silylene dianion, and $\Delta\rho_2(r)$ the polarisation of the sp^2 silylene lone pair towards the metals, very comparable to $\Delta\rho_2(r)$ in the neutral case in both density and energy (-10.3 vs -8.7 kcal·mol^{-1}) but more diffuse due to the higher initial charge. Beyond these, even $\Delta\rho_3(r)$ is difficult to ascribe any meaningful purpose beyond the expected polarisation and relaxation caused by bringing the charged guest and assembly together.

While $\Delta\rho_1(r)$ and $\Delta\rho_2(r)$ are somewhat directional, interacting between the silylene dianion and the charged assembly mostly in the regions of the silylene dianion p-like lone pair and the silylene dianion sp^2-like lone pair respectively, each are of small magnitudes and opposite symmetries, and beyond this the small contribution relaxations are essentially independent of the guest's orientation within the assembly. This is in excellent agreement with the

experimental evidence that there is very minimal directional preference within the cavity, with a crystallographic preference at 150 K in the same orientation as that computed, and no difference in assembly resonances in the ^{1}H NMR spectra showing no significant orientational preference and essentially free rotation at room temperature.

This is what would be expected for a system where the densities are already "correct" in the noninteracting regime: limited benefit beyond the semiclassical electrostatic attraction between the fragments, and vague, diffuse relaxation of the densities in an orbital sense. Even the Pauli repulsion is significantly smaller than in the uncharged case, as the orbitals only need to orthogonalise in their tails.

The remaining $\Delta\rho$ (-63.0 kcal·mol^{-1}, 51.6%) accounts for more than half of the remaining orbital relaxation energy, but again cannot be ascribed to any one major interaction and is all ascribed to similar intra/inter-fragment relaxations and polarisations each individually of a small amount of energy.

Overall, we suggest that the description of a silylene dianion bound within the assembly only by semiclassical electrostatic interactions yields the best description of the overall system.

The following Figure 14-Figure 20 show the significant contributions to each deformation eigenfunction.

3.3.3.3 Charged Interactions

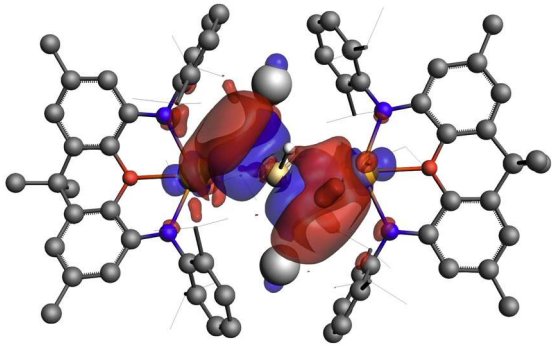
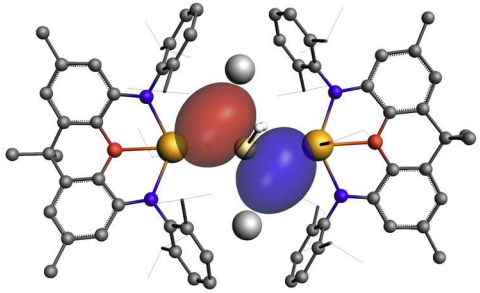


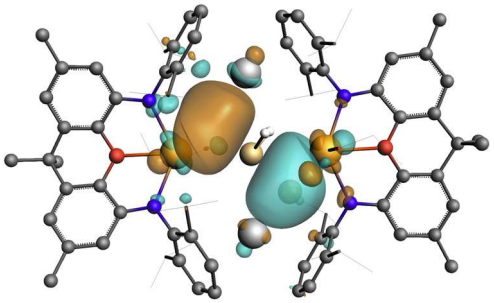
Figure 14 First deformation density eigenfunction, showing inter-fragment relaxation. The only occupied orbital connected with this is the HOMO p-like lone pair of the silylene dianion fragment, and the unoccupied orbitals including a high energy pi symmetry orbital on the silylene dianion, and two vacant metal-based LUMOs on the assembly, broadly representing a polarisation away from the dianion pi lone pair towards the assembly. (Red shows charge depletion, blue shows accumulation). The two columns opposite show the relevant basis molecular orbitals, the middle column for the silylene dianion and the right column for the assembly.

$\Delta E_{orb1} = -25.5\ kcal \cdot mol^{-1}$

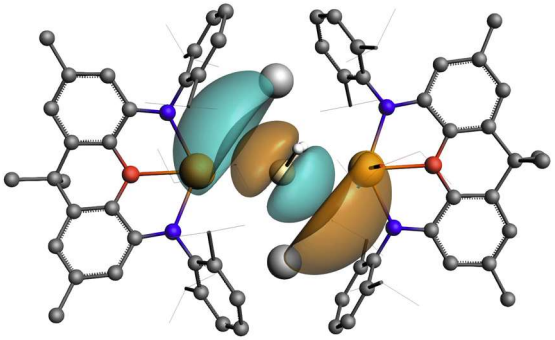
$v_1 = \pm 0.528$



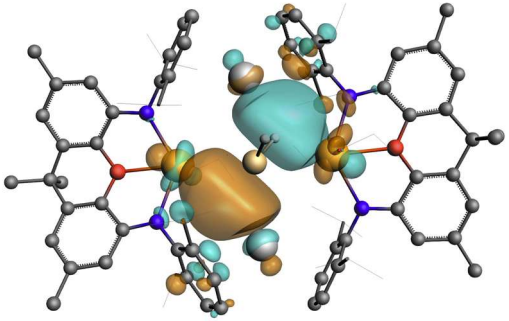
HOMO



LUMO+1



LUMO+4



LUMO+2

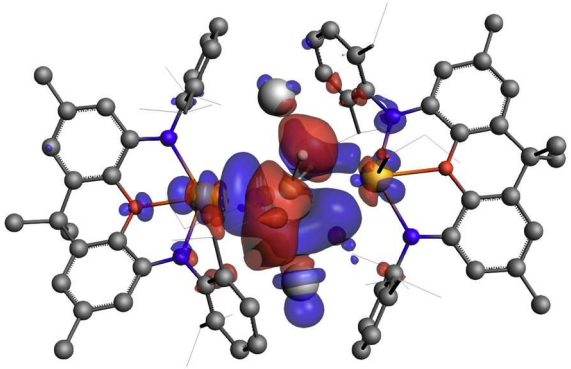
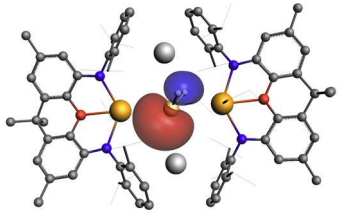


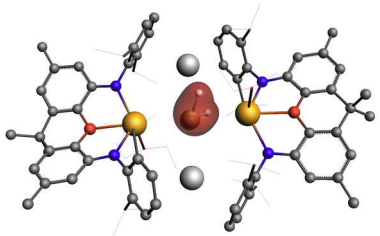
Figure 15. Second deformation density eigenfunction, showing a minor intrafragment relaxation. The occupied orbitals connected with this are the sigma symmetry orbitals of the silylene dianion fragment, and the unoccupied orbitals include two diffuse sigma orbitals on the silylene dianion fragment, the vacant all in-phase unoccupied metal orbital, and another metal-based sigma orbital of appropriate spatial extent. The eigenfunction broadly represents a polarisation away from the dianion sigma lone pair towards the assembly. (Red shows charge depletion, blue shows accumulation). The two columns opposite show the relevant basis molecular orbitals, the middle column for the silylene dianion and the right column for the assembly.

ΔE_{orb2} = -10.3 kcal·mol^{-1}

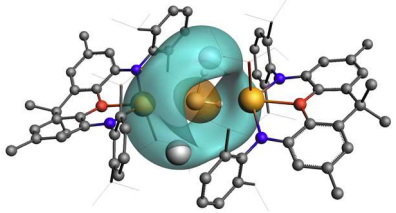
v_2 = ±0.294



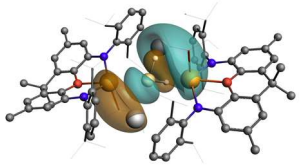
HOMO-1



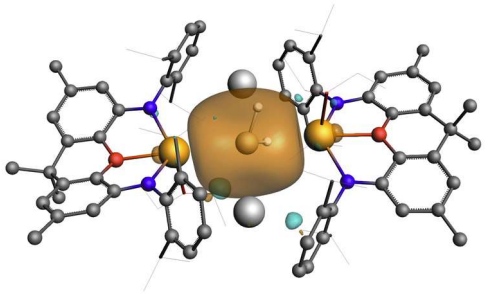
HOMO-3



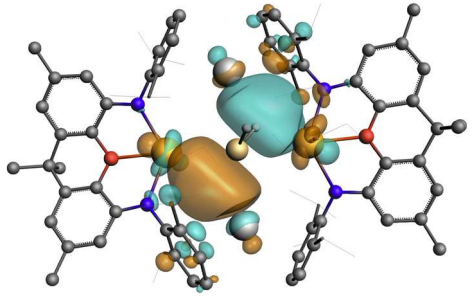
LUMO



LUMO+2



LUMO



LUMO+2

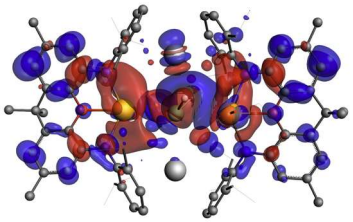
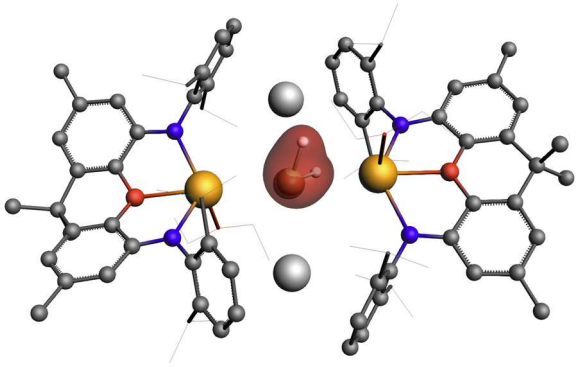


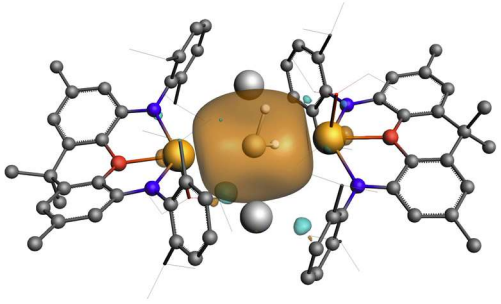
Figure 16 Third deformation density eigenfunction. A very large number of contribution orbitals have very small contributions to this eigenfunction, showing a complex relaxation over both fragments. (Red shows charge depletion, blue shows accumulation). The two columns opposite show the relevant basis molecular orbitals, the middle column for the silylene dianion and the right column for the assembly.

ΔE_{orb3} = -5.6 kcal·mol^{-1}

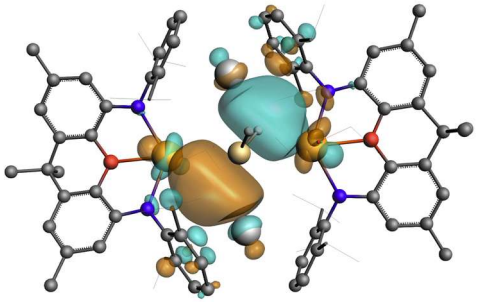
v_3 = ±0.191



HOMO-3



LUMO



LUMO+2

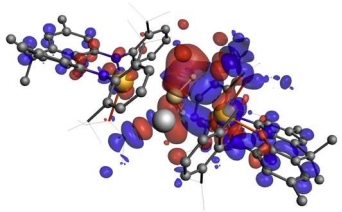
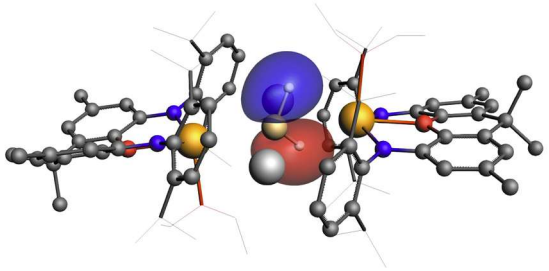


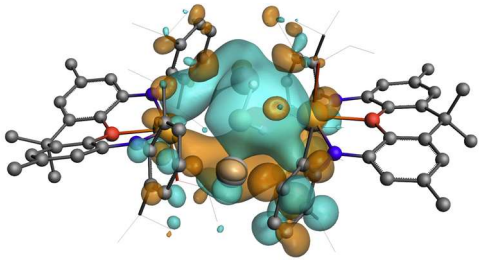
Figure 17 Fourth deformation density eigenfunction. A very large number of contribution orbitals have very small contributions to this eigenfunction, showing a complex relaxation over both fragments. (Red shows charge depletion, blue shows accumulation). The two columns opposite show the relevant basis molecular orbitals, the middle column for the silylene dianion and the right column for the assembly.

$\Delta E_{orb4} = -4.4$ kcal·mol^{-1}

$v_4 = \pm 0.162$



HOMO-2



LUMO+3

3.3.3.4 Uncharged Interactions

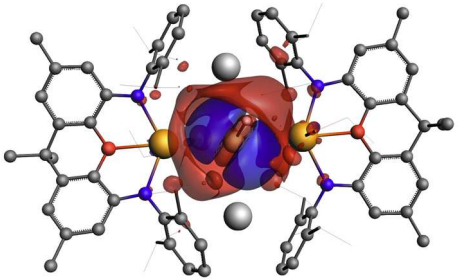
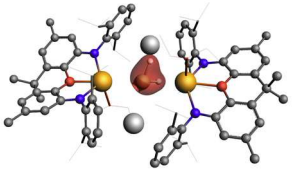


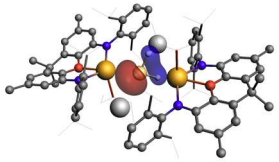
Figure 18 First deformation density eigenfunction, showing charge flow from the diffuse Ca-K-K-Ca sigma orbital in the neutral assembly to the vacant p-orbital of the silicon in the neutral silylene. That the value of ΔE_{orb1} is two orders of magnitude greater than the other contributions shows that almost all the energetic benefit of the orbital relaxation originates from this interaction. (Red shows charge depletion, blue shows accumulation). The two columns opposite show the relevant basis molecular orbitals, the middle column for the silylene and the right column for the assembly.

$\Delta E_{orb1} = -250.0\ kcal{\cdot}mol^{-1}$

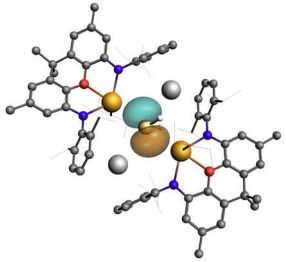
$v_1 = \pm 2.000$



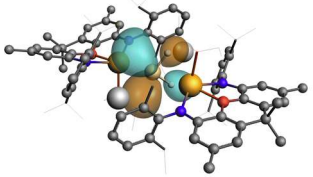
HOMO-2



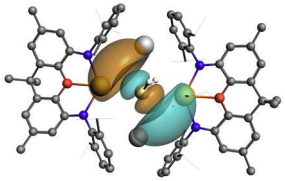
HOMO



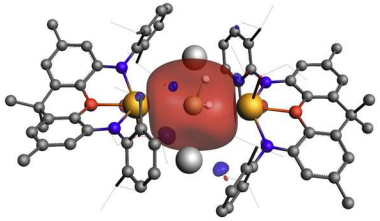
LUMO



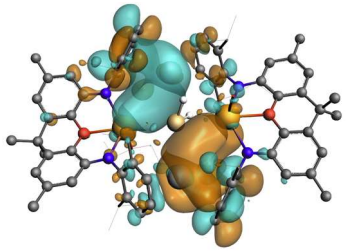
LUMO+1



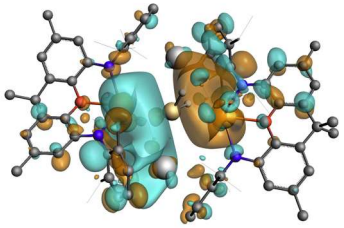
LUMO+5



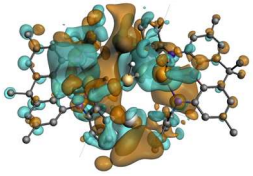
HOMO



LUMO+8



LUMO+9



LUMO+31

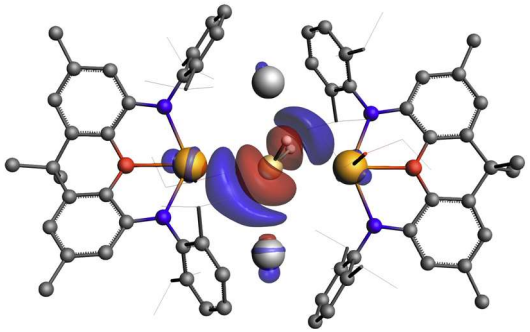
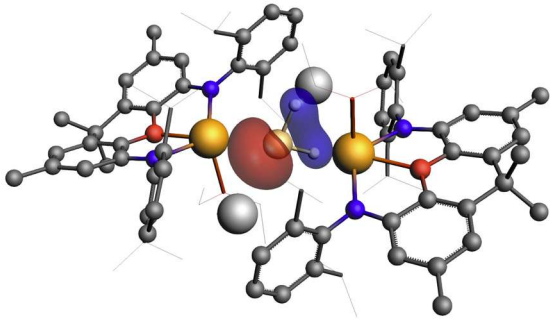


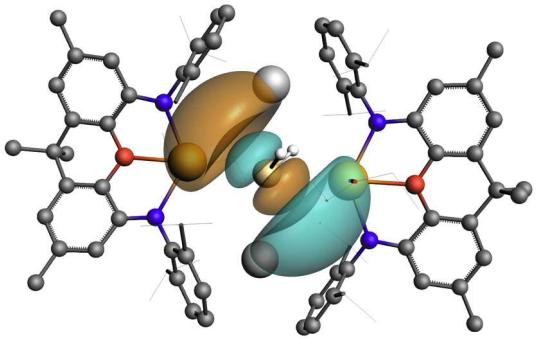
Figure 19 Second deformation density eigenfunction, showing charge flow polarising from the silylene sigma lone pair orbital towards the low-lying orbitals on the Ca/K centres. The low value ΔE_{orb2} shows the minimal energetic importance of this eigenfunction compared with $\Delta E_{orb1.}$ (Red shows charge depletion, blue shows accumulation). The two columns opposite show the relevant basis molecular orbitals, the middle column for the silylene and the right column for the assembly.

$\Delta E_{orb2} = -8.7$ kcal·mol^{-1}

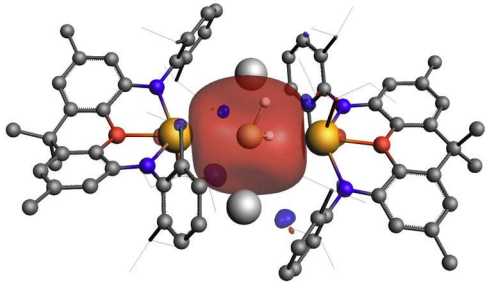
$v_2 = \pm 0.324$



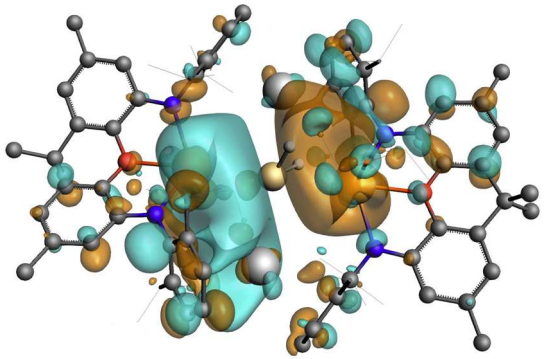
HOMO



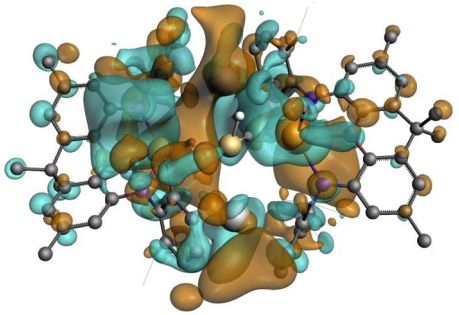
LUMO+5



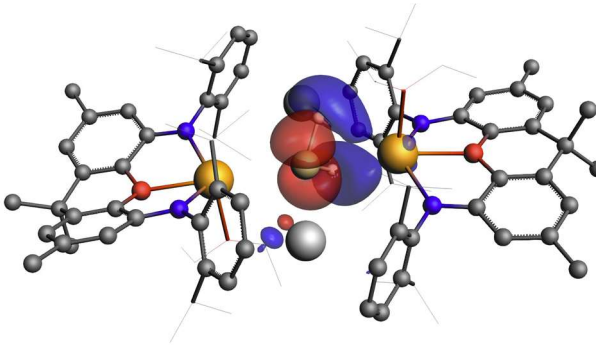
HOMO

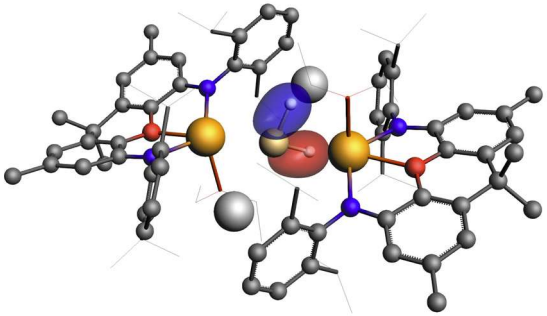


LUMO+9

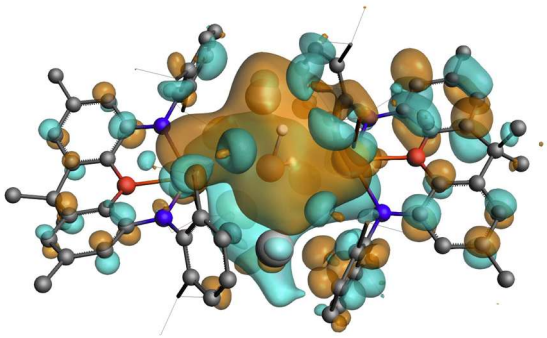


LUMO+31





HOMO-1



LUMO+2

Figure 20 Third deformation density eigenfunction, showing relaxation. The low value ΔE_{orb3} shows the minimal energetic importance of this eigenfunction compared with $\Delta E_{orb1.}$ (Red shows charge depletion, blue shows accumulation). The two columns opposite show the relevant basis molecular orbitals, the middle column for the silylene and the right column for the assembly.

$$\Delta E_{orb3} = -4.4 kcal \cdot mol^{-1}$$

$$v_3 = \pm 0.234$$

3.4 Mechanism of Formation

Formation of the silylene dianion from the silicate is a profoundly unexpected result not only because of the unique electronic structure of the daughter, but also because of the mysterious circumstances of its conception. Experimental evidence shows evolution of hydrogen as the sole by-product of the reaction, as well as the difficult but possible reversibility of the process by exposing the silylene dianion to multiple atmospheres of hydrogen gas. This subchapter details a computational investigation of the mechanism of formation.

3.4.1 Gas Phase Anion Exploration

The most obvious explanation is, of course through parallels with transition metal chemistry, a series of two reductive elimination-like processes from the central silicon atom (Figure 21) with the remaining metal-ligand assembly remaining essentially unchanged.

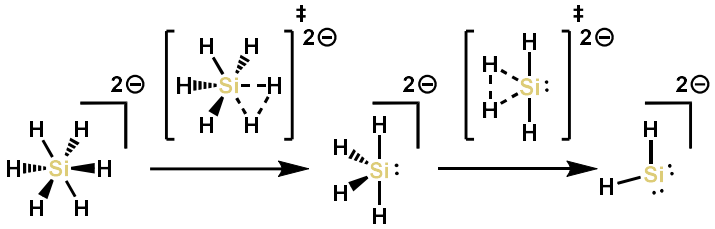


Figure 21 The simplest possible pathway for the anion to transform from the silicate to the silylene dianion, through two reductive elimination-like steps.

However, reductive elimination is orbitally forbidden from an octahedral centre without d-orbitals. This can be determined through Woodward-Hoffmann analysis and is a well-known result.[48,49]

This is perhaps best understood by comparison with transition metals and in the reverse process (through microscopic reversibility), wherein the dihydrogen bond is broken through donation from a π-symmetry orbital into the vacant σ* orbital of dihydrogen and donation from the dihydrogen σ bond into a vacant metal-centred orbital. No orbitals of appropriate symmetry are available to the SiH_4^{2-} to donate into the dihydrogen σ* orbital, nor a vacant orbital of appropriate symmetry and energy on the already hypervalent silicon centre to accept the σ-bond from the dihydrogen (Figure 22).

Gas-phase calculations on the SiH_6^{2-} dianion were unable to elucidate a concerted reductive elimination-like transition state, instead always resulting in the extrusion of a hydride.

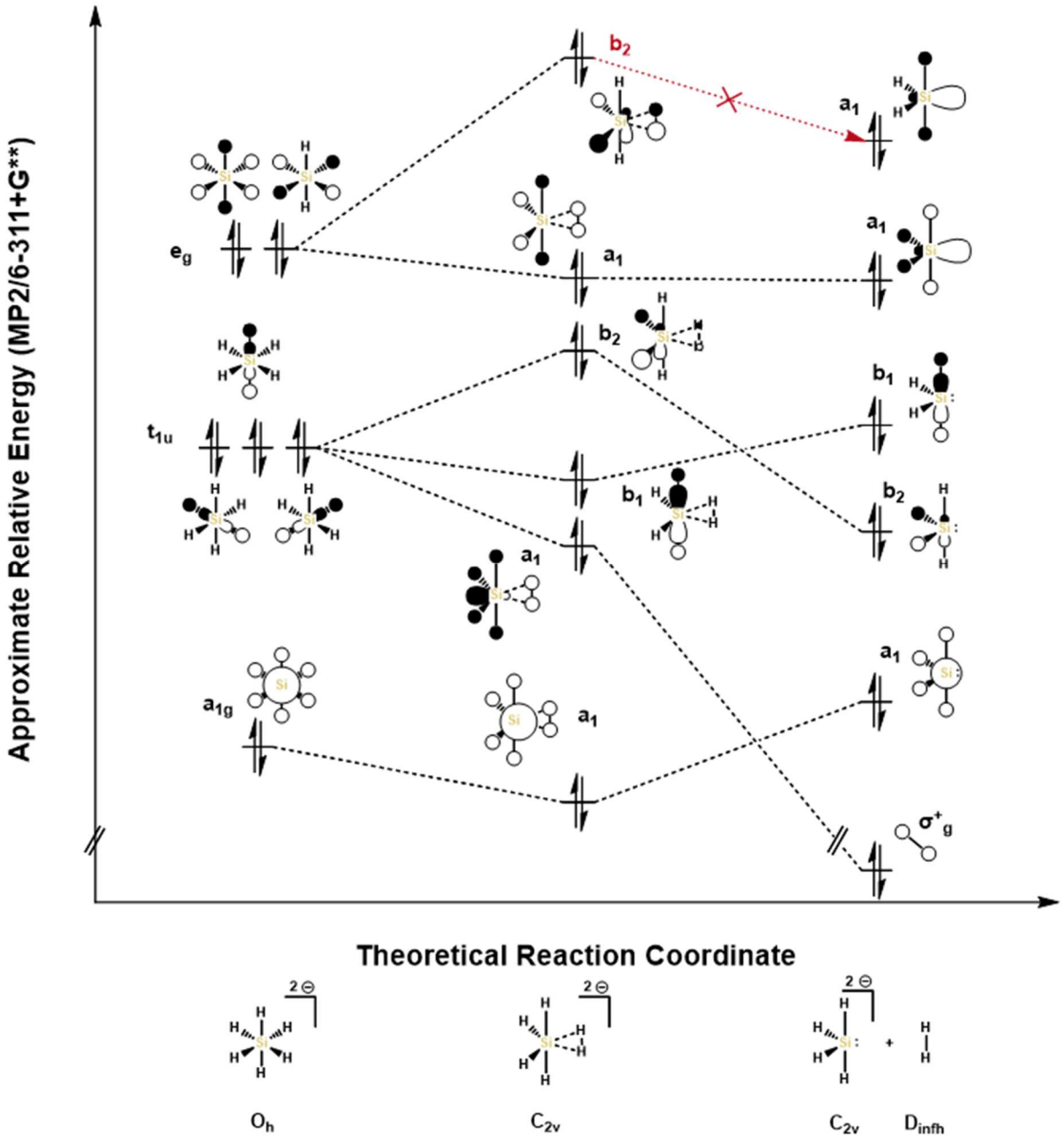


Figure 22 Correlation diagrams for the valence orbitals involved in the reductive elimination of dihydrogen from the silicon centre for both gas-phase [SiH_6^{2-}].

Additionally, (in the forward direction), the orbital which must become the lone pair (again, no such one orbital *etc. vide supra*) begins as a b_2-symmetry orbital (e_g in the silicate) but must end as an a_1, which is the source of the orbitally forbidden nature (as much as a single orbital can thereof be responsible). If instead the complex in question were trigonal bipyramidal, a favourable reordering of valence orbitals splits the previously e_g set into the nondegenerate a'_1 and a''_2, and parity is preserved for all the symmetry elements of the transition state.

The D_{3h} species can be seen as losing a hydride, so the assembly could be seen as supporting both a hydride and a SiH_5^- anion. Unfortunately, while no longer being symmetry forbidden, the acceptor orbitals on the silicon centre remain too high in energy and gas-phase calculations of the SiH_5^- concerted reductive elimination remains elusive, with the C_{2v} transition state elucidated being an unphysical second order saddle point (two imaginary frequencies, -1239.22 cm^{-1} [H-H coupling] and -220.24 cm^{-1} [perturbation to lower symmetry]). An alternative C_s symmetry transition state can be found with two different Si-H bond lengths, perhaps more akin to one of the hydrides on the SiH_5^- anion attacking a "proton" (*vide supra*), but still linking the two minima (SiH_5^- and $SiH_3^- + H_2$).

Evidently, hydrogen gas can be evolved through the simple acid-base reaction between a hydride and a "proton". In the case of the gas-phase anion SiH_4^-, a transition state can be found which amounts to a hydride attacking SiH_3^- to form the gas-phase silylene dianion and hydrogen gas. This is evidently quite difficult for electrostatic reasons, as the hydrogens in the SiH_3^- should be considered more hydridic than protic due to their greater electronegativity than silicon and the overall charge on the species already being negative. This process could be imagined for different combinations of hydride and formal Brønsted acids, giving rise to multiple possible pathways utilising either hydride proton coupling or concerted reductive elimination-like processes.

A gas-phase pathway for the separated ions alone (*i.e.* without the assembly) calculated at the MP2/6-311+G** level of theory[50] is presented in Figure 23. Beyond an approximately 60-80 $kcal \cdot mol^{-1}$ columbic penalty/relief for adding/removing a negative charge from the already anionic system (*i.e.* 1 to 3 and 5 to 7 respectively), Figure 23 presents a potentially feasible (or at least not unphysical) mechanism. This was a promising beginning to suggest the assembly could possibly alter the energies of a similar mechanism to result in the experimentally observed process. This was the only elucidated pathway we could discern for the gas phase anions, but preempts the multitude of possibilities within the assembly.

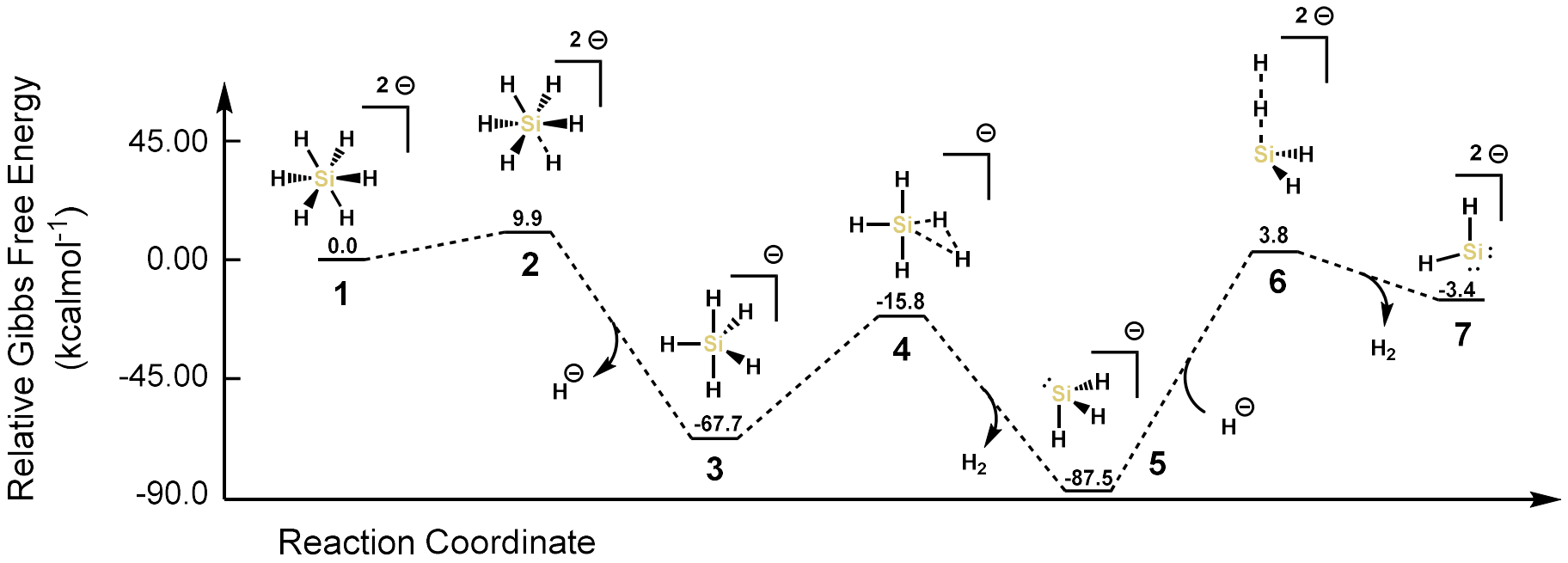


Figure 23 A gas-phase pathway for the anions calculated at the MP2/6-311+G level of theory. The process shows the hexahydridosilicate 1 losing a hydride through transition state 2 to form the pentahydridosilicate 3. This consequent species undergoes formal reductive elimination and loss of dihydrogen to produce the silyl anion 5, which undergoes hydride-proton coupling with the previously ejected hydride in transition state 6 to eliminate the second equivalent of H_2 and form the gas-phase silylene dianion 7.**

3.4.2 Mechanism Within the Assembly

As discussed above, a great many pathways are available for the two formal reductive eliminations to produce the product. A great many pathways were attempted in the elucidation of the reaction mechanism but only those which proved productive or saliently unproductive are presented here for the sake of brevity.

Analogously to the gas phase pathway, the first attempted transition state was concerted reductive elimination from the hexahydridosilicate. Due to second-order Jahn-Teller distortion mixing the low-lying unoccupied a_{1g} orbital with the HOMO e_g set in the hexahydridosilicate anion, causing a minor descent in symmetry from the O_h point group to the D_{4h} point group ($O_h \rightarrow D_{4h}$: $E_g \rightarrow A_{1g} + B_{1g}$, allowing the mixing of previously orthogonal e_g (filled) and a_{1g} (vacant) orbitals. This does not occur in the well-known SiF_6^{2-} anion due to the much more electronegative nature of the fluoride ligands and consequently much greater HOMO-LUMO gap.), in tandem with the asymmetrical environment of the assembly cavity (although this allows for very nearly C_i symmetry to be preserved), there is a possibility for different coupling pathways for the reductive elimination, necessitating the investigation of 3 different H-H decreasing angle scans. However, none were able to elucidate a transition state for the formation of dihydrogen gas, simply raising in energy with a lowering angle until an unphysical HH distance, as expected from the preliminary investigations.

Instead, hydride transfer from the central silicon to the surrounding assembly was attempted, successfully in the case of only one of the unique hydrides, resulting in TS1 (Figure 26). The resultant intermediate [SiH_5 H] possesses two anions in the cavity of the assembly, each bearing a 1^- charge. Interestingly, elimination from the SiH_5^- pseudo-D_{3h} species is no longer orbitally forbidden.[51] Consequently, equatorial-equatorial, axial-axial, and axial-equatorial angle decreasing scans were attempted, although none were fruitful.

Interestingly the hydride-proton distance decreasing scan resulted in a local maximum and promising transition state, however the optimised transition state structure was a methyl rotation from a truncated tert-butyl group. Manually checking each point in the optimisation and restarting it from the most promising step where the largest contributors to the most negative eigenvector involved the silicon and the relevant hydrogens resulted in a remarkable and unintended transition state: the previously sought SiH_5^- C_s transition state. Most saliently, the coupling hydrogens were facing “out” of the cavity, and the IRC resulted in the unexpected extrusion of H_2 from the cavity in tandem with its formation. Serendipitously, this transition

state, “TS2 R. E.” in Figure 26, did in fact link back to the [SiH_5 H] intermediate. Unfortunately, the barrier height was calculated to be an unphysical 53.7 kcal·mol^{-1}, and was the only concerted reductive elimination transition state we were able to elucidate, perhaps expectedly due to silicon’s lack of valence d-orbitals.

Revisiting the hydride-proton coupling transition state, by tightening the convergence requirements and decreasing step size, we were able to elucidate the desired transition state, TS2, at a much lower energy of 35.0 kcal·mol^{-1}, however, experimentally this would result in an unpromising half-life of *ca*. 60 years at 70 °C. The IRC method linked this transition state back to the SiH_5 H and to the new intermediate SiH_4^{2-} H_2. Despite many attempts, we were unable to elucidate a transition state for the evolution of H_2, no maximum was ever discerned for H_2 moving from the inside of the assembly’s cavity to the next intermediate, the H_2 adduct on the surface of the assembly (“SiH_4 H_2 (outside)”). Predictably, the H_2 adduct dissociation also possesses no discernible maximum from which a transition state could be elucidated to form the next intermediate SiH_4^{2-}.

The SiH_4^{2-} moiety itself, perhaps predictably, also barrierlessly ejects a hydride. The C_{2v} dianion readily ejects an axial proton to form the well-known silyl anion SiH_3^- and a hydride. This is expected of the unstable hypervalent SiH_4^{2-} as the axial hydrogen-silicon bonds are already highly elongated and in the gas phase dianion would possess a bond order of ½ by molecular orbital theory. This results in the formation of the more stable “SiH_3 H” intermediate with the silyl anion bound to a calcium, and the other hydride in the familiar position bridging the other calcium and both potassium centres, analogously to the parent hydride complex [K_2{(NON)Ca}$_2H_2$] with one hydride replaced by a silyl moiety.[5]

An alternative pathway to formation of [SiH_3 H] intermediate was explored in a similar hydride-proton coupling reaction, however instead of using the SiH_5^- anion as the source of the “proton”, silane gas can be used instead. This involves the initial dissociation of another hydride from the SiH_5^- anion in “TS H” to form the intermediate [SiH_4 H H] which is very much the known hydride complex with a molecule of silane also within the assembly’s cavity. We expected this to be a lower energy transition state, as it involves deprotonation of a neutral rather than anionic species, but also possesses greater steric pressure from three formally separate molecules within the cavity. The scan and subsequently elucidated hydride-proton coupling transition state TS2′ yielded a slightly higher energy transition state at 38.4 kcal·mol^{-1}, suggesting that the basicity of the hydride or the steric crowding within the cavity is more

important than the electrophilicity of the proton, a salient fact for the silylene dianion autocatalysis (*vide infra*).

From the [SiH_3 H] intermediate it is unnoteworthy that the silyl anion does not reductively eliminate hydrogen gas, as it is observed to be stable in its own right at elevated temperatures in other cases,[52] although we dogmatically searched for such a transition state ourselves and were unsurprised by its absence.

Consequently, hydride-proton coupling was again explored and elucidated, ultimately yielding TS3. This proved more challenging to elucidate than initially suspected, as the pseudo-C_s transition state was repeatedly elucidated as a second-order saddle point, with the Si-H-H axis colinear with the Ca-Ca axis, the SiH_2 moiety (the portion without the hydrogens which will become H_2) rotates around the Ca-H-H-Ca axis as the second imaginary frequency. Perturbing the structure along the unproductive imaginary frequency and searching for the transition state resulted in the same unperturbed structure. Ultimately the transition state was found by perturbing along the unproductive frequency, freezing the geometry of the SiH_2-H-H moiety and optimising to a minimum, and then optimising for a transition state from the resultant structure. The elucidated transition state TS3 (in Figure 26), which was confirmed to connect the intermediates [SiH_3 H] and [SiH_2 H_2] *via* the IRC method in both directions.

Similarly to the previous dihydrogen leaving step, difficulty was encountered elucidating the transition state for its removal from the assembly, and no local maximum was discernible.

Taken together, we were able to elucidate a mechanism (shown in black in Figure 26) with a rate determining barrier height of 35.00 kcal·mol^{-1}. This is evidently unfeasible in the experimental temperature ranges, and an alternative mechanism must be posited. We were able to describe in some detail, from experimental results, an unexpected alternative mechanism involving an *autocatalytic cycle*, using the silylene dianion to react with the starting hexahydridosilicate directly, discursively removing the dihydrogen gas through repeated uses of the energetically viable 27.2 kcal·mol^{-1} barrier TS3. DFT-motivated explanations are presented below.

3.4.3 Density Functional Theory Explanations in Autocatalytic Dehydrogenation

As alluded to above and will be explained below (*e.g.* Figure 37), the actual reaction occurs through an autocatalytic mechanism.

Due to hybrid density functional theory (*i.e.* PBE0-D3BJ) scaling at a minimum as $O(n^2 \cdot \log(n))$ but naïvely as $O(n^4)$ (where n is a measure of the system size, typically number of basis functions), we are computationally limited in the size of the system we can compute. Even the 2091 symmetry-adapted basis functions of the silylene dianion at the double-zeta level of theory of BS1 is taxing, moving to the *ca.* 4200 basis functions of a system contacting 4 copies of the **NON**Ca moiety would be computationally intractable.

But perhaps computing smaller, 2-ligand systems as before is enlightening. We deem several observations to be salient:

1. A redox process must occur between the Si(0) in the silylene dianion and the Si(IV) in the hexahydridosilicate, and conveniently the posited intermediate silyl anion is Si(II), the result of a formal comproportionation. We assume this must be in the form of the silylene dianion acting as a potent nucleophile to formally transfer ownership of that electron pair.
2. The anionic calcium hydride [H H] does not interconvert with the intermediate in cyclohexane on the NMR timescale as each species is independently integrable in ^{1}H NMR kinetics experiments.
3. Experimental activation entropy of the autocatalytic step is mildly exotropic (2.2/6.3 $calmol^{-1}K^{-1}$ in the forward/reverse directions, less than the 45 $calmol^{-1}K^{-1}$ for TS2), which indicates only a small organisational cost in the transition state. We suggest this is unlikely for a 4-**NON**Ca-containing transition state as the "tetramerisation" should cost at least 6 translational/rotational degrees of freedom, on the order of 80 $calmol^{-1}K$ (most likely resulting in an endotropic activation entropy).
4. We might assume "metametathesis" (swapping of anions between assemblies) to be fast, considering the barrier should be essentially solely coulombic. Monomerisation is evidently very uphill, but it is possible to imagine anion swapping pathways which avoid complete dissociation, and losing neutral fragments from the assembly (such as silane) is experimentally facile at elevated temperatures.

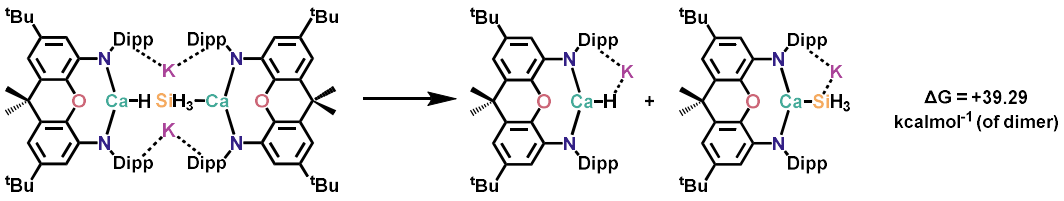


Figure 24 Proposed intermediate [SiH_3 H] as a dimer computationally (PBE0-D3BJ-CPCM(benzene)/Def2TZVPP//PBE0-D3BJ/BS1) split into its constituent monomers, K[NONCaSiH_3] and K[NONCaH], highlighting the highly endergonic nature of such a dissociation.

By virtue of these arguments, we propose the possibility of an intramolecular mechanism (Figure 25) by a stepwise transfer of silicon centres between assemblies, and subsequent deprotonation of silane by the silylene dianion to produce two silyl anions, which can then metathesise anions to produce two equivalents of the mixed silyl-hydride intermediate implicated immediately before the second hydride-proton coupling step TS3.

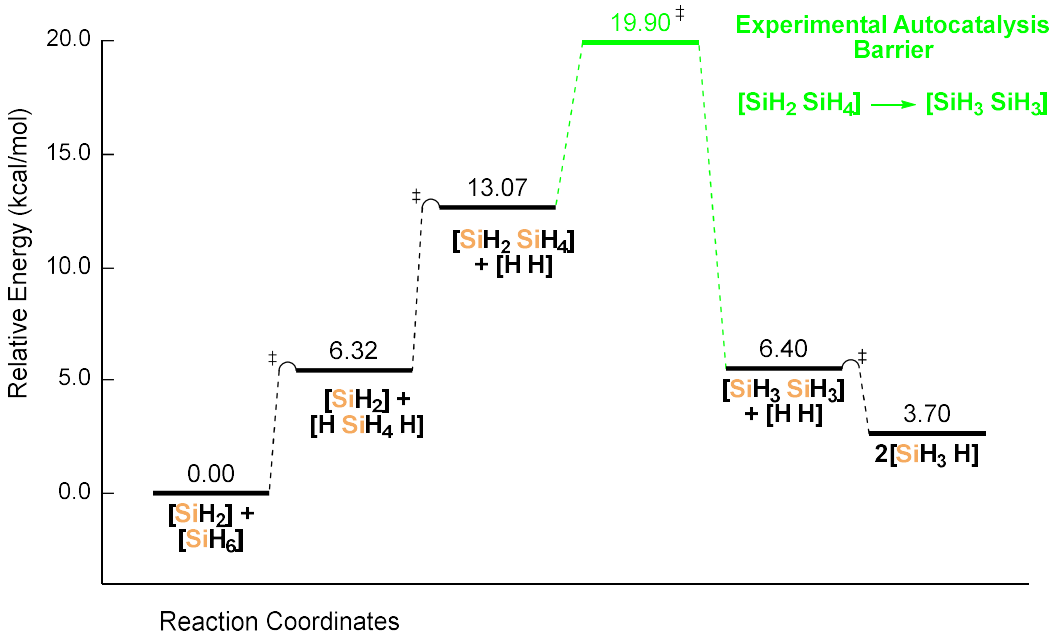


Figure 25 Proposed autocatalysis silicon transfer intermediates, transition states between intermediates are not calculated and presumed to be small, the green barrier is the empirical autocatalysis barrier from the kinetics experiments.

This approach seems to come at the cost of losing the experimental bimolecular rate law, $k_A[SiH_2][SiH_6]$. However repeated uses of the steady state approximation for each intermediate can rigorously reproduce the bimolecular rate law. More intuitively, in the limiting case where each process is barrierless except for the rate 19.90 kcal·mol^{-1} barrier in Figure 25, then the profile therein presented can be considered to have only one reaction coordinate in each direction around the highest barrier, from $[SiH_2]$+$[SiH_6]$ to 2$[SiH_3$ H].

3.4.4 Calculated Autocatalysis

Once it became evident that the reaction was autocatalytic, we slowly investigated the prospect of calculating an autocatalytic mechanism. This, while readily summarised here, constituted some years of machination.

Firstly, the autocatalytic sequence is initiated by constructing and optimising the silane adduct of the silylene dianion, denoted $[SiH_2].SiH_4$ (with an equivalent of silane gas emitted by another assembly of hexahydridosilicate). This species is treated as the minimal chemically meaningful encounter complex, because it embodies the experimentally salient proposition that silane may exist transiently in the vicinity of the reduced silicon centre without requiring the full assembly-to-assembly encounter that becomes computationally intractable at larger system size. The optimised adduct is found to be uphill by 7.70 kcal·mol^{-1} relative to the silicate, which unsurprisingly renders it energetically feasible.

Secondly, this adduct is then scanned along an ingress coordinate that transports the silane moiety from outside the assembly into the host environment, thereby as is necessary for the intended silicon-silicon interactions to occur.

Unexpectedly, this suggested ingress actually also forms the silicon-silicon bond forming step. No minimum was located of the silane within the pocket, following the IRC of the silicon entering the pocket produces a "disilane dianion", and also induces hydride from the silane to the silylene fragment. This transition state, "Si-Si Nu. Atk. TS" in Figure 26, possesses a barrier of 19.07 kcal·mol^{-1}. Crucially, this is feasible at the experimental temperatures and matches the calculated barrier heights from the kinetics data presented at the end of the chapter. The barrier provides the necessary redox step in forming the Si-Si bond, formally comproportionating through the bond formation.

In the gas phase, one would expect the resulting "disilane dianion" to be intrinsically unstable, as the LUMO of a H_3SiSiH_3 is the Si-Si σ*, and the population of this orbital (by virtue of the dianionic nature of the species) would result in a net 0 bond order between the silicon centres and spontaneous rupturing into two silyl anions. However, within the pocket, instead of the previously silylene silicon, it distorts so as to have a lone pair on it, stabilised by the nearby calcium and potassium, making a hypervalent silicon centre- the silyl adduct of a silyl anion.

Attempts to locate a direct transition state corresponding to fragmentation of the "disilane" dianion into two discrete silyl anion equivalents do not converge to a chemically meaningful

first-order saddle point. Scanning the silicon centres away from each other predictably reformed the transition state which formed them, and attempts to "push" one of the silicon centres to the other side of the pocket, or bond with bond of the metals, all proved unproductive.

Consequently, we attempted to elucidate the reaction in the reverse direction. Assuming once the autocatalytic portion is complete, guest "shuffling" is free to occur. The constitution of the intermediate is [H_3Si H], which is conveniently the metathesis product of [H_3Si SiH_3] and [H H], which is evidently very facile. This encouraged us to start from the necessary product of the dissociation step, two silyl anions within the pocket.

Two silyl anions were artificially placed within the pocket and optimised to a local minimum geometry, denoted [SiH_3 H_3Si]. This structure functions as the product-side anchor point for a subsequent homolysis-style coordinate scan, thereby providing a controlled means by which a genuine connecting transition state may be sought without presuming a particular dissociation pathway *a priori*. A constrained scan was performed in which the two silicon centres of the optimised [SiH_3 H_3Si] arrangement were brought together along a silicon-silicon decreasing coordinate. The scan revealed a local maximum, which is refined to a transition state denoted "Homolysis TS", which encouragingly proved to link [H_3Si SiH_3] and the disilane dianion intermediate, which links all the required intermediates and transition states necessary for the autocatalytic portion of the reaction profile, shown in green in Figure 26. See Figure 31 for the autocatalytic steps alluded to here.

In the sections that follow, these elementary steps are placed within the full reaction network that reproduces the observed autocatalytic kinetics, and they are used to rationalise the experimentally inferred barrier heights and activation parameters on which the kinetic model relies.

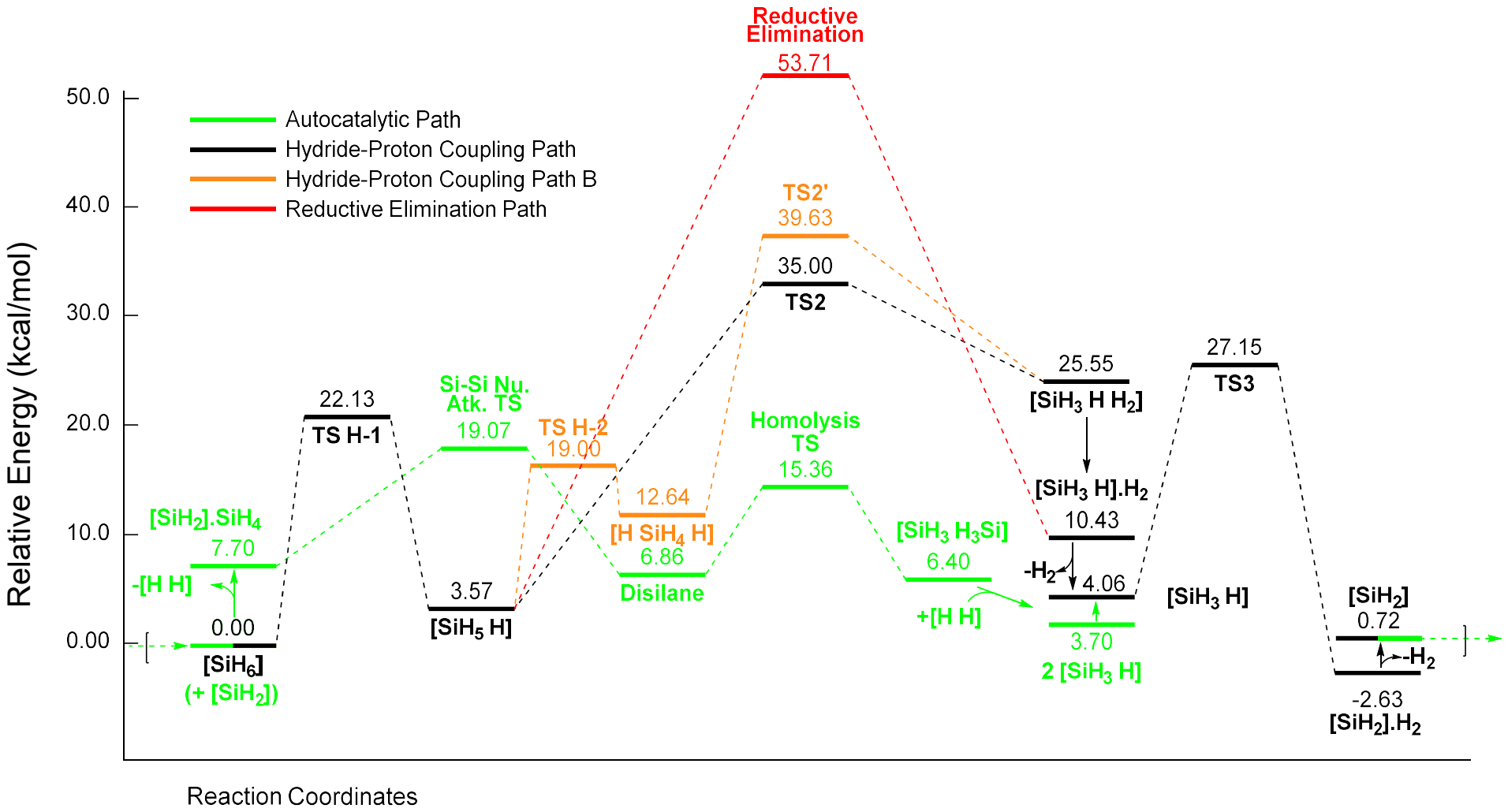


Figure 26 Reaction profile for the formation of the silylene dianion $[K_2\{(NON)Ca\}_2(SiH_2)]$ from the hexahydridosilicate $[K_2\{(NON)Ca\}_2(SiH_6)]$ ($\Delta G_{298.15}$ at the PBE0-D3BJ-CPCM(benzene)/Def2TZVPP//PBE0-D3BJ/BS1 level of theory). Brackets denote the $[K_2\{(NON)Ca\}_2]^{2+}$ assembly. The black path shows the lowest energy computed pathway, red shows the energetically unfeasible reductive elimination-like pathway, orange shows a similar pathway also including hydride-proton coupling from different intermediates albeit higher in energy, and green shows the autocatalytic pathway. Each of these barrier heights is supported by a detailed kinetics analysis presented in the next subchapter.

3.5 Kinetics

I am often told that “transition states are not real”, rather blithely that only Schrödinger's cat can see them. Fundamentally, this is true, and the organometallic literature is riddled with baseless guesses and low-quality computation, a graveyard that this work easily could have joined except in the face of rigorous experimental support. This final subchapter outlines the processing and modelling of the necessary experimental kinetics data to support or refute what could otherwise easily be the idle vapourings of a mind diseased.

3.5.1 Methodology

^{1}H NMR intensity over time plots were collected by Mr Huo, with many experimental concerns over the amount of time taken for various runs at various temperatures in various solvents best addressed in his thesis.[9]

For each of the runs in the temperature series (75, 80, 85 °C) of ^{1}H NMR spectra as a function of time, the data were processed as follows: Using MNova Mestrelab Research’s software package MestReNova 14.2.2-28739, the default 0.3 Hz exponential window function was removed (in efforts to retain quantitivity), followed by automatic phase correction. No baseline correction was used due to the broad nature of some signals, which were heavily modified by all baseline corrections (or removed entirely using a splines correction), and the spectra not referenced ($\delta^{1}H_{C6D11H}$ = 2.3030 in the unreferenced spectra) due to the difficulty in adjusting several hundred spectra. The intensity of each resonance within the 2D kinetics plot was then integrated with respect to time with much difficulty. Examples of typical integration are shown in Figure 27-Figure 29, with Figure 28 showing how little chemical shifts can change from reactant to product.

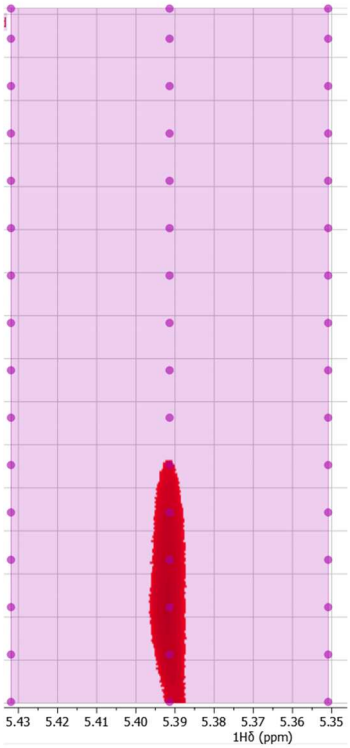


Figure 27 Typical integration of a resonance in a region disparate from other resonances, in this case of the six hydrido protons of the silicate. Time is on the vertical axis starting at zero at the bottom, and the red portion is the bitmap concentration of the concerned resonance.

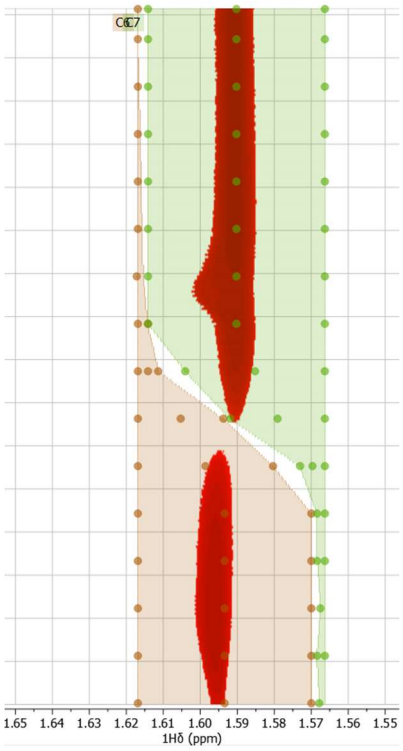


Figure 28 Integration of two resonances which unfortunately overlap, resulting in their artificial demarcation and less reliable integral. Time is on the vertical axis starting at zero at the bottom, and the red portion is the bitmap concentration of the concerned resonance.

Many resonances occur at very similar shifts between the different products due to minimal changes in the chemical environment of the supporting ligand assembly (Figure 28), and while the initial silicate and final silylene dianion hydride shifts are well defined, they have problematic silicon coupling satellites of appreciable magnitude (*ca*. 15%) which overlap with other resonances, and we presume due to the wide range of conformations available particularly to the intermediate, these resonances were not observed at all. Figure 29 demonstrates the specific challenges associated with the highly overlapping alkyl region, which would otherwise be ideal for tracking the various concentrations due to its intrinsically high signal-to-noise ratio and predominance of singlet resonances, but was ultimately used only for normalisation (*vide infra*) due to the inseparable nature of the resonances.

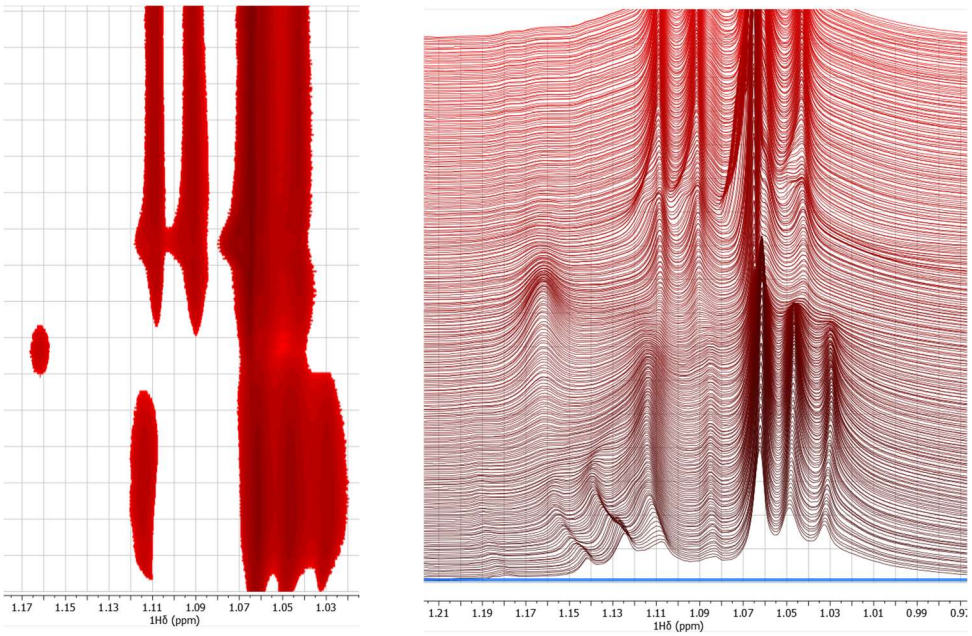


Figure 29 Specific highlight of the alkyl region of the ^{1}H NMR spectrum over time (vertical axis) for the 80 °C kinetics plot. Left shows the bitmap representation useful for defining integration regions and right shows the stacked 1-dimensional spectra of the same region, demonstrating the difficulty in assigning specific resonances and their integrals.

After integration of the resonances, the data for each species was processed. From each time point integral was subtracted the lowest value recorded during the experiment in an attempt to remove background noise, and then divided by the total number of protons associated with the resonance to normalise it. Each signal was then assigned to a molecular species and the average taken to represent the intensity associated with each species at each time. Each of these were then converted to concentration by assuming the initial total mass weighed for the experiment was all the hexahydridosilicate, converted to moles, the total intensity at any time normalised to this molar concentration. This leads to kinetics plots such as Figure 30 (left).

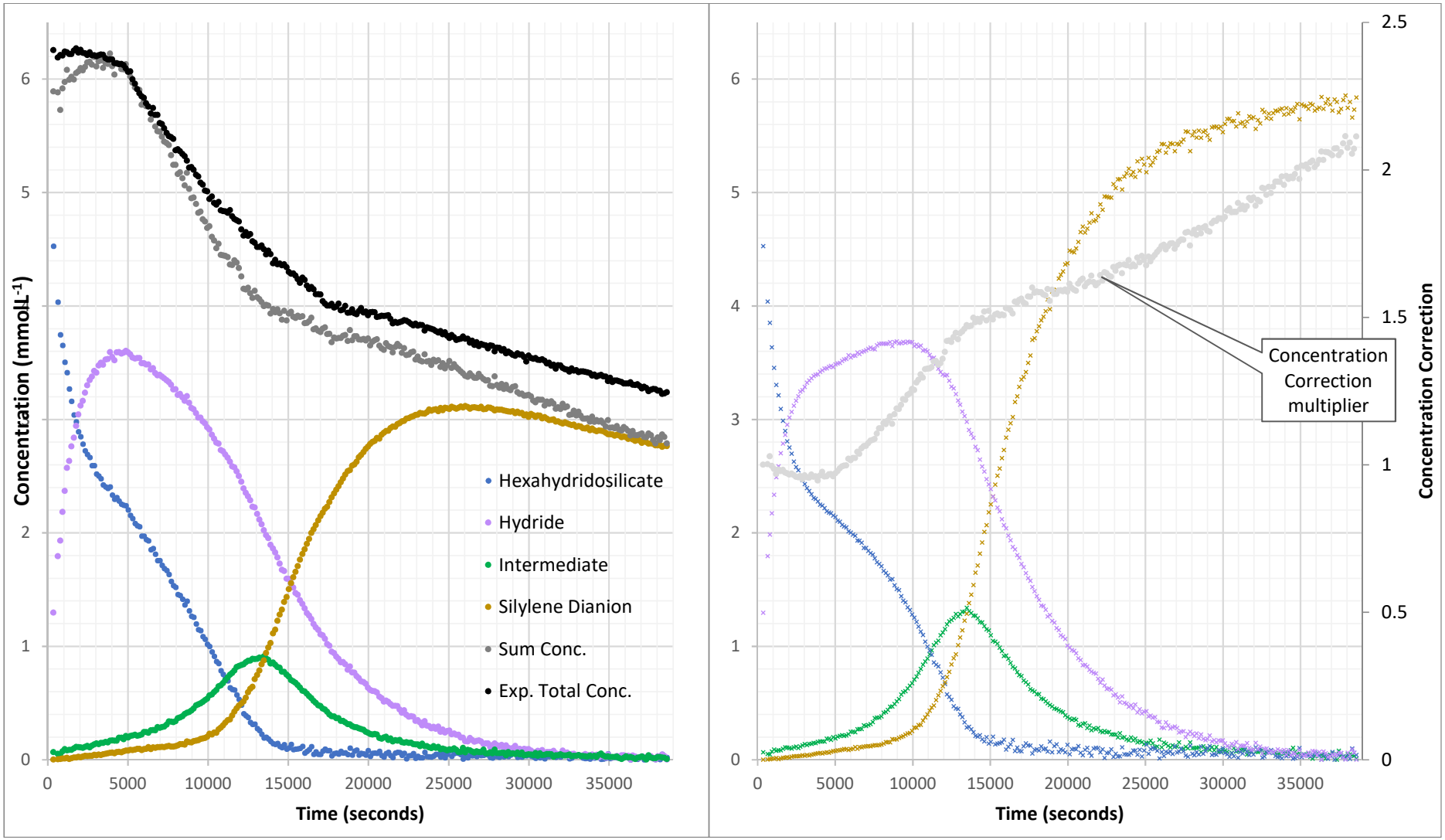


Figure 30 Left: Example (80 °C run) of initial data after integration and normalisation processing, particularly salient is the good agreement between the summed concentrations (grey) and the normalised integral of the alkyl protons in the ^{1}H NMR spectra. Right: Concentration-corrected data used for the kinetic modelling, particularly showing the concentration correction multiplier (right vertical axis) in grey.

Unfortunately, an additional more insidious treatment proved necessary.

Due to the lessened solubility and consequent precipitation of various products, as well as the reduced solubility of crystals compared with powders, over time the total concentration of **NON**-containing products in solution reduced due to precipitation and crystallisation. As discussed above, the region in the ^{1}H spectra associated with the alkyl moieties (tert-butyl groups, dimethylmethylene, and methyl termini of isopropyl groups) is disparate from any other resonances and *in summa* can be used to normalise the total concentration of ligand containing products, assuming no ligand is created or destroyed throughout the reaction. This (taken to correspond to 120 protons) "experimental total ligand concentration" (black dots, Figure 30, "Exp. Total Conc.") over time was compared for each temperature with the sum of the concentrations of the identified species (SiH_6, intermediate, hydride, and SiH_2). Assuming the first measurement to be fully dissolved, the measured concentration of each species was summed at each time, and then the total at each time divided by the initial concentration, allowing for an estimation of the total dissolved ligand containing species. To account for this change in concentration, the reciprocal of the ratio of total ligand concentration to initial ligand concentration was taken at each integration time, and then each species multiplied by said reciprocal to create a graph with constant ligand concentration over time (Figure 30, right). Luckily, this is evidently a good approximation as can be seen with the good agreement between the experimental value of total concentration (normalised total alkyl region integral) and the sum of all other proposed species concentrations in solution.

This, of course, introduces a wide array of errors, principal amongst being:

1. The rate of reaction for the measured species and the modelled species are no longer the same; changes in rate due to spurious changes in concentration will unphysically be absorbed into k values, which will manifest as an unphysical time dependence (which we are unable to model).
2. The species are all assumed to be in the same proportion in precipitate as in solution. We assume this to be approximately true due to the structural similarities between the species and the almost identical unit cell dimensions, but it evidently must be untrue as evidenced by the total concentration changing over time: the products must be less soluble than the starting materials. The exact relative solubilities are unclear, and consequently the calculated concentrations of more soluble species are underestimated, and inversely less soluble species will be overestimated. This seems particularly true in

the case of the hydride and the silylene dianion, the former being much more soluble than the latter, and in the 85 °C experiment they are the two principal components of the reaction mixture. Attempts to mitigate this in kinetic modelling by including precipitation equilibria would introduce several more parameters into an already highly complicated model, and we deem the potential increase in accuracy with such modelling to be counteracted by increased degrees of freedom without statistical basis.

The net result is that k-values are more accurate at the beginning of the experiments than at the end, particularly evident in the loss of symmetry of the sigmoidal concentrations of the silylene dianion, and consequently the beginning of the experiments was given more credence in modelling the kinetics. Details and derivation of the model are given below.

Kinetic modelling was done using CoPaSi 4.44 (Complex Pathway Simulator). The model used was as follows in Figure 31, justified in section 3.6.4.

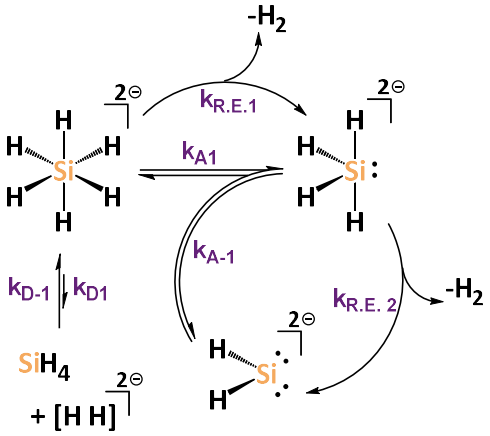


Figure 31 Reaction network of the kinetic model used. Each dianion is implied to exist within the $[K_2\{(NON)Ca\}_2]^{2+}$ assembly and the simplified form of the intermediate dianion SiH_4^{2-} is used, each for clarity.

k-values were modelled by manual variation as described in the next paragraph until self-consistency with the agreement between the model, calculated data, and expected linearity with the associated Eyring plots.

Each component of the dissociation equilibrium ($K_{D\ 1/-1}$) is much faster than the first reductive-elimination-like step, and the autocatalytic process is unable to proceed at the beginning of the reaction due to the absence of catalyst. Consequently, each graph (particularly 75 and 80 °C) begins by converting silicate to hydride through the release of silane gas until equilibrium is reached. Thus the ratio $K_{D\ 1}/K_{D\ -1}$ can be modelled easily by matching the modelled equilibrium to the experimental one (the flat section near the beginning of the graph), and then once the ratio is found, their absolute values can be found by adjusting the rates until they match the

observed exponential decay at the very beginning of the graph. The remaining constants are much less separable and were modelled iteratively by associating different features of the kinetics plots with different constants. The position of the maximum concentration of the intermediate is well associated with the value of $k_{R.E.\ 1}$, if $k_{R.E.\ 1}$ is faster than the peak appears sooner and *vice versa*. The rate of formation of silylene dianion is dependent obviously on $k_{R.E.\ 2}$, consequently the gradient at the sharpest point of the sigmoid is controlled by $k_{R.E.\ 2}$ but clearly is also dependent on the concentration of intermediate, which is dependent on a myriad of other things. $k_{A\ 1}$ and $k_{A\ -1}$ roughly control the height and breadth of the intermediate. Once a reasonable set of constants (ones which reproduce the features of the graphs but in the wrong places or wrong magnitudes) is found, the constants can be perturbed self-consistently until they match the data. No least squares or other statistical measure is used due to the inconsistencies in how well the model matches the experimental data at the beginning and end of the experiments (*vide infra*) and many other reasonable fits likely exist, but for possible variations in rate constant the variation in activation barrier is small (*vide supra*).

Formally, all reactions are reversible, evidenced by the reverse reaction of silylene dianion under a high pressure of H_2 gas reforming the silicate. However, including the reverse reaction in the kinetic modelling proved very difficult. Both what would be $k_{R.E.\ -1}$ and $k_{R.E.\ -2}$ suffer from the same difficulty as $k_{D\ -1}$ in that they would inadvertently absorb the solubility of hydrogen gas into themselves and consequently give limited theoretical insight into the reaction. Additionally, they should contribute extremely little to the observed rates because of their higher barriers in reverse (although the reverse may make use of the same autocatalytic pathway), the very limited solubility of hydrogen in hydrocarbon solvents, and second-order nature of the reaction compared with the first-order nature of the forwards direction. We thus assume their effect to be negligible and omit their contribution to the observed kinetics.

3.5.2 A note on experimental and computational errors.

Principally, the kinetics data are used to (in)validate a computed mechanism, which was calculated using DFT. DFT uses only an approximation to the true density functional as the true form density functional is not known, and with these approximations come intrinsic errors.[53] Additionally, there are issues of basis set incompleteness (and basis set superposition error), integration accuracy, parameterisation of dispersion and solvation, anharmonicity in vibrational modes, errors in the rigid rotor approximation for large molecules with many soft modes, *et cetera ad nauseum*. Many of these errors are exacerbated by large molecule sizes

and have no guarantee of favourable error cancellation in their relative energies. Consequently, even with the most appropriate choice of density functional approximation and appropriate corrections even relative energies can only hope to be accurate to experiment to within a few kcal·mol^{-1}.

In a landmark benchmarking paper by Mardirossian and Head-Gordon, similar to our method, the PBE0-D3BJ/Def2-TZVP method possesses a root mean square deviation (RMSD) (mean absolute deviation in parentheses) of 4.91 (5.01), 3.62 (4.68) and 3.79 (4.67) kcal·mol^{-1} for the relevant Hydrogen-Transfer Barrier Height (HTBH38), Non-Hydrogen Transfer Barrier Height (NHTBH38), and Diverse Barrier Height (DBH24)[54] test sets respectively (in the MGCDB84 data base). While the signed errors are not presented in the manuscript, global hybrid density functionals tend to underestimate the barrier heights.[55] Consequently, we assume an approximate -3 ± 3 kcal·mol^{-1} error associated with the computed barrier heights and would be content with a similar uncertainty with the experimental barrier heights.

Barrier heights are calculated from kinetic data using the Eyring equation[56]:

$$k = \frac{\kappa k_B T}{h} e^{-\frac{\Delta G^{\ddagger}}{RT}}$$

Equation 4 The Eyring equation.

Where κ is the transmission coefficient (which is assumed to be 1 in the absence of quantum tunnelling) k_B is the Boltzmann constant, T is the temperature, h is the Planck constant, R is the universal gas constant, and $\Delta G^{\ddagger}$ is the associated barrier height. Any uncertainty in activation barrier height (*i.e.* $\Delta G^{\ddagger} \pm \delta\Delta G^{\ddagger}$) manifests itself as uncertainty in *k* as multiplication by . If $\delta\Delta G^{\ddagger}$ is merely 1 kcal·mol^{-1} then $\in$ [0.24, 4.24] (at 75 °C), a range greater than an order of magnitude (although within *ca*. ×/÷ 4). Conversely, changes in *k* result only in logarithmic changes in $\Delta G^{\ddagger}$. *Quad sequitur* changes in the order of magnitude of the modelled k result in *ca*. less than 1 kcal·mol^{-1} in the experimental barrier at relevant temperatures. Given the above *ad hoc* modifications to the kinetics plots change either the concentration or rates by a maximal factor of 2.11 (Figure 30), and mostly at the end of the experiment, and the errors associated with the integration and processing of the ^{1}H NMR data, we shall take a viable uncertainty in experimental barrier to be *ca*. ±3 kcal·mol^{-1}, assuming the modelled process is similar to the true mechanism.

3.5.3 Kinetics Plots

Presented follow are the kinetics plots (Figure 32, Figure 33, and Figure 34) of the: crude experimental data (circles), the processed data (crosses), and the CoPaSi models (solid curves). Additionally given are the data for the total experimental ligand concentration (black), and the sum of all ligand-containing species (grey) to show the good agreement between the two.

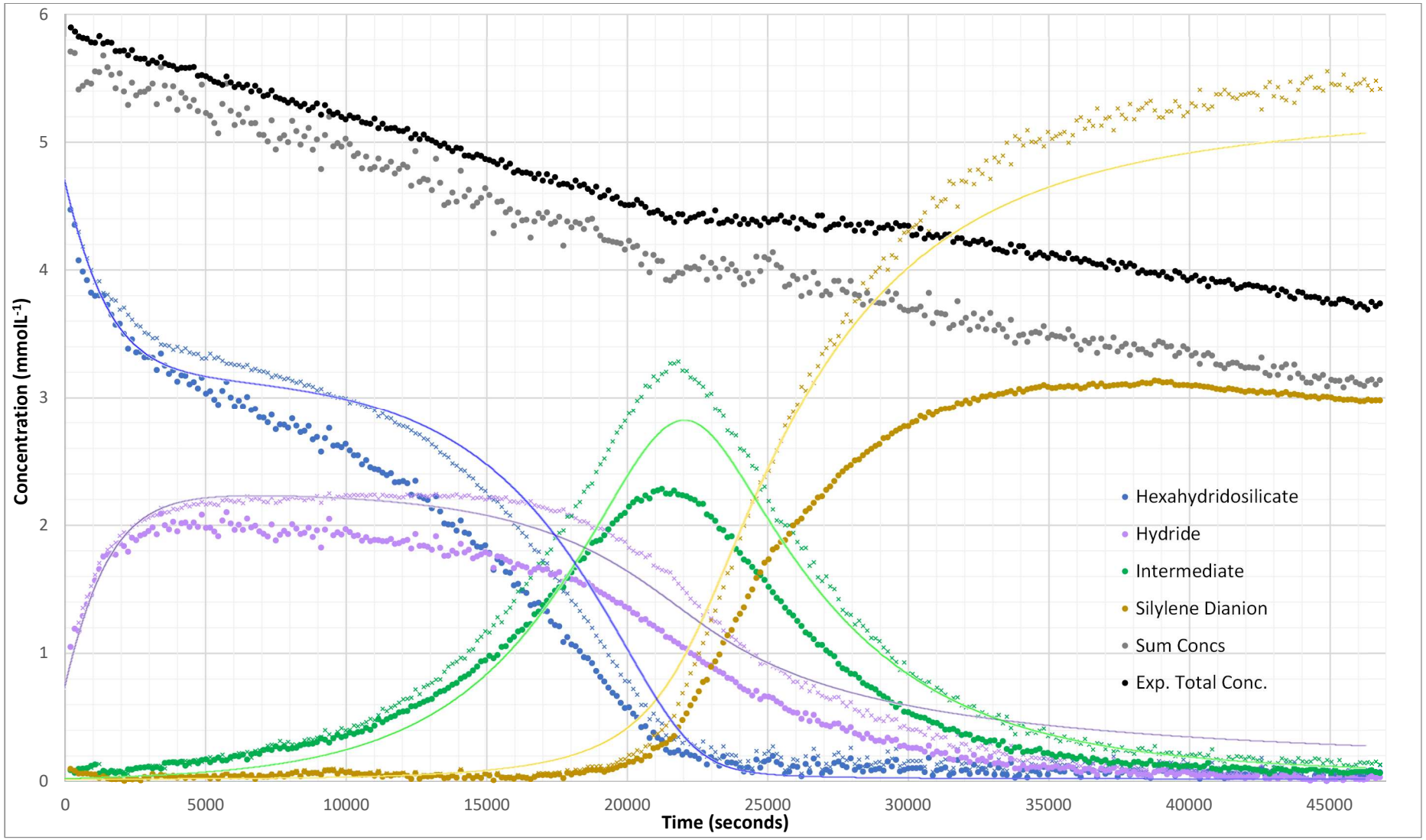


Figure 32 Concentration over time of the H_2 elimination reaction from $[K_2\{(NON)Ca\}_2(SiH_6)]$ to $[K_2\{(NON)Ca\}_2(SiH_6)]$. Various implicated species by the integrated, normalised ^1H NMR spectra kinetics for the 75 °C (348.15 K) experiment. Solid circles, crosses, and lines are the unprocessed experimental data, processed data, and CoPaSi models respectively.

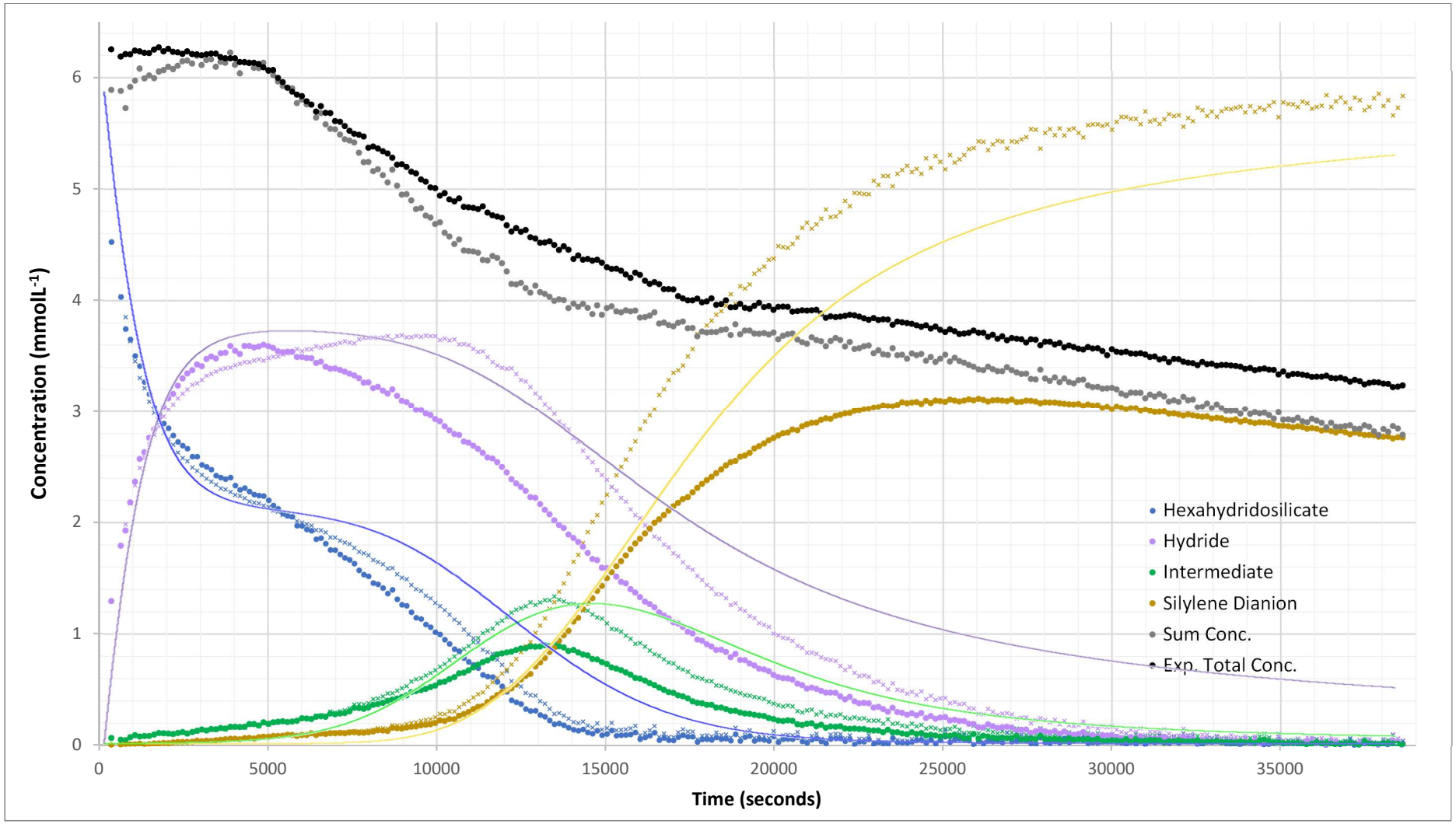


Figure 33 Concentration over of time of the H_2 elimination reaction from $[K_2\{(NON)Ca\}_2(SiH_6)]$ to $[K_2\{(NON)Ca\}_2(SiH_6)]$. Various implicated species by the integrated, normalised ^1H NMR spectra kinetics for the 80 °C (348.15 K) experiment. Solids circles, crosses, and lines are the unprocessed experimental data, processed data, and CoPaSi models respectively

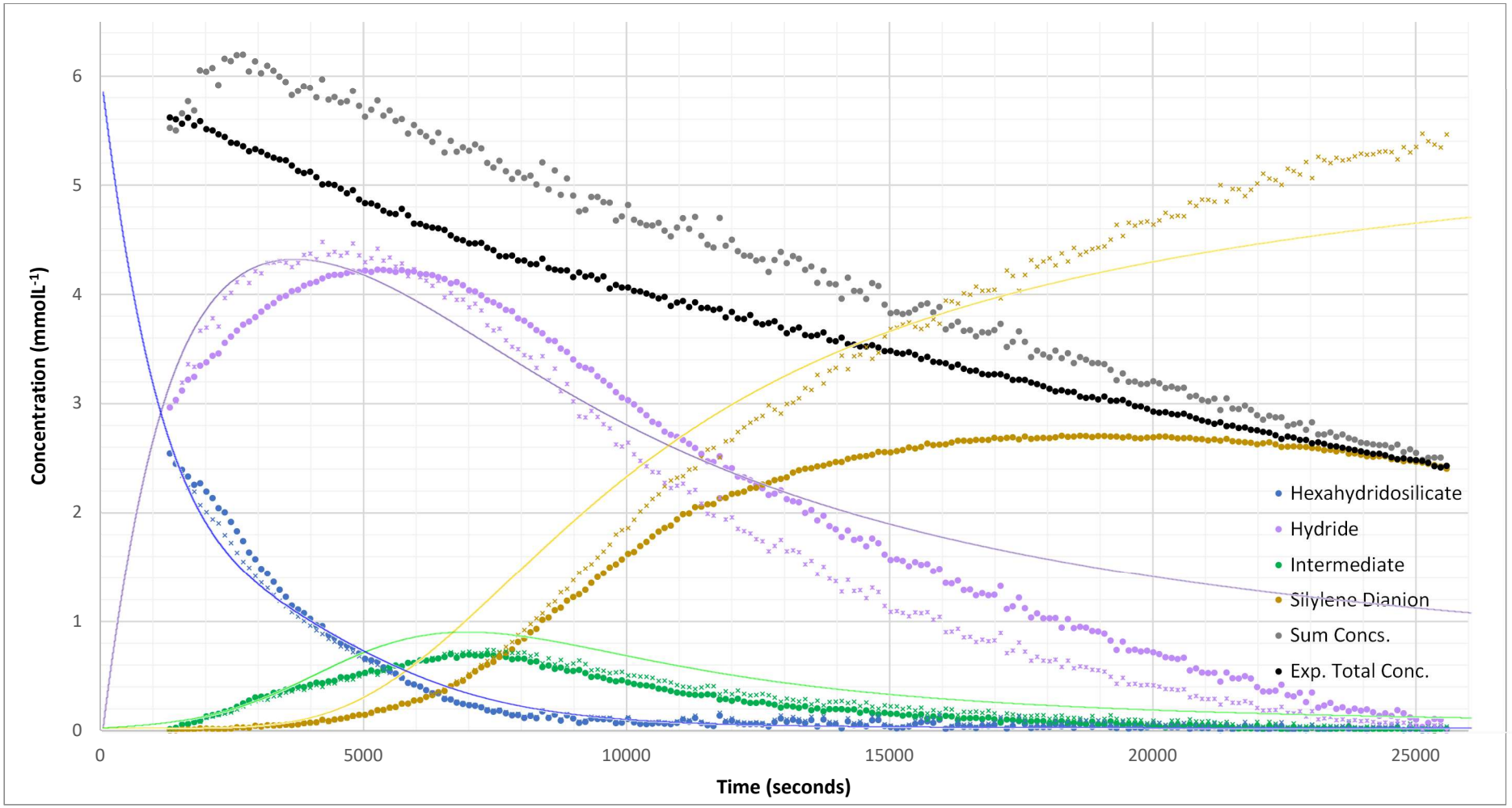


Figure 34 Concentration over of time of the H_2 elimination reaction from $[K_2\{(NON)Ca\}_2(SiH_6)]$ to $[K_2\{(NON)Ca\}_2(SiH_6)]$. Various implicated species by the integrated, normalised ^1H NMR spectra kinetics for the 85 °C (348.15 K) experiment. Solids circles, crosses, and lines are the unprocessed experimental data, processed data, and CoPaSi models respectively.

3.5.4 Autocatalysis

As previously discussed, tandem experimental and computational methods (*vide supra*) were used to probe the reaction mechanism. *Prima facie*, the system seems ideal for kinetic investigation: the reaction goes to completion typically overnight, indicating a half-life on the order of hours (rather than days or milliseconds); the product is thermodynamically and kinetically stable at temperatures as high as 120 °C; and the reaction appears quantitative by ^{1}H NMR spectroscopy. Unfortunately, upon experimental kinetic investigation a more difficult picture presented itself. No constant-order (let alone integer) rate law could be extracted from any concentration over time graphs or their respective linearised forms. Formation of the product followed a sigmoidal shape, and additionally a competing, faster, unproductive equilibrium was observed, that of the hexahydridosilicate dissociating into silane and the parent hydride complex. Density functional calculations of the mechanism, however, was vindicated by the observation of a predicted stable intermediate.

This section details the evidence for and against competing models for the reaction mechanism, leading to our ultimate assessment of autocatalysis.

3.6.4.1 Expected Reaction Kinetics

The expected rate law for any of our intuited, intramolecular mechanisms is first order.

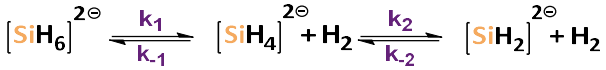


Figure 35 An idealised, mechanistically noncommittal representation of the stepwise reactions to form the silylene dianion from the hexahydridosilicate, ignoring the solubility equilibrium of dihydrogen.

Regardless of the relative rates k_n and the solubility or irreversibility of involving hydrogen, it is always possible to justify a steady state approximation which leads in each case to posit a first-order rate law. That we do not experimentally observe a first-order rate law indicates that at least one of the underlying assumptions is wrong: that the steady state approximation does not hold (i.e., the concentration of the intermediate changes significantly over the course of the reaction), or that the reaction pathway involves a significant step which is not a simple, unimolecular process like those assumed, or both.

3.6.4.2 Experimental Reaction Kinetics

Initial ^{1}H NMR spectroscopic monitoring of reaction completion at high temperatures (when the reaction was nearing completion) of course gave us little reason to doubt a simple rate law, as under such conditions the reaction appears simply first-order (Figure 36).

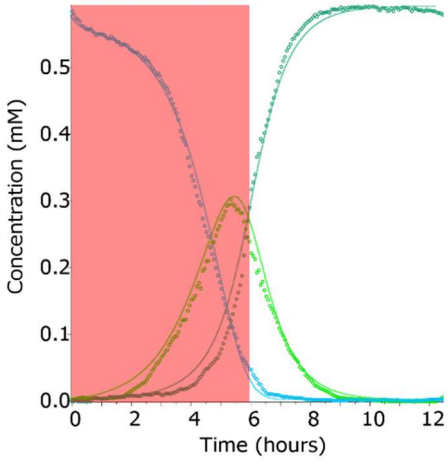


Figure 36 Observing only the post-induction kinetics, (e.g., right of the red box [ca. 6 hours onwards]), it is easy to mistake the order of the reaction.

However, a cursory analysis of the k-values yields a puzzling result: a rate constant of *ca*. 87 μs^{-1} implies a barrier of *ca*. 23 kcal·mol^{-1} by the Eyring equation, and a half-life in the vicinity of 2 hours. This immediately raises the question why was the reaction only half converted after 6 hours instead of 2? One may also notice that the species are different, *i.e*. what is becoming the product is not the starting material which was placed in the reaction vessel, however this was not trivially obvious due to a great similarity in the ppm shift of the resonances in the two species. Detailed kinetics studies were evidently necessary to discern the complex reaction pathway.

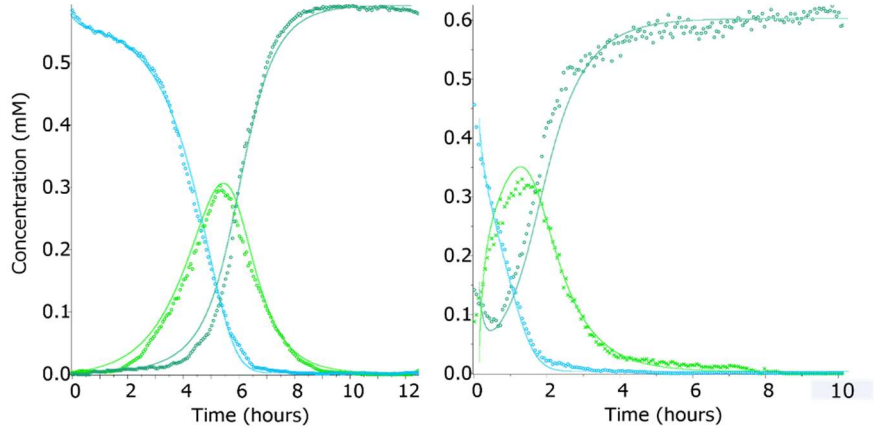


Figure 37 Concentration over time plots for the conversion of [K_2{(NON)Ca}$_2$(SiH_6)] to [K_2{(NON)Ca}$_2$(SiH_2)] by ^{1}H NMR spectroscopy at 75 °C. Left begins with only the hexahydridosilicate, showing the surprising sigmoidal curve; right uses an initial 20% of the silylene dianion to bypass the induction period and demonstrate the autocatalytic nature of the reaction.

Initial reaction kinetics are shown in Figure 37. Key to their discernment is the left half of the curve, particularly of the starting material. There are few sensible reasons for the rate to start slowly and suddenly increase – this could be the result of a strongly exothermic reaction significantly increasing the temperature, or if only looking at the product it may be due to the initial necessary build-up of an intermediate, but it is also reasonable to propose a different, lower-energy pathway has become available to consume the reactant, necessarily due to a new reagent present in appreciable quantities. It is easiest to differentiate these two possibilities by looking at the concentration of the starting material: in the case of intermediate build-up, it should have no reason to start slow and then increase, instead decreasing in accordance with the expected exponential rate law.

Instead, considering the shape of the curve for the consumption of the starting silicate may be more revealing. This shape, and it will become evident consequently also the shape of the curve for the formation of the product, is sigmoidal. Autocatalytic reaction mechanisms are characterised by a sigmoidal concentration over time, consequent of a flux initially principally dependent on the concentration of the product and terminally principally dependent on the concentration of the substrate. The rate of decrease will increase as the concentration of catalyst (product) increases, causing an initially flat and then increasingly steep graph until the starting material is consumed, slowing the rate due to a scarcity of starting material. This is reminiscent of two exponential curves "stuck together" at the midpoint and smoothed into a continuous curve. This can be seen most clearly in the low-temperature concentration over time graph in Figure 37.

The catalyst (product) is initially formed by some slow, kinetically unfeasible process (referred to as the "induction period"), and then once some useful amount of the catalyst is formed this way the rate of formation becomes dominated by the much faster catalytic route, causing a runaway rate increase until the amount of substrate becomes limiting and the rate slows.

It is easy to mistake such a curve for a first-order two-step reaction like that described above when the concentration of the intermediate is high and changes rapidly, as is observed here. Looking only at the right half of the curve (*i.e.*, regions exclusively to the right of the second-derivative zero of the sigmoid) it is forgivable to misidentify it as an exponential, particularly with an intermediate which can be used to mask the anomalous behaviour, such as after 6 hours in the left of Figure 37.

Additionally, it is readily shown experimentally that the process is autocatalytic by simply using an initial 20% product in the kinetics experiment (Figure 37, right) and observing that no induction period is required (as the slow pathway is not required to form the catalyst) but otherwise the kinetics remain the same, showing that either the product or some species derived thereof (of which there should be none, as it is the observed final product) is changing the rate of reaction.

3.6.4.3 Theoretical Models for Autocatalysis

After establishing the autocatalytic nature of the reaction, in order to model the kinetics and extract barrier heights, it is required to generate a model *de novo* involving all of the necessary reaction steps.

It is at this point prudent and necessary to highlight two further equilibria which complicate the kinetics, "D1" the dissociation of silane from the complex, and "D2" the dissolution of silane gas.

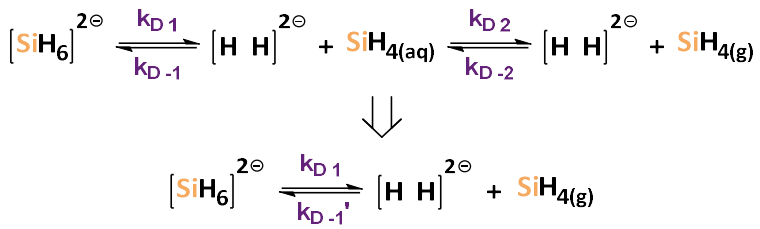


Figure 38 Top: Two equilibria, the reversible dissociation of silane from the hexahydridosilicate, and the "boiling off" dissolution of silane gas in and out of solution complicate the kinetics experiments by changing the concentration of the starting material in a non-productive fashion. Bottom: As justified in the text, this can be simplified to the equilibrium presented.

This off-target reactivity is reversible and thermodynamically uphill from the silylene dianion (and the silicate at room temperature), but empirically very rapid and strongly temperature dependent. Predictably, as temperature increases the entropic species are favoured, which lowers the concentration of the enthalpic (in this case, the productive hexahydridosilicate) species. This is exacerbated by the lower solubility of gases at increased temperatures and the shifting of the second equilibrium, pushing silane into the headspace and further reducing the concentration of the starting material. For the purposes of the kinetic modelling, the silane dissolution was not included, assumed to be extremely fast compared to all other processes, and instead it was modelled as though the silane remained in solution. The rate of the reverse dissociation step should be strictly equal to the theoretically apt $k_{D\text{-}1}$[Hydride][$SiH_{4(aq)}$]. However, if the rate of dissolution (in both the forward and reverse direction) is much faster than any of the other processes in the reaction pathway, then reaction modelling is greatly simplified by using just the total concentration of silane rather than just the dissolved concentration, and merely absorbing the dissolution equilibrium constant into the dissociation rate constant.

$$\left[SiH_{4(tot)}\right] = \left[SiH_{4(aq)}\right] + \left[SiH_{4(g)}\right] \quad \textbf{(5)}$$

$$At\ equilibrium\ K_{D2} = \frac{\left[Si_{\ 4(g)}\right]}{\left[SiH_{4(aq)}\right]} \quad \textbf{(6)}$$

$$At\ equilibrium\ \ \left[SiH_{4(aq)}\right] = K_{D2}^{-1}\left[SiH_{4(g)}\right] = K_{D2}^{-1}\left(\left[SiH_{4(tot)}\right] - \left[SiH_{4(aq)}\right]\right) \quad \textbf{(7)}$$

$$\therefore \left[SiH_{4(aq)}\right] = \frac{1}{K_{D2}+1}\left[SiH_{4(tot)}\right] \quad \textbf{(8)}$$

$$\frac{d[hydride]}{dt} = -k_{D-1}[hydride]\left[SiH_{4(aq)}\right] \quad \textbf{(9)}$$

$$\therefore \frac{d[hydride]}{dt} = \frac{-k_{D1}}{K_{D2}+1}[hydride]\left[SiH_{4(tot)}\right] = -k_{D-1'}[hydride]\left[SiH_{4(tot)}\right] \quad \textbf{(10)}$$

Equations 5 through 10 provide a theoretical basis for the dimensional reduction of the two parameters k_{D1}, and K_{D2} (although K_{D2} can itself be considered two parameters []), reduced by the assumption that both components are very fast so only their ratio is important, to the single parameter $k_{D\text{-}1'}$, using the definition of the k-values in Figure 5.

This is evident from eq 11 differing from eq 10 only by the form of the constant when [$SiH_{4(aq)}$] is replaced by [$SiH_{4(tot)}$], although the temperature dependence of the two expressions will evidently be different. Eyring plots of $k_{D\text{-}1'}$ evidently show it to be highly endotropic compared with the true $k_{D\text{-}1}$ (*vide supra*). This useful manipulation has the net effect of reducing the reactions in Figure 38 to the simple equilibrium in the lower part of Figure 38. The impact of

the equilibrium, however, is insidious. Heating the reaction reduces the concentration of the starting material in direct opposition to the increase in reaction rate, so the total reaction time barely decreases with temperature.

Plasson *et al.* provide an excellent review on autocatalytic processes,[57] which we used to identify a likely mechanism of direct autocatalysis with intermediate, shown most simply in Figure 39, which we used in our kinetic model.

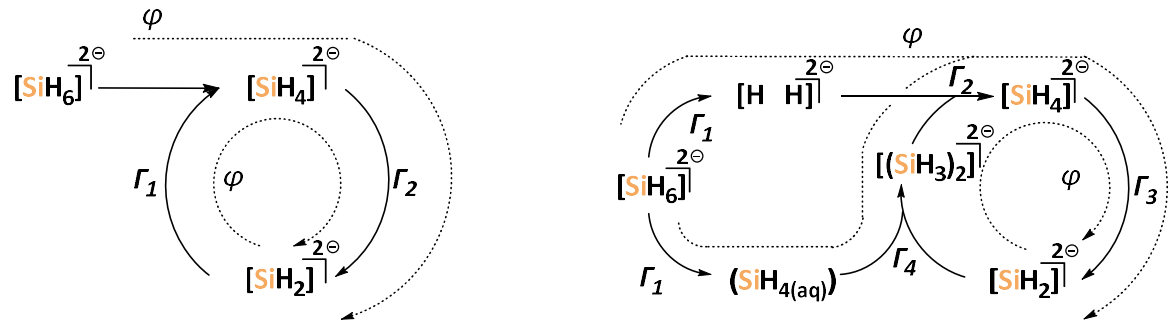


Figure 39 Reaction networks for the transformation of $[K_2\{(NON)Ca\}_2(SiH_6)]$ to $[K_2\{(NON)Ca\}_2(SiH_2)]$. Left shows the direct autocatalysis with the comproportionation of $[SiH_6]^{2-}$ and $[SiH_2]^{2-}$ to two $[SiH_4]^{2-}$ intermediate species; right includes the equilibrium of the silicate with silane gas and hydride, having indirect autocatalysis through deprotonation of the silane gas by the silylene dianion before a redistribution reaction with hydride to form the implicated intermediate.

It is possible to draw other networks of varying complexity with the design of avoiding interactions between sterically demanding complexes such as that shown in Figure 39 (right). While we were able to model such mechanisms as having adequate agreement with the data, the associated rate constants were unrealistic in magnitude (such as the reaction between silylene dianion and silane gas requiring a barrier *ca.* 11 kcal·mol^{-1}) and careful inclusion of the solubilities of hydrogen and/or silane gases with only rough estimates of the volume of the headspace and poor ^{1}H NMR spectroscopic data associated with those signals made the parameter spaces too large to abstract meaningful values. Additionally, any reaction network involving silane gas must handle the reaction between silane gas and the silylene dianion, which experimentally produces the hexahydridosilicate, which we propose is accompanied by the extrusion of elemental silicon.

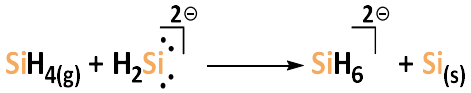


Figure 40 Silane gas reacts with the silylene dianion to produce the hexahydridosilicate and presumably elemental silicon; such a reaction is evidently minor in the kinetics as no equivalents of silicon seem to leave the system.

We have not included such a process in our models as it implies that over time the reaction mixture should tend towards hydride as elemental silicon is generated if it occurs with significant velocity to compete with silylene dianion production, which is not observed experimentally.

Given an intermediate is seen in the kinetic studies but not in silylene dianion-silane experiments, no induction period is seen when including an initial 20% silylene dianion in kinetics experiments, the anecdotal independence of reaction rates to vessel headspace volume, and no (productive) reaction with silane gas, we are led to suggest silylene dianion autocatalysis. Most imply, this is allowed for by the comproportionation shown in Figure 41.

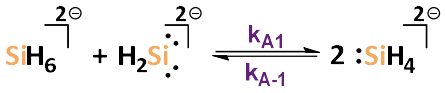


Figure 41 Proposed comproportionation between the silylene dianion and the hexahydridosilicate to two equivalents of the proposed intermediate with associated rate constants k_{A1} and k_{A-1} ("A" for autocatalysis).

By DFT, out final model is akin to that of Figure 39 (right), which as discussed is mathematically intractable. However, noting several things motivates using the simplified graph of Figure 39 (left):

1. Experimentally, at elevated temperatures the hexahydridosilicate dissociates into $[K_2\{(\mathbf{NON})CaH\}_2]$ and silane, which then presumably equilibrates between the gas phase and dissolved in solution.
2. By DFT under standard conditions, this is uphill by 8.2 kcal·mol^{-1}.
3. By DFT under standard conditions, the adduct of silane gas on the outside of another $[K_2\{\mathbf{NON}Ca\}_2(SiH_2)]$ unit, $[K_2\{\mathbf{NON}Ca\}_2(SiH_2)].SiH_4$, is only 7.7 kcal·mol^{-1} uphill.

This indicates the adduction of silane gas is minorly favoured over complete dissociation. If all the steps in dissociations are rapid and energetically uphill from the adduct, then we can justify all the steps leading from the silicate to the adduct to be immaterial, and could in some lights be considered merely to be a single (admittedly complex) reaction pathway from the perspective of thermodynamics. As such the rate law depends solely upon the concentration of the silicate, which acts as a reservoir of silane gas to give to the adduct and continue along the reaction pathway. This significant, but greatly simplifying, approximation leads us to the final

reaction map shown in Figure 31, including (simplified) unproductive equilibria and autocatalytic loop.

3.6.4.4 Experimental Model

Each of the kinetics plots proceeds with different rates and, of course, consequently a different set of rate constants need to be used in the associated model. Table 8 gives all the used values and their corresponding barrier heights.

Rate Constant	Temperature (°C)	Value (s^{-1})	Experimental $\Delta G^{\ddagger}$ ($kcal \cdot mol^{-1}$)
$k_{R.E.\ 1}$	75	7.16×10^{-7}	30.3
	80	1.55×10^{-6}	30.2
	85	4.74×10^{-6}	29.8
$k_{R.E.\ 2}$	75	2.81×10^{-4}	26.1
	80	5.74×10^{-4}	26.0
	85	9.65×10^{-4}	26.0
$k_{A\ 1}$	75	50.2	17.8
	80	68.4	17.8
	85	102.7	17.8
$k_{A\ -1}$	75	21.2	18.4
	80	35.2	18.3
	85	41.7	18.4
$k_{D\ 1}$	75	2.18×10^{-4}	26.3
	80	4.91×10^{-4}	26.1
	85	6.43×10^{-4}	26.3
$k_{D\ -1}'$	75	1.36×10^{-1}	21.9
	80	1.02×10^{-1}	22.4
	85	3.91×10^{-2}	23.4

Table 8 Rate constants used to model the k values of the various reaction steps and their corresponding $\Delta G^{\ddagger}$ as calculated by the Eyring equation, assuming $\kappa = 1$.

Additionally, the Eyring equation can be used to decompose the $\Delta G^{\ddagger}$s into their enthalpic and entropic components by linearising the equation and plotting against the reciprocal temperature (assuming κ=1, which is typically a safe assumption in molecular chemistry but may fail where significant barrier tunnelling/reflection occurs such as in reactions involving only hydrogen at low temperatures), which is shown in Figure 42. The derived slopes and intercepts give the

energetic , which were tabulated and compared with the corresponding DFT-calculated values (where both possible and meaningful) in Table 9.

Using k_B in kcal·K^{-1}, *h* in kcal·s^{-1}, R in kcal·mol^{-1}·K^{-1}, and 1/T in K^{-1} gives the graph with the gradient as the negative of the enthalpic contribution to the barrier height ($\Delta H^{\ddagger}$) in kcal·mol^{-1} and the intercept as the entropic contribution to the barrier height ($\Delta S^{\ddagger}$) in kcal·mol^{-1}·K^{-1} (which was converted to cal·mol^{-1} for readability in Table 9).

Rate Constant	Experimental $\Delta H^{\ddagger}$ (kcal·mol^{-1})	Experimental $\Delta S^{\ddagger}$ (cal·mol^{-1}·K^{-1})	Empirical $\Delta G_{298.15}^{\ddagger}$ (kcal·mol^{-1})	Computed $\Delta G_{298.15}^{\ddagger}$ (kcal·mol^{-1})
$k_{R.E.\ 1}$	46.1	45.4	32.6	35.0
$k_{R.E.\ 2}$	29.9	10.8	26.7	27.2
$k_{A\ 1}$	17.0	2.2	16.3	19.1
$k_{A\ -1}$	16.1	6.3	14.2	15.4
$k_{D\ 1}$	26.1	-0.4	26.2	-
$k_{D\ -1}'$	-31.5	-153.0	-	-

Table 9 Enthalpies and entropies of activation for the various reaction steps as derived from the modelled data compared with the corresponding DFT $\Delta G_{298.15}^{\ddagger}$s. As discussed earlier, $k_{D\ -1}'$ unphysically absorbs the associated rate constants for silane gas dissolution and is not comparable with $k_{D\ 1}$ or the other experimental barrier heights.

This agreement between the experimental and DFT values for the calculated barrier heights is quite remarkable, given the *ad hoc* corrections to the data, large number of calculated steps and competing pathways, and the methodological flaws required of DFT and of large molecules. The greatest deviation is seen in the autocatalytic step, differing by 2.8 kcal·mol^{-1}, which is admittedly outside the posited uncertainty but remains within 15% of the relative barrier height, with each other barrier heights within 2.4 kcal·mol^{-1} and 8% of the experimental value.

Due to the DFT-inspired starting values of the rate constants, the criticism that the barrier heights should consequently agree is a valid one, however the solution remains consistent with the data and we do not believe a purely experimental solution to have be possible elicitable.

Three values within a narrow temperature range also decreases the legitimacy of the associated Eyring plot from which the barrier heights were extracted, however experimental difficulties seem to restrict the accuracy with which can refine them.

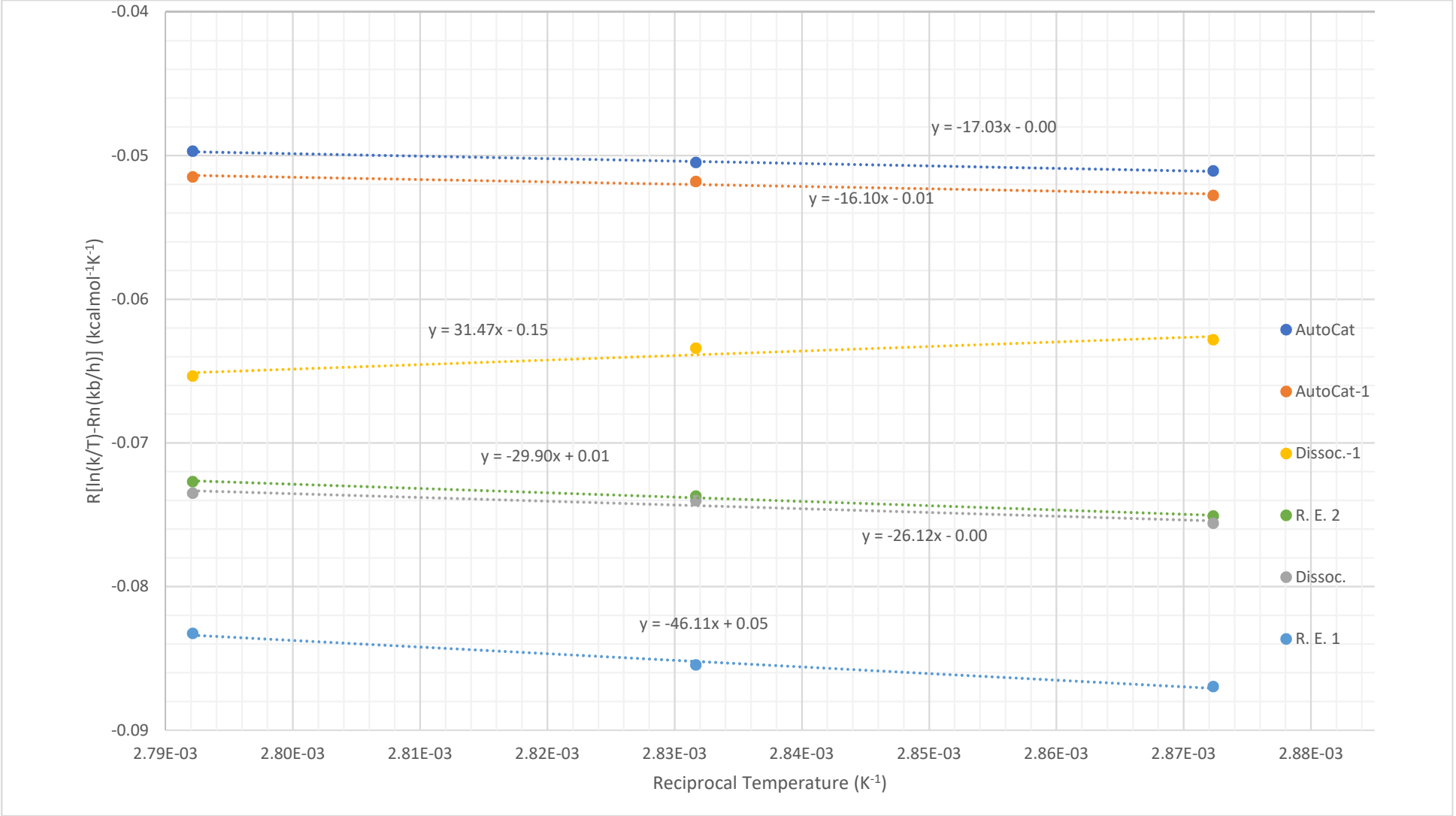


Figure 42 Eyring plot for each of the modelled rates in units such that the equations are of the form $f(T^{-1}) = -\Delta H^{\ddagger} \cdot T^{-1} + \Delta S^{\ddagger}$ in kcal·mol^{-1} / kcal·mol^{-1}·K^{-1}, tabulated in Table 9.

3.6 Conclusions

This chapter establishes a coherent description of the reversible interconversion between an encapsulated hexahydridosilicate dianion and its formally reduced silylene dianion daughter, and it does so by through the lenses of geometry, electronic structure, DFT mechanisms, and processes of experimental kinetics.

The chapter begins with an experimental anchor for all subsequent electronic and mechanistic inference by benchmarking the geometry and key observables of the encapsulated hexahydridosilicate against neutron diffraction, vibrational spectroscopy, and computed NMR parameters. Each of these is confirmed against experiment and shows the characteristic differences between each identified species and supports the identities as posited by the experimental data.

Electronic structure of both the silylene dianion and the hexahydridosilicate were investigated *via* a variety of electronic structure methods including NBO, QTAIM, and EDA ETS-NOCV to confirm their structures as those posited in the introduction of the chapter and provide insight into their underlying bonding motifs.

Beyond electronic structure, substantial efforts of this chapter were involved in the two-fold elucidation and confirmation of the reaction profile of the unusual system and its origins. This was achieved by using density functional theory to provide a reaction profile including fully characterised barriers for all crucial steps in the process, verified by modelling the complex system of differential equations under simple, justified approximations.

The work presented in this chapter (beyond the characterisation of the hexahydridosilicate presented in reference 5) is the subject of a manuscript currently under preparation.

3.7 References

[1] Gabaldón, T., *Annu. Rev. Microbiol.*, **2021**. *75,* 631
[2] Arnold, P. K.; Finley, L. W. S., *J. Biol. Chem.,* **2023**, *299*, *2*, 102838
[3] Jensen, W. B., *J. Chem. Educ.,* **1984**, *61*, *3*, 191
[4] Asimov, I., *The Left Hand of the Electron*, **1972**, Doubleday, Garden City, USA
[5] Huo, R.; Armstrong, J. A.; Nelmes, G. R.; Lawes, D. J.; Edwards, A. J.; McMullin, C. L.; Hicks, J., *Chem. Eur. J.*, **2024**, *30*, e202400662
[6] Huo, R. & Nelmes, G. R.; Edwards, A. J.; McMullin, C. L.; Hicks, J., *Manuscript in Preparation*, **2026**
[7] Hayes, A. G, *Annu. Rev. Earth Planet. Sci.* **2016**, *44*, 57
[8] McMullen, J. S.; Huo, R.; Vasko, P.; Edwards, A. J.; Hicks, J., *Angew. Chem. Int. Ed.*, **2023**, *62*, e202215218
[9] Huo, R., PhD Thesis, **2026**
[10]Cordero, B.; Gómez, V.; Patero-Prat, A. E.; Revés, M.; Echeverría, J.; Cremades, E.; Barragán, F.; Álvarez, S., *Dalton Trans.*, **2008**, 2832
[11] Allred, A. L., *J. Inorg. Nucl. Chem.*, **1961**, *17*, 215
[12] Tatewaki, H.; Koga, T., *Chem. Phys. Lett.*, **1994**, *228*, 562
[13] Norman, N. C.; Pringle, P.G., *Chemistry*, **2022**, 4, 1226
[14] Landis, C. R.; Weinhold, F., *J. Comput. Chem.*, **2016**, *37*, *2*, 237
[15] Rumble, J. R., Ed. *CRC Handbook of Chemistry and Physics*, 106th ed.; CRC Press: Boca Raton, FL, **2025**
[16] a) Zalkin, A.; Forrester, J. D.; Templeton, D. H., *Acta Crystallogr.*, **1964**, *17*, 11, 1408; b) Edge, R. A.; Taylor, H. F. W., *Acta Crystallogr., Sect. B*, **1971**, *27*, 594–601
[17] Lipke, M. C.; Tilley, T. D., *Angew. Chem., Int. Ed.*, **2012**, *51, 44*, 11115
[18] Höllerhage, T.; Ghana, P.; Spaniol, T. P.; Carpentier, A.; Maron, L.; Englert, U.; Okuda, J., *Angew. Chem., Int. Ed.,* **2022**, *61, 10*, e202115379
[19] Puhakainen, K.; Benson, D.; Nyln, J.; Konar, S.; Stoyanov, E.; Leinenweber, K.; Hussermann, U., *Angew. Chem. Int. Ed.*, **2012**, *51*, 3156
[20]Connelly, N. G.; Damhus, T.; Hartshorn, R. M.; Hutton, A. T., Eds. *Nomenclature of Inorganic Chemistry: IUPAC Recommendations,* **2005**, *RSC Publishing*, Cambridge, The United Kingdom
[21] Hicks, J.; Vasko, P.; Goicoechea, J. M.; Aldridge, S., *Nature*, **2018**, *557*, 92
[22] a) Laing, M., *J. Chem. Educ.*, **1987**, *64*, *2*, 124;
[23] Clauss, A. D.; Nelsen, S. F.; Ayoub, M.; Moore, J. W.; Landis, C. R.; Weinhold, F., *Chem. Educ. Res. Pract.*, **2014**, *15*, 417
[24] Nakazawa, H., *Organometallic Chemistry*, **2021**, Royal Society of Chemistry, The United Kingdom
[25] Driess, M., *Nature Chem.*, **2012**, 4, 525
[26] Wang, L.; Li, Y.; Li, Z.; Kira, M., *Coord. Chem. Rev.*, **2022**, *457*, 214413.
[27] Mondal, K. C.; Roesky, H. W.; Schwarzer, M. C.; Frenking, G.; Niepötter, B.; Wolf, H.; Herbst-Irmer, R.; Stalke, D., *Angew. Chem. Int. Ed.,* **2013**, *52, 10*, 2963
[28] Breitwieser, K.; Munz, D., *Adv. Organomet. Chem.*, **2022**, 78, 79
[29] a) Hurst, M. R.; Zakharov, L. N.; Cook, A. K. *Chem. Sci.* **2021**, *12*, 13045; b) Smith, P. W.; Dong, Y.; Tilley, T. D. *Chem. Sci.* **2020**, *11*, 7070; c) Stahl, T.; Hrobárik, P.; Königs, C. D. F.; Ohki, Y.; Tatsumi, K.; Kemper, S.; Kaupp, M.; Klare, H. F. T.; Oestreich, M., *Chem. Sci.* **2015**, *6*, 4324; d) Zhang, X.-H.; Chung, L. W.; Lin, Z.; Wu, Y.-D. *J. Org. Chem.* **2008**, *73*, 820; e) Ríos, P.; Rodríguez, A.; Conejero, S. *Chem. Sci.* **2022**, *13*, 7392 f) Nowicki, M.; Zaranek, M.; Pawluć, P.; Hoffmann, M. *Catal. Sci. Technol.* **2020**, *10*, 1066
[30] Hejda, M.; Hupf, E.; Růžička, A.; Dostál, L.; Beckmann, J. Chem. Eur. J. **2025**, *31*, e202403496
[31] Hu, S.-W.; Wang, Y.; Wang, X.-Y.; Chu, T.-W.; Liu, X.-Q., *J. Phys. Chem. A*, **2003**, *107*, 43, 9189
[32] Elsen, H.; Fischer, C.; Knüpfer, C.; Escalona, A.; Harder, S., *Chem. Eur. J.*, **2019**, *25*, 16141
[33] a) Hariharan, P. C.; Pople, J. A., *Theor. Chim. Acta.*, **1973**, *28*, 213; b) Hehre, W. J.; Ditchfield, R.; Pople, J. A., *J. Chem. Phys.*, **1972**, 56, 2257
[34] Andrae, D.; Häußermann, U.; Dolg, M.; Stoll, H.; Preuß, H., *Theor. Chim. Acta.*, **1990**, *77*, 123
[35] Grimme, S.; Ehrlich, S.; Goerigk, L., *J. Comp. Chem.*, **2011**, *32*, 1456
[36] Becke, A. D., *J. Phys. Rev. A*, **1988**, *38*, *6*, 3098
[37] Becke A. D., *J. Chem. Phys.*, **1993**, *98*, 5648
[38] Ernzerhof, M.; Scuseria, G. E., *J. Chem. Phys.*, **1999**, *110*, 5029
[39] Perdew, J. P., *Electronic Structure of Solids*, **1991**, 11
[40] Chai, J.-D., Head-Gordon, M., J. Chem. Phys., **2008**, *128*, 084106
[41] Weigend, F., Ahlrichs, R., *Phys . Chem. Chem. Phys*., **2005**, *7*, 3297
[42] Makulski, W., Jackowski, K., *J. Mag. Res.*, **2020**, *313*, 106716
[43] Wolinski, K., Hinton, J. F., Pulay, P., *J. Am. Chem. Soc.*, **1990**, *112*, *23*, 8251

[44] Glendening, E. D.; Badenhoop, J. K.; Reed, A. E.; Carpenter, J. E.; Bohmann, J. A.; Morales, C. M.; Karafiloglou, P.; Landis, C. R.; Weinhold, F., *NBO 7.0*, Theoretical Chemistry Institute, University of Wisconsin, Madison, USA, **2003**
[45] Jabłoński, M., *J. Phys. Chem. A*, **2016**, *120*, *24*, 4211
[46] Mitoraj, M. P.; Michalak, A.; Ziegler, T.; *J. Chem. Theory Comput.*, **2009**, *5*, *4*, 962
[47] Rösch, B.; Gentner, T. X.; Langer, J.; Färber, C.; Eyselein, J.; Zhao, L.; Ding, C.; Frenking, G.; Harder, S., *Science* **2021**, *371*, 1125
[48] Hoffmann, R.; Wan, C. C.; Neagu, V., *Mol. Phys.*, **1970**, *19*, 113
[49] Hoffmann, R.; Howell, J. M.; Muetterties, E. L.; *J. Am. Chem. Soc.*, **1972**, 94, 9
[50] a) Frisch, M. J.; Head-Gordon, M., Pople, J. A., *Chem. Phys, Lett.*, **1990**, *166*, *3*, 281; b) Head-Gordon, M.; Pople, J. A.; Frisch, M. J., *Chem. Phys, Lett.*, **1988**, 153, 6, 503; c) Frisch, M. J.; Head-Gordon, M.; Pople, J. A., *Chem. Phys, Lett.*, **1990**, 166, 3, 275
[51] Hoffmann, R.; Hoewll, J. M.; Muetterties, E. L., *J. Am. Chem. Soc.*, **1972**, 94, 9, 3047
[52] Präsang, C.; Scheschkewitz, D. *Silyl Anions In: Scheschkewitz, D. (eds) Functional Molecular Silicon Compounds II. Structure and Bonding*, **2013**, *156*, Springer, Cham
[53] Hohenberg, P.; Kohn, W.; *Phys. Rev.*, **1964**, *136*, B864
[54] Mardirossian, N.; Head-Gordon, M., Mol. Phys., **2017**, *115*, *19*, 2315
[55]Goerigk, L.; Hansen, A.; Bauer, C.; Ehrlich, S.; Najibi, A.; Grimme, S., *Phys. Chem. Chem. Phys.*, **2017**, *19*, 32184
[56] a) Evans, M. G.; Polanyi, M., *Trans. Faraday Soc.*, **1935**, 31, 875; b) Eyring, H., *J. Chem. Phys.*, **1935**, *3*, 107
[57] Plasson, R.; Brandenburg, A.; Jullien, L.; Bersini, H., *J. Phys. Chem. A*, **2011**, *115*, 8073

4 Boryl Radicals, Anions, and Oxygen Extrusion Reactions

"I see the next-door house from a certain angle, but it would be seen differently from the right bank of the Seine, or from the inside, or again from an aeroplane: the house itself is none of these appearances: it is, as Leibnitz said, the geometrized projection of these perspectives and of all possible perspectives, that is, the perspectiveless position from which all can be derived, the house seen from nowhere. But what do these words mean? […] I am trying to express in this way a certain manner of approaching the object, the 'gaze' in short, which is as indubitable as my own thought, as directly known by me."

-Merleau-Ponty, M., *Phenomenology of Perception*, **1945**, translated by Colin Smith 1962

4.1 Introduction

4.1.1 Experimental context for the work

Over the course of her PhD, Ms Emily Nahon within our research group was investigating the low-valent boron species using a range of modified ligands derived from the (NON) framework, work which was expanded upon into low-valent aluminium chemistry by Dr Fabian Kallmeier, which culminated in the work "Xanthene-to-fluorene skeletal editing via oxygen deletion mediated by boron and aluminium radicals".[1]

The experimental work began by reducing boron halides ligated by modifications to the (NON) ligand (only the diisopropylphenyl-substituted (NON) ligand will be discussed within this work) with potent alkali metal reductants in anhydrous, anaerobic conditions in initial attempts to produce novel boryl anions (Figure 1).

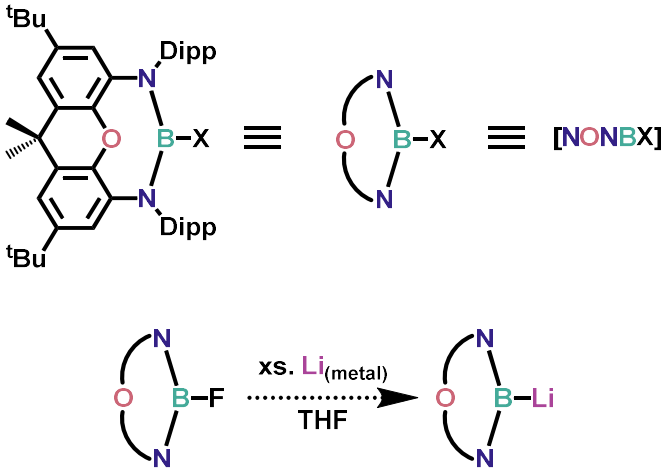


Figure 1 The targeted reaction of reducing the [(NON)BF] compound to the expected [(NON)BLi] boryl lithium, which has not been observed.

Such reductions are well known to require very precise and exacting conditions, and to produce a boryl anion is a significant synthetic feat, so it was unsurprising that the synthesis of the intended compound proved elusive. However, unexpectedly, reproducibly, and quantitatively, Ms Nahon isolated a core motif shown in Figure 2:

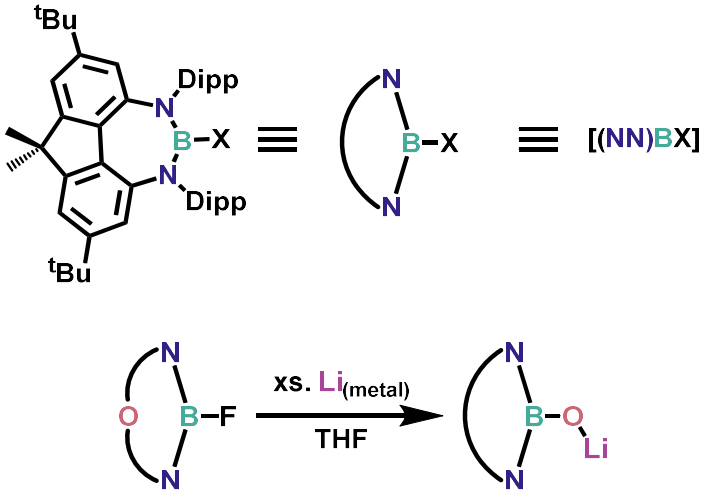


Figure 2 The observed reaction after reduction of [(NON)BF] using lithium metal, showing the unexpected oxygen extrusion product and the consequent boryloxyl lithium.

After initial crystallographic characterisation, this product was assumed to be unrepresentative of the bulk reaction, originating from an impurity in the starting material or not representative of the bulk reaction. Over time however, the reaction proved extremely robust and was even expanded to include examples of related aluminium systems.[1]

The net process seems to involve removing the oxygen from the xanthene backbone, as if with tweezers, closing the two previously ethereal carbon centres into a ring, and inserting the oxygen into the B-Li bond of the presumed boryl anion intermediate. Such processes are often called late-stage modification or skeletal editing, with no small amount of controversy over how this differs from traditional synthetic processes.[2]

The contribution to this "skeletal editing" project presented within this work attempts to explain how and why such an unexpected process occurs through extensive investigation of possible potential energy surfaces for several potentially implicated species, and comparison with the experimental and spectroscopic evidence.

4.1.2 A Brief History of Boron Chemistry

The deoxygenation using boron is actually not unprecedented.[3,4] Two other reports by Frenking, Driess and co-workers, and Frenking, Driess, and co-workers show similar ring contraction products from highly strained xanthenes directly substituted with boron moieties including sterically demanding ligands. However, in each case the boron centres are bound directly to the xanthene 4,5 carbon centres and not through amides (as in the instance presented here).

In their 2025 paper,[4] the authors provide a potential mechanism for the oxygen extrusion at the BP86-D3BJ/def2-SVP level of theory, although their free energy profile posits an unphysically high barrier $\Delta G^{\ddagger}$ of 53.7 kcal mol^{-1}, Figure 3. This barrier cannot feasibly be surmounted at the cryogenic temperatures reported, which the authors freely admit, instead suggesting that the excess reductant KC_8 could be involved in an "unspecified" way. See Figure 6 (of the article) and related text for further details. For reasons of comparison with this work and the fully local nature of the method (*vide infra*), we also use the BP86-D3BJ density functional and a modified double-zeta basis (Pople's 6-31G** with Stugart-Dresden for heavy atoms with an additional polarisation function).

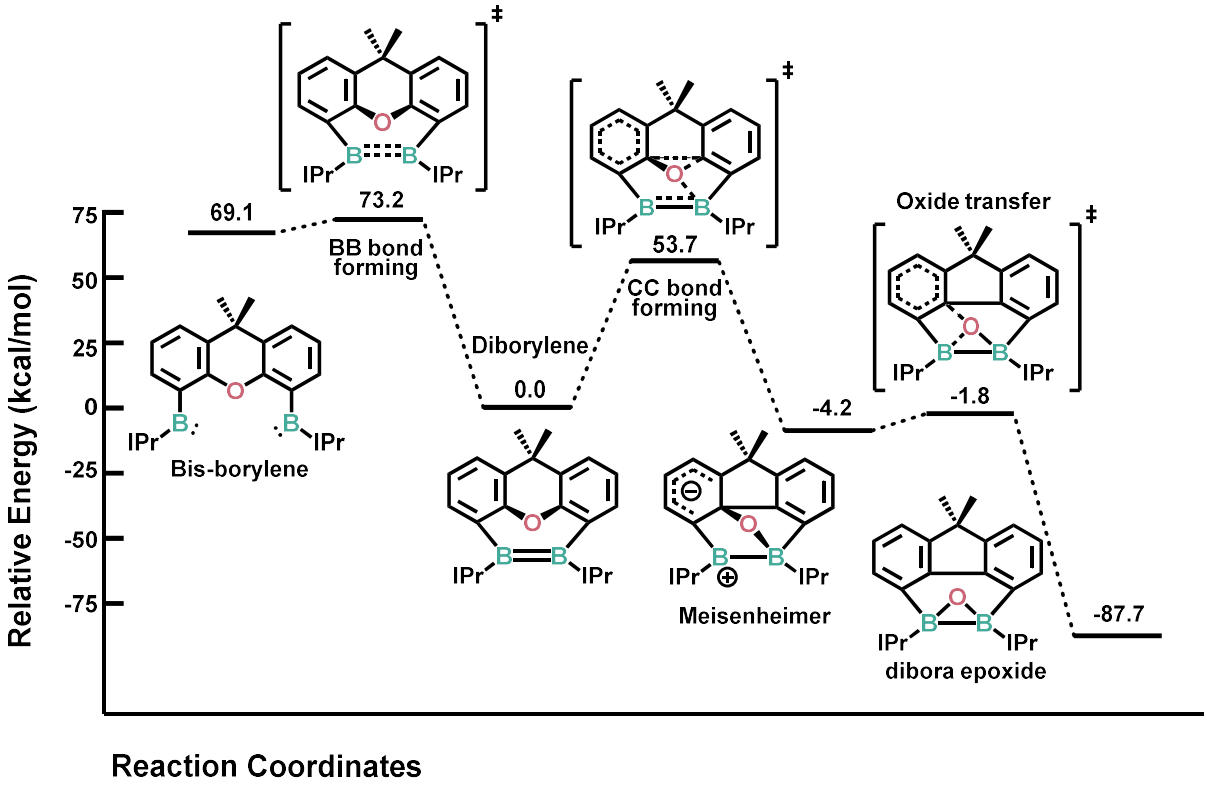


Figure 3 Reproduction of the reaction profile presented by Driess, Frenking and coworkers in reference 4. In the rate determining step the diborene double bond acts as a nucelophile to concerteredly rupture. IPr = [C{N(iPr)CMe}$_2$] is an N-heterocyclic carbene acting as a base to stabilise the reactive boron intermediates.

Evidently, a direct nucleophilic attack by the boron centres at the ether motif is energetically unfeasible for even the electron-rich diborene at the highly strained xanthene backbone. However, the authors present limited evidence that either the diborene or the bis-borylene is the reactive species, perhaps a less reduced, higher multiplicity intermediate could be implicated instead.

4.1.3 Boryl Radicals

Boryl radicals, which will become relevant at the termination of the chapter, are boron-centred open-shell species that in their simplest conception, comprise a formally three-coordinate boron atom bearing an unpaired electron.[5] Secondly, their intrinsic electronic structure renders them both highly reactive and highly sensitive to stabilisation strategies, because a boron centre that is simultaneously electron-deficient (half-vacant sp^2 orbital) and electron-rich (formal oxidation state of II compared with the typical III) tends to undergo rapid follow-on reactions unless steric shielding and/or donor-acceptor compensation is present.

From the standpoint of synthetic and mechanistic chemistry, the modern resurgence of boryl radicals is closely associated with their ability to participate in single-electron pathways that complement traditional two-electron organoboron reactivity. Notably, comprehensive accounts emphasise that NHC-boryl radicals have matured from spectroscopic curiosities into practical intermediates for radical reductions, and boryl radical addition processes, with broad ramifications for C-B bond construction and radical-polar crossover sequences.

Within this computational work, we approach the boryl radical not as an isolable, target species but instead as a highly reactive intermediate which has been invoked in reaction mechanisms since boron-halide reductions in the 1960s.[6]

4.1.4 Boryl Anions

Boryl anions (often referred to as "boryl-metal", *e.g.* boryl lithium) have long been regarded as boron analogues of carbanions, in the sense that they can, under suitable stabilisation, behave as boron-centred nucleophiles rather than the more familiar Lewis-acidic boranes and borates.[7] Secondly, the historical difficulty in isolating such species reflects the electronic mismatch between typical boron valence preferences and the requirements for a persistent, nucleophilic, low-coordinate boron centres, due to boron's comparatively low electronegativity it broadly lacks the ability to stabilise negative charges.[8]

The modern field begins with the isolation of boryl lithium by Yamashita and Nozaki, in which diamino substitution and ring constraint stabilise an anionic boron centre that is isoelectronic with an N-heterocyclic carbene.[9] This work demonstrated canonical boron-nucleophile reactivity, and structurally authenticated the existence and possibility of mononuclear B(I) species.

A key theme that emerges is that boryl anions frequently require strong electronic stabilisation (commonly by π-donor substituents such as amino groups, analogous to N-heterocyclic carbene chemistry[10]) and steric protection to suppress aggregation, disproportionation, or reaction with even very weak electrophiles (*e.g.* solvent molecules). Ligand design is consequently crucial to stabilise these highly reactive low-valent main group species, and researchers are constantly seeking to expand the very limited number of isolated examples.

Computational studies of boryl anion reactivity are well established in the literature, typically centred around their reactivity once they have formed,[11] however some examples exist when the circumstances of their synthesis are curious, such as those by Hill, McMullin, and coworkers, using a similar BP86 methodology.[12]

We employ the similar methodology described below for sake of comparison with literature methods, and for the ability of this methodology to describe closed and open shell pathways with similar (albeit somewhat limited) accuracy.

4.2 Methodology

Density functional theory (DFT) calculations for geometry optimisation were performed using the Gaussian 16 program[13] using Becke's 1988 exchange functional[14] and Perdew 1986 correlation functional[15,16] approximations with Grimme's D3 dispersion correction with Becke-Johnson dampening[17], and Pople's 6-31G** basis set[18,19] with the ultrafine integration grid. The BP86-D3BJ functional was used because of its good agreement with barrier heights and low computational cost, and for its comparable treatment of open- and closed-shell systems, [20] for which comparison proved necessary. Conveniently, the similar system xanthene deoxygenation studied by Driess and Frenking was investigated at the comparable BP86-D3BJ/def2-SVP level of theory.[4]

The structures were confirmed as minima on the potential energy surface *via* analytical frequency calculations, yielding no negative eigenvalues, except for transition states, which were verified as saddle points on the potential energy surface with a single negative eigenvalue unless otherwise stated. The corresponding imaginary modes were verified as connecting the appropriate intermediates *via* the intrinsic reaction coordinate (IRC) method.

Transition states were found *via* relaxed potential energy surface (PES) scans from the indicated intermediate along a specific coordinate in Gaussian 09 A.02[21] (BP86-D3BJ/6-31G** scf=(conver=6) and opt=(gdiis, maxcyc=10, stepsize and number

dependent on the intermediates), taking the local energy maximum along the scan as a starting geometry and using the Berny eigenvector-following algorithm with the initial Hessian matrix calculated *via* analytical frequencies, as implemented in Gaussian 16.

Thermochemical properties were calculated at a pressure of 1.0 atmospheres, unscaled frequencies, and a temperature of 298.15 K. Single point Gibbs free energies were obtained by adding the Gibbs free energy calculated at the BP86/6-31G** level of theory to the differences in self-consistent field energies calculated using the larger basis (ΔE_{Basis} = $SCF_{BP86\text{-}D3BJ/6\text{-}311++G**}$ - $SCF_{BP86\text{-}D3BJ/6\text{-}31G**}$) and solvation corrections ($\Delta E_{Solvation}$ = $SCF_{BP86\text{-}D3BJ\text{-}CPCM(THF)/6\text{-}31G**}$ - $SCF_{BP86\text{-}D3BJ/6\text{-}31G**}$) for a final corrected Gibbs energy G_{corr} = $G_{BP86\text{-}D3BJ/6\text{-}31G**}$ + ΔE_{Basis} + $\Delta E_{Solvation}$. The larger basis set used was the triple-zeta Pople basis with polarisation and diffuse functions[22,23,24] 6-311++G**, and the solvation correction used was the conductor-like polarisable continuum (CPCM) model[25,26,27,28] using tetrahydrofuran as the solvent (ε = 7.4257).

Motivated by the experimental work, we suggest a facile reaction (*ca*. 20 $kcalmol^{-1}$ barrier height) for the oxygen extrusion as a faster reaction than the second reduction, as evidenced by an experimentally observed radical species by electron paramagnetic resonance (EPR) of the reaction mixture. This mechanism is presented anachronistically, as efforts were initially spent in seeking a closed shell mechanism, which we were unable to find using either an intramolecular activation from a boryl anion, or with reactions between a boryl anion and the starting boron fluoride (*vide infra*).

For the open shell mechanism, we presume the reaction starts with the boryl radical resultant of a one electron reduction of the borane fluoride, which was elucidated by taking the solid-state X-ray structure of the corresponding fluoride, deleting the fluorine, and optimising the neutral doublet as described in the methodology.

For the closed shell reaction mechanism, we presume the starting material to be the corresponding two-electron reduced species- either the naked boryl anion or the corresponding lithiated (“charge-balanced”) species.

4.3 Auto-Deoxygenative Ring Contraction Mechanisms

4.4.2 Closed Shell Mechanisms

4.4.2.1 Intramolecular Closed Shell Mechanisms

We attempted to elucidate a possible pathway for the oxygen extrusion from closed-shell species as either boryl anions, boryl lithium, or intermolecular activations following a series of possible pathways laid out in Figure 4, predicting that the mechanism would occur through a traditional closed-shell, rapid intramolecular process. As the [(**NON**)BF] complex does not experimentally extrude the oxygen, only doing so in the presence of lithium metal, we presumed the reactive species to be the corresponding boryl lithium, presumed to be stable by analogy with many other reported isolable species.[3,4]

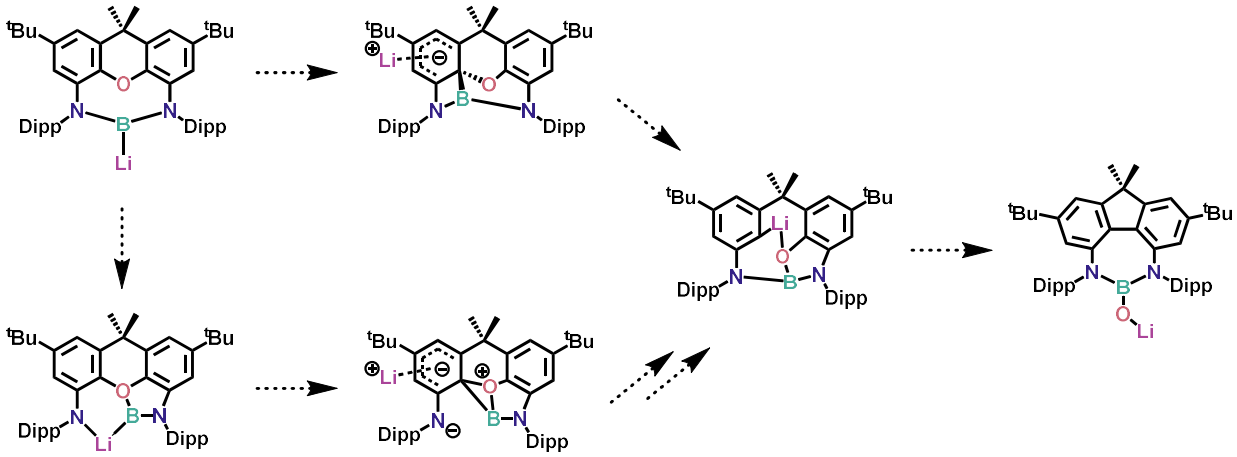


Figure 4 Possible pathways for oxygen extrusion starting from the boryl lithium and going through nucleophilic attack.

Initial attempts to elucidate a mechanism started with a monomeric boryl lithium. Immediate issues were encountered with an intramolecular mechanism with regards to the necessary redox processes. At some point in the reaction, the boron centre must act as a nucleophile so that it can formally transfer its electrons to the carbon centres in the backbone which are being reduced, as initially the boron species is B(I), but the isolated oxygen extrusion product is B(III). However, no scans decreasing the boron-carbon bond coordinate result in potential energy surfaces with appropriate transition states, always instead possessing discontinuities and leading to unrelated intermediates, no matter how fine the step size and generous the relaxation parameters.

Instead, we hoped a better geometry could be found by migrating the boron centre to be chelated by the oxygen and just one nitrogen, ("Borylene Amide", Figure 4 lower pathway).

Even from this improve geometry however, the species must still form a three-membered ring with the boron-carbon-oxygen motif, and we were still unable to elucidate nucleophilic attack by the boron centre on either ethereal carbon centre. Broadly, we find this comforting in that experimentally, more nucleophilic but related species like the aluminyl anion of the same **NON** ligand are not observed to extrude the oxygen once they are formed, regardless of temperature, so we believe this type of intramolecular nucleophilic attack to be unobserved in experiment, suggesting we are unlikely to find anything reasonable in computation.

With no viable nucleophilic attack, an alternate path was motivated by starting with the crucial C-C coupling step. Imagining the most potent carbon nucleophile which could be formed to be the aryl lithium, and the best electrophile to be the borane ether with the oxygen also coordinated to the lithium, we attempted to find a pathway from this artificially contrived intermediate (Aryl lithium, Figure 5).

After minimising this fictitious intermediate and confirming it to be a local minimum on the potential energy surface, scanning the two previously ethereal carbon centres closer together elucidates an appropriate transition state which links directly to the observed boryloxy lithium. We presumed this would result in a Meisenheimer intermediate, however no minimum could be elucidated, likely due to the facile leaving group nature of the lithium boryloxide moiety, instead computationally progressing to the observed product.

With this promising transition state starting the pathway, efforts were made to then continue "backwards" along the reaction path from the carbanion back to the presumed boryl lithium starting material. Unfortunately, scanning the boron centre towards the carbon centre from either the same or opposite face as the oxygen in attempts to elucidate the previous Meisenheimer intermediate which we hoped to be resultant from the nucleophilic attack each proved unfruitful and only increased in energy, never yielding a maximum on the PES from which to elucidate a transition state (or even possible intermediate), finding ourselves parochially dead in the water.

Ultimately, even if we were able to find a pathway linking the boryl lithium to the elucidated C-C coupling transition state, it still suffers an exceptionally high $\Delta G^{\ddagger}$ of *ca*. 28 kcalmol^{-1} with respect to the boryl lithium starting material, unfeasible even at room temperature, let alone the observed cryogenic temperatures (Figure 5 demonstrates the futility in this intramolecular C-C coupling pathway, even in the face of our inability to find a traversable potential energy surface).

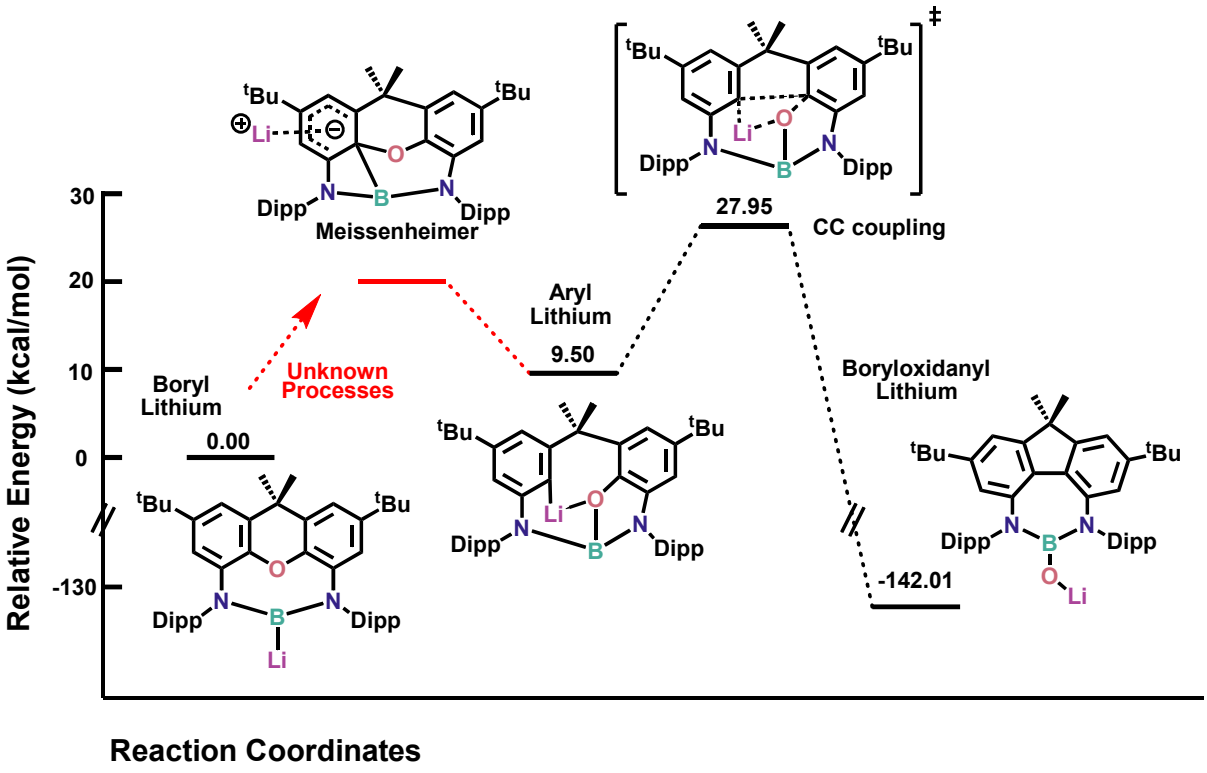


Figure 5 Attempted elucidation of the reaction profile for the intramolecular, closed-shell oxygen extrusion starting from a presumed aryl lithium intermediate, for which we were unable to find a pathway backwards to the presumed boryl lithium starting material. Calculated at the BP86-D3BJ-CPCM(THF)/6-311++G//BP86-D3BJ/6-31G** level of theory.**

It was suggested to us by Professor Anthony Hill that the initial reduction of the complex may actually not involve the boron centre or fluoride at all, and instead lithium metal may be directly reducing the ether to the aryl lithium, in which case the barrier may be approximately only 18 kcalmol^{-1} (taking the "Aryl Lithium" carbanion as the starting material and assuming introduction of the fluoride will not dramatically change the energy or geometries involved). Experimentally, however, the corresponding methyl borane species (i.e., a methyl group in place of the fluoride) is not reduced by lithium metal under the same conditions as the fluoride, and no intermediate or oxygen-extruded product is observed. Consequently, we did not consider a theoretical route not involving the boron centre to be viable. Qualitatively, if the system were considered as in Figure 5 with an additional fluoride bound to the boron centre (making the system anionic but presuming the C-O bond had been reduced and the BF remaining intact), we presume the aryl lithium to be a comparable nucleophile, but the borane to be a significantly worse Lewis acid and consequently the ethereal carbon centre to be a significantly worse electrophile, likely even resulting in a larger barrier.

Our inability to find any *intra*molecular redox process involving the boron centre directed us towards *inter*molecular processes, having a boryl anion attack another ligand-containing

species to trigger the oxygen extrusion. Such a process seemed unlikely as isoelectronic, but more nucleophilic, systems such as the aluminyl anion of the same ligand, do not display analogous oxygen extrusion even at elevated temperatures. However, the small and more carbophilic nature of boron may nonetheless allow for different reactivity. We tentatively suggest that such processes do not occur, as the barriers we were able to elucidate appear to possess an unfeasible barrier height between 35 and 55 kcalmol^{-1}.

As an aside, several key intermediates were also optimised including explicit tetrahydrofuran (THF) solvation of the lithium cation, with both one and two molecules of THF. This did not appreciably change the relative Gibbs free energy of the intermediates involved, but did make elucidation of transition state significantly more difficult due to the shallow PES for the Li-O bond lengths and the geometry of the THF molecules, as well as the uncertainty of the number of THF molecules coordinated and the possibility that this changes over the course of the mechanism. We were unable to improve upon the mechanism by exploratory inclusion of explicit coordination, and the increased difficulty for possibly no material reward was deemed unnecessary. Consequently, it is possible that the pathways involving lithium presented here are viable but only under explicit coordination of THF, however we deem this unlikely in the face of the feasible radical mechanism.

4.4.2.2 Intermolecular Charge-Balanced Mechanism

As an intramolecular pathway was deemed unfeasible, we investigated the possibility of intermolecular pathways. Typically, the sterically demanding nature of the associated ligand protects it from reacting with itself, allowing for the formation of isolable potent nucleophiles and other reduced species. However, boron is one of the smallest elements on the periodic table, which may allow for unexpected reactivity in the face of the steric bulk.[29] This reduced atomic radius may, instead of burying the element deeper within the protective framework, allow for a more facile approach to potential electrophiles, even including the protective framework of another complex. Computationally, this did not prove to be the case, but was the initial motivation for the investigation, or perhaps merely out of desperation at the lack of intramolecular success.

Similarly as in the monomeric case, the closed shell system was the initial target. Due to the large number of possible geometries for intermolecular nucleophilic attack, the mechanism was investigated starting from an imagined Meisenheimer intermediate presumed to be the product

of the boryl lithium complex attacking a boron fluoride complex ("Meisenheimer" in Figure 6).

In the forward direction (*i.e.* towards the lithium boryloxide product), the idea was to produce again the most potent nucleophile available to the process, the aryl lithium intermediate. Regardless of the consequent C-C coupling transition state being the same as in the intramolecular case, we hoped that the formal oxidation of the boryl lithium from B(I) to B(III) over the course of the reaction profile might provide the necessary energy to overcome the barrier, and even in an energetically unfeasible regime, it would possibly be an insightful pathway.

With this goal in mind, we sought to continue on through an intuitive series of steps to produce the aryl lithium intermediate.

Scanning the oxygen away from the Meisenheimer carbon centre resulted in the predictably low-barrier transition state of the CO heterolysis, linking through IRC to the phenoxide intermediate., *ca*. 7 kcalmol^{-1} downhill from the Meisenheimer. This undergoes a small rearrangement to coordinate the ethereal oxygen centre to the boron centre to which it must inevitably bond, forming "borate 1".

Our initial hope was that this species would form a potent enough nucleophile to induce the C-C coupling with the excellent borate leaving group, however no scans were able to elucidate such a transition state. Instead, we resumed out goal of forming the aryl lithium intermediate. To this end, we removed the fluorine from the borate, presumed to be a facile process possibly facilitated by other salts or Lewis acids present in solution, and returned it to the other boron centre, forming "borate 2", predictably very similar in energy due to the presence of the same number and type of bonds present.

This new borate was deemed a good leaving group, and scanned away from the arene, elucidating the "Migration" transition state, where the lithium moves from the back of the ring to be bonded to the arene sp^2 lone pair, and the newly formed borane coordinated to the same carbon centre through the boron centre. This transition state was shown to link "borate 2" and "Meisenheimer 2" through the IRC method.

Simply scanning away the borane revealed no local maximum, instead smoothly increasing to the starting [(**NON**)BF] leaving as the borane and the desired aryl lithium intermediate.

The aryl lithium intermediate then forms the product through the same mechanism indicated in the intramolecular process (*vide supra*), completing the forward direction of the reaction profile.

The reverse from the initially presumed "Meisenheimer 1" proceeds with similar facility. Increasing the B-C bond results in the "Nucleophilic Attack" transition state, with both the lithium centre and boron centre losing their interactions with the [(NON)BF] complex.

Interestingly, the elucidated nucleophile was not the previously elucidated [(NON)BLi], but instead a 5-memebered ring form of the boron nucleophile, having inserted the lithium into the B-N bond to form a structure labelled "Amido Borylene". Removing this amido borylene adduct back into its constituent parts of the [(NON)BF] and the lone amido borylene, in order to return to the presumed starting materials, all that is necessary is to "deinsert" the lithium from the B-N bond, through a transition state already characterised (labelled as "Li migration"), known to us from attempting to use the amido borylene as the intramolecular nucleophile.

This yields the initial monomers and completes the pathway in the reverse direction.

With the reaction elucidated from a necessary intermediate in both the forward and backward directions, the reaction profile is complete. It is immediately obvious however, that the nucleophilic attack transition state has an impressive barrier of 55.1 $kcalmol^{-1}$, higher than that reported by Frenking and Driess and coworkers by 1.4 $kcalmol^{-1}$, we deem this pathway to be similarly unfeasible.

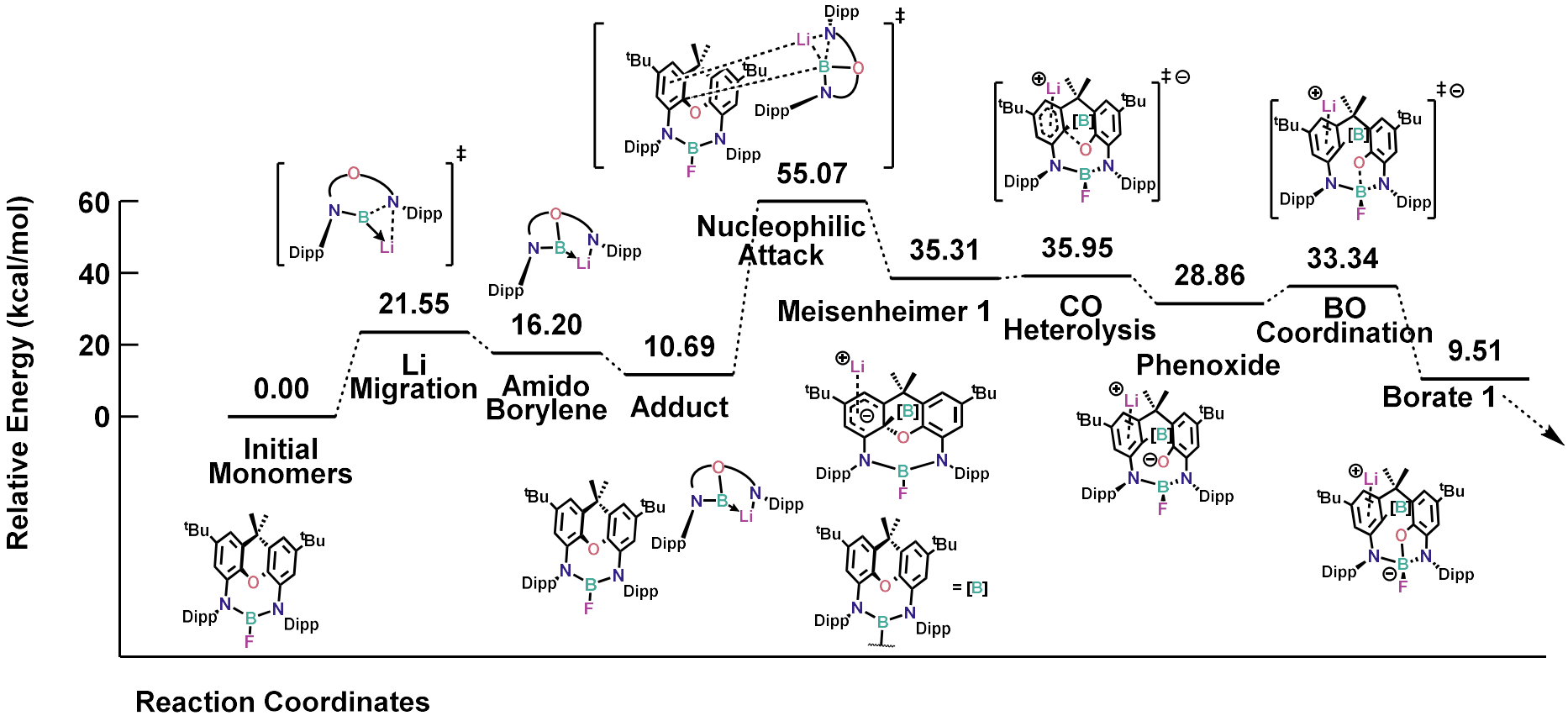


Figure 6 Free energy reaction profile (part 1) for the dimeric, lithiated (charge-balanced) pathway for the deoxygenative ring contraction at the BP86-D3BJ-CPCM(THF)/6-311++G//BP86-D3BJ/6-31G** level of theory starting from the monomeric boryl lithium and fluorido borane species. First, the boryl lithium is "prepared" for the nucleophilic attack by inserting the lithium into the boron-nitrogen bond, forming the amido borylene intermediate. Subsequent nucleophilic attack occurs at the ethereal carbon centre with an unfeasibly high 55.1 kcal mol^{-1} barrier before continuing to the anionic mechanism presented in Figure 10 until the step "borate 2", continued in Figure 7.**

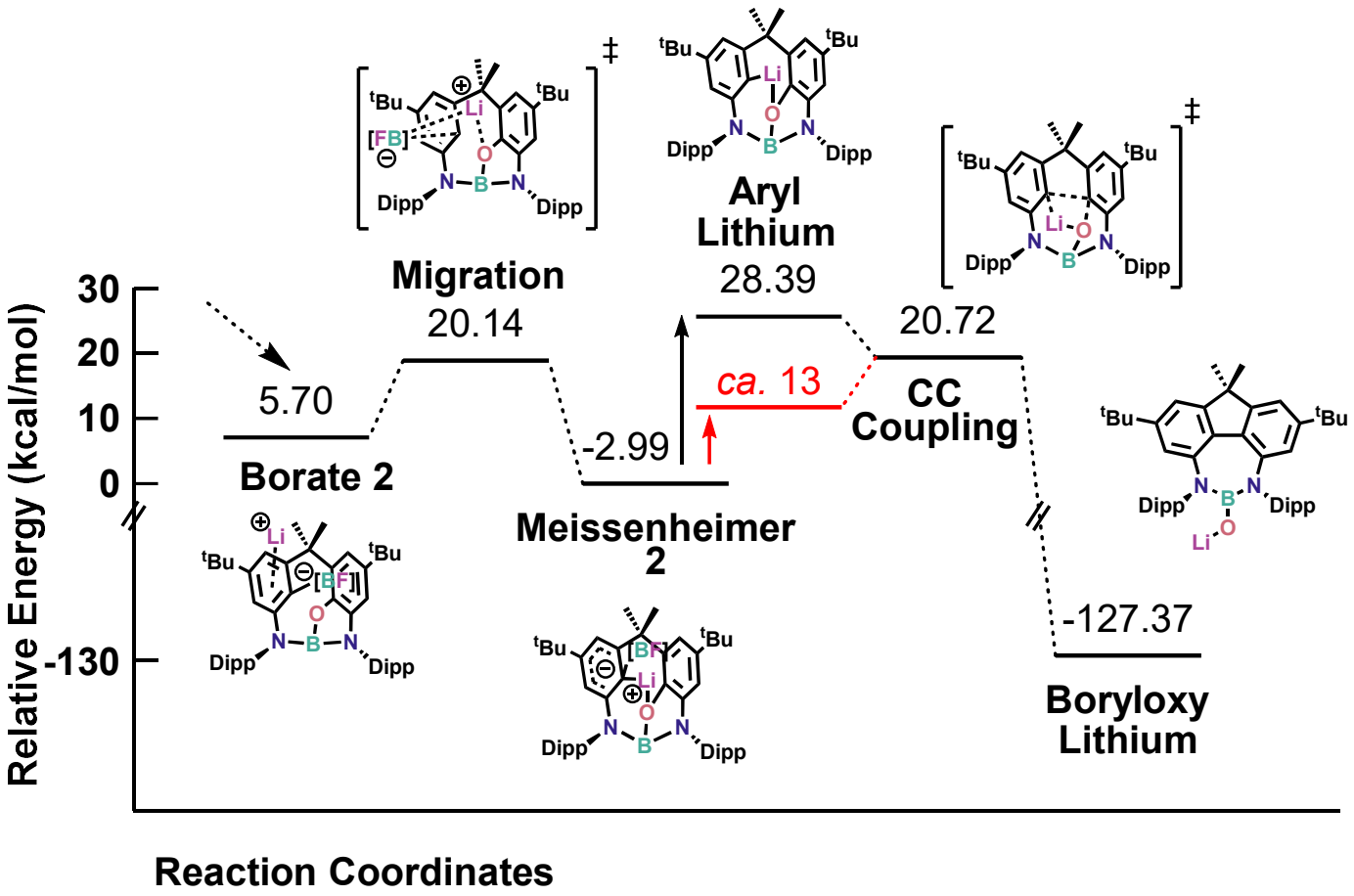


Figure 7 Free energy reaction profile (part 2) for the dimeric, lithiated (charge-balanced) pathway for the deoxygenative ring contraction at the BP86-D3BJ-CPCM(THF)/6-311++G//BP86-D3BJ/6-31G** level of theory starting from the monomeric boryl lithium and fluorido borane species, continued from Figure 6. Beyond the second borate, in order to form the necessary aryl lithium nucleophile, the lithium migrates from the aromatic ring to the lysed oxygen, from which the fluorido borane barrierlessly dissociates leaving the monomeric aryl lithium complex. Relative free energies in kcal mol^{-1}. *N.b.* The final C-C coupling TS at 20.7 kcalmol^{-1} was located as a true maximum of the electronic energy PES during the optimisation process. Subsequent solvation and basis set corrections have resulted in lowering the free energy to below the preceding aryl lithium intermediate. The energy of the aryl lithium intermediate is inexplicably higher than its subsequent C-C coupling transition state, which appears to be due to unusual behaviour of the basis set correction, explored in Figure 8 and given an estimate of an expected 13 kcalmol^{-1} in place of the unphysical 28.39.**

The keen-eyed reader may note that the final, C-C coupling transition state (Figure 7, then step 15 in Figure 8) is (unphysically) lower in energy than the preceding aryl lithium intermediate (step 14, Figure 8). This is an unfortunate consequence of the methodology, where both the basis set and solvation corrections greatly increased the relative energy of the aryl lithium intermediate (resulting in a relative increase of 20.64 and 15.24 $kcalmol^{-1}$ respectively for a total of 35.88 $kcalmol^{-1}$ to the Gibbs energy of the intermediate) but only did so modestly for the transition state (4.92 and -0.47 $kcalmol^{-1}$ respectively for a 4.44 $kcalmol^{-1}$ total increase), changing their respective positions on the PES from -7.49 and 16.28 $kcalmol^{-1}$ to the reported 28.39 and 20.72 $kcalmol^{-1}$ respectively (see Figure 8 for details).

Basis set superposition error (BSSE) is unlikely to blame for the relative changes between steps 14 and 15, as they are both in the monomeric part of the mechanism and have the same number of and similar distances between atoms, which likely indicates significant basis set incompleteness error (BSIE) at the BP86/6-31G** level.[30] This appears to be due to the relatively improved description of intermediate 14 ("Aryl Lithium" in Figure 7), which has significantly less basis set correction (-546.15 $kcalmol^{-1}$) than any of the other monomeric species (1, 2, 3, 15, and 16, of Figure 8, mean ± stddev = -561.66 ± 0.25 $kcalmol^{-1}$), resulting in the aryl lithium having *ca*. 15.5 less basis set correction. Repeats of each calculation were identical and we could find no user error to explain the particularly adequate description of the aryl lithium intermediate by 6-31G**, perhaps significant error arises from the neglect of explicit solvation of the lithium cation with THF ligands, which were neglected due to computational cost and not revisited in light of the open shell mechanism's success.

Unperturbed, we instead set our sights on an anionic closed shell intermolecular mechanism presented in the next section.

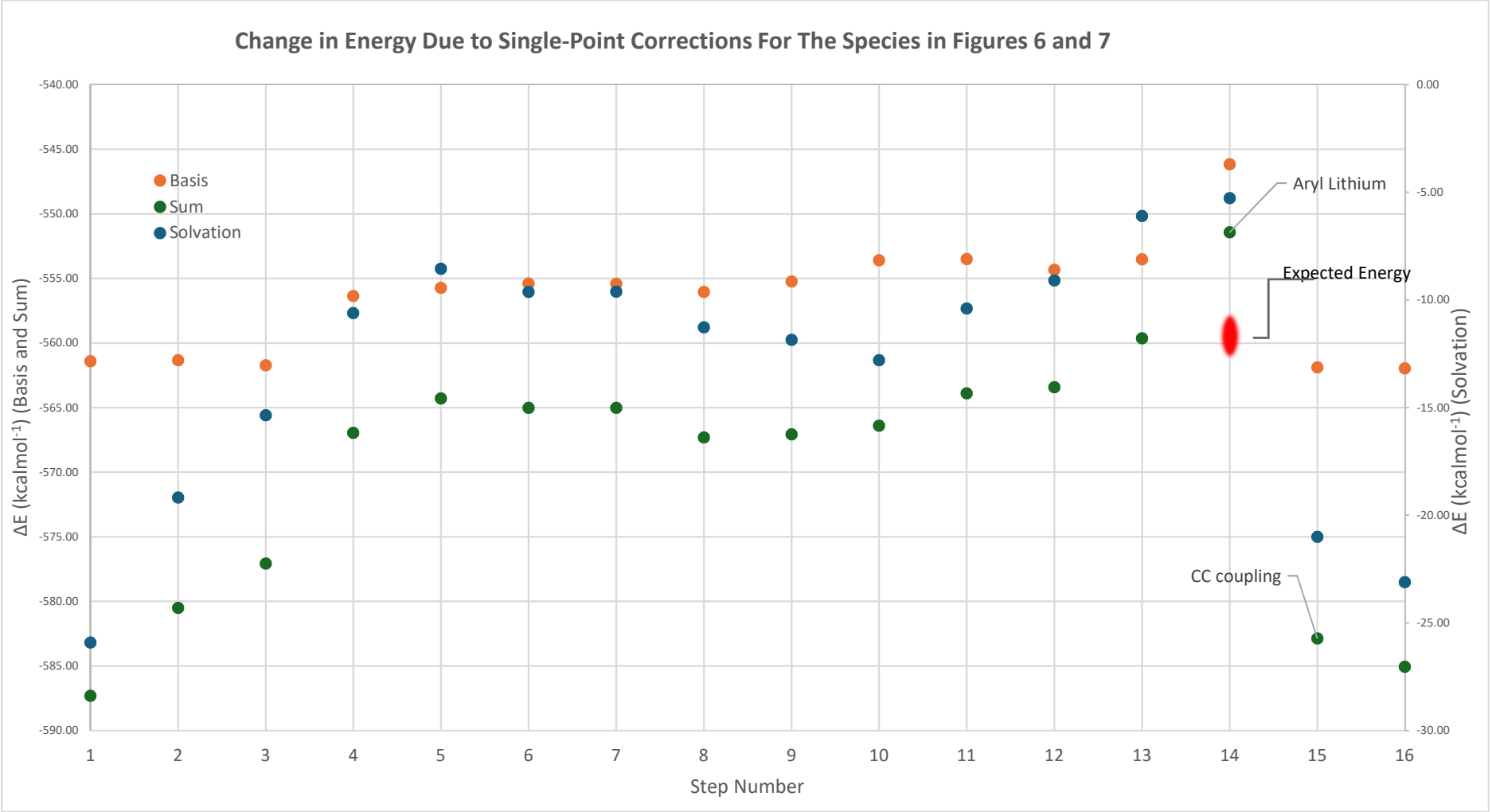


Figure 8 Energy corrections to each species (and consequently their relative energy) for each solvation, basis set, and their sum, for each member of the reaction profile in Figure 6 and 7. Evident from the sharp increase in the magnitude of the correction between aryl lithium and C-C coupling, the C-C coupling transition state has fallen lower in energy than the preceding intermediate, evidently principally from basis set correction. (Note that the solvation correction is much smaller and plotted on a separate axis). Salient is the unexpectedly large difference in single point correction for the C-C coupling transition state and the preceding intermediate, changing their relative energies by 31.44 kcalmol^{-1}.

4.4.2.3 Intermolecular Anionic Mechanism

It is possible that the reactivity is due to a dissociated ion pair, which is difficult to calculate the exact energy of but has previously been indicated as the reactive species in low-valent chemistry.[31]

We again began with the Meisenheimer intermediate, this time as the anion, generated simply by deleting the lithium from the analogous charge-balanced structure and optimising again, the mechanism shown in Figure 10. Beyond this, the C-C bond forming step requires a nucleophile and an electrophile, the chosen electrophile being the potent diboryloxidane "leaving group", and the nucleophile being the poor base aryl borate. Originally, the more potent aryl anion was chosen to be the nucleophile, however, transferring the borane from the carbon centre to the oxygen triggered the C-C coupling without having to separately form the indicated species. In this fashion, moving forward from the Meisenheimer intermediate was possible through dissociation of the oxygen (C-O heterolysis transition state) to form the aryloxide intermediate, which undergoes facile coordination to the other boron centre to form "borate 1". The preparation of the electrophilic carbon centre is not possible from borate 1, as the borane proved too sterically encumbered to form a borate with the previously ethereal oxygen, no transition state or productive intermediate was able to be elucidated. Instead, dissociation of one half of the chelating NON ligand proved necessary, which was only possible from a borate anion. Consequently, swapping boron centres was assumed facile for the fluoride ligand, and one half of the NON ligand was dissociated from "borate 2". This process proved barrierless, to then form the next xanthene amide intermediate. The remaining steps are somewhat straight-forward, and revolve around reforming the fluorido borane and the observed product.

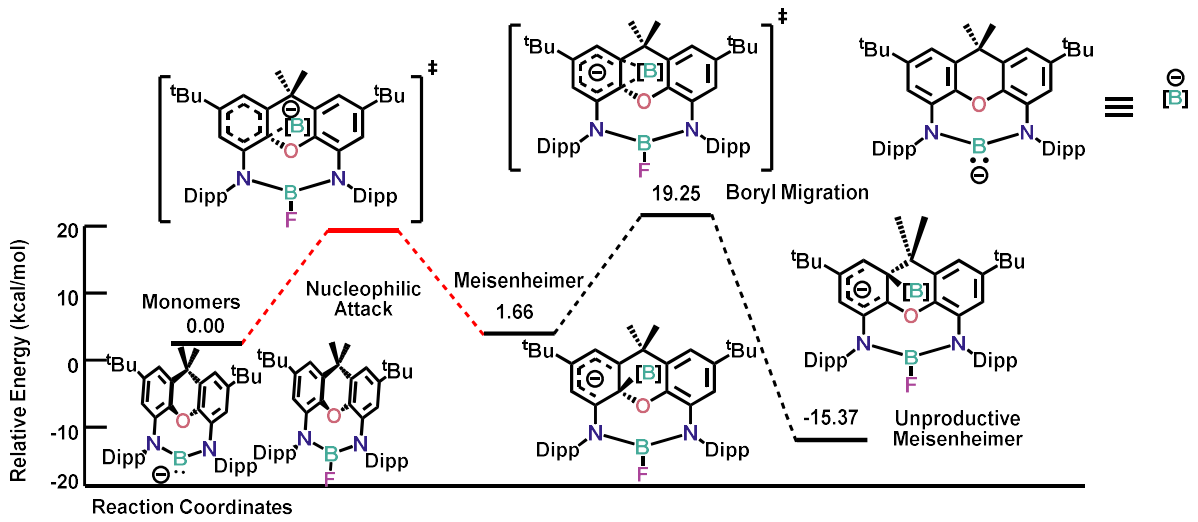


Figure 9 Nucleophilic attack attempted reaction pathway calculated at the BP86-D3BJ/6-31G level of theory. We were unable to elucidate any nucleophilic attack transition state (red) starting from the boryl anion, instead all characterised transition states were that of a 1,2-boryl migration.**

In the backwards direction (from "Meisenheimer" to "Monomers" in Figure 9), scans were attempted to increase the B-C distance, but the only transition state found was that of a 1,2-boryl migration towards the dimethylmethylene-bridged carbon centre. Again scanning from this product ("Unproductive Meisenheimer") reproduced the same transition state, and constraining various angles and dihedrals were unable to resolve the issue and find a nucleophilic attack. A nucleophilic attack transition state was only found for the lithiated Meisenheimer (*vide supra*), so formally the energy of each species in the forward direction for the boryl anion case in Figure 9 depends on the energy of the lithiated Meisenheimer intermediate plus the energy associated with charge separation (*i.e.* further solvating the lithium and then a difficult theoretical treatment with extended Debey-Hückel theory[32]), but we have presented the reaction diagram with the boryl anion as the relative zero, as either: a) the rate limiting step in the lithiated pathway is the nucleophilic attack and that barrier is higher than any presented in the anionic pathway, so the anionic pathway inherits this rate limiting step, or b) there is a lower energy nucleophilic attack transition state we were unable to elucidate and the rate limiting step in the anionic reaction is still an unphysical 30.04 kcalmol^{-1}. However it is of little consequence as neither intermolecular mechanism matches experiment and are only presented here in contrast with the open shell extrusion.

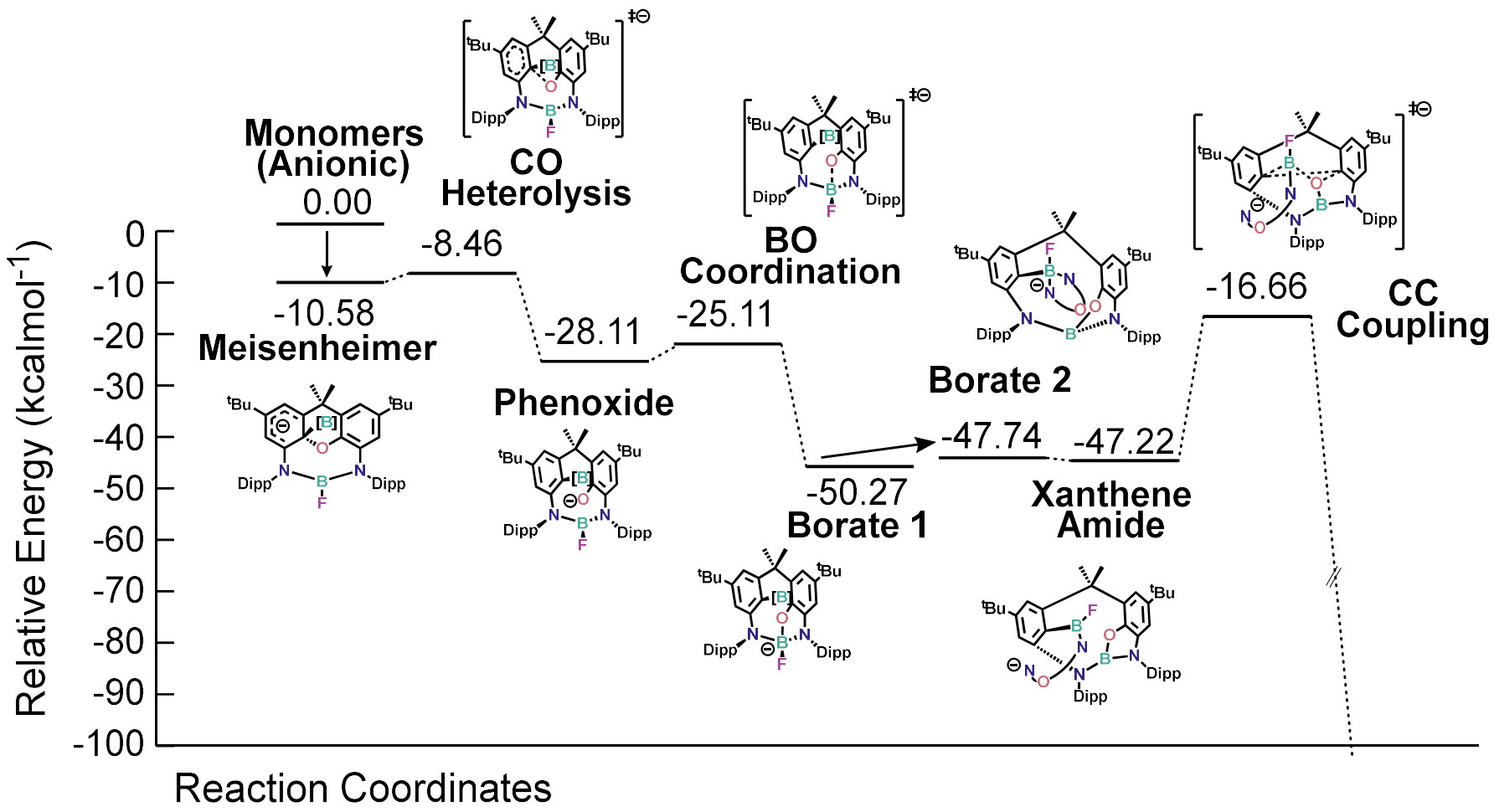


Figure 10 Free energy profile (part 1) for the dimeric, anionic pathway for the deoxygenative ring contraction at the BP86-D3BJ-CPCM(THF)/6-311++G//BP86-D3BJ/6-31G** level of theory starting from a presumed Meisenheimer intermediate. Initially, the Meisenheimer intermediate eliminates the aryloxide, forming the intermediate "phenoxide". The oxygen then has a facile coordination to the trivalent boron centre forming "borate 1". BO coordination and C-C coupling occurr concertedly through "C-C Coupling" TS with a barrier height of 30.0 kcal mol^{-1}. The profile is continued in Figure 11 for clarity, connecting through the C-C coupling transition state.**

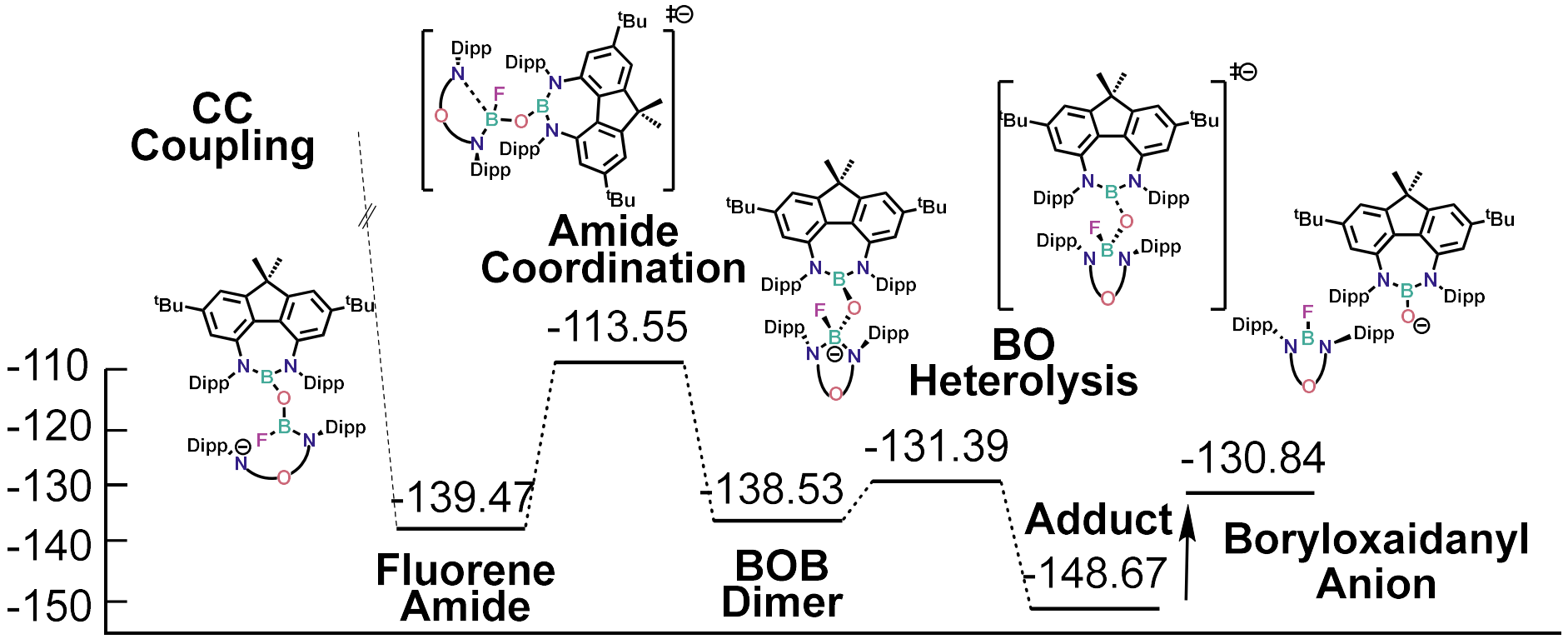


Figure 11 Free energy profile (part 2) for the dimeric, anionic pathway for the deoxygenative ring contraction at the BP86-D3BJ-CPCM(THF)/6-311++G//BP86-D3BJ/6-31G** level of theory, continuing from Figure 10. The C-C coupling TS results in the fluorene amide intermediate, which must re-coordinate the amide arm to allow for heterolysis and the separation of the observed product. The limited coordination shuffling of this post-C-C coupling portion of the mechanism is unsurprising and included for completeness. The highest barrier present in this portion is 25.92 kcalmol^{-1} for the recoordination of the amide to the boron centre, significantly less than the 33.61 kcamol^{-1} barrier from borate 1 to the C-C coupling TS in the first portion of the mechanism.**

4.4.1 Radical Mechanism

With our options for various charges and number of participating complexes seemingly exhausted, we decided to change the multiplicity of the reaction pathway, choosing a neutral, monomeric, doublet starting point, a presumed single electron reduction of the boron fluoride starting material.

Typically, open shell reaction mechanisms are suggested only if closed shell pathways prove intractable, or if experimental evidence suggests open shell intermediates/products. This is partly because the vast majority of known chemistry occurs through closed shell mechanisms, and so without further evidence Occam's razor would imply closed-shell species to be responsible, and partly because starting from a boron halide, the reduction from an alkali metal is proposed to go through first a 1-electron reduction from the metal into the B-X sigma hole, eliminating a salt and a boryl radical. Then, to form a boryl anion, a second equivalent of the reductant can reduce the radical in a typically more facile reaction than the first reduction.

The assumption is that the boryl radical is too short lived to undergo other processes before being reduced again under conditions in which the first reduction was facile, evident from the isolation of boryl anions. However, if sufficiently low-barrier processes are available (such as dimerisation or larger cluster formation in the absence of sterics), or the second reduction is not greatly more facile than the first (such as in significant geometric distortion), then of course other reactions may occur.

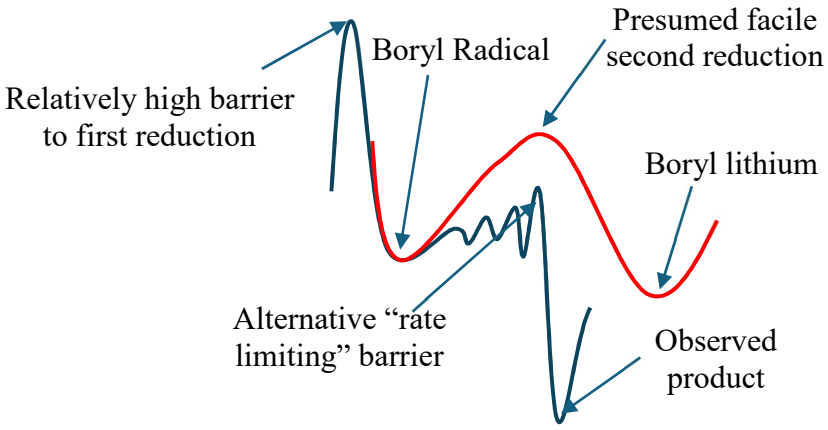


Figure 12 Crude potential energy surface to illustrate the possibility of a radical pathway yielding the observed oxygen extrusion product against the intuition of progressing through a boryl anion.

Despite the great challenges associated with our earlier endeavours, the pathway presented in the next pages proved comparatively very easy to elucidate, as is so often the case, one wishes they had started at the end.

Using the presumed boryl radical starting point, intramolecular nucleophilic attack at the ethereal carbon centre was initially investigated. However, the potential energy surfaces of our relaxed PES scans were discontinuous at even fine step sizes and strict convergence criteria (C-B distance -0.01 Å, maxcyc=15) and yielded no maxima from which to elucidate transition states. This was only to be expected as the boron sp^2-like SOMO would have to invert itself, and we suggest the SOMO would have poor overlap with the xanthene unoccupied orbital due to a wrong angle of approach (ideally in a plane containing the ethereal and para carbon centres, also perpendicular to the plane of the ring) necessitated by the constrained geometry around the boron centre, and form a 4-membered ring in the transition state. We suggest this is similarly the reason no intramolecular attack can happen from the monomeric boryl anion.

Instead, Figure 14 shows the elucidated pathway. First, coordination of the ether oxygen to the boron centre (initially motivated by the B-O bond present in the product, and to allow the oxygen to become a viable leaving group) allows for through-bond C-O cleavage and formation of an aryl radical, elucidated by scanning along the indicated C-O bond length (in Figure 14 this is labelled as "Coordination" followed by "Ether-Boranyl" and subsequently "Radical Shift" to the first "Aryl" intermediate).

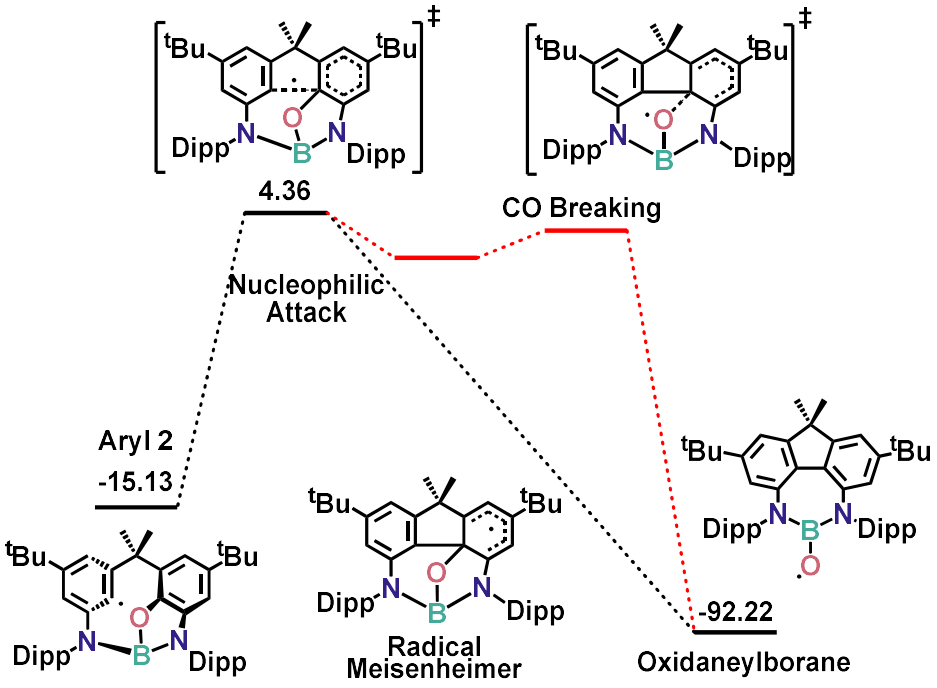


Figure 13 Modified detail of Figure 14, the attempted elucidation of the pathway involving a Meisenheimer-like radical intermediate (red, not found) with corresponding CO heterolysis, and the calculated concerted addition of the aryl radical and elimination of the oxalyl radical (black), which results in the same net transformation. Relative energies in kcalmol^{-1}.

This new aryl radical must evidently attack the other ethereal carbon centre, but is on the same side of the ring as the oxygen leaving group, consequently a minor geometric adjustment must occur ("Wagging" in Figure 14) before the nucleophilic attack. Scanning along a decreasing C-C coordinate from the second aryl radical intermediate results in C-C bond formation and C-O bond cleavage. We attempted to elucidate an intermediate akin to a Meisenheimer intermediate wherein the radical was delocalised throughout the attacked ring as a formal minimum on the PES before the extrusion of the oxydaneyl radical, but were unable to do so. If such a minimum exists it proved too shallow for us to characterise and the intrinsic reaction coordinate method linked the second aryl radical and the oxydaneyl borane (Figure 14). It is then assumed that the oxydaneyl borane can be further reduced to the observed boryloxy lithium.

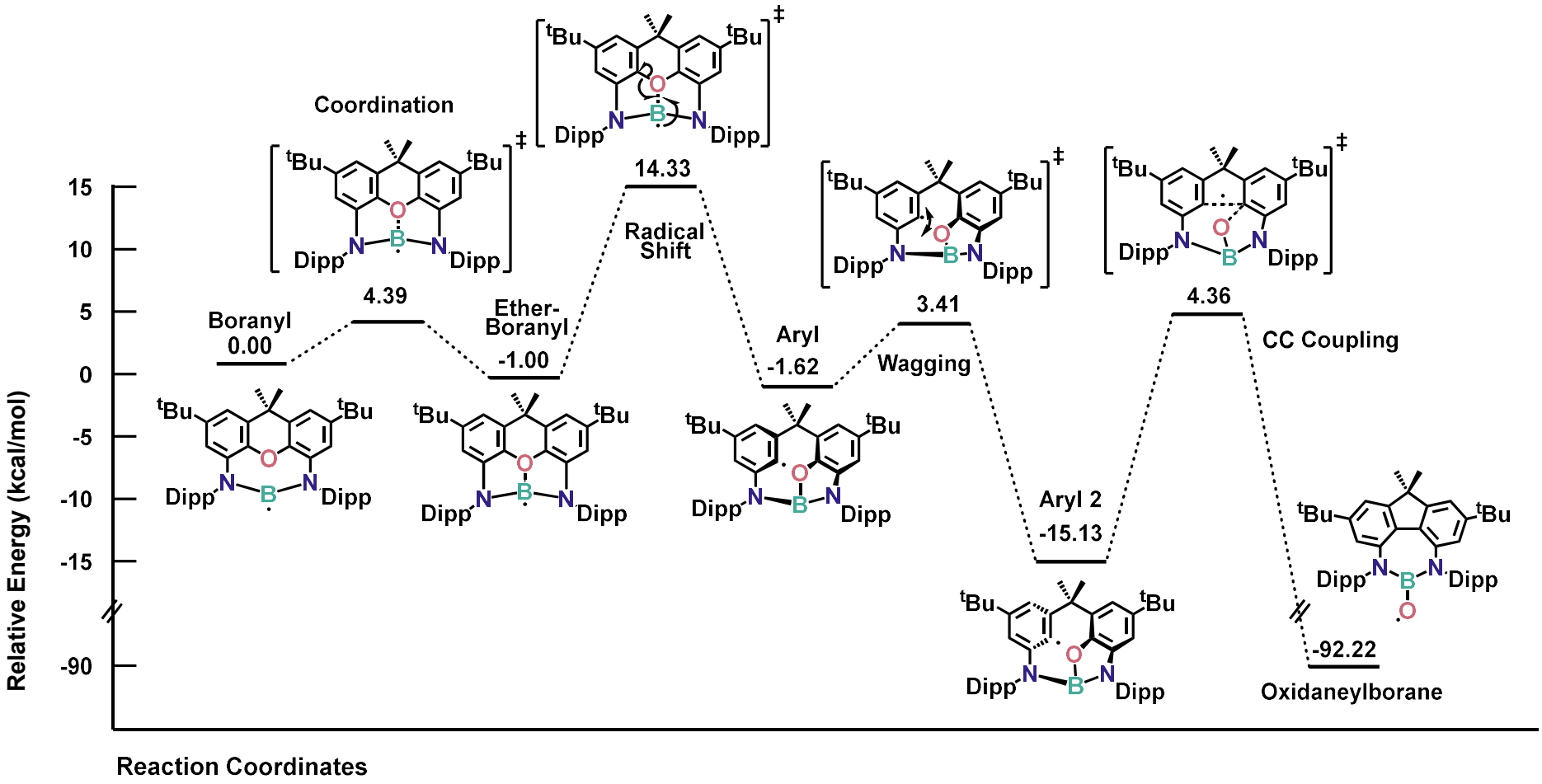


Figure 14 Computed open-shell free energy reaction profile for the extrusion of the xanthene oxygen to the observed boryloxy radical [(*NN*)BO·] starting from the boryl radical [(*NON*)B·]. Relative free energies in kcalmol^{-1}.

4.4 Electronic Structure of the Reactive Species

As discussed, invoking a radical pathway is rarely wise without experimental evidence to support its existence. As such, we asked our experimental and spectroscopic collaborators to either isolate a radical intermediate, or more fruitfully observe a transient one spectroscopically through electron paramagnetic resonance (EPR). Through great effort on their parts, Ms Emily Nahon and Mr Li Feng Lim were able to observe a signal *via* EPR spectroscopy associated with hyperfine coupling to four hydrogens and two nitrogens, likely a highly delocalised and not boron-centred radical.

Calculating the spin density of the two most stable implicated radical species, *i.e.* the starting boryl radical, and boryloxidanyl radical, sheds light on the spectroscopically observed species. Inspection of the spin density (Figure 15) indicates that this species is likely not the one observed by EPR, as the majority of the spin density is associated with the boron centre in an sp^2-like orbital. Similarly, the boryloxy radical shows a much higher delocalised spin density and is in better agreement with the observed EPR spectrum, qualitatively agreeing with the observed hyperfine coupling involving the four hydrogens and two nitrogens, not expected for the calculated boryl radical spin density.

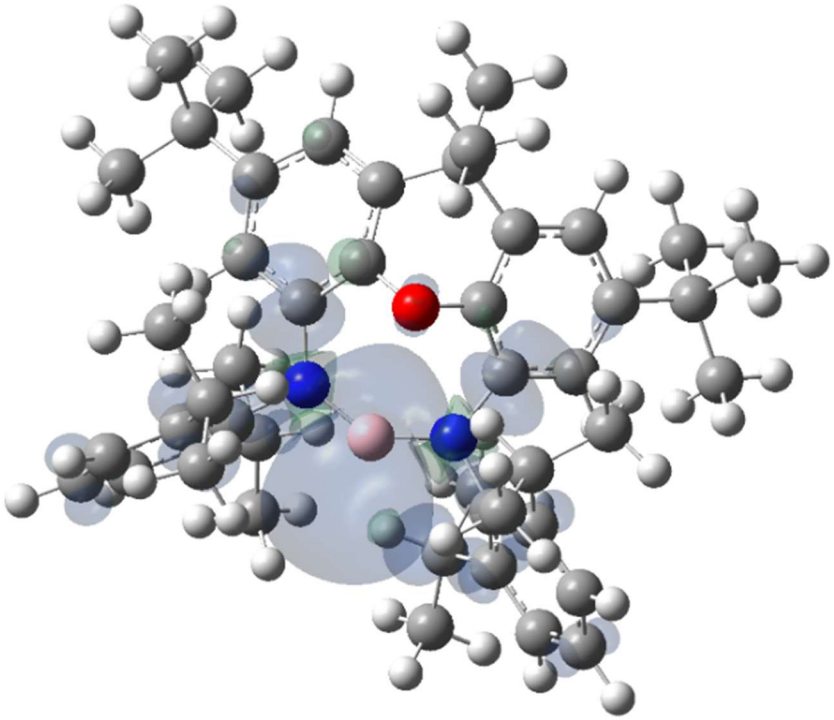


Figure 15 Spin density of [(NON)B•] at the BP86-D3BJ-CPCM(THF)/6-311++G//BP86-D3BJ/6-31G** level of theory. Carbon in grey, hydrogen in white, oxygen in red, nitrogen in blue, and boron in pink.**

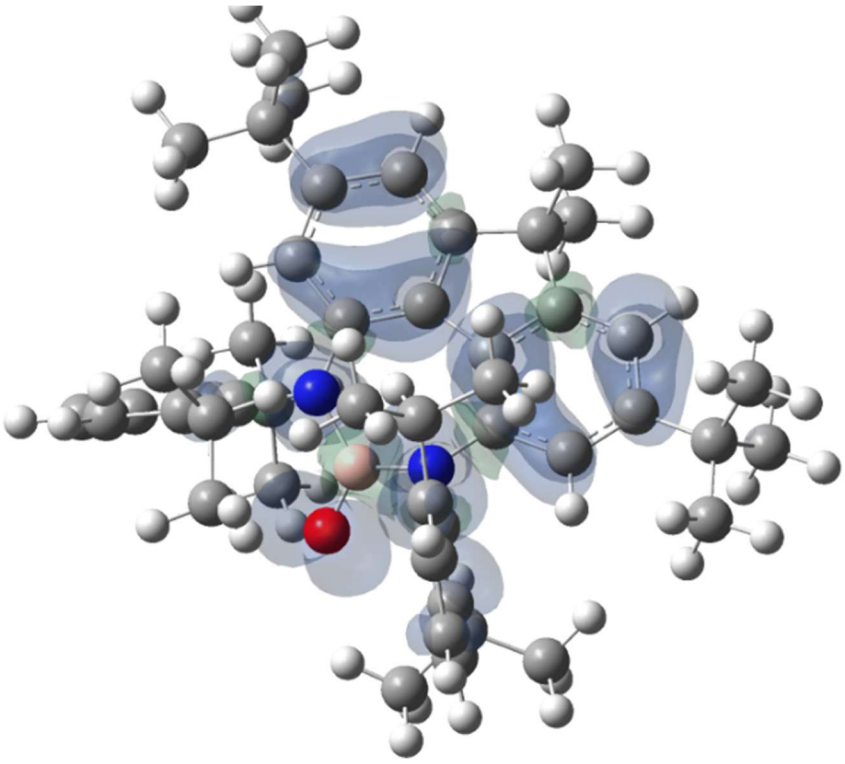


Figure 16 Spin density of (*NN*)BO˙ at the BP86-D3BJ-CPCM(THF)/6-311++G//BP86-D3BJ/6-31G** level of theory. Carbon in grey, hydrogen in white, oxygen in red, nitrogen in blue, and boron in pink.**

One, by energy alone, might have expected observation of the aryl radical intermediate, as this is the lowest minimum before the rate determining step, but it would posses a similar hyperfine coupling in the EPR spectrum to the boryl radical (without quadrupolar boron coupling), being in a similar sp^2 orbital with minimal delocalisation; it is evident that the oxygen extrusion is more facile than both the first reduction to the boryl radical and the unobserved second reduction of the boryl radical to the boryl anion.

4.5 Conclusion

This chapter sought to investigate and explain an observed oxygen deletion reaction, comprehensively describing the potential energy surfaces associated with the processes and matching the experimental evidence, leaving only the radical pathway as coherent with all evidence.

We provided three possible reaction pathways calculated using density functional theory, showing a radical intramolecular reaction results in the extrusion of the oxygen from the ligand backbone, contravening conventional wisdom. This gave rise to the falsifiable prediction that such a pathway would suggest the observation of radical intermediates, which was ultimately experimentally vindicated by synthetic and spectroscopic collaborators.

4.6 References

[1] E. Nahon, G. R. Nelmes, E. Dallerba, L. F. Lim, N. Cox, C. L. McMullin, M. Massi, F. Kallmeier, J. Hicks**,** *Chem. Sci.*, **2026**, *17*, *21*, 10755
[2] Sharma, R.; Arisawa, M.; Takizawa, S.; Salem, M. S. H., *Org. Chem. Front.*, **2025**, *12*, 1633
[3] Fan, J.; Xu, J.; Ma, Q.; Yao, S.; Zhao, l.; Frenking, G.; Driess, M., *J. Am. Chem. Soc.*, **2024**, *146*, 20458
[4] Fan, J.; Pan, S.; Yao, S.; Ding, C.; Frenking, G.; Driess, M., *J. Am. Chem. Soc.*, **2025**, *147*, 8, 6925
[5] Taniguchi, T., *Chem. Soc. Rev.*, **2021**, *50*, 8995
[6] Hurd, D. T., *J. Am. Chem. Soc.*, **1949**, *71*, *1*, 20
[7] Braunschweig, H.; Dewhurst, R. D.; Schneider, C.*, Chem. Rev.,* **2010**, 110, 3924
[8] Shmakov, M. M.; Prikhod'ko, S. A.; Panchenko, V. N.; Timofeeva, M. N.; Bardin, V. V.; Parmon, V. N.; Adonin, N. Y., *Catal. Rev.: Sci. Eng.*, **2025**, *67*, 497
[9] Yamashita, M.; Nozaki, K., *J. Am. Chem. Soc.,* **2006**, *128*, 3492
[10] Braunschweig, H.; Dewhurst, R. D.; Schneider, A., *Chem. Rev.*, **2011**, *111*, 131
[11] Sakae, T.; Matsumoto, T.; Yamashita, M.; Nozaki, K.*, J. Am. Chem. Soc.*, **2008**, *130*, 12368
[12] Pécharman, A. F.; Colebatch, A.; Hill, M.; McMullin, C. L.; Mahon, M. F.; Weetman, C., *Nat Commun*., **2017**, *8*, 15022
[13] Gaussian 16, Revision C.01, Frisch, M. J.; Trucks, G. W.; Schlegel, H. B.; Scuseria, G. E.; Robb, M. A.; Cheeseman, J. R.; Scalmani, G.; Barone, V.; Petersson, G. A.; Nakatsuji, H.; Li, X.; Caricato, M.; Marenich, A. V.; Bloino, J.; Janesko, B. G.; Gomperts, R.; Mennucci, B.; Hratchian, H. P.; Ortiz, J. V.; Izmaylov, A. F.; Sonnenberg, J. L.; Williams-Young, D.; Ding, F.; Lipparini, F.; Egidi, F.; Goings, J.; Peng, B.; Petrone, A.; Henderson, T.; Ranasinghe, D.; Zakrzewski, V. G.; Gao, J.; Rega, N.; Zheng, G.; Liang, W.; Hada, M.; Ehara, M.; Toyota, K.; Fukuda, R.; Hasegawa, J.; Ishida, M.; Nakajima, T.; Honda, Y.; Kitao, O.; Nakai, H.; Vreven, T.; Throssell, K.; Montgomery, J. A., Jr.; Peralta, J. E.; Ogliaro, F.; Bearpark, M. J.; Heyd, J. J.; Brothers, E. N.; Kudin, K. N.; Staroverov, V. N.; Keith, T. A.; Kobayashi, R.; Normand, J.; Raghavachari, K.; Rendell, A. P.; Burant, J. C.; Iyengar, S. S.; Tomasi, J.; Cossi, M.; Millam, J. M.; Klene, M.; Adamo, C.; Cammi, R.; Ochterski, J. W.; Martin, R. L.; Morokuma, K.; Farkas, O.; Foresman, J. B.; Fox, D. J., *Gaussian Inc.*, Wallingford CT, **2016**
[14] Becke, A. D., *Phys. Rev. A*, **1988**, 38, 3098
[15] Perdew, J. P., *Phys. Rev. B*, **1986**, 33, 8822
[16] Perdew, J. P., *Phys. Rev. B*, **1986**, 34, 7406
[17] Grimme, S., Ehrlich, S., Goerigk, L., *J. Comp. Chem.*, **2011**, 32, 1456
[18] Hariharan, P. C., Pople, J. A., *Theor. Chim. Acta.*, **1973**, 28, 213
[19] Hehre, W. J., Ditchfield, R., Pople, J. A., *J. Chem. Phys.*, **1972**, 56, 2257
[20] Madrossian, N., Head-Gordon, M., *Mol. Phys.*, **2017**, 11, 19, 2315
[21] Gaussian 09, Revision A.02, Frisch, M. J.; Trucks, G. W.; Schlegel, H. B.; Scuseria, G. E.; Robb, M. A.; Cheeseman, J. R.; Scalmani, G.; Barone, V.; Mennucci, B.; Petersson, G. A.; Nakatsuji, H.; Caricato, M.; Li, X.; Hratchian, H. P.; Izmaylov, A. F.; Bloino, J.; Zheng, G.; Sonnenberg, J. L.; Hada, M.; Ehara, M.; Toyota, K.; Fukuda, R.; Hasegawa, J.; Ishida, M.; Nakajima, T.; Honda, Y.; Kitao, O.; Nakai, H.; Vreven, T.; Montgomery, J. A., Jr.; Peralta, J. E.; Ogliaro, F.; Bearpark, M.; Heyd, J. J.; Brothers, E.; Kudin, K. N.; Staroverov, V. N.; Kobayashi, R.; Normand, J.; Raghavachari, K.; Rendell, A.; Burant, J. C.; Iyengar, S. S.; Tomasi, J.; Cossi, M.; Rega, N.; Millam, J. M.; Klene, M.; Knox, J. E.; Cross, J. B.; Bakken, V.; Adamo, C.; Jaramillo, J.; Gomperts, R.; Stratmann, R. E.; Yazyev, O.; Austin, A. J.; Cammi, R.; Pomelli, C.; Ochterski, J. W.; Martin, R. L.; Morokuma, K.; Zakrzewski, V. G.; Voth, G. A.; Salvador, P.; Dannenberg, J. J.; Dapprich, S.; Daniels, A. D.; Farkas, O.; Foresman, J. B.; Ortiz, J. V.; Cioslowski, J.; Fox, D. J., *Gaussian Inc.*, Wallingford, CT, **2009**
[22] McLean, A. D., Chandler, G. S., *J. Chem. Phys.*, **1980**, 72, 5639
[23] Clark, T., Chandrasekhar, J., Spitznagel, G. W., Schleyer, P. v. R., *J. Comp. Chem.*, **1983**, 4, 3294
[24] Frisch, M. J., Pople, J. A., Binkley, J. S., *J. Chem. Phys.*, **1984**, 80, 7, 3265
[25] Klamt, A., Schüürmann, G., *J. Chem. Soc., Perkin Trans. 2*, **1993**, 2, 799
[26] Andzelm, J., Kölmel, C., Klamt, A. J., *Chem. Phys.*, **1995**, 103, 9312
[27] Barone V., Cossi, M., *J. Phys. Chem. A*, **1998**, 102, 1995
[28] Cossi, M., Rega, N., Scalmani G., Barone, V., *J. Comput. Chem.*, **2003**, 24, 669
[29] Cordero, B.; Gómez, V.; Patero-Prat, A. E.; Revés, M.; Echeverría, J.; Cremades, E.; Barragán, F.; Álvarez, S., *Dalton Trans.*, **2008**, 2832
[30] Pitman, S. J., Evans, A. K., Ireland, R. T., Lempriere, F., McKemmish, L. K., *J. Phys. Chem. A*, **2023**, *127*, 10295
[31] Power, P. P., *Nature*, **2010**, *463*, 171
[32] a) Debye P, Hückel E, *Phys Z*, **1923**, *24*, 185; b) Costa Reis, M., *ChemTexts*, **2021**, *7*, 9

5 Aluminyl Anions

"Why man, he doth bestride the narrow world like a colossus, and we petty men walk under his huge legs, and peep about to find ourselves dishonourable graves."

–Shakespeare, W., *Julius Caesar*, **1599**

5.1 Introduction

In addition to the work presented in Chapters 2-4, several smaller research projects were undertaken over the course of this degree. This chapter summarises the results of two such studies relevant to the content of this thesis, both concerning the chemistry of aluminyl anions. The first investigates the steric and electronic properties of a series of diamido iron aluminyl complexes, [(^{R}N{…}^{R}N)AlFe(CO)$_2$Cp] (where (^{R}N{…}^{R}N) represents a ligand with two R-substituted amides linked by a backbone {…} R is aromatic or aliphatic), and examines how these factors influence their carbonyl stretching frequencies as a proxy for their electronic effects. The second investigates the mechanism underlying the mono- and bis-CH activation of benzene by a highly nucleophilic aluminyl anion, the synthetic work for which was performed by Dr Fabian Kallmeier and Dr Aidan Matthews within the group. Both of these studies have recently been published.[1,2]

Reproduced here with limited commentary or alteration are my contributions to the publications, principally through the supporting information.

5.2 Aluminyl Anions

Aluminium was the first element of group 13 to be discovered (or at least isolated in its elemental form),[3] being the most abundant in the Earth's crust and perhaps the most amenable to electrochemical isolation. As discussed in chapter 1, aluminium exclusively exists in the +III oxidation state in its naturally occurring chemistry because of its high oxophilicity: the element's small covalent radius (1.43 Å),[4] very low electronegativity (1.61, the lowest in the p-block by the Pauling scale), and intrinsically electron deficient nature (fewer than four valence electrons intrinsically precludes fulfillment of the octet rule *via* 2-centre-2-electron covalent, non-dative bonds) grant aluminium highly metallic character which governs its terrestrial chemistry. It possesses a highly reducing standard electrode potential of *ca*. -2.3 V,[5] making it quite a potent reductant due to the element's strong electronic preference for the trivalent oxidation state.

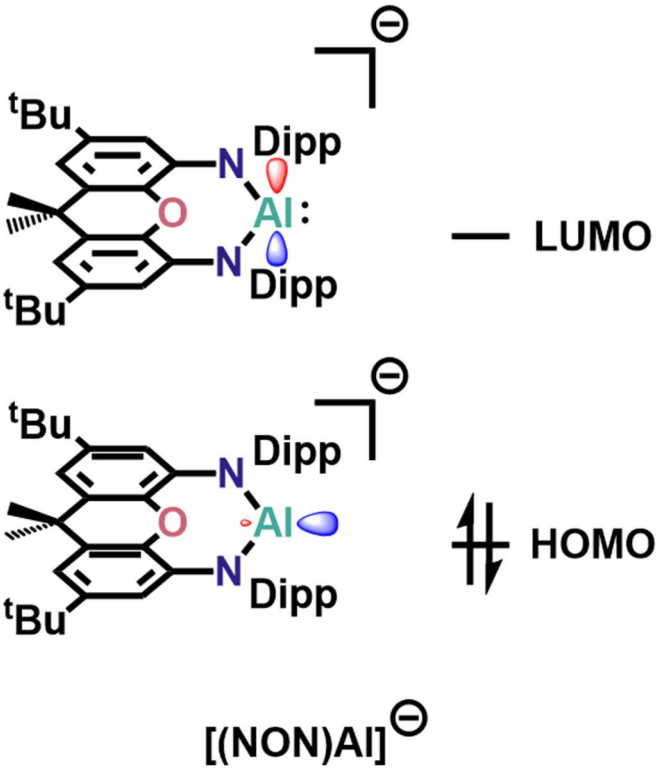


Figure 1 Archetypal features of an aluminyl anion, demonstrated by the seminal species reported by Aldridge, Goicoechea and coworkers. The nucleophilic, high energy HOMO is localised in an sp^2-like σ-orbital of aluminium, while maintaining the vacant p-orbital.

This is experimentally evident particularly from its uses as a Lewis acid catalyst in molecular chemistry, famously for the Friedel-Crafts alkylation and acylation reactions,[6] and by the oxides and fluorides which dominate its chemistry in the solid-state of highly ionic compounds.[7]

In 2018, this typical behaviour was shown not to be aluminium's exclusive purview by the production of the first formally anionic Al(I) species.[8] Instead, the reduction of [(NON)AlI] with potassium graphite was able to effectively transmute the iodide into a potassium cation, which is more electropositive than aluminium (K being 0.82 by the Pauling scale) and consequently results in an aluminium possessing a lone pair. In the Lewis sense, owning two electrons compared with the three in the neutral state formally yields Al(I), which displays entirely opposite chemistry to the traditional Al(III).

So-called "umpolung" behaviour is observed in the low-valent species, with $[(NON)AlK]_2$ (Figure 1) capable of nucleophilic attack by the aluminium centre on even kinetically and thermodynamically stable moieties like those in benzene (both CH and CC bonds)[9] or dihydrogen. Since their initial discovery, great interest has been shown in their potential for

catalysis, and their ability to activate otherwise inert substrates such as aliphatic CF bonds. Both the ligands and bonded metal (or weakly coordinating cation) can be tuned to influence their steric and electronic properties, and a broad church of aluminyl anions has been reported since, showing clearly differentiable reactivity.[10]

Prior to the isolation of aluminyl anions, a few examples of analogous iron complexes have been reported, as early as 1997 by Nöth and coworkers.[11] These are typically considered to have significantly different electronic structures to alkali metal aluminyl anions, partly because iron is more electronegative than aluminium (Pauling electronegativity of 1.83), but also because of the significant multiple bonding character of the Al-Fe interaction, as the vacant aluminium p orbital acts as a strong π-acceptor for the filled iron t_{2g} orbitals, and the strong σ-donor ability of the highly electropositive aluminium making the (typically low-valent) iron centre very electron rich. Consequently, this work finishes with an exploratory foray into understanding the differing steric and electronic properties of iron aluminyl complexes.

5.3 Project 1: Steric and Electronic Properties of Iron-Aluminyl Complexes

In the Hicks research group, a series of five iron-aluminyl complexes [(^{R}N{…}^{R}N)AlFe(CO)$_2$Cp] were synthesised. All complexes were essentially identical, only deviating by the bidentate ligand coordinating to the Al centre. As such, this was a perfect opportunity to investigate what effects (if any) the sterics and the electronics of the Al-coordinated ligand had on the iron aluminyl complex.

The five complexes investigated in this study are shown in Figure 2. Four of these are xanthene-based diamido ligands, with the fifth being a diamidosilane backbone resulting in a 4-membered ring for the aluminyl anion, which we presumed would result in different electronic properties of the moiety. In general, these were named ^{R}NON, where R indicates the varied substituents on the amide donors. "DAS" is the abbreviation for DiAmidoSilane, with the R groups attached to the amide donors as 2,6-diisopropylphenyl, which is the most prevalent substitution on the xanthene system.

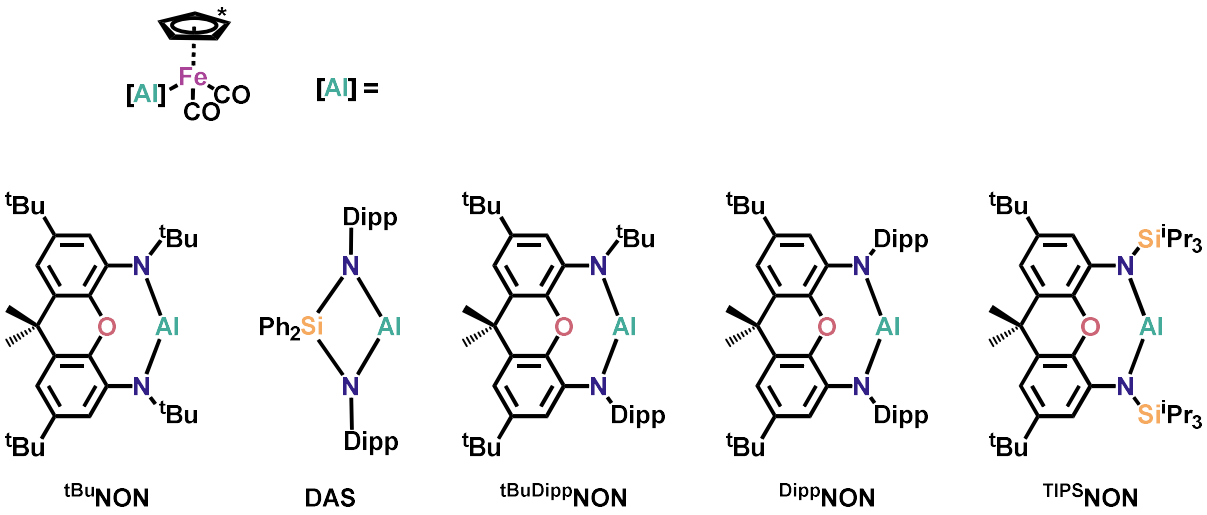


Figure 2 The five iron aluminyl complexes investigated. * indicates the pentamethyl substituted cyclopentadienyl ligand.

5.3.1 Computational Details

Density functional theory (DFT) calculations for geometry optimisation were performed using the Gaussian 16 program[12] using the PBE0 hybrid density functional approximation[13] and Grimme's D3 dispersion correction with Becke-Johnson dampening,[14] Stuttgart ECPs and associated basis sets[15] for Fe and Al (ζ_d = 0.190), with listed additional polarisation function, and Pople's 6-31G** basis set[16] for all other atoms (BS1), and the ultrafine integration grid.

A hybrid density functional may seem excessively computationally expensive for geometry optimisations of such large species, however recent benchmarking presented in the previous chapter[17] suggests the presented method reproduces experimental data more accurately for low-valent main group species than other more inexpensive methods. Additionally, the relatively small admixture of Hartree-Fock exchange in the PBE0 hybrid (25%) makes it *a priori* more appropriate for a 3d-metal containing species,[18] although this effect is minimal for closed-shell low-spin $3d^6$ pseudo-octahedral complexes like the presented iron complexes.

Starting geometries were taken from solid-state structures from X-ray diffraction, removing errant solvent molecules and taking only one part of modelled disorder, corresponding to the most symmetrical structure. In the case of the DAS aluminyl, only one of the two isostructural molecules (in this case, the un-disordered one) in the unit cell. The geometries were confirmed as minima on the potential energy surface *via* analytical frequency calculations, yielding no negative eigenvalues. Thermochemical properties were calculated at a pressure of 1.0 atmospheres, unscaled frequencies, and a temperature of 298.15 K. Single point calculations were performed on the optimised geometries using the PBE0-D3BJ level of theory, with the cc-pVTZ basis[19] and conductor-like polarisable continuum model[20] solvation correction (CPCM) with benzene as the solvent. Gibbs free energies were obtained by adding the thermal contribution to Gibbs free energy calculated at the PBE0-D3BJ/BS1 level of theory to the electronic energy calculated at PBE0-D3BJ-(CPCM=benzene)/cc-pVTZ level, which was also used to calculate the presented molecular orbitals.

5.3.2 Percent Buried Volume

Percent buried volume (%BV) was calculated using SambVca 2.1,[21] pruning the complex of the Cp and CO moieties to leave just the (**NON**)Al or (**DAS**)Al "ligand" coordinated to the Fe centre. The conventionally reported %BV uses a radial cut-off of 3.5 Å, however this is because it is most often used when the majority of the steric bulk is geminal to the atom at the centre of the sphere. In the case of the complexes presented, the steric bulk provides kinetic protection

to the Fe centre but is further away due to its vicinal relation. As such, the 3.5 Å radial cut-off was deemed potentially inappropriate and we have presented the %uBV at several cut-off distances for each complex in order to elucidate appropriate radial cut-offs (Figure 3 and Figure 4).

The expected behaviour of the %BV when radially encountering steric bulk is, initially, to increase as the integration volume engulfs the encountered atoms. Once the engulfing sphere expands into the empty space beyond the atoms, the integrated volume increases but maintains the integrated quantity, leading to a decrease in the %BV. As such, the size of the steric protection can be proxied *via* the magnitude of %BV, and the location of (or rather the distance to) the steric bulk is indicated by the critical points in %BV. Additionally, presented herein is actually percent *un*buried volume (%uBV), found by simply subtracting the %BV from 100%, as this is more directly compatible with percent accessible surface area (a larger %BV is more protecting, as is a smaller accessible surface area) also presented.

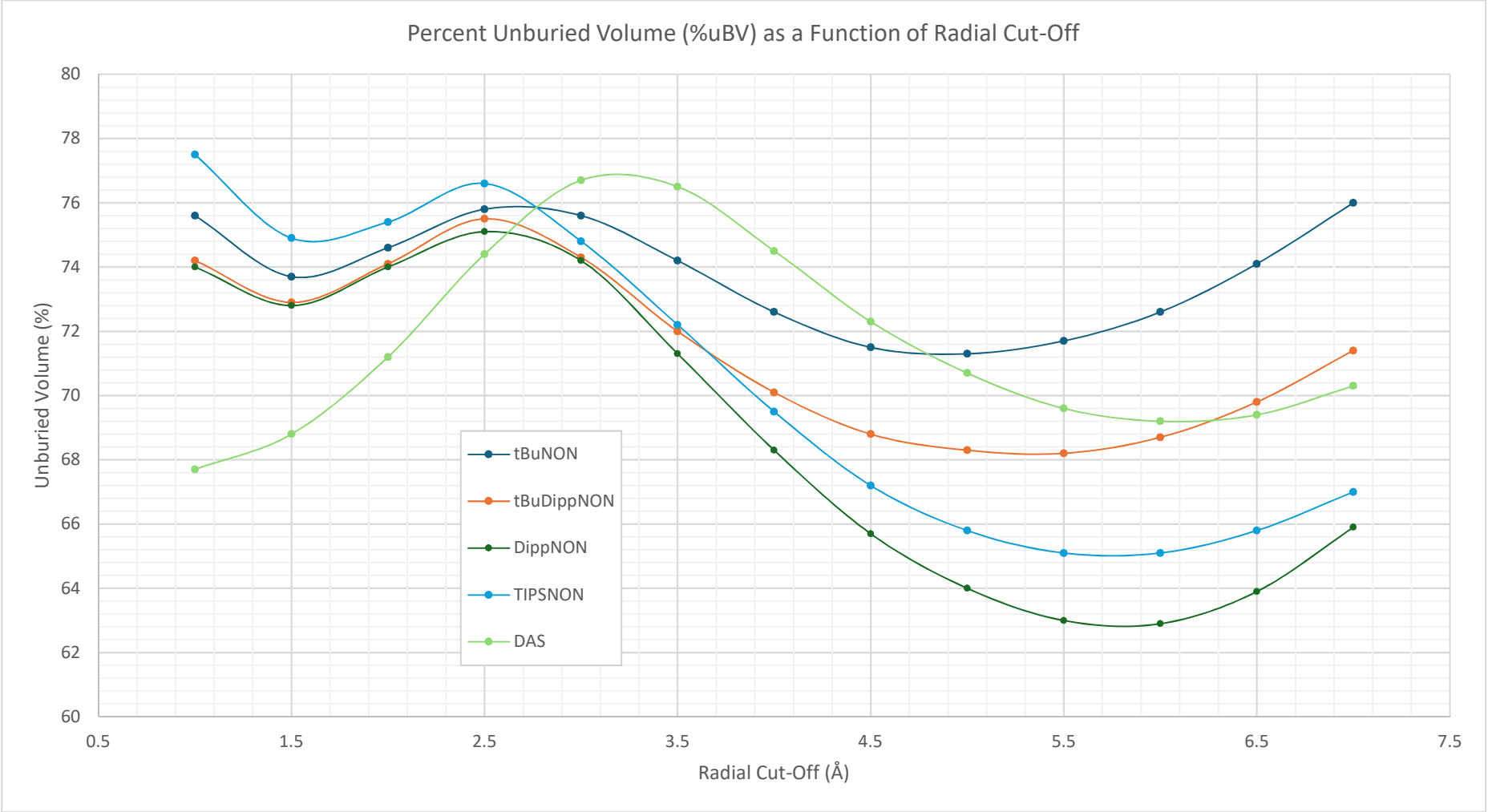


Figure 3 Percent unburied volume as a function of radial cut-off for the 5 reported complexes. Unburied volume (%uBV, i.e. 100% - %BV) was used for ready comparison with accessible surface area (vide supra). The minima in the 4.8-6.2 Å range are due to the associated ligands, with approximate minima abscissae shown from the numerical derivative (*vide infra*). The magnitude of the associated ordinates is qualitatively reflective of the steric protection afforded by the indicated moiety, leading to the relative size of the ligand substituents to be ^{tBu}NON < DAS < ^{tBuDipp}NON < ^{TIPS}NON < ^{Dipp}NON.

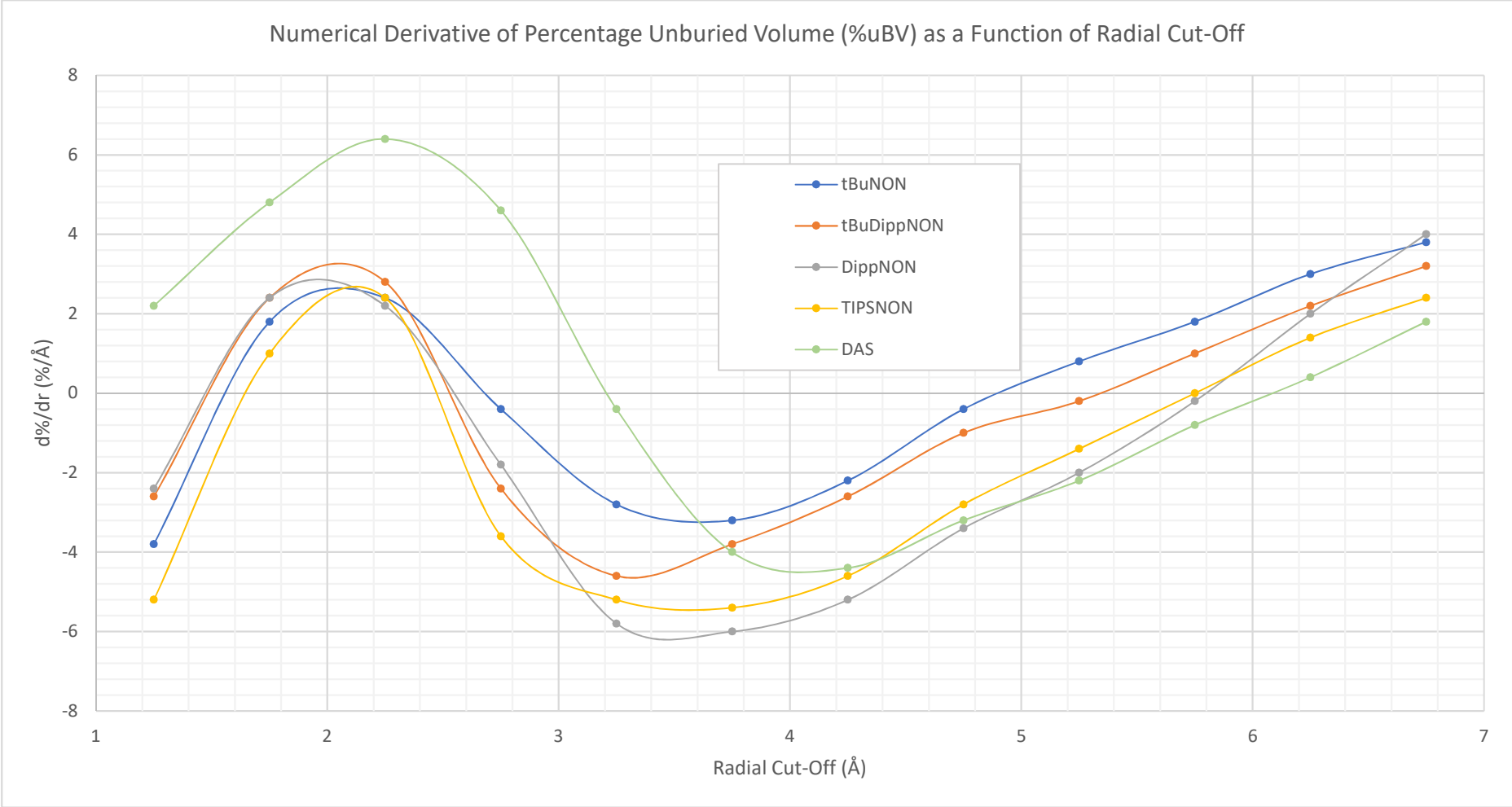


Figure 4 The numerical derivative of the %uBV with respect to radial cut-off shows the location of the maxima, evidently where the gradient is 0 and thus where this graph crosses the axis. The zeroes before 3.5 Å are due to the iron and aluminium atoms themselves. The zeroes between 4.8 and 6.2 Å show the location of the ligand-based steric bulk. As each of the ligands are similar, the small number of data points and single geometries taken, rather than appropriate conformationally sampled distributions, we stress that only a qualitative comparison of the systems can be drawn. A qualitative set of zeros we propose is: ^{tBu}NON , 4.9 Å; ^{tBuDipp}NON, 5.4 Å; ^{TIPS}NON, 5.8 Å; ^{Dipp}NON, 5.8 Å; DAS, 6.1 Å.

5.3.3 Atom Access

Atom Access[22] was also used for comparison, calculating the accessible surface area of a sphere at different radii using ray tracing. The complexes were pruned identically as for %BV, removing the Cp and CO moieties. Atom Access calculates a similar parameter to %BV, however instead of the integral over the volume of the sphere, it is the (proxy for the) integral over the *surface* of the sphere. Poignantly, this value can never decrease with cut-off radius- once at a cut-off radius that blocks a ray from the surface, the object blocking it remains blocking said ray at any subsequent distance. The expected qualification of steric bulk is thus to have a gradient as the sphere engulfs the full extent of the object providing steric bulk, then plateau until another object is encountered. Thus, the start of the plateaus in the graphs (Figure 5 and Figure 6) is where the steric bulk is, and the change in accessible surface area from one plateau to the next is an appropriate proxy for the magnitude.

In conclusion, the work presented in this part of the chapter has provided a detailed assessment of the steric environments present within the iron-aluminyl complex series. Through the application of complementary steric metrics, including %BV, AtomAccess, and DFT calculations, clear trends in ligand-derived steric protection were identified across the ligand framework investigated. While each method adopts a distinct approach to quantifying steric influence, all yielded consistent qualitative rankings in terms of steric protection (^{tBu}NON < DAS < ^{tBuDipp}NON < ^{TIPS}NON < ^{Dipp}NON) and highlighted the important role of ligand architecture in controlling accessibility to the Fe-Al bonding unit. The analysis further demonstrated that variations in both substituent size and ligand backbone structure contribute to differences in steric shielding, with these effects readily apparent across the complexes examined. Collectively, these results establish a robust understanding of the steric characteristics of the iron-aluminyl complexes and provide an important foundation for evaluating how ligand design influences the properties of this class of compounds.

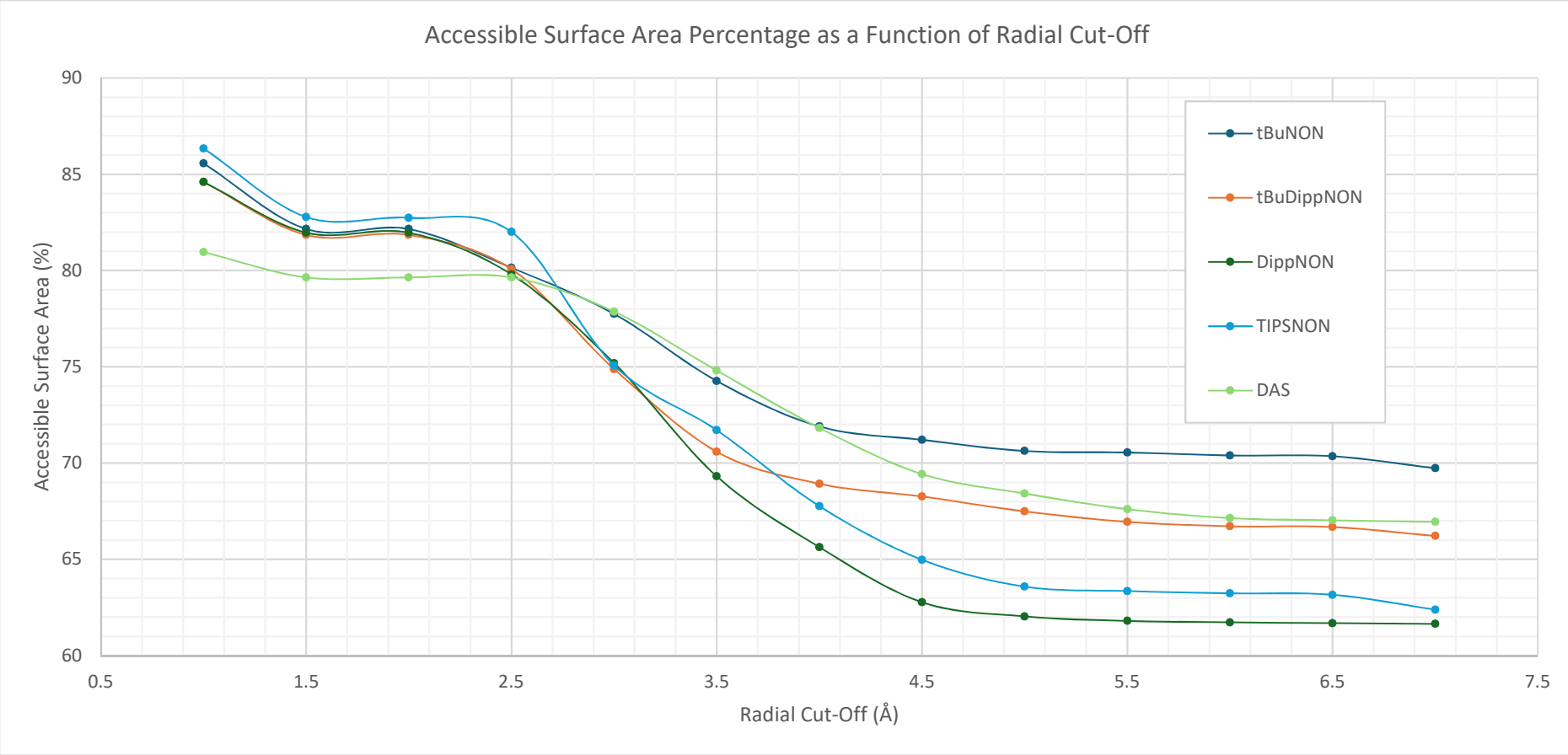


Figure 5 Accessible surface area as a function of radial cut-off for the 5 reported complexes. The magnitude of the accessible surface area percentage at the plateaus gives a qualitative relative measure of the steric protection afforded by the associated ligands (vide infra). It is difficult to quantify a plateau due to only the centre of such a feature possessing a true turning point, empirically evident from the numerical derivative (*vide infra*). Consequently, where the plateau begins, and thus the distance to the steric bulk, is far more difficult to quantify in the accessible surface area model than for %BV. However, as all the compared ligands appear at similar distances from the Fe centre, a qualitative ranking of their sizes is possible by comparing the heights of the plateaus in the 4.5-7.0 Å region. Encouragingly, this is the same ordering established by %BV: ^{tBu}NON < DAS < ^{tBuDipp}NON < ^{TIPS}NON < ^{Dipp}NON.

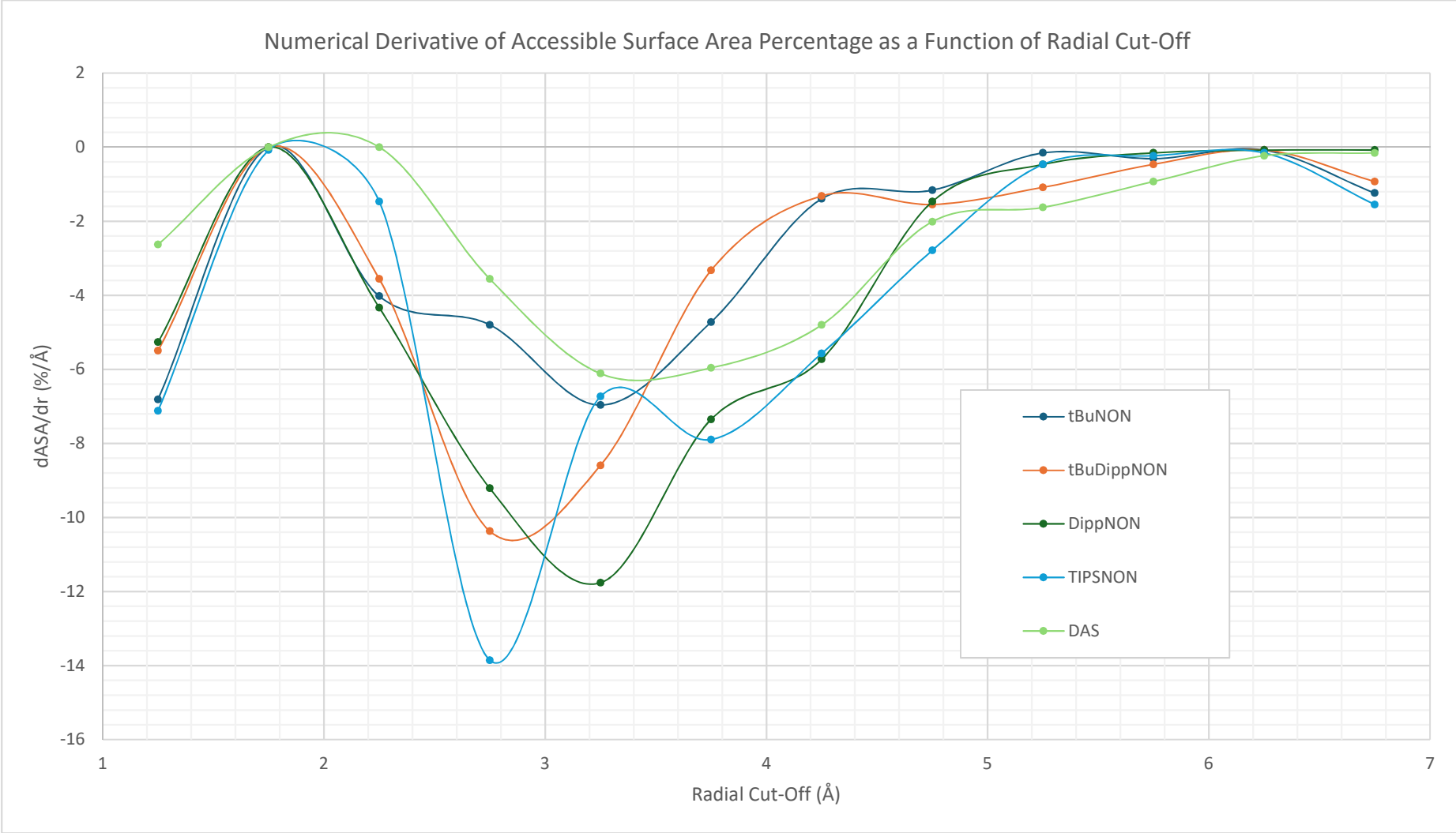


Figure 6 Numerical derivative of accessible surface area percentage as a function of radial cut-off. As for %uBV above, the derivative is used here to indicate the location of turning points. However, as the critical points in the parent graph are inflections rather than stationary points, the zeroes are more difficult to quantify, and the location of the critical points in the parent graph are less important to the interpretation of the data. Consequently, the interpretability of a graph such as that above is limited.

5.3.4 Vibrational Frequencies and Electronic Inferences

Relevant calculated orbital and vibrational frequency data for the 5 reported iron aluminyl complexes and two previously reported complexes (**TMP$_2$**AlFp and **Tbb(Br)**AlFp, where TMP = tetramethylpiperidine, and Tbb = 4-^{t}Bu-2,6-[CH-(SiMe$_3$)$_2$]-C$_6$H$_2$)[11a,11c] containing a 3-coordinate aluminium centre bonded to an iron centre, free carbon monoxide, and three complexes demonstrating oxidation states of Fe in the Fp moiety (KFp, Fp dimer and FpBr)[23,24,25] are presented in Table 1. Canonical molecular orbitals were calculated at the PBE0-D3BJ-CPCM(C$_6$H$_6$)/cc-pVTZ//PBE0-D3BJ/BS1 level of theory, and vibrational frequencies at the PBE0-D3BJ/BS1 level.

Experimental CO stretches for the 5 reported iron aluminyl complexes were measured from solid-state samples prepared by Dr Fabian Kallmeier or Dr Aidan Matthews. Vibrational spectra were calculated from optimised structures with starting geometries taken from single-crystal diffraction data, ideally reflecting a similar geometry and consequently similar vibrational frequencies. This was quite successful, with the largest change in N-Al-Fe-CO dihedral being 5.5° for (**DAS**)AlFp. A scaling factor of 0.9343 was applied to the calculated stretching frequencies to best fit the experimental CO stretches, which is quite similar to our previously established scaling factor[17] (0.9380) at this level of theory.

It was hoped that a trend between the CO stretching frequency (easily measured by IR spectroscopy) and the sterics or electronics of the aluminyl fragment could be determined. However, after extensive investigation, no clear relation between the steric distance or magnitude, calculated using either %BV or accessible surface area, and any of the Al-Fe σ-bonding orbital energy, Al-Fe bond distance, and experimental or calculated CO stretching frequencies was elucidated.

Ligand-AlFp	Computed Al-Fe length (Å)	Al-Fe σ-bonding orbital energy (eV)	Al-Fe σ-bonding orbital	Calculated CO stretching frequencies (cm^{-1})		Scaled (0.9343) calculated CO stretching frequencies (cm^{-1})			Experimental average CO stretch *
				Symmetric	Asymmetric	Symmetric	Asymmetric	Average	
(**^{tBu}NON**)-	2.363	-7.120	HOMO-6	2103	2055	1964	1920	1942	1941
(**^{tBuDipp}NON**)-	2.352	-7.131	HOMO-7	2095	2052	1957	1917	1937	1930
(**^{Dipp}NON**)-	2.326	-7.375	HOMO-10	2104	2060	1966	1925	1945	1956
(**^{TIPS}NON**)-	2.390	-7.120	HOMO-6	2095	2054	1957	1919	1938	1949
(**DAS**)-	2.285	-7.009	HOMO-5	2119	2083	1980	1946	1963	1950
TMP$_2$-[11a]	*2.450	-				1982	1927	-	1955
Tbb(Br)-[11c]	*2.319	-				1991	1921	-	1956
C≡O	-								2143
KFp[23]	-					1868	1782†	-	1825
Fp dimer[25]	-					2005	1961	-	1983
FpBr[11b]	-					2035	1984	-	2010

Table 1 *Values for scaled calculated CO stretches for previously reported complexes are the experimental values, and thus the average stretch is reported only in the experimental column and not also in the average calculated column. †averaged from split asymmetrical stretches in THF. Likely, no meaningful conclusion can be drawn between CO stretching frequencies and other relevant metrics due to single-conformation reporting of the stretches, both in silico and in the solid state.

5.4 Project 2: Two-Fold Nucleophilic Attack of Benzene

In attempting initial, exploratory modifications to the H_2(**NON**) proligand by changing out the traditional 2,6-diisopropylphenyl moieties for triisopropylsilyl substituents instead, somewhat unusual reactivity was observed. Despite many other potassium aluminyls being synthesised by reducing the corresponding aluminium iodide precursor with potassium graphite (KC_8) in benzene, using [(^{TIPS}**NON**)AlI] (**1**, Figure 7) yielded only Al(III) aluminate complexes of CH activations of benzene. While both the mono-[8] and di-[28] activated benzene species (**2** and **3**, Figure 7) are not unprecedented, each requires high temperatures or long times, and seemingly produces one of the two products preferentially. This project sought to investigate a mechanistic pathway towards both observed products in an attempt to justify the observed reactivity.

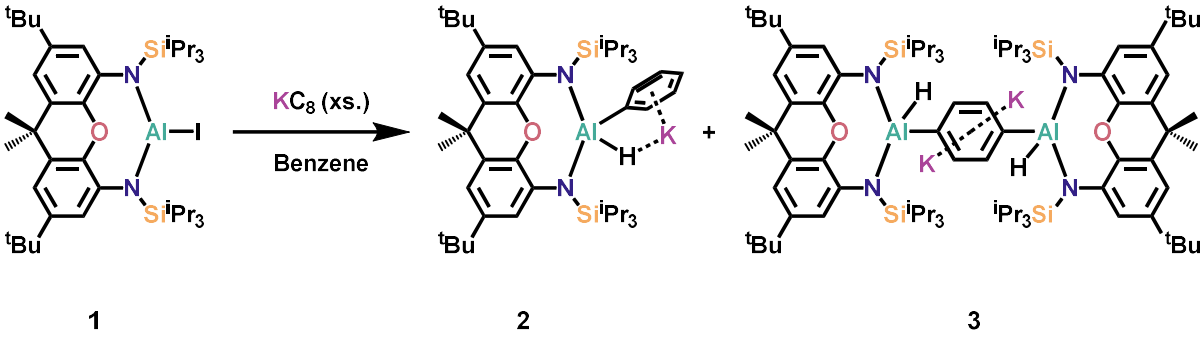


Figure 7 The reduction of [(^{TIPS}NON)AlI] with excess KC_8 resulted in an unexpected mixture of benzene CH activations at room temperature.

5.4.1 Methodology

Density functional theory (DFT) calculations for geometry optimisation were performed using the Gaussian 16 program[12] using the PBE0 hybrid density functional approximation[13] with Grimme's D3 dispersion correction with Becke-Johnson dampening,[14] Stuttgart ECPs and associated basis sets[15] for Si (ζ_d = 0.284), K (ζ_d = 1.000), and Al (ζ_d = 0.190), with listed additional polarisation functions and Pople's 6-31G** basis set[16] for all other atoms (BS1), and the ultrafine integration grid.

The structures were confirmed as minima on the potential energy surface *via* analytical frequency calculations, yielding no negative eigenvalues, except for transition states, which were verified as saddle points on the potential energy surface with a single negative eigenvalue. The corresponding imaginary modes were verified as connecting the appropriate intermediates *via* the intrinsic reaction coordinate method. Thermochemical properties were calculated at a pressure of 1.0 atmospheres, unscaled frequencies, and a temperature of 298.15 K. Single point

calculations were performed on the optimised geometries again using PBE0-D3BJ, with the def2-TZVPP basis[26] and conductor-like polarisable continuum model[20] solvation correction (CPCM) with benzene as the solvent. Gibbs free energies were obtained by adding the thermal contribution to Gibbs free energy calculated at the PBE0-D3BJ/BS1 level of theory to the electronic energy calculated at PBE0-D3BJ-(CPCM=benzene)/def2-TZVPP level.

5.4.2 Reaction Pathways

Shortly prior to the publication of this work, McMullin, Coles, and Mulvey published very similar results for a series of 1,4 benzene two-fold activations for an aluminyl anion coordinated to a range of different group one cations, including potassium, rubidium, and caesium.[30]

For di-activations involving species which exist in either monomeric and dimeric (or oligo- or poly- meric) forms or equilibria between them, multiple possible pathways exist: in the presented case, the difference is in whether the first activation occurs from a monomer, or from a dimer. The second activation is necessarily dimeric in nature due to the phenyl moiety to be activated already being tethered to an aluminium centre.

Figure 8 shows the possible pathways between the aluminyl (in either monomeric or dimeric forms) and the observed 1,4-diactivation product, as well as the observed monomeric activation product necessarily *inter viam*.

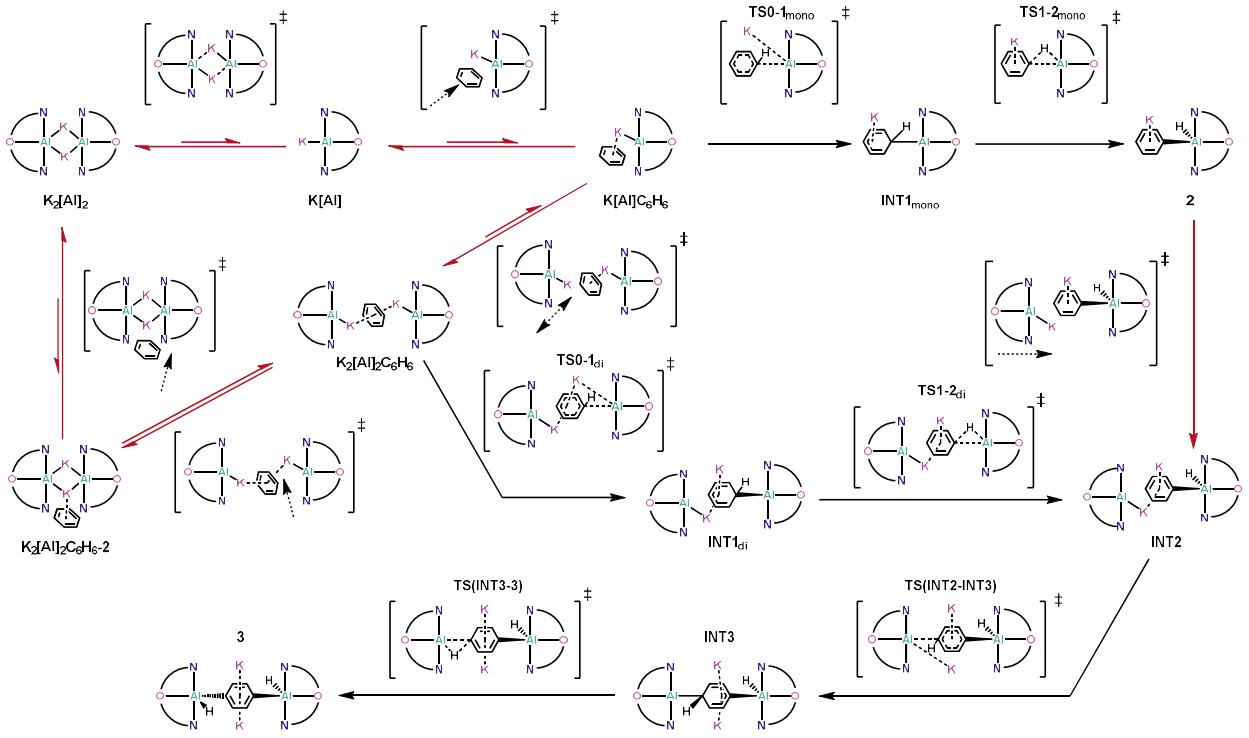


Figure 8 Theorised reaction pathways from the proposed aluminyl dimer "1" to the experimentally observed 1,4-activated benzene dialuminate 3. Structures above arrows within brackets and with double-daggers are transition states, and structures between reaction arrows are local minima. Red arrows indicate transition states we were unable to be elucidated, likely due to their (dis)associative natures. Two possible pathways exist, based upon whether the initial activation is performed by a monomeric or dimeric aluminyl. Both pathways necessarily link in INT2, as the second activation must occur on the already activated ring to produce the di-activated product.

5.4.2.1 Common Pathway

The reaction pathways for both the monomeric and dimeric mechanisms were elucidated along the entirety of each pathway with the exception of associative/dissociative steps, for which we were (expectedly) unable to discern a local maximum on the potential energy surfaces (PESs) to identify the transition states between the minima, due to their flat shapes and absence of critical points between the connected intermediates. Structures were largely elucidated by working backwards from the experimental solid-state structure of the 1,4-diactivation product **3**. The starting geometry for **3** was taken from the corresponding solid-state structure, keeping only the major component of disordered portions, errant solvent molecules, and the other reaction products within the unit cell (mono- and di- activation products both occur within the same crystal). **TS(INT3-3)** (ifreq = -383.21) was then found *via* a relaxed PES scan along a decreasing hydride-benzene carbon coordinate in Gaussian 09 A.02 (PBE0/BS1 scf=(conver=6) and opt=(gdiis, maxcyc=10) options, without empirical dispersion corrections), taking the local energy maximum along the scan as a starting point and using the Berny eigenvector-following algorithm with the initial Hessian matrix calculated *via* analytical

frequencies, as implemented in Gaussian 16. This did not result in the expected transition state, instead the point along the optimisation which still resembled the scan maximum while having the lowest RMS gradient was selected for a frequency calculation, fortunately yielding a single negative eigenvalue, but not subjected to transition state optimisation. The single imaginary mode taken from structure **TS(INT3-3)** was then subjected to intrinsic reaction coordinate calculations in both directions, confirming it linked to **3** and leading to structure **INT3**. **TS(INT2-INT3)** (ifreq = -126.71 cm^{-1}) was found in a similar fashion to **TS(INT3-3)**, although starting from **INT3** and scanning along the corresponding increasing Al-C distance, and the TS optimisation of the scan maximum yielded the expected structure. **INT2** was again found by following the IRC of **TS2-3**'s imaginary mode to a new intermediate. Backwards from **INT2** the two possible pathways diverge.

5.4.2.2 Monomeric Pathway

Although several scans (lengthening Al'-C1, Al'-C4, K'-C1, K'-C4) were attempted to dissociate **2** from **INT2**, none were successful in elucidating a corresponding transition state, all finding smooth curves with no intermediate local maximum. Consequently, a starting point for structure **2** was generated by taking **3** and deleting one half of the dimer (leaving the benzene whole and with the necessary extra proton) before subsequent optimisation. The same process as previous was used to find **TS1-2$_{mono}$** (ifreq = -351.52 cm^{-1}), *i.e.* scanning along a decreasing hydride-carbon coordinate and TS optimising the scan maximum. **INT1$_{mono}$** was found *via* IRC from **TS1-2$_{mono}$**'s imaginary mode. **TS0-1$_{mono}$**, and subsequently **K[Al]C_6H_6** from **TS0-1$_{mono}$**'s imaginary mode, was found by scanning from **INT1$_{mono}$** along the corresponding increasing aluminium-carbon coordinate and performing a TS optimisation as above, however the algorithm led to errant methyl rotation on a tert-butyl group on the backbone. Instead, the optimisation steps were manually inspected and a likely candidate step selected. Performing a frequency calculation on this geometry did indeed reveal a single imaginary mode, and this structure was resubmitted for TS optimisation, leading to **TS0-1$_{mono}$** (the initial guess structure and the optimised structure differed by 0.10 $kcalmol^{-1}$, although the stretching frequency changed from -33.11 to -118.14 cm^{-1}, indicating a larger, more localised movement of the hydrogen in the optimised TS).

Similarly, a dissociation process to link **K[Al]C_6H_6** and **K[Al]** was sought, however no transition state was found. One structure contained a low-frequency eigenvalue (-10.08 cm^{-1}) corresponding to a coupled benzene-tert-butyl rocking mode, however neither direction of the IRC corresponds to the dissociation of benzene. **K[Al]** was instead found by taking the solid-

state structure of [(**TIPSNON**)AlI] and replacing the iodine with a potassium before geometry optimisation. **K[Al]** is the intended starting material as the presumed monomeric reduction product of [(**TIPSNON**)AlI].

5.4.2.3 Dimeric Pathway

The dimeric path was found in the "forward" fashion rather than the "reverse" fashion used above for the monomeric pathway.

Structure **K_2[Al]$_2$** was found with some difficulty. A previously optimised structure of K_2[Al(**^{tBu}NON**)]$_2$ with ^{t}Bu groups instead of Si^{i}Pr$_3$ groups was taken as a starting point, removing the ^{t}Bu groups and replacing them with Si^{i}Pr$_3$ groups, rotating each isopropyl moiety manually in GaussView to avoid egregious steric clashes. This structure was then optimised at the BP86/STO-3G level of theory, and a suitable structure optimised again at the BP86/6-31G** level of theory (each without frequencies). The resultant structure was finally optimised again at the matching PBE0-D3BJ/BS1, yielding **K_2[Al]$_2$**.

Scans increasing the Al-Al, or an Al-K distance in **K_2[Al]$_2$** were attempted and produced no discernible intermediate local maximum, and thus no candidate for the dissociation transition state, as expected from the other a/dissociative steps.

K_2[Al]$_2$$C_6H_6$-2 was found by starting with **K_2[Al]$_2$** and placing a benzene nearby the molecule and performing a geometry optimisation. Again, scans were performed moving the benzene away from the complex, but no intermediate local maximum was determined to use for a transition state. **K_2[Al]$_2$$C_6H_6$** was found by scanning along a decreasing C-K distance in **K_2[Al]$_2$$C_6H_6$-2** followed by a geometry optimisation (again, no candidate for the transition state between the two was found).

Scanning a decreasing Al-C distance in **K_2[Al]$_2$$C_6H_6$** yielded an appropriate candidate for **TS0-1$_{di}$**, elucidating the transition state, and from the transition state the IRC method was again used to lead to **INT1$_{di}$**. From **INT1$_{di}$**, a scan decreasing the appropriate Al-H distance yielded an appropriate candidate for transition state **TS1-2$_{di}$**, confirmed in the same method as above. The IRC method then confirmed **TS1-2$_{di}$** linked to the existing structure for **INT2**.

5.4.2.4 Reaction Profile

Figure 9 shows the elucidated reaction profile for both the monomeric and dimeric pathways with approximate relative energies to the arbitrary 0 of the potassium bridged aluminyl dimer **K_2[Al]$_2$**. Each process proceeds in a similar fashion, starting with nucleophilic attack of a

benzene carbon by the aluminyl, with the potassium associated with the aluminium serving to polarise and presumably activate the benzene in the transition state, leading to a Meisenheimer complex, followed by hydride transfer from the C_6H_6 to the aluminium, forming an aluminate. The majority of enthalpy released is evidently from the hydride transfer steps. Once the aluminate is formed, the process is repeated on the 4 position of the phenyl moiety with a second equivalent of aluminyl.

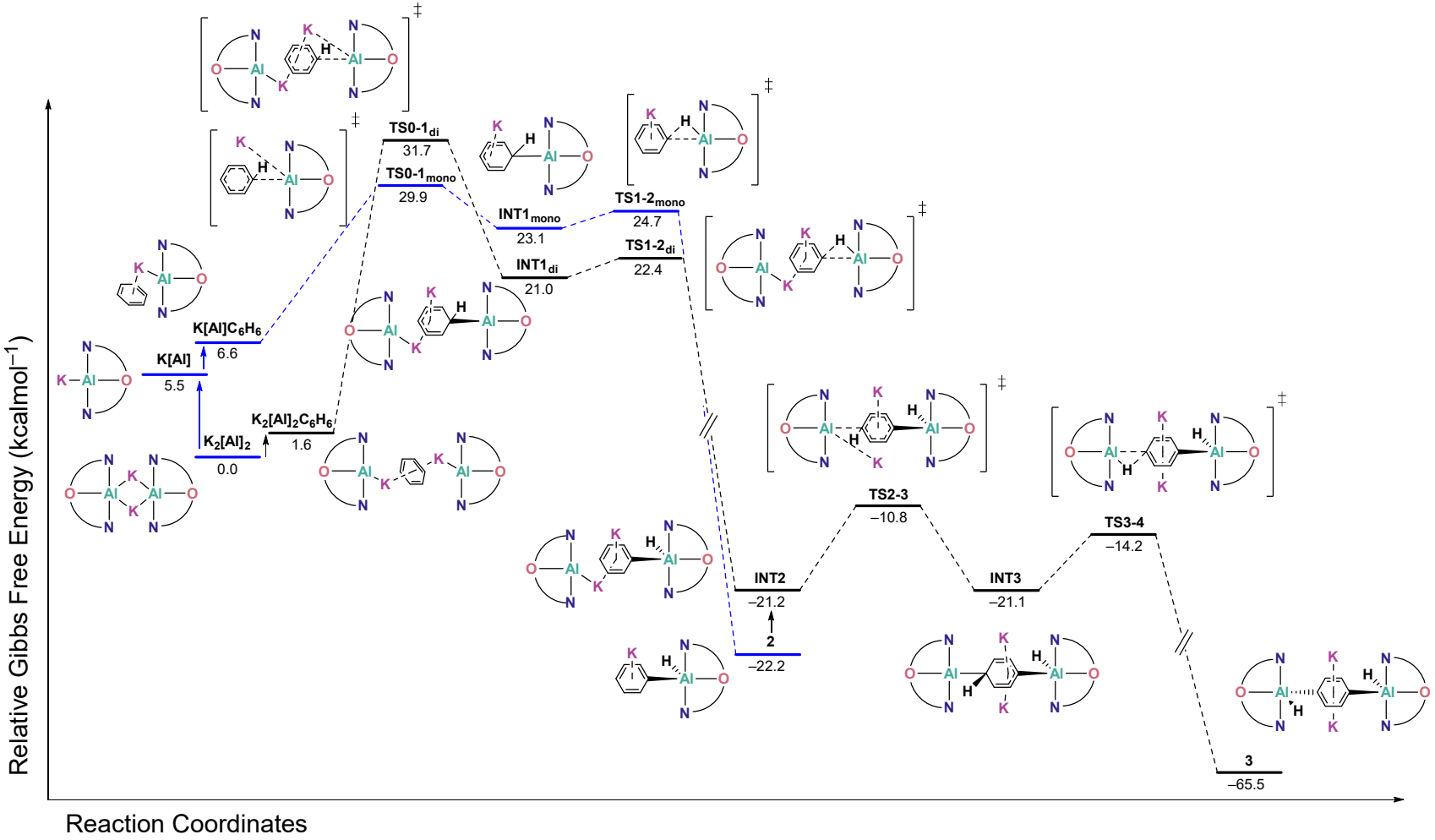


Figure 9 Reaction profile for the 1,4-di-activation of benzene by "1". The reaction profile arbitrarily chooses the potassium bridged dimer as the relative Free Energy "0". The first Al-C nucleophilic attack transition state for both the monomeric and dimeric paths until hydride migration from the C_6H_6 moiety to the aluminium forms the first aluminate, followed by the second Al-C nucleophilic attack transition state and the final hydride migration to form the observed 1,4-dialuminate "3", with the second large enthalpic release. Double bars along dotted lines in the diagram represent omitted, discontinuous changes in the energy axis. Vertical arrows represent structural changes without elucidated transition states, which are all associative/dissociative steps. Monomeric pathway in blue, dimeric/combined in black.

5.4.3 Comparison with Experiment

The Al-C nucleophilic attack is evidently the rate determining step in each part of the process for both the monomeric and dimeric pathways. This barrier is similar in both the monomeric (29.9 kcalmol^{-1}) and dimeric (31.7 kcalmol^{-1}) pathways, with the monomeric pathway slightly lower by 1.8 kcalmol^{-1}, which is barely distinguishable within similar methodological errors.[27] However, if the monomeric aluminyl is formed and then reacts with benzene before being able to dimerise, as if it were reduced from the corresponding aluminium iodide complex (which is monomeric, at least in the solid state) in dilute conditions and thus considering the monomer as the energetic "0", then the monomeric pathway is more energetically favoured, having a barrier height of only 24.4 kcalmol^{-1}. In each case, the hydride transfer has an activation barrier of less than 1.6 kcalmol^{-1}, and is, as expected, essentially barrierless.

These results are similar to those reported by Harder and co-workers,[28] showing that a Meisenheimer-intermediate mechanism is more facile that an oxidative addition-type mechanism for aluminyls, with a calculated barrier of 30.3 kcalmol^{-1} (using the ωB97XD-PCM(benzene)/6-311+G**//ωB97XD-PCM(benzene)/6-31+G** method[16]) for Roesky's (deprotonated) β-diketiminate potassium aluminyl,[29] which experimentally performs C-H activation of benzene over a period of 7 days at 35 °C. This activation barrier does not agree well with experiment, with the Eyring equation predicting a $t_{1/2}$ of *ca.* 10 years for such an energy, suggested to be due to overestimation of entropic factors in the original report.

The activation barrier herein reported (24-32 kcalmol^{-1}) agrees with the previously reported results. Despite the activation proceeding rapidly at room temperature, the Eyring equation predicts a half-life of 609 years at 298.15 K for the monomeric barrier of 31.7 kcalmol^{-1}, and 23.8 hours for the dimeric $\Delta G^{\ddagger}$ = 24.4 kcalmol^{-1}, and we suggest a similar overestimation of entropic effects (*ca.* 4 kcalmol^{-1}), which leads to a half-life of *ca.* 2 minutes at 25 °C for the monomeric "0" pathway, or *ca.* 12 days for the dimeric "0" $\Delta G^{\ddagger}$.

Harder and co-workers also shed light on the para-selectivity, showing a thermodynamic preference for the 1,4-substitution using the parent AlH_2^{2-} aluminyl, which the authors deem due to templating by the potassiums. They also calculate barriers of $\Delta G^{\ddagger}$ = 31.8 kcalmol^{-1} for the first, and $\Delta G^{\ddagger}$ = 34.3 kcalmol^{-1} for the second activations of benzene for the Roesky aluminyl (diisopropylphenyl moieties computationally pruned to phenyl, likely lowering the activation barrier by decreasing steric interactions). In contrast, the second nucleophilic attack transition state for **TS2-3** is calculated to have an activation barrier of only 10.3 kcalmol^{-1},

significantly lower (by at least 14 kcalmol^{-1}) than the initial Meisenheimer intermediate formation barrier of 24-32 kcalmol^{-1}.

McMullin, Coles, and Mulvey[30] also report similar results for the differences between the monomeric and dimeric forms of the first C-H activation of benzene for rubidium and caesium aluminyls, calculating the dimeric forms to have a barrier *ca.* 18 kcalmol^{-1} lower than the monomeric forms.

5.4.4 Summary

Overall, a mechanism is proposed for the formation of the 1,4-diactivation of benzene which matches similar computational work by both Harder and coworkers[28] and McMullin, Coles, and Mulvey and coworkers.[30] Two pathways, one from a monomeric aluminyl anion and one from the dimeric, were investigated, yielding similar barrier heights, with the small differences going some way to explain the experimentally observed mixture of mono- and di- substitution events of benzenes.

5.5 References

[1] Kallmeier, F.; Matthews, A. J. R.; Nelmes, G. R.; Lawson, N. R.; Hicks, J., *Dalton Trans.*, **2024**, *53*, 12450
[2] Kallmeier, F.; Nelmes, G. R.; McMullin, C. L.; Edwards, A. J.; Hicks, J., *Chem. Sci.*, **2025**, *16*, 10750
[3] Runge, J. M., *A Brief History of Aluminum and Its Alloys.* In: *The Metallurgy of Anodizing Aluminum*., **2018**, Springer, Cham
[4] Cordero, B.; Gómez, V.; Platero-Prats, A. E.; Revés, M.; Echeverría, J.; Cremades, E.; Barragan, F.; Alvarez, S., *Dalton Trans.*, **2008**, 2832
[5] Vanýsek, P., *CRC Handbook of Chemistry and Physics*, **1989**, *91*, D-221, CRC Press, Boca Raton
[6] Friedel, C.; Crafts, J. M., *Compt. Rend.*, **1877**, *84*, 1392
[7] Brown, T. L.; LeMay, H. E. Jr.; Bursten, B. E., *Chemistry: The Central Science*, **2000**, *8*, 270, Prentice-Hall, Upper Saddle River
[8] Hicks, J.; Vasko, P.; Goicoechea, J. M.; Aldrige, S., *Nature*, **2018**, *557*, 92
[9] Hicks, J.; Vasko, P.; Goicoechea, J. M.; Aldrige, S., *J. Am. Chem. Soc.*, **2019**, *141*, *28*, 11000
[10] a) Hicks, J.; Vasko, P.; Goicoechea, J. M.; Aldrige, S., *Angew. Chem. Int. Ed.*, **2021**, *60*, 1702; b) Coles, M. P.; Evans, M. J., *Chem. Commun.*, **2023**, *59*, *5*, 503; c) Coles, M. P., *Chem. Commun.*, **2025**, *61*, *78*, 15125
[11] a) Anand, B. N.; Krossing, I.; Nöth, H., *Inorg. Chem.*, **1997**, *36*, *9*, 1979; b) Agou, T.; Yanagisawan, T.; Sasamori, T.; Tokitoh, N., *Bull. Chem. Soc. Jpn.*, **2016**, *89*, 1184; c) Yanagisawa, T.; Mizuhata, T.; Tokitoh, N., *Heteroatom Chem.*, **2018,** *29*, e21465; d) Kong, R. Y.; Crimmin, M. R., *Dalton Trans.*, **2021**, *50*, 7810
[12] Gaussian 16, Revision A.02, M. J. Frisch, G. W. Trucks, H. B. Schlegel, G. E. Scuseria, M. A. Robb, J. R. Cheeseman, G. Scalmani, V. Barone, G. A. Petersson, H. Nakatsuji, X. Li, M. Caricato, A. Marenich, J. Bloino, B. G. Janesko, R. Gomperts, B. Mennucci, H. P. Hratchian, J. V. Ortiz, A. F. Izmaylov, J. L. Sonnenberg, D. Williams-Young, F. Ding, F. Lipparini, F. Egidi, J. Goings, B. Peng, A. Petrone, T. Henderson, D. Ranasinghe, V. G. Zakrzewski, J. Gao, N. Rega, G. Zheng, W. Liang, M. Hada, M. Ehara, K. Toyota, R. Fukuda, J. Hasegawa, M. Ishida, T. Nakajima, Y. Honda, O. Kitao, H. Nakai, T. Vreven, K. Throssell, J. A. Montgomery, Jr., J. E. Peralta, F. Ogliaro, M. Bearpark, J. J. Heyd, E. Brothers, K. N. Kudin, V. N. Staroverov, T. Keith, R. Kobayashi, J. Normand, K. Raghavachari, A. Rendell, J. C. Burant, S. S. Iyengar, J. Tomasi, M. Cossi, J. M. Millam, M. Klene, C. Adamo, R. Cammi, J. W. Ochterski, R. L. Martin, K. Morokuma, O. Farkas, J. B. Foresman, and D. J. Fox, Gaussian, Inc., Wallingford CT, **2016**.
[13] Ernzerhof, M.; Scuseria, G. E., *J. Chem. Phys.*, **1999**, *110*, 5029
[14] Grimme, S.; Ehrlich, S.; Goerigk, L., *J. Comp. Chem.*, **2011**, *32*, 1456.
[15] a) Bergner, A.; Dolg, M.; Küchle, W.; Stoll, H.; Preuß, H., *Mol. Phys.*, **1993**, *80*, 1431; b) Fuentealba, P.; Preuß, H.; Stoll, H.; Szentpály, L. V., *Chem. Phys. Lett.*, **1982**, *89*, 418
[16] Hariharan, P. C.; Pople, J. A., *Theor. Chim. Acta.*, **1973**, *28*, 213; b) Hehre, W. J.; Ditchfield, R.; Pople, J. A., *J. Chem. Phys.*, **1972**, *56*, 2257 c) Chai, J.-D., Head-Gordon, M., *Phys. Chem. Chem. Phys.*, **2008**, *10*, 6615
[17] Huo, R.; Armstrong, A. J.; Nelmes, G. R.; Lawes, D. J.; Edwards, A. J.; McMullin, C. L.; Hicks, J., *Chem. Eur. J.*, **2024**, *30*, e202400662
[18] Ganzenmüller, G.; Berkaïne, N.; Fouqueau, A.; Casida, M. E.; Reiher, M., *J. Chem. Phys.,* **2005**, *122*, 234321
[19] a) Dunning, T. H. Jr., *J. Chem. Phys.*, **1989**, *90*, 1007; b) Kendall, R. A.; Dunning, Jr.; Harrison, R. J., *J. Chem. Phys.*, **1992**, *96*, 6796
[20] a) Klamt, A.; Schüürmann, G. J., *Chem. Soc., Perkin Trans.* **1993**, *2*, 799; b) Andzelm, J.; Kölmel, C.; Klamt, A. J., *Chem. Phys.*, **1995**, *103*, 9312; c) Barone, V.; Cossi, M., *J. Phys. Chem. A*, **1998**, *102*, 1995; d) Cossi, M.; Rega, N.; Scalmani, G.; Barone, V., *J. Comput. Chem.*, **2003**, *24*, 669
[21] Falivene L.; Cao, Z.; Petta, A.; Serra, L.; Poater, A.; Oliva, R.; Scarano, V.; Cavallo, L., *Nat. Chem.*, **2019**, *11*, 872
[22] Gransbury, G. K.; Corner, S. C.; Kragskow, J. G. C.; Evans, P.; Yeung, H. M.; Blackmore, W. J. A.; Whitehead, G. F. S.; Vitorica-Yrezabal, I. J.; Oakley, M. S.; Chilton, N. F.; Mills, D. P., *J. Am. Chem. Soc*., **2023**, *145*, *41*, 22814
[23] Ellis, J. E.; Flom, E. A., *J. Organomet. Chem.*, **1975**, *99*, *2*, 263
[24] Cotton, F. A.; Yagupsky, G., *Inorg. Chem.*, **1967**, *6*, *1*, 15
[25] Torubaev, Y. V.; Skabitskiy, I. V.; Rusina, P.; Pasynskii, A. A.; Raic, D. K.; Singh, D., *Cryst. Eng. Comm.*, **2018**, *20*, 2258
[26] Weigend, F., Ahlrichs, R., *Phys. Chem. Chem. Phys*., **2005**, *7*, 3297
[27] Goerigk, L.; Hansen, A.; Bauer, C.; Ehrlich, S.; Najibi, A.; Grimme, S., *Phys. Chem. Chem. Phys.*, **2017**, *19*, 32184
[28] Grams, S.; Mai, J.; Langer, J.; Harder, S., *Dalton Trans.*, **2022,** *51*, *33*, 12476
[29] Cui, C.; Roesky, H. W.; Schmidt, H.-G.; Noltemeyer, M.; Hao, H.; Cimpoesu, F.; *Angew. Chem. Int. Ed.,* **2000** *39*, *23*, 4274

[30] Gentner, T. X., Evans, M. J., Kennedy, A. R., Neale, S. A., McMullin, C. L., Coles, M. P., Mulvey, R. E., *Chem. Commun.*, **2022**, *58*, 1390